AB INITIO STUDY OF RAMAN AND OPTICAL SPECTRA OF CRYSTALLINE MATERIALS AND THEIR TEMPERATURE DEPENDENCE

Dissertation présentée en vue de l'obtention du grade de
Docteur en Sciences de l'Ingénieur

YANNICK GILLET

Membres du jury
Prof. Bernard Piraux, président
Prof. Xavier Gonze, promoteur
Prof. Gian-Marco Rignanese, secrétaire
Prof. Philippe Ghosez
Prof. Jens Kreisel

Janvier 2017

Yannick Gillet: *Ab initio study of Raman and optical spectra of crystalline materials and their temperature dependence,* January 2017

If we knew what it was we were doing,
it would not be called research, would it ?

— A. Einstein

To my parents

PUBLICATIONS

Some ideas and figures have appeared previously in the following publications, of which I am a (co-)author:

[1] Y. Gillet, M. Giantomassi, and X. Gonze, "First-principles study of excitonic effects in Raman intensities," Phys. Rev. B **88**, 094305 (2013).

[2] B. Van Troeye, Y. Gillet, S. Poncé, and X. Gonze, "First-principles characterization of the electronic and optical properties of hexagonal $LiIO_3$," Opt. Mater. **36**, 1494–1501 (2014).

[3] S. Poncé, G. Antonius, Y. Gillet, P. Boulanger, J. Laflamme Janssen, A. Marini, M. Côté, and X. Gonze, "Temperature dependence of electronic eigenenergies in the adiabatic harmonic approximation," Phys. Rev. B **90**, 214304 (2014).

[4] S. Poncé, Y. Gillet, J. Laflamme Janssen, A. Marini, M. Verstraete, and X. Gonze, "Temperature dependence of the electronic structure of semiconductors and insulators," J. Chem. Phys. **143**, 102813, – (2015).

[5] Y. Gillet, M. Giantomassi, and X. Gonze, "Efficient on-the-fly interpolation technique for Bethe-Salpeter calculations of optical spectra," Comput. Phys. Comm. **203**, 83–93 (2016).

[6] M. C. Weber, M. Guennou, C. Toulouse, M. Cazayous, Y. Gillet, X. Gonze, and J. Kreisel, "Temperature evolution of the band gap in $BiFeO_3$ traced by resonant Raman scattering," Phys. Rev. B **93**, 125204 (2016).

[7] X. Gonze et al., "Recent developments in the ABINIT software package," Comput. Phys. Comm. **205**, 106 (2016).

[8] E. del Corro et al., "Atypical exciton-phonon interactions in WS_2 and WSe_2 monolayers revealed by resonance Raman spectroscopy," Nano Lett. **16**, 2363–2368 (2016).

[9] J. Laflamme Janssen, Y. Gillet, S. Poncé, A. Martin, M. Torrent, and X. Gonze, "Precise effective masses from density functional perturbation theory," Phys. Rev. B **93**, 205147 (2016).

[10] S. P. Ramkumar, Y. Gillet, A. Miglio, M. J. van Setten, X. Gonze, and G.-M. Rignanese, "First-principles investigation of the structural, dynamical, and dielectric properties of kesterite, stannite, and PMCA phases of Cu_2ZnSnS_4," Phys. Rev. B **94**, 224302 (2016).

[11] Y. Gillet, S. Kontur, M. Giantomassi, C. Draxl, and X. Gonze, "Ab initio approach to second-order resonant Raman scattering including exciton-phonon interaction," Submitted to Scientific Reports (2016).

[12] Y. Gillet, F. Abreu Araujo, and X. Gonze, "ABINITGUI: a Graphical User Interface for the ABINIT software package," To be submitted (2016).

We have seen that computer programming is an art,
because it applies accumulated knowledge to the world,
because it requires skill and ingenuity, and especially
because it produces objects of beauty.

— Donald E. Knuth, 1974

ACKNOWLEDGMENTS

Firstly, I would like to express my sincere gratitude to my advisor Prof. Xavier Gonze for the continuous support of my Ph.D study and related research, for his patience, motivation, and immense knowledge. His guidance helped me in all the time of research and writing of this thesis. I could not have imagined having a better advisor and mentor for my Ph.D study.

Besides my advisor, I would like to thank the other members of my thesis committee: Prof. Gian-Marco Rignanese, Prof. Philippe Ghosez, Prof. Jens Kreisel, and Prof. Bernard Piraux, for their insightful comments and encouragement, but also for the hard questions which incented me to widen my research from various perspectives.

My sincere thanks also goes to Prof. Claudia Draxl, who provided me an opportunity to join her team in Berlin, and who gave access to the laboratory and research facilities.

I thank my fellow lab mates in for the stimulating discussions and for all the fun we have had in the last four years. In particular, I am grateful to Samuel Poncé, for sharing tons of ideas and discussions. I'm at the same time grateful to him as well as Jonathan Laflamme Janssen and Yongchao Jia for sharing my office during several years. I also want to thank Matteo Giantomassi for following my work since I was a master student and Benoit Van Troeye for the numerous interesting discussions we have shared together.

I want to thank all the members of the NAPS who lived in the "Parc Meteo" building with me: Sadia, Anna, David, Vinciane, Fabienne, Abderrezak, Jan, Wei, Guillaume, Viet-Anh, Francesco R. and N., Guodong, Aurélie, Simon, Samuel D. and P., Jean-Joseph, Andres, Aurélien, Viet-Hung, Nicolas D. and L., Gil, Martin, Marco, Guido, Davide, Sriram, Vishank, Benoit, Yongchao, Thierry, Jonathan, Michiel, Matteo, Jean-Michel, Gian-Marco, Jean-Christophe, Xavier D. and G. and Geoffroy.

Last but not the least, I would like to thank my family: my parents, my two sisters Vinciane and Chrystelle, Philippe, and my three nieces Alexandra, Elisabeth and Emeline for supporting me spiritually throughout writing this thesis and in my life in general.

CONTENTS

ACRONYMS

AHC	Allen Heine Cardona
BEC	Born effective charge
BFO	$BiFeO_3$
BSE	Bethe-Salpeter Equation
BZ	Brillouin Zone
DFPT	Density-Functional Perturbation Theory
DFT	Density-Functional Theory
FGR	Fermi-Golden Rule
FP	Frozen phonon
IPA	Independent-Particle Approximation
LEO	Linear Electro-Optic
LDA	Local Density Approximation
MBPT	Many-Body Perturbation Theory
REP	Resonant Excitation Profile
RI	Raman Intensity
RL	Rohlfing and Louie
RPA	Random-Phase Approximation
SHG	Second Harmonic Generation
SOC	Spin-orbit coupling
TMD	Transition Metal Dichalcogenides
ZPR	Zero-Point Renormalization

1 INTRODUCTION

Whenever light propagates in the vacuum or in the air and it meets a different material, several processes may take place at the surface as well as in the bulk, as illustrated in Fig. 1. Reflection and transmission are well-known surface phenomena observed in daily life. The transmitted portion of the light propagates into the bulk region and leads to additional phenomena such as absorption and scattering processes. These latter processes are due to the presence of inhomogeneities: in addition to defects, light may also be scattered due to elementary excitations such as vibrations of the material. Inelastic scattering of light by the quanta of vibrations (phonons) is called either Brillouin or Raman scattering depending whether the phonon is acoustic or not. Raman scattering is the main subject of this thesis.

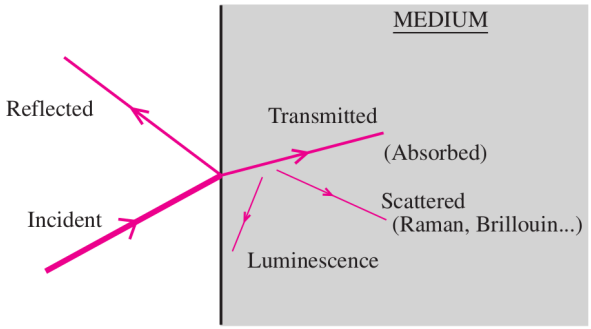

Figure 1: Schematic representation of the different processes involved in light-matter interactions [1].

However, the process of Raman scattering involves interaction with these excitations and therefore is much less intense than elastic scattering, i.e. when the energy is conserved. A schematic representation of a typical Raman experiment is displayed in Fig. 2. Monochromatic light produced by a laser impinges on the sample and the (small) fraction of inelastically scattered light is extracted and amplified with optical devices. The signal is then sent to a computer for the final analysis that produces a Raman spectrum, where the intensity of light is measured with respect to the different scattered frequencies.

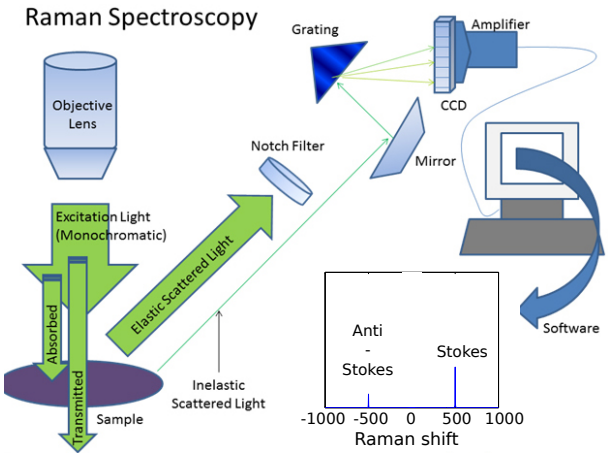

Figure 2: Schematic representation of the Raman spectroscopy. [1]

In Raman spectroscopy, the modification of frequency and intensity of a laser light, inelastically scattered by a material or nanostructure, allows one to collect a rich set of information on the system. This is especially true when the frequency of the incoming light is varied [1, 2].

This relatively low-cost experimental technique is very mature, and used routinely in numerous laboratories worldwide. In most systems, the energy loss is due to the creation of phonons. Raman spectroscopy is therefore widely used to characterize materials by means of their vibrational fingerprint.

Indeed, the position of the features in the Raman spectrum is directly related to the phonon energies. Different possible scattering processes can contribute, depending on the system and on the sensitivity of the experimental setup. The first-order contribution, in which only one phonon is emitted, provides direct information on vibrations with very low crystalline momentum, due to momentum conservation. By contrast, higher-order Raman processes exhibit features coming from the entire Brillouin Zone (BZ). They are more complex and also more difficult to interpret.

The spectrum gives more information than only the position of the peaks (or features of the spectrum). Actually, the intensities are induced by the coupling of the different particles in the material (phonons, electrons, holes ...) with the light. The intensities therefore depend on the material but also on the frequency of the incident light. The dependence

1 Figure extracted from https://www3.nd.edu/~kamatlab/facilities_spectroscopy.html

of the Raman Intensity (RI) on the frequency of the incident light is well-known. It is, for example, used to amplify the Raman response, resulting in the appearance of a resonance phenomenon when the frequency of the exciting light is close to electronic transitions of the investigated system [2]. A simplified view of the process is presented in Fig. 3, in the case of isolated levels. Starting from the ground state level E_0, the incoming light of frequency ν_1 brings the system to a virtual level. Then, the systems goes back to a level differing from the initial level by a quantum of vibration with frequency ν_{vib}. When the light frequency used for the experiment changes, the initial and final states stay the same but the position of the virtual level is modified. At some point, the virtual level may cross the position of a real excited state of the material E_1. In this case, a resonance phenomenon appears and the intensity increases significantly. For condensed matter materials, this pictures is more complex as energy levels are not discrete anymore and form energy bands in the case of a crystal. The resonance appears when the frequency of the incoming light comes close to an electronic resonance (e.g. excitonic absorption peak).

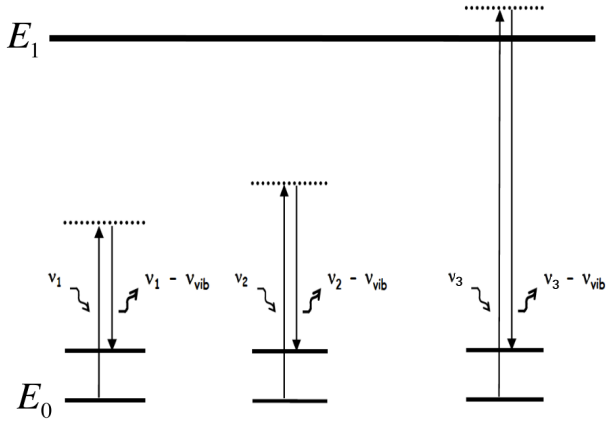

Figure 3: Illustration of the Raman process as the frequency of the light changes.

In such a case, the absolute RI can change by several orders of magnitude, and relative changes between different mode contributions might be observed. Usual experiments take advantage of these resonant conditions to enhance the Raman signal but frequency-dependent Raman spectroscopy can also be used to extract information on electronic and vibrational properties. Unfortunately the second technique is rarely used

in experiments because results are difficult to discuss without a microscopic description of the different processes [3].

In order to interpret experimental results, the use of first-principles techniques comes naturally to one's mind. These techniques are based on the fundamental equations of quantum mechanics and do not require any external parameters. As a consequence, ab initio simulations facilitate the interpretation of experimental results and can be used to predict the behavior of materials under conditions that are difficult to achieve experimentally.

The application of first-principles techniques to the calculation of Raman intensities is not entirely new. In what follows, we provide a brief historical overview of the techniques and methods that have been used so far to study Raman spectra from first principles.

The RI is related to the derivative of the macroscopic dielectric function with respect to collective atomic displacements [3]. Different first-principle formalisms have been proposed for the computation of the dielectric function. These formalisms often trade computational speed for predictive power, or vice versa. In the present thesis, a method that provides an accurate description of the dielectric properties of material was chosen in order to establish the importance of different physical effects, and in particular, excitonic effects.

Within the static limit (i.e. for vanishing light frequency), the dielectric response can be computed with Density-Functional Theory (DFT) [4–6] followed by Density-Functional Perturbation Theory (DFPT) [7–9]. Although DFT is plagued by the well-known band gap problem [6], its prediction of the static dielectric tensor is reasonably accurate (to within 5-10%) except when the gap is very small.[2] Subsequent computation of the derivative of the dielectric tensor with respect to an atomic displacement can be performed by using either finite differences [12] in a Frozen phonon (FP) approach or the $2n + 1$ theorem of perturbation theory [13–15]. Such methodology has been applied in numerous studies [16, 17]. As an example, more than four hundred Raman spectra are provided in the WURM database [18, 19].

The FP approach can be generalized to study frequency-dependent dielectric functions. A general methodology for describing multi-phonon scattering processes up to arbitrary order has been proposed by Knoll and Draxl [20], but its application had been long restricted to the *ab initio* calculations of first-order resonant Raman scattering, in the

2 A true semiconductor might be described as a metal by DFT *e.g.* with usual local or semi-local functionals [10, 11]

Independent-Particle Approximation (IPA), without excitonic effects, e.g. in various superconducting materials [21–23] and ladder compounds [24–26]. It should be stressed, however, that dielectric properties computed within DFT become less reliable when the excitation frequency is comparable to the gap. Not only does the proximity of the resonance increase the need to rely on an accurate band gap, but excitonic effects also drastically modify the optical properties of most semiconductors [1]. The role of excitons in first-order and second-order frequency-dependent Raman spectra of materials had been emphasized in earlier theoretical or semi-empirical studies, based on sum-over-states approaches [1, 3, 27, 28]. The agreement with experiments obtained in these pioneering works is not completely satisfactory with deviations that, in some cases, reach almost one order of magnitude.

The Many-Body Perturbation Theory (MBPT) can be used to correct the inaccuracies of DFT in first-principles calculations of dielectric properties. The band-gap correction is usually treated within the *GW* approximation, while the Bethe-Salpeter Equation (BSE) is the method of choice to introduce excitonic effects [29, 30]. To our knowledge, the BSE has not yet been used to compute RI of solids. This formalism has been applied since 1998 [31] for the first-principles computation of the optical spectra of semiconductors and insulators. Even if its application to simple materials is reasonably frequent nowadays, the calculation of optical properties of complex materials with more than two dozen of atoms in the unit cells is still challenging (see e.g. the work of Kresse *et al.* [32] and Rinke *et al.* [33]) and is still an active field of research, with different algorithmic improvements [34–37].

Excitonic effects can also be addressed within the framework of time-dependent density functional theory [30, 38–40]. This approach, which is computationally cheaper, allows one to include excitonic effects, with an accuracy that depends on the choice of the exchange-correlation kernel. Recent studies reported interesting agreement with experiment for the macroscopic dielectric function (see e.g. Ref. [41]). This route is not pursued in the present study. Instead, we rely on the best theoretical approach available today to compute the frequency-dependent RI, and examine its predictive power in comparison with experimental data.

Experimentally, the second-order part of the Raman spectrum is often used to characterize low-dimensional or layered materials, such as e.g. graphene [42] or graphite [43], and more recently also transition-metal dichalcogenides [44–48]. The few existing first-principles studies relied on the IPA [49, 50], in which the formation of excitons is neglected.

As these low-dimensional materials exhibit very well-defined and specific spectral features [51], their second-order Raman spectra can still be interpreted quite easily, at least concerning the location of the peaks. However, for many applications, bulk materials form the vast majority of relevant materials. Their Raman spectra contain a larger number of features, and are thus difficult to decipher.

On top of all these previous developments, a first objective of this thesis is the evaluation of accurate frequency-dependent Raman intensities for first and second-order scattering processes. A general methodology, based on the evaluation of multiple dielectric function, i.e. FP technique, will allow including excitonic effects at the level of the BSE.

Up to this point, temperature effects have not been discussed yet. In the materials, the atoms are not frozen but are vibrating around their equilibrium positions. Even at 0K, the atoms move because of the zero-point motion. As temperature increases, the vibrations of the atoms are more and more activated. In our materials, the inclusion of temperature has two main effects: a modification of the lattice parameters induced by thermal expansion and a change of electronic properties via electron-vibration coupling. The former effect arises from the anharmonic shape of the potential felt by the atoms. In this work, we will mainly assume this effect is small with respect to the latter[3]. Indeed, in our calculations, the potential will be approximated as quadratic. As a second effect of temperature, the vibrations can influence the electronic properties of the materials. As an example, the band gap of a semiconductor materials usually shrinks with increasing temperature. Actually, the entire band structure changes at 0K and at any temperature if electron-vibrations interactions are taken into account. As a consequence, optical properties are also modified by these vibrations and in particular resonance Raman conditions may change.

A large effort has been devoted to the calculation of temperature dependence of the band structure from first principles. Allen, Heine, and Cardona have developed a theory [52–54] to compute the Zero-Point Renormalization (ZPR) as well as the temperature dependence of electronic eigenenergies. The so-called Allen Heine Cardona (AHC) theory originates from the diagrammatic method of many-body perturbation theory. It has been applied in several recent contributions in the field, including the computation of temperature-dependence of the optical

3 For example, for silicon at room temperature, the change of the direct gap with temperature induced by the thermal expansion is -0.3×10^{-4} eV/K while the total temperature coefficient is -2.2×10^{-4} eV/K [52].

properties [55], the computation of the surprisingly large ZPR of the diamond bandgap [56, 57], the demonstration of large non-rigid ion corrections for molecules [58], the inclusion of dynamical effects beyond the adiabatic approximation [59–61], the study of the anharmonic electron-phonon contribution to the indirect bandgap of diamond [62], and the inclusion of electronic many-body effects (in the GW approximation) in the ZPR of diamond [63], noticing a large increase of the renormalization with respect to DFT. Also, the confusion in the theoretical understanding of the relationship between molecular dynamics, FP, and AHC as well as the inaccuracies in first-principles software implementations of AHC have been largely eliminated in two recent publications [57, 64].

In this thesis, we want to pursue this effort and include temperature dependence of the band structure for optical properties, to obtain a temperature-dependent dielectric function. As a second objective of this thesis, we aim at describing temperature effects on the resonance Raman.

The thesis is structured as follows. Chap. 2 reviews the ab initio calculations of optical properties. It presents numerical techniques which allow to decrease their computational load. Chap. 3 details the methodology that we have developed to compute first-principles frequency-dependent Raman intensities. This methodology is then applied to silicon at the first and second-order and validated by comparison with experimental measurements. In Chap. 4, we study zinc-blende materials that require additional caution because of the polarity of the vibrations that can couple with the light. We also study 2D Transition Metal Dichalcogenides (TMD), WS_2 and WSe_2 and show the importance of excitonic effects in the resonance effects to reproduce the differences between the two materials. The temperature effects are studied in Chap. 5. We first review the calculation of temperature-dependent band structure. We apply it for calculating temperature-dependent optical properties at the BSE level and finally for resonance RI of silicon. Finally, we study a more complex material, $BiFeO_3$ (BFO) in Chap. 6. Recent experimental measurements are described and a complete ab initio study is performed starting from ground state properties towards resonant RI and temperature-dependent band structure.

2 AB INITIO SIMULATION OF OPTICAL PROPERTIES

The simulation of optical properties from first principles can be done at several approximation levels ranging from computationally very cheap but not very accurate towards highly expensive and accurate techniques.

In this chapter, we briefly introduce the main ingredients that will be used extensively in the rest of the thesis.

The final goal is the simulation of the dielectric function, which is the main quantity of interest for optical properties. As a first step, the ground state of the material must be computed, giving access to the wavefunctions and the eigenenergies of the system, as described in Sec. 2.2.1. We then move to optical properties, that can be evaluated easily at the independent-particle level, as illustrated in Sec. 2.2.2. If more accurate dielectric functions are needed, the MBPT includes many-body effects, as described in Sec. 2.3. Usually, the calculations within the BSE framework are quite expensive and we therefore developed an interpolation technique to speed up the convergence of such calculations. An article describing this methodology has been published and is presented in Sec. 2.4.

2.1 INTRODUCTION

A macroscopic polarization $\mathbf{P}(t)$ is induced by an applied electric field at several orders

$$\mathbf{P}(t) = \int dt' \chi^{(1)}(t,t')\mathbf{E}(t') + \int dt' dt'' \chi^{(2)}(t,t',t'')\mathbf{E}(t')\mathbf{E}(t'') + ... \tag{1}$$

From that expression one can define the first-order susceptibility $\chi^{(1)}$, the second-order susceptibility $\chi^{(2)}$ and so forth. By Fourier transforming, and using the invariance under time translations, the frequency-domain expression for the polarization becomes

$$\begin{aligned}\mathbf{P}(\omega) = {} & \chi^{(1)}(\omega)\mathbf{E}(\omega) \\ & + \int\int d\omega' d\omega'' \delta(\omega - \omega' - \omega'')\chi^{(2)}(-\omega,\omega',\omega'')\mathbf{E}(\omega')\mathbf{E}(\omega'') \\ & + ...\end{aligned} \tag{2}$$

In linear optics, we consider only the first-order response. The displacement field $\mathbf{D}$ is then obtained from

$$\mathbf{D}(\omega) = \mathbf{E}(\omega) + 4\pi\mathbf{P}(\omega) = \varepsilon_{\mathbf{M}}(\omega)\mathbf{E}(\omega), \tag{3}$$

where the well-known macroscopic dielectric tensor is defined by

$$\varepsilon_{\mathbf{M}}(\omega) = 1 + 4\pi\chi(\omega). \tag{4}$$

The second-order susceptibility plays a major role for non-linear optics, applied for example to frequency doubling. It also plays a role in Raman intensities in the case of polar optical phonons. This will be explained in Sec. 3.2.

In the remaining of this chapter, we focus on the computation of linear optical properties from first principles.

2.2 BASIC INGREDIENTS

In this section, we present a very brief reminder of the main ingredients that will be needed afterwards, mainly electronic states in terms of their energies and the wavefunctions, and the dielectric function.

2.2.1 *Electronic energies and wavefunctions*

According to the basic principles of quantum mechanics, in the adiabatic approximation, the physical properties of a system of N electrons in an external potential V_{ext} (such as typically induced by the nuclei) can be obtained by solving the Schrödinger equation

$$\left[\sum_i \left(-\frac{1}{2}\nabla_i^2 + V_{ext}(\mathbf{r}_i)\right) + \sum_{i<j} \frac{1}{|\mathbf{r}_i - \mathbf{r}_j|}\right] \Psi_n(\mathbf{x}_1, \mathbf{x}_2, \ldots, \mathbf{x}_N) = E_n^{el}\Psi_n(\mathbf{x}_1, \mathbf{x}_2, \ldots, \mathbf{x}_N) \tag{5}$$

where i is an index running over the electrons, $\sum_{i<j} \frac{1}{|\mathbf{r}_i - \mathbf{r}_j|}$ is the interaction potential, $\mathbf{x}_i$ are the coordinate of the electrons (i.e. space and spin), and E_n^{el} is the total electronic energy of the eigenstate n. Atomic units are used throughout this work ($\hbar = m_e = e = \frac{4\pi}{\varepsilon_0} = 1$).

However, Eq. (5) cannot be solved exactly except for systems with very few electrons. For this reason, we are going to reformulate the problem in terms of the density in the framework of DFT. For a complete review of DFT, we refer the reader to Ref. [6]. DFT allows one to replace this

very difficult problem in terms of the density of the system thanks to the Hohenberg-Kohn theorems [4].

Thanks to these two theorems, all the physical properties of the ground state can be expressed in terms of the ground state density n that minimizes the energy functional

$$E[n] = T_s[n] + \int n(\mathbf{r}) V_{ext}(\mathbf{r}) + \frac{1}{2} \int \frac{n(\mathbf{r}_1) n(\mathbf{r}_2)}{|\mathbf{r}_1 - \mathbf{r}_2|} d\mathbf{r}_1 d\mathbf{r}_2 + E_{xc}[n], \quad (6)$$

where $T_s[n]$ is the kinetic energy of the system and $E_{xc}[n]$ is the exchange-correlation functional.

In the formulation of DFT proposed by Kohn and Sham [5] in 1965, the minimization of the energy functional is replaced by a set of equations for a fictitious set of non-interacting electrons whose density equals the one of the interacting system. The wavefunctions of the non-interacting system are obtained by solving the set of self-consistent equations

$$\left(-\frac{1}{2} \nabla^2 + V_{KS}(\mathbf{r}) \right) \psi_i(\mathbf{r}) = \epsilon_i \psi_i(\mathbf{r}), \quad (7)$$

for the effective potential

$$V_{KS}(\mathbf{r}) = V_{ext}(\mathbf{r}) + \int \frac{n(\mathbf{r}_1)}{|\mathbf{r}_1 - \mathbf{r}|} d\mathbf{r}_1 + v_{xc}[n](\mathbf{r}), \quad (8)$$

where $v_{xc}[n](\mathbf{r}) = \frac{\partial E_{xc}[n]}{\partial n(\mathbf{r})}$.

The theory presented above is exact in principle, however, the functionals E_{xc} and therefore v_{xc} are not exactly known and must be approximated. Most of the results presented in this work are obtained with the so-called Local Density Approximation (LDA) where $E_{xc}[n]$ is simply given by the exchange-correlation energy of the homogeneous electron gas [5].

As all this work focuses on periodic systems, we index the electronic states with $n\mathbf{k}\sigma$ with n being a band index, $\mathbf{k}$ the BZ vector and σ the spin index. Spin indices are generally omitted as we mainly deal with non-spin polarized systems.

From DFT, a set of Kohn-Sham wavefunctions and the corresponding eigenenergies $\{\psi_{n\mathbf{k}}, \epsilon_{n\mathbf{k}}\}$ are therefore available. It is important to stress, however, that the Kohn-Sham energies do not have a direct physical meaning: they are just auxiliary tools used to obtain the ground-state density of the interacting system of electrons. Nevertheless, the eigenenergies obtained within LDA provide a good starting point for band dispersions in many solids. However, it usually fails to provide good band

gaps, this problem being well-known as the band-gap failure of DFT. There is an exact relation connecting the true fundamental gap E_g to the exact Kohn-Sham gap

$$E_g = E_g^{KS} + \Delta_{xc}, \tag{9}$$

where Δ_{xc} is a term that originates from the discontinuity in v_{xc} upon addition of a particle [65–67]. Functionals such as LDA usually underestimate the gap, with relative errors that can be as high as 100% [29].

In order to compute excited states properties, including many-body effects consistently, one can rely on MBPT. Quantities of interest are spectroscopic quantities such as photoemission and inverse photoemission spectra, optical spectra as well as Raman spectra, as we will see in Chap. 3. In this framework, the quasiparticle amplitudes ψ_i^{QP} and the quasiparticle energies ϵ_i^{QP} are computed by solving the following non-linear equation

$$\left(-\frac{1}{2}\nabla^2 + V_{ext}(\mathbf{r}) + V_H(\mathbf{r})\right)\psi_i^{QP}(\mathbf{r}) + \int d\mathbf{r}'\Sigma(\mathbf{r},\mathbf{r}';\omega = \epsilon_i^{QP})\psi_i^{QP}(\mathbf{r}') = \epsilon_i^{QP}\psi_i^{QP}(\mathbf{r}), \tag{10}$$

with $V_{ext}(\mathbf{r})$ the electrostatic potential of the ions and $V_H(\mathbf{r})$ the Hartree potential originating from the electronic density $n(\mathbf{r})$. In Eq. (10), $\Sigma(\mathbf{r},\mathbf{r}';\omega)$ is the self-energy, that, in the so-called GW approximation, is given by

$$\Sigma(\mathbf{r},\mathbf{r}';\omega) = \frac{i}{2\pi}\int d\omega' G(\mathbf{r},\mathbf{r}',\omega+\omega')W(\mathbf{r},\mathbf{r}',\omega') \tag{11}$$

where G is the Green's function, that defines the probability amplitude for the propagation of an added or removed electron in a many-body system [68] and W the screened Coulomb interaction [30]

$$W(\mathbf{r},\mathbf{r}') = \int d\mathbf{r}''\epsilon^{-1}(\mathbf{r},\mathbf{r}'')v(\mathbf{r}''-\mathbf{r}'), \tag{12}$$

with $\epsilon^{-1}(\mathbf{r},\mathbf{r}')$ the inverse microscopic dielectric function and $v(\mathbf{r})$ the Coulomb potential,

$$v(\mathbf{r}) = \frac{1}{|\mathbf{r}|}. \tag{13}$$

It can be shown that G obeys to the Dyson equation [68]

$$G(\mathbf{r},\mathbf{r}',\omega) = G^0(\mathbf{r},\mathbf{r}',\omega) + \iint G^0(\mathbf{r},\mathbf{r}'',\omega)\Sigma(\mathbf{r}'',\mathbf{r}''',\omega)G(\mathbf{r}''',\mathbf{r}',\omega)d\mathbf{r}''d\mathbf{r}''', \tag{14}$$

where G^0 is the independent-particle Green's function. G^0 can be computed explicitly in terms of the single-particle wavefunctions.

Several levels of self-consistency can be used to evaluate (12), depending whether self-consistency is applied on G, on W or both. In this work, we only use G_0W_0 applied on the starting point provided by DFT wavefunctions and energies.

Quasiparticle band gaps show a much better agreement with experimental measurements than their DFT counterparts. The main effect of the quasiparticle corrections is an opening of the band gap between valence and conduction states. The scissor operator can be used as a cheap alternative to mimic the gap opening induced by GW. It assumes the corrections to be given by a simple rigid shift of the entire conduction bands.

2.2.2 *Independent-particle dielectric function*

For a monochromatic light with frequency ω, a photon of energy $E = \hbar\omega$ is impinging on the material. This energy can be used to excite electrons from the valence band to the conduction band for specific energies. The probability amplitude of such a transition from the valence (v) to the conduction (c) band at a particular wavevector ($\mathbf{k}$) is obtained from the so-called oscillator matrix elements

$$\left\langle \Psi_{c\mathbf{k}+\mathbf{q}} \left| e^{i\mathbf{q}.\mathbf{r}} \right| \Psi_{v\mathbf{k}} \right\rangle, \tag{15}$$

where $\mathbf{q}$ is the wavevector of the light.

As we are working with light in the visible range, the momentum of photon can be neglected in comparison to typical wavevectors in the BZ. In this long-wavelength limit ($\mathbf{q} \to 0$), the oscillator matrix elements can be approximated by the dipole momentum matrix elements

$$\left\langle \Psi_{c\mathbf{k}+\mathbf{q}} \left| e^{i\mathbf{q}.\mathbf{r}} \right| \Psi_{v\mathbf{k}} \right\rangle \overset{\mathbf{q}\to 0}{\approx} i\mathbf{q}. \left\langle \Psi_{c\mathbf{k}} \left| \mathbf{r} \right| \Psi_{v\mathbf{k}} \right\rangle. \tag{16}$$

The direct calculation of such matrix elements is problematic in the case of solids as the expression Eq. (16) is ill-defined when Born Von-Karman periodic conditions are enforced. For this reason, the dipole matrix elements can be obtained in two different ways. The first possibility is to use the commutator of the Hamiltonian with the position operator

$$\left\langle \Psi_{c\mathbf{k}} \left| \mathbf{r} \right| \Psi_{v\mathbf{k}} \right\rangle = \frac{\left\langle \Psi_{c\mathbf{k}} \left| [H, \mathbf{r}] \right| \Psi_{v\mathbf{k}} \right\rangle}{\epsilon_{c\mathbf{k}} - \epsilon_{v\mathbf{k}}}, \tag{17}$$

leading to a well-defined matrix element that can be used since the commutator between the Hamiltonian and the position operator can be evaluated numerically [69].

The other way to evaluate Eq. (16) is the use of the derivative with respect to wavevector. These derivatives are available using DFPT. These two techniques are used throughout this work.

For independent particles, the Fermi-Golden Rule approach leads to the IPA formula for the dielectric function

$$\varepsilon(\omega, \hat{\mathbf{q}}) = 1 - \lim_{q\to 0} \frac{4\pi}{q^2} \sum_{vc\mathbf{k}} \left[\frac{\left|\langle \Psi_{c\mathbf{k}+\mathbf{q}} \left| e^{i\mathbf{q}.\mathbf{r}} \right| \Psi_{v\mathbf{k}} \rangle\right|^2}{\epsilon_{c\mathbf{k}+\mathbf{q}} - \epsilon_{v\mathbf{k}} - \omega - i\eta} + \frac{\left|\langle \Psi_{c\mathbf{k}+\mathbf{q}} \left| e^{i\mathbf{q}.\mathbf{r}} \right| \Psi_{v\mathbf{k}} \rangle\right|^2}{\epsilon_{c\mathbf{k}+\mathbf{q}} - \epsilon_{v\mathbf{k}} + \omega + i\eta} \right], \tag{18}$$

where $\hat{\mathbf{q}}$ is a unitary vector along the $\mathbf{q}$ direction, q is the norm of $\mathbf{q}$, and where resonant (valence to conduction transitions, with positive energies) and anti-resonant transitions (conduction to valence transitions, with negative energies) have been taken into account.

It should be noted that the long-wavelength limit may lead to different values along different $\mathbf{q}$ directions. The direction can be factorized out in the dipole limit, to give

$$\varepsilon(\omega, \hat{\mathbf{q}}) = \frac{\mathbf{q}^T \hat{\boldsymbol{\varepsilon}} \mathbf{q}}{\mathbf{q}^T \mathbf{q}} \tag{19}$$

where $\hat{\boldsymbol{\varepsilon}}$ is the dielectric tensor.

In this paragraph, we have considered the optical properties for independent particles. In the next section, we discuss how many-body effects change the picture.

2.3 BETHE-SALPETER EQUATION

The computation of the macroscopic dielectric susceptibility $\chi(\omega)$ follows the standard procedure used in ab initio MBPT. Two steps are needed: the computation of the quasiparticle energies, followed by the computation of the dielectric response of the material.

In the second part of the calculation, we include excitonic effects by working with the BSE.

As already mentioned in the previous section, DFT aims to describe ground state properties but it is not supposed to reproduce the polarizability of the many-body system. In fact, the IPA for the dielectric function does not usually lead to a good agreement with experiments. A

rigorous description of optical properties requires more advanced theories that are able to take into account time dependence and screening effects. MBPT provides a framework for the description of such effects since it is able to describe at the many-body level the (screened) interaction between the excited particle (electron) and the remaining electrons (hole). The GW approximation gives a reasonable value for charged excitations [29] but the description of optical properties (neutral excitation energies) is quite unsatisfactory. The BSE allows for the description of an interacting electron-hole pair, giving rise to the so-called excitonic effects. These three levels of theory are schematized in Fig. 4.

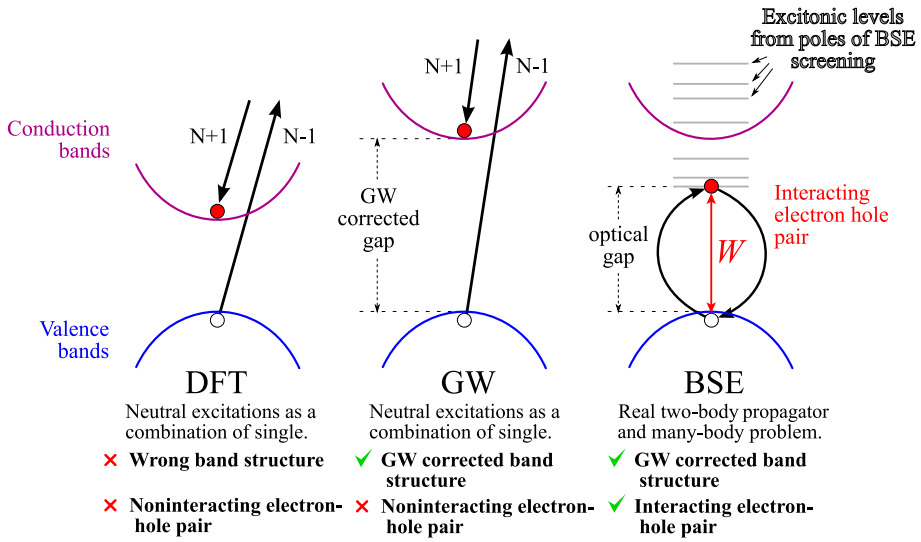

Figure 4: Schematic representation of the effect of the different approximations (DFT, GW, and BSE) on the band structure and on optical properties [70].

2.3.1 *Bethe-Salpeter Equation formalism*

In what follows, we summarize the most important equations of the BSE formalism, our discussion closely follows the presentation done in Ref. [30].

We start by introducing a generalized four-point polarizability[1] $L(1,2;3,4)$ from which the macroscopic dielectric function is obtained according to

$$\varepsilon_M(\omega) = 1 - \lim_{\mathbf{q}\to 0} v(\mathbf{q}) \int d\mathbf{r}d\mathbf{r}' e^{-i\mathbf{q}\cdot(\mathbf{r}-\mathbf{r}')} L(\mathbf{r},\mathbf{r},\mathbf{r}',\mathbf{r}';\omega). \tag{20}$$

It is possible to show that L satisfies the integral equation

$$\begin{aligned} L(1,2,3,4) =& L^0(1,2,3,4) + \\ & \int d(5678) L^0(1,2,5,6) K(5,6,7,8) L(7,8,3,4), \end{aligned} \tag{21}$$

which involves the four-point generalization of the independent-particle polarizability, L^0

$$L^0(1,2,3,4) = iG^0(1,3)G^0(4,2) \tag{22}$$

from the non-interacting Green's functions G^0.

The kernel K is given by

$$K(1,2,3,4) = \delta(1,2)\delta(3,4)\bar{v}(1,3) - \delta(1,3)\delta(2,4)W(1,2) \tag{23}$$

where W is the screened interaction, and $\bar{v}$ is the modified Coulomb potential

$$\bar{v}(\mathbf{q}) = \begin{cases} v(\mathbf{q}) \text{ if } \mathbf{q} \neq 0 \\ \quad 0 \text{ if } \mathbf{q} = 0. \end{cases} \tag{24}$$

The integral equation (21) is solved by expanding the four-point functions in the so-called transition space (products of two Kohn-Sham orbitals) according to

$$F(1,2,3,4) = \sum_{(n_1n_2)(n_3n_4)} F_{(n_1n_2)(n_3n_4)} \psi^\dagger_{n_1}(1)\psi_{n_2}(2)\psi_{n_3}(3)\psi^\dagger_{n_4}(4) \tag{25}$$

where n is a short-hand notation for band index, $\mathbf{k}$-point and spin.

In transition space, L^0 is represented by the diagonal matrix

$$L^0_{(n_1n_2)(n_3n_4)}(\omega) = \frac{(f_{n_2} - f_{n_1})}{(\epsilon_{n_2} - \epsilon_{n_1} - \omega)} \delta_{n_1n_3}\delta_{n_2n_4}, \tag{26}$$

1 To simplify the notation, space-time coordinates $(\mathbf{r}_1, t_1)$ are denoted with a natural number (1). Integrals like $\int d1$ represents integration over time and space: $\int d\mathbf{r}_1 \int dt_1$

and this property considerably simplifies the solution of the integral equation in (21). After some tedious algebra,[2] one obtains the following expression for the matrix elements of the four-point polarizability L

$$L_{(n_1n_2)(n_3n_4)}(\omega) = [H^{eff} - \omega]^{-1}_{(n_1n_2)(n_3n_4)}(f_{n_4} - f_{n_3}), \tag{27}$$

where H^{eff} can be interpreted as an effective two-particle Hamiltonian describing the interaction between electron and hole.

In the transition space, the BSE Hamiltonian has the following block form

$$H^{eff} = \begin{pmatrix} & |v'c'\mathbf{k}'\rangle & |c'v'\mathbf{k}'\rangle \\ \langle vc\mathbf{k}| & R & C \\ \langle cv\mathbf{k}| & -C^* & -R^* \end{pmatrix} \tag{28}$$

where v, c and $\mathbf{k}$ denotes the valence band index, the conduction band index and the wavevector respectively.

The resonant sub-block R is Hermitian, and the coupling term C is symmetric. Due to the coupling sub-blocks that connect resonant and anti-resonant transitions, the Bethe-Salpeter Hamiltonian is not Hermitian, although it has real eigenvalues. This complicates the solution of the problem, although iterative algorithms already exist, as in Ref. [36]. In crystalline systems, however, the matrix elements of C are usually much smaller than the matrix elements of R [31, 34, 71]. For this reason, the matrix elements of C are usually neglected when solving the Bethe-Salpeter problem in extended systems, leading to the so-called Tamm-Dancoff approximation (TDA) [72]. One should note that even if this approximation works very well for optical absorption it may fail for other properties such as EELS [73]. As we are mainly interested in optical absorption, this approximation is used in the rest of this work.

The matrix elements of the resonant block are given by

$$R_{(vc\mathbf{k}),(v'c'\mathbf{k}')} = H^{diag}_{(vc\mathbf{k}),(v'c'\mathbf{k}')} + H^{exch,R}_{(vc\mathbf{k}),(v'c'\mathbf{k}')} + H^{coul,R}_{(vc\mathbf{k}),(v'c'\mathbf{k}')} \tag{29}$$

where

$$H^{diag}_{(vc\mathbf{k}),(v'c'\mathbf{k}')} = (\epsilon_{c\mathbf{k}} - \epsilon_{v\mathbf{k}})\delta_{vv'}\delta_{cc'}\delta_{\mathbf{k}\mathbf{k}'} \tag{30}$$

$$\begin{aligned} H^{exch,R}_{(vc\mathbf{k}),(v'c'\mathbf{k}')} &= 2\langle vc\mathbf{k}|\bar{v}|v'c'\mathbf{k}\rangle \\ &= 2\int\int \psi_{v\mathbf{k}}(\mathbf{r})\psi^*_{c\mathbf{k}}(\mathbf{r})\bar{v}(\mathbf{r}-\mathbf{r}')\psi^*_{v'\mathbf{k}'}(\mathbf{r}')\psi_{c'\mathbf{k}'}(\mathbf{r}')\,d\mathbf{r}'\,d\mathbf{r} \end{aligned} \tag{31}$$

2 The derivation assumes a spin-unpolarized insulator. See [30] for a derivation of the result.

$$
\begin{aligned}
&H^{coul,R}_{(vck),(v'c'k')} \\
&= -\left\langle vck \left| W \right| v'c'k' \right\rangle \\
&= -\int\int \psi_{vk}(r)\psi^*_{v'k'}(r)W(r,r',\omega=0)\psi^*_{ck}(r')\psi_{c'k'}(r')dr'dr. \qquad (32)
\end{aligned}
$$

For the derivation of Eqs. (20) to (32), we refer to Ref. [30].

With local-field effects included, the macroscopic dielectric function can be obtained from an average of the microscopic dielectric function $\varepsilon(q+G,q+G',\omega)$ as

$$
\varepsilon^M(q,\omega) = \frac{1}{\varepsilon^{-1}(q+G,q+G',\omega)|_{G=G'=0}} \qquad (33)
$$

where $\varepsilon^{-1}(q+G,q+G',\omega)$ is the inverse microscopic dielectric function.

If no local-field effects were included, the macroscopic dielectric function would simply be obtained as $\varepsilon(q,q,\omega)$.

The inclusion of the $\bar{v}(q)$ term in the Hamiltonian H is a mathematical trick used to include local-field effects in the final result for the dielectric function [30, 69].

The macroscopic dielectric susceptibility $\chi^M(\omega)$ and dielectric function $\varepsilon^M(\omega)$ are then obtained from

$$
\begin{aligned}
\varepsilon^M(q,\omega) =& 1 + 4\pi\chi^M(\omega) \\
=& 1 - \lim_{q\to 0} v(q) \left\langle P(q) \left| ((\omega+i\eta) - H)^{-1} F \right| P(q) \right\rangle \qquad (34)
\end{aligned}
$$

where η is a broadening factor, F allows one to take the occupation numbers into account

$$
F = \begin{pmatrix}
 & |v'c'k'\rangle & |c'v'k'\rangle \\
|vck\rangle & 1 & 0 \\
|cvk\rangle & 0 & -1
\end{pmatrix} \qquad (35)
$$

and

$$
P(q)_{(n_1n_2)} = \left\langle n_2 \left| e^{iq\cdot r} \right| n_1 \right\rangle, \qquad (36)
$$

are the so-called oscillator matrix elements. In the rest of this work, as we are interested in the macroscopic function, the M index will be omitted.

The Random-Phase Approximation (RPA) is a simplification of the BSE approach in which the Coulomb term (32) is neglected. The IPA can be obtained by neglecting also the exchange term (31). Therefore, in the IPA,

the BSE Hamiltonian H is diagonal, and the spectrum is obtained directly as a simple sum over transitions between valence and conduction bands, weighted by the proper oscillator matrix elements. In such an IPA, no excitonic effects are present. The importance of the excitonic effects on the optical spectrum is well-known, with prominent peaks being created below the band gaps in most wide-gap insulators or semiconductors, and the spectral weight being redistributed.

The wavefunctions and eigenenergies are usually obtained from a standard Kohn-Sham calculation [4, 5] and a scissor operator may be employed to avoid GW calculations. For BSE applications, it is common to compute the direct term with a screened interaction obtained at the single particle level [74, 75]. Alternatively, one can employ the much cheaper model dielectric function proposed by Cappellini *et al.* in Ref. [76].

2.3.2 *Solution of the Bethe-Salpeter Equation*

The solution of the Bethe-Salpeter equation is a two-step process. First, the matrix elements of the Hamiltonian are computed from Eqs. (30)-(32). Then, the macroscopic dielectric function is derived using Eq. (34).

Two different approaches are commonly used nowadays: direct diagonalization and Lanczos algorithms following the seminal work of Haydock [77]. The Lanczos approach was employed for the first time to solve the BSE by Benedict *et al.* [78, 79]. It is based on the construction of a chain of vectors obtained by performing simple matrix-vector operations. By using Krylov subspaces, it is possible to express Eq. (34) in terms of a continued fraction formula.

The Lanczos algorithm can be summarized as follows. We start by setting

$$b_1 = 0 \tag{37}$$

$$|\psi_1\rangle = \frac{|P(\mathbf{q})\rangle}{\| |P(\mathbf{q})\rangle \|}. \tag{38}$$

Then the algorithm iterates with i starting at 1

$$a_i = \langle \psi_i | H | \psi_i \rangle \tag{39}$$

$$b_{i+1} = \| H |\psi_i\rangle - a_i |\psi_i\rangle - b_i |\psi_{i-1}\rangle \| \tag{40}$$

$$|\psi_{i+1}\rangle = \frac{H |\psi_i\rangle - a_i |\psi_i\rangle - b_i |\psi_{i-1}\rangle}{b_{i+1}}. \tag{41}$$

The frequency dependence of the dielectric function is computed efficiently in terms of the continued fraction

$$\varepsilon_M(\omega) = 1 - \lim_{\mathbf{q}\to 0} v(\mathbf{q}) \frac{\|P(\mathbf{q})\|^2}{(\omega + i\eta) - a_1 - \dfrac{b_2^2}{(\omega+i\eta) - a_2 - \dfrac{b_3^2}{\ddots}}} \tag{42}$$

and the iteration is stopped when $\varepsilon_M(\omega)$ is converged for each frequency.

The construction of the Krylov chain Eqs. (39-41) requires only the application of the Hamiltonian on different wavefunctions or, in linear algebra language, simple matrix-vector products. The computational cost scales as $\mathcal{O}(mN^2)$ with m the number of iterations of the Lanczos algorithm and N the dimension of the matrix. In our approach, the BSE Hamiltonian is expressed in the electron-hole basis thus $N = N_v N_c N_k$ where N_v is the number of valence bands, N_c the number of conduction bands and N_k the number of points in the BZ.

The number of iterations m needed to converge $\varepsilon_M(\omega)$ is much smaller than the size of the Hamiltonian and almost independent of the size of the system. As a consequence, Lanczos methods are much more efficient than direct diagonalization techniques that scale as $\mathcal{O}(N^3)$. Unfortunately, unlike diagonalization methods, the Lanczos approach does not give direct access to the exciton levels and the corresponding two-body or electron-hole wavefunctions.

The computation of the BSE matrix elements and the storage of the Hamiltonian represent the most CPU-intensive and memory demanding parts. For example, a converged computation of the dielectric function of bulk silicon requires few bands (3-4 valence bands, 4-6 conduction bands) but numerous wavevectors in the BZ (from $14\times14\times14$ to $40\times40\times40$, depending on the accuracy required) which means that the calculation involves ca. 10^3 to 10^4 wavevectors. This gives, for sequential computers, from days to years of computation, and in terms of memory, matrices of size ranging from 32928×32928 (ca. 16 GB) to 1536000×1536000 (ca. 34 TB). Such a huge amount of memory and the corresponding computation time render BSE calculations challenging even on modern supercomputers. These issues are even more severe when BSE results are used to perform resonant Raman scattering calculations that, as illustrated later in Sec. 3.4, require an extremely dense BZ sampling.

In order to solve these issues, we have worked on numerical techniques to interpolate BSE matrix elements. As a first step, we have been working on the design and the implementation of these numerical tech-

niques. We started with a simple model as a proof of concept, developing some code in Matlab to tests different approaches (these Matlab tests and developments have been presented in Ref. [80]). Finally, these prototypes have been implemented and tested in the Abinit software. The main results of these studies are presented in the next section.

2.4 SPEEDING UP CALCULATIONS AT THE BETHE-SALPETER LEVEL

Independently of the approximations used, the precise description of the dielectric properties usually requires numerous wavevectors to sample the BZ. Indeed, each wavevector of the BZ gives contributions at different transition energies and small changes in the mesh density can induce oscillations in the dielectric properties [81]. The construction of the BSE Hamiltonian requires the computation of matrix elements connecting different points in the wavevector mesh. This computation is the most time-consuming part of the BSE flow and its cost renders well-converged results difficult to achieve. The extraction of the macroscopic dielectric function from the inversion of the Hamiltonian matrix constitutes the last step of the BSE flow. In this section, we are using the Lanczos-Haydock solver already presented in Sec. 2.3.

Since 1998, different numerical methods have been proposed to help to reduce the computational cost. Rohlfing and Louie (RL) [34] proposed a double-grid technique where the kernel is interpolated starting from a homogeneous coarse mesh. This approach is used, for example, in the BerkeleyGW code [82]. Another technique by Fuchs *et al.* [83], uses an inhomogeneous mesh and refines the sampling to extract specific information for bound excitons. The large Hamiltonian matrices obtained with these methods are then treated either by direct diagonalization or with the Lanczos algorithm. Alternatively, one can perform the average of optical properties obtained using several independent shifted coarse grids, as introduced by Paier *et al.* [35] and, later, by ourselves in the study of frequency-dependent Raman spectroscopy. More detail about this technique is available in Sec. 3.4.

A completely different approach to the BSE problem has been proposed recently by Kammerländer *et al.* [84]. The authors focus on a single frequency and avoid the setup of the entire matrix and the direct diagonalization by using an iterative technique that takes advantage of a double grid to solve the Dyson equation.

In the present section, we propose a new method that combines the RL interpolation with the Lanczos-Haydock algorithm without requiring

the storage of the full matrix. We also generalize the RL approach to include multi-linear interpolation, and we reformulate the algorithm to render it more scalable and less memory demanding. We present different levels of interpolation, with different computational loads.

This section is organized as follows. Sec. 2.4.1 presents the interpolation methodology while the technical details of the implementation are discussed in Sec. 2.4.2. Finally, in Sec. 2.4.3, we apply our technique with different interpolation levels to three different crystalline systems: bulk silicon, gallium arsenide and lithium fluoride. We conclude with a comparison between our method and the averaging techniques proposed by Paier *et al.* [35] and ourselves (see Sec. 3.4 for a detailed description), and the work of Kammerländer *et al.* [84].

These two bottlenecks can be reduced by using the technique presented in the next section.

2.4.1 *Presentation of the interpolation technique*

The interpolation scheme that we propose is based on two meshes of wavevectors in the BZ (double-grid technique). Later, we will distinguish different levels of interpolation, all based on this double-grid technique.

To facilitate the discussion, we introduce the following notation. The coarse mesh contains $\tilde{N}_k$ homogeneous wavevectors, denoted as $\tilde{\mathbf{k}}$. The dense mesh contains $N_k = \tilde{N}_k \times N_{div}$ homogeneous wavevectors obtained by refining the coarse mesh. The refinement in each direction is achieved by defining equally spaced n_i points in the i-th direction. The wavevectors of the coarse mesh are given by

$$\tilde{\mathbf{k}}_{(i_1,i_2,i_3)} = i_1\hat{\mathbf{k}}_1 + i_2\hat{\mathbf{k}}_2 + i_3\hat{\mathbf{k}}_3, \tag{43}$$

where i_j are integer coordinates and $\hat{\mathbf{k}}_j$ are the basis vectors of the coarse mesh.

The dense wavevectors have fractional coordinates

$$\mathbf{k}_{(i_1,i_2,i_3),(j_1,j_2,j_3)} = (i_1 + \frac{j_1}{n_1})\hat{\mathbf{k}}_1 + (i_2 + \frac{j_2}{n_2})\hat{\mathbf{k}}_2 + (i_3 + \frac{j_3}{n_3})\hat{\mathbf{k}}_3 \tag{44}$$

where n_1, n_2 and n_3 are the number of divisions along the basis vectors while $0 \leqslant j_i \leqslant (n_i - 1)$. For the sake of simplicity, we assume the same number of divisions, $n_1 = n_2 = n_3 = n_{div}$, along the three directions and therefore $N_{div} = n_{div}^3$.

The neighborhood of a dense point, $N(\mathbf{k})$, is defined as the set of the eight wavevectors of the coarse mesh around $\mathbf{k}$. The reduced coordinates of this set of points are given by

$$N(\mathbf{k}_{(i_1,i_2,i_3),(j_1,j_2,j_3)}) = \left\{\tilde{\mathbf{k}}^{lmn}_{(i_1,i_2,i_3),(j_1,j_2,j_3)}\right\} \text{ with } l,m,n = 0,1 \quad (45)$$

where $\tilde{\mathbf{k}}^{lmn}$ is the lmn^{th}-neighbor of $\mathbf{k}$ in the coarse mesh

$$\tilde{\mathbf{k}}^{lmn}_{(i_1,i_2,i_3),(j_1,j_2,j_3)} = \tilde{\mathbf{k}}_{(i_1+l,i_2+m,i_3+n)}. \quad (46)$$

The dense set of a coarse point, $S(\tilde{\mathbf{k}})$, is defined as

$$S(\tilde{\mathbf{k}}_{(i_1,i_2,i_3)}) = \left\{\mathbf{k}_{(i_1,i_2,i_3),(j_1,j_2,j_3)}\right\} \forall (j_1,j_2,j_3). \quad (47)$$

Using these definitions, we can derive the following important relation

$$\begin{aligned}\sum_{\mathbf{k}} \sum_{\tilde{\mathbf{k}}\in N(\mathbf{k})} f(\mathbf{k},\tilde{\mathbf{k}}) &= \sum_{\tilde{\mathbf{k}}'} \sum_{\mathbf{k}\in S(\tilde{\mathbf{k}}')} \sum_{\tilde{\mathbf{k}}\in N(\mathbf{k})} f(\mathbf{k},\tilde{\mathbf{k}}) \\ &= \sum_{\tilde{\mathbf{k}}'} \sum_{\mathbf{k}\in S(\tilde{\mathbf{k}}')} \sum_{\tilde{\mathbf{k}}\in N(\tilde{\mathbf{k}}')} f(\mathbf{k},\tilde{\mathbf{k}}) \\ &= \sum_{\tilde{\mathbf{k}}'} \sum_{\tilde{\mathbf{k}}\in N(\tilde{\mathbf{k}}')} \sum_{\mathbf{k}\in S(\tilde{\mathbf{k}}')} f(\mathbf{k},\tilde{\mathbf{k}}) \end{aligned} \quad (48)$$

where Eq. (45) has been used. This property will be used afterwards to perform the interpolation of data defined on the coarse mesh.

As discussed in the previous section, the Lanczos algorithm is based on matrix-vector products. In our method, we perform these operations on-the-fly to avoid the storage of the BSE Hamiltonian in memory. The matrix elements of the kernel are interpolated while performing the matrix-vector operations. As discussed in more detail in the next paragraphs, different levels of interpolation can be employed in this part of the algorithm.

Since the periodic parts of the Bloch states at a given wavevector form a complete basis set, any wavefunction on the dense mesh can be expressed as [34]

$$|u_{n\mathbf{k}}\rangle = \sum_{n'} d^{n'\tilde{\mathbf{k}}}_{n\mathbf{k}} |u_{n'\tilde{\mathbf{k}}}\rangle \quad (49)$$

where

$$d^{n'\tilde{\mathbf{k}}}_{n\mathbf{k}} = \langle u_{n'\tilde{\mathbf{k}}} | u_{n\mathbf{k}}\rangle . \quad (50)$$

In the transition basis set, the electron-hole wavefunction $\Psi(\mathbf{r},\mathbf{r}')$ is given by a linear combination of products of single-particle orbitals according to

$$\Psi(\mathbf{r},\mathbf{r}') = \sum_{vck} A_{vck}\phi_{vck}(\mathbf{r},\mathbf{r}') \tag{51}$$

where

$$\phi_{vck}(\mathbf{r},\mathbf{r}') = e^{-i\mathbf{k}.\mathbf{r}}u^*_{vk}(\mathbf{r})e^{i\mathbf{k}.\mathbf{r}'}u_{ck}(\mathbf{r}') = e^{i\mathbf{k}.(\mathbf{r}'-\mathbf{r})}U_{vck}(\mathbf{r},\mathbf{r}'). \tag{52}$$

One basis function on the dense mesh can then be expanded in terms of the wavefunctions located on a coarse point by means of

$$|U_{vck}\rangle = \sum_{n_1 n_2} (d^{n_1\tilde{k}}_{vk})^* d^{n_2\tilde{k}}_{ck} |U_{n_1 n_2 \tilde{k}}\rangle\,. \tag{53}$$

The method developed by Rohlfing and Louie in Ref. [34] uses a single reference point $\tilde{\mathbf{k}}$ to expand the kernel according to

$$K^i_{vck,v'c'k'} = \sum_{n_1 n_2} d^{n_1\tilde{k}}_{vk}(d^{n_2\tilde{k}}_{ck})^* \sum_{n_3 n_4} (d^{n_3\tilde{k}'}_{v'k'})^* d^{n_4\tilde{k}'}_{c'k'} K_{n_1 n_2\tilde{k},n_3 n_4\tilde{k}'} \tag{54}$$

and we generalize their approach by including eight coarse points in the expansion of the wavefunctions

$$|U_{vck}\rangle = \sum_{\tilde{k}\in N(k)} f(\mathbf{k},\tilde{\mathbf{k}}) \sum_{n_1 n_2} (d^{n_1\tilde{k}}_{vk})^* d^{n_2\tilde{k}}_{ck} |U_{n_1 n_2\tilde{k}}\rangle\,, \tag{55}$$

where $f(\mathbf{k},\tilde{\mathbf{k}})$ are interpolation prefactors. The RL interpolation scheme is a special case of Eq. (55) in which $f(\mathbf{k},\tilde{\mathbf{k}}) = 1$ for a chosen neighbor and 0 for all the other ones.

In order to accelerate the convergence of the expansion, we perform a trilinear interpolation of the coefficients. In this case, the prefactors are given by

$$\begin{aligned} f(\mathbf{k},\tilde{\mathbf{k}}) &= 0 && \text{if } \tilde{\mathbf{k}} \notin N(\mathbf{k}) \\ f(\mathbf{k},\tilde{\mathbf{k}}^{lmn}) &= f^{lmn}_{\mathbf{k}_{(i_1,i_2,i_3),(j_1,j_2,j_3)}} = f^l_{j_1} f^m_{j_2} f^n_{j_3} \end{aligned} \tag{56}$$

with

$$f^l_j = \begin{cases} 1 - \dfrac{j}{n_{div}} \text{ if } l = 0 \\ \dfrac{j}{n_{div}} \text{ if } l = 1. \end{cases} \tag{57}$$

Using Eq. (55), one obtains the following expression for the interpolated matrix elements

$$K^{i}_{vck,v'c'k'} = \sum_{\tilde{k}\in N(k)} f(k,\tilde{k}) \sum_{n_1 n_2} d^{n_1,\tilde{k}}_{vk} (d^{n_2\tilde{k}}_{ck})^* \sum_{\tilde{k}'\in N(k')} f(k',\tilde{k}') \sum_{n_3 n_4} (d^{n_3\tilde{k}'}_{v'k'})^* d^{n_4\tilde{k}'}_{c'k'} K_{n_1 n_2\tilde{k},n_3 n_4\tilde{k}'}. \quad (58)$$

By using the overlaps of the periodic parts of the wavefunctions, we are thus able to include correctly their phases and these phases will cancel out with the oscillator matrix elements $P(q)$ computed with the wavefunctions on the dense mesh.

It should be stressed, however, that the matrix elements of the Coulomb interaction diverge when $q = k - k' \to 0$. Following Ref. [34], we rewrite the matrix elements as

$$K_{vck,v'c'k'} = \frac{a_{vck,v'c'k'}}{q^2} + \frac{b_{vck,v'c'k'}}{q} + c_{vck,v'c'k'} \quad (59)$$

and we note that an accurate interpolation technique should try to reproduce the divergent behavior as much as possible.

The different schemes we have implemented to treat the divergence are discussed in more detail in the next section.

2.4.2 *Combining Lanczos algorithm with interpolation*

As previously discussed, the dimension of the matrix on the coarse mesh is $N_{coarse} = N_c N_v \tilde{N}_k$, while the dimension of the matrix on the dense mesh is $N_{dense} = N_c N_v N_k = N_c N_v \tilde{N}_k N_{div}$. The calculation of the matrix elements of the Hamiltonian as well as the Lanczos algorithm scale as $\mathcal{O}(N^2)$. The numerical complexity of the standard BSE solution on the coarse mesh is thus

$$\mathcal{O}(N_c^2 N_v^2 \tilde{N}_k^2) \quad (60)$$

while the complete solution on the dense mesh scales as

$$\mathcal{O}(N_c^2 N_v^2 \tilde{N}_k^2 N_{div}^2). \quad (61)$$

To fix the ideas, supposing a halving of the coarse mesh for the three directions giving the dense mesh, $N_{div} = 8$ and $N_{div}^2 = 64$, which points out the significant burden of using the dense meshes. If $\tilde{N}_k$ is kept constant, and N_{div} is increased, the use of the dense mesh is even more unfavorable.

The most memory-demanding part is the storage of the Hamiltonian which scales quadratically with the size of the Hamiltonian. The interpolation technique given in Eq. (58) can be implemented in two different ways. The interpolated matrix elements can be stored in memory and then used as a standard matrix for the Lanczos technique. This is the approach followed by RL in [34]. It is worth noting, however, that although the RL method allows one to avoid the explicit computation of the matrix elements on the dense mesh, the numerical complexity and the memory requirements of the approach are still the ones of a standard BSE.

Alternatively, one can reformulate the equations so that the interpolation is done on-the-fly without allocating extra memory for the dense Hamiltonian. This is the central result of this section. As the Lanczos technique requires only matrix-vector multiplications, the full-matrix vector multiplication with the Hamiltonian can be written as

$$\phi^{(n+1)}_{vck} = \sum_{v'c'k'} H^{i}_{vck,v'c'k'} \phi^{(n)}_{v'c'k'} \tag{62}$$

$$= (\varepsilon_{ck} - \varepsilon_{vk})\, \phi^{(n)}_{vck} + \sum_{v'c'k'} K^{i}_{vck,v'c'k'} \phi^{(n)}_{v'c'k'} \tag{63}$$

that can be evaluated with $\mathcal{O}(N_c N_v \tilde{N}_k N_{div})$ scaling. The matrix-vector product with the kernel becomes

$$s_{vck} = \sum_{v'c'k'} K^{i}_{vck,v'c'k'} p_{v'c'k'} \tag{64}$$

$$= \sum_{\tilde{k}\in N(k)} f(k,\tilde{k}) \sum_{n_1 n_2} d^{n_1,\tilde{k}}_{vk} (d^{n_2\tilde{k}}_{ck})^* \sum_{\tilde{k}''} \sum_{\tilde{k}'\in N(\tilde{k}'')} \sum_{n_3 n_4} K_{n_1 n_2 \tilde{k}, n_3 n_4 \tilde{k}'} \sum_{k'\in S(\tilde{k}'')} f(k',\tilde{k}') \sum_{v'c'} (d^{n_3\tilde{k}'}_{v'k'})^* d^{n_4\tilde{k}'}_{c'k'} p_{v'c'k'} \tag{65}$$

and can be computed in three steps using

$$q^{uvw}_{n_3 n_4 \tilde{k}''} = \sum_{k'\in S(\tilde{k}'')} f(k',\tilde{k}') \sum_{v'c'} (d^{n_3\tilde{k}'}_{v'k'})^* d^{n_4\tilde{k}'}_{c'k'} p_{v'c'k'} \text{ with } \tilde{k}' = \tilde{k''}^{uvw} \tag{66}$$

$$r_{n_1 n_2 \tilde{k}} = \sum_{\tilde{k}''} \sum_{uvw} \sum_{n_3 n_4} K_{n_1 n_2 \tilde{k}, n_3 n_4 (\tilde{k''}^{uvw})} q^{uvw}_{n_3 n_4 \tilde{k}''} \tag{67}$$

$$s_{vck} = \sum_{\tilde{k}\in N(k)} f(k,\tilde{k}) \sum_{n_1 n_2} d^{n_1,\tilde{k}}_{vk} (d^{n_2\tilde{k}}_{ck})^* r_{n_1 n_2 \tilde{k}}. \tag{68}$$

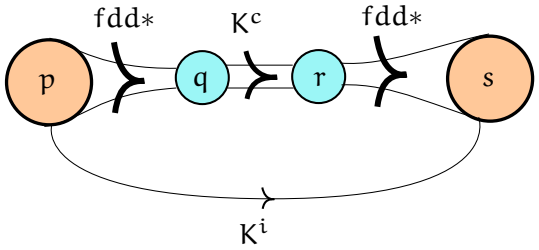

Figure 5: Schema illustrating the interpolated matrix-vector product. Small circles represent coarse mesh data while big circles correspond to dense mesh data. $fdd*$ refers to the $f(k,\tilde{k})d_{vk}^{n_1,\tilde{k}}(d_{ck}^{n_2\tilde{k}})^*$ prefactors of Eq. (66) and Eq. (68). K_c is the application of the coarse kernel on the coarse vector q that gives r in Eq. (67).

A schematic representation of the algorithm is given in Fig. 5. The application of the interpolated Hamiltonian is equivalent to averaging dense vector (p) on a coarse vector (q), then applying the coarse Hamiltonian (r) and finally rebuilding the full vector information on the dense mesh (s).

The numerical complexity of Eq. (66), (67) and (68) is $\mathcal{O}(N_c^2N_v^2\tilde{N}_kN_{div})$, $\mathcal{O}(N_c^2N_v^2\tilde{N}_k^2)$, and $\mathcal{O}(N_c^2N_v^2\tilde{N}_kN_{div})$ respectively instead of the $\mathcal{O}(N_c^2N_v^2\tilde{N}_k^2N_{div}^2)$ scaling of a BSE run done on the same dense mesh without interpolation. This first approach is called "Method 1" (M1) in the rest of this section.

As stated at the end of Sec. 2.4.1, a better treatment of the divergence is expected to improve the accuracy of the interpolation. Considering Eq. (59), one can interpolate the coefficients and then divide the interpolated quantities by the $\mathbf{q}$ computed on the dense mesh. The drawback of this approach, however, is that it requires the computation of the whole matrix since the fast algorithm developed in Eq. (65) is not applicable thus resulting in $\mathcal{O}(N_c^2N_v^2\tilde{N}_k^2N_{div}^2)$ scaling. This approach is called "Method 2" (M2) in the rest of this section.

The last method ("Method 3", M3) has been developed as a trade-off between accuracy and numerical complexity. In this case, the divergent behavior is reproduced only in a small region along the diagonal with a width that can be adjusted by the user (see Fig. 6). This approximation allows us to employ the fast interpolation of Eq. (65) for the full matrix. The computational cost needed to treat the divergence is negligible provided that the width is small with respect to the number of points on the coarse mesh. Under this assumption, the overall complexity of M3 is $\mathcal{O}(N_c^2N_v^2\tilde{N}_kN_{div}^2)$.

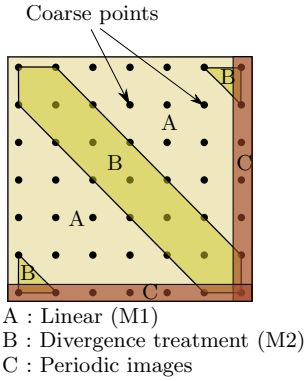

Figure 6: Regions of the Hamiltonian where the interpolation is applied in "Method 3", for a width $w = 1.0$.

We define the width w relatively to the smallest distance between two points in the coarse grid d. Then, all (k, k') pairs in the dense mesh so that $||k - k'|| > w \times d$ are treated with Method 1 and for the other pairs, the coefficients of Eq. (59) are interpolated and used together with the dense $\mathbf{q}$ to treat the divergence.

2.4.3 *Comparison of the interpolation schemes*

In this section, the different interpolation schemes are tested and compared in detail. Our method has been implemented in the open source ABINIT code [85–87] and is available in version 8. First, three different prototype systems, silicon, gallium arsenide and lithium fluoride, are studied and the accuracy of the three schemes discussed in the previous section is studied in detail. Then, a non-physical test case with very low convergence parameters is used to analyze how the computational cost scales with the total number of points employed to sample the BZ.

2.4.3.1 *Accuracy on test cases*

Silicon and gallium arsenide have relatively high dielectric constant (10.9 for GaAs and 12 for Si [1]) and therefore Mott-Wannier-like excitons with small binding energies (4-5 meV for GaAs [1, 88] and 15 meV for Si [89]). LiF, on the other hand, has a relatively small dielectric constant of 1.9 [88], yielding a weak screened interaction and therefore Frenkel-like excitons (i.e. with strong excitonic effects) with binding energy on the order of 3 eV [78, 88, 90, 91]. We decided to use these prototype semiconductors because, as discussed in [37], their BSE matrices have very

different behavior in k-space and it is important to understand how our interpolation scheme performs in two different scenarios.

Si and GaAs have been simulated using cut-off energies of 16 Ha for the wavefunctions and 4 Ha for the dielectric matrix, while for LiF, a cut-off energy of 50 Ha has been employed for the wavefunctions and 4 Ha for the dielectric matrix. In all case, three valence bands and four conduction bands were included in the electron-hole basis set. Lanczos chain iterations were stopped when the full dielectric spectrum reached a maximum relative difference of 1% both on the real part and the imaginary part. The model dielectric function of Ref. [76] has been used to avoid the computation of the inverse dielectric matrix, with the parameter ϵ^{∞} set to 12, 10 and 2 for Si, GaAs and LiF respectively. A scissor shift is applied on top of the LDA Kohn-Sham eigenvalues to mimic the effect of the GW approximation (0.8 eV for Si and GaAs, 5.7 eV for LiF). The broadening factor (see Eq. (34)) is $\eta = 0.1$ eV.

Results with two coarse grids of $4 \times 4 \times 4$ and $8 \times 8 \times 8$, interpolated to $8 \times 8 \times 8$ and $16 \times 16 \times 16$, respectively, are presented in Fig. 7, 8 and 9 for silicon, gallium arsenide and lithium fluoride respectively. The three main peak positions and maximum amplitudes extracted from these results are presented in Tab. 1, 2 and 3. All the calculations are done with BZ meshes shifted by $(0.011, 0.021, 0.031)$ in order to improve the accuracy of the sampling.

By comparing the interpolation schemes with 8 neighbors (8NB) and standard BSE computations done on the dense mesh, we observe that M1 (8NB) tends to shift the entire spectrum by a small energy and the excitonic binding energy is therefore underestimated. M2 (8NB) and M3 (8NB) give similar results for Si and GaAs that are almost on top of the computation done on the dense mesh. The case of lithium fluoride is more complicated to interpret. In this system, indeed, M1 (8NB) gives inaccurate results for the position of the first exciton (0.2 eV of error for a $8 \times 8 \times 8$ coarse mesh). M2 (8NB) performs better than M1 (8NB) although the error in the position of the first peak is still on the order of 0.12 eV. M3 (8NB) gives the best results: the excitonic binding energy is reproduced with 0.05 eV error and also the behavior at higher frequency is correctly reproduced. It should be stressed, however, that this agreement is somehow fortuitous and related to the particular value of the width w used for the treatment of the divergence. Fig. 10 shows the optical spectra of LiF computed with M3 and different values of w. Our results indicate that the value of the width used in M3 has a significant impact on the position of the first peak of LiF. Therefore, some sort of

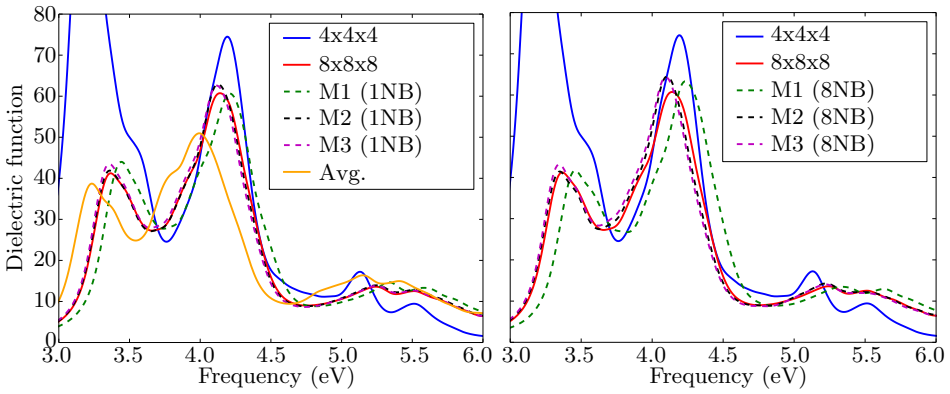

(a) $4 \times 4 \times 4$ with 1 neighbor (b) $4 \times 4 \times 4$ with 8 neighbors

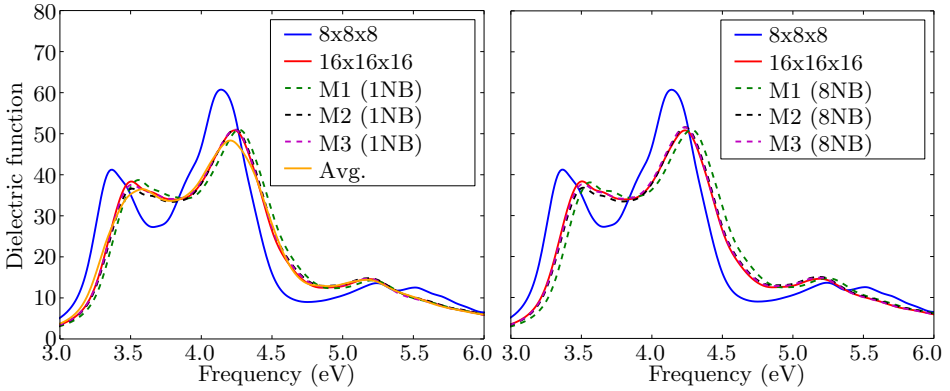

(c) $8 \times 8 \times 8$ with 1 neighbor (d) $8 \times 8 \times 8$ with 8 neighbors

Figure 7: Comparison between the absorption spectra of silicon obtained with the standard (non-interpolated) BSE solution and with the six levels of interpolation developed in this section. (1NB) refers to the 1-neighbor Rohlfing and Louie technique, whose results are presented in the left column. (8NB) refers to the multilinear technique with 8 neighbors presented in this section, whose results are presented in the right column. "Avg." refers to the multiple-shift technique. The results presented in the upper row correspond to the interpolation from the 4x4x4 grid to the 8x8x8 grid, while the lower row corresponds to the interpolation from the 8x8x8 grid to the 16x16x16 grid.

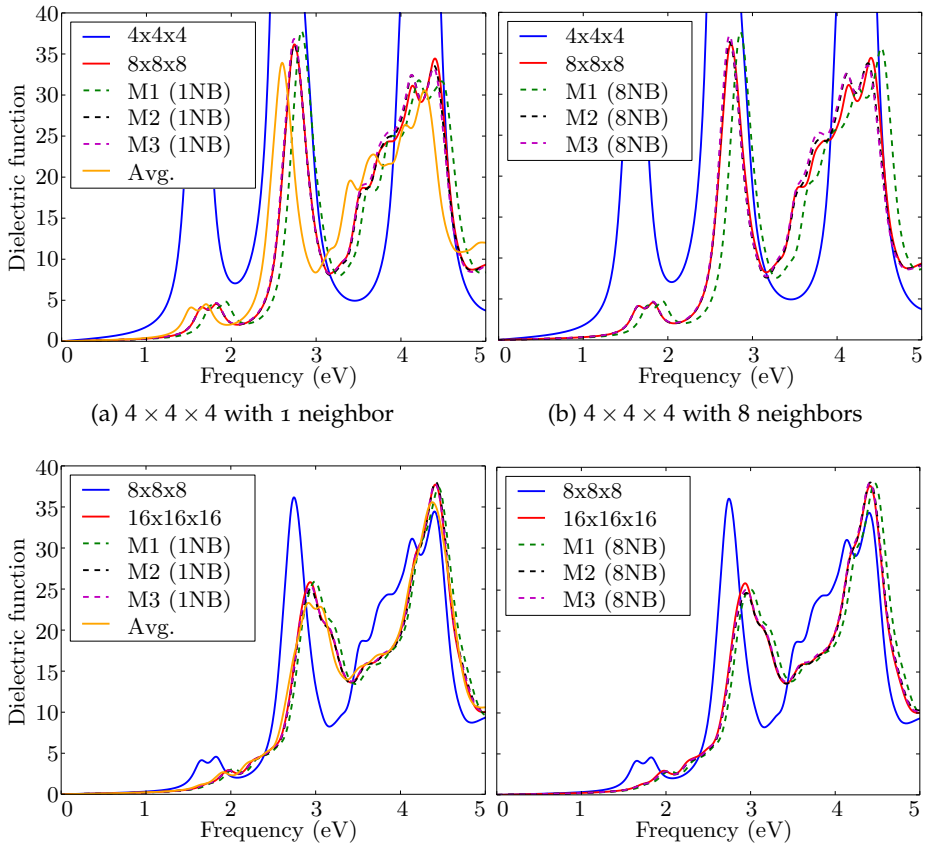

(a) $4 \times 4 \times 4$ with 1 neighbor

(b) $4 \times 4 \times 4$ with 8 neighbors

(c) $8 \times 8 \times 8$ with 1 neighbor

(d) $8 \times 8 \times 8$ with 8 neighbors

Figure 8: Comparison between the absorption spectra of gallium arsenide obtained with the standard (non-interpolated) BSE solution and with the six levels of interpolation developed in this section. (1NB) refers to the 1-neighbor Rohlfing and Louie technique, whose results are presented in the left column. (8NB) refers to the multilinear technique with 8 neighbors presented in this section, whose results are presented in the right column. "Avg." refers to the multiple-shift technique. The results presented in the upper row correspond to the interpolation from the 4x4x4 grid to the 8x8x8 grid, while the lower row corresponds to the interpolation from the 8x8x8 grid to the 16x16x16 grid.

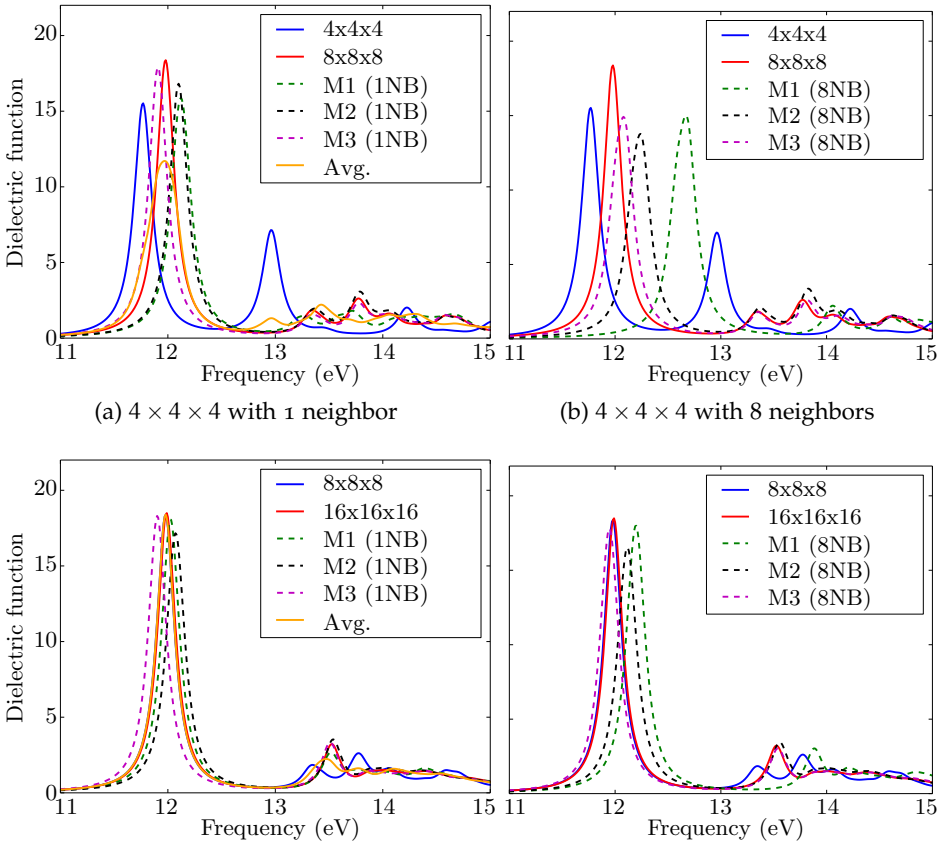

(a) $4 \times 4 \times 4$ with 1 neighbor

(b) $4 \times 4 \times 4$ with 8 neighbors

(c) $8 \times 8 \times 8$ with 1 neighbor

(d) $8 \times 8 \times 8$ with 8 neighbors

Figure 9: Comparison between the absorption spectra of lithium fluoride obtained with the standard (non-interpolated) BSE solution and with the six levels of interpolation developed in this section. (1NB) refers to the 1-neighbor Rohlfing and Louie technique, whose results are presented in the left column. (8NB) refers to the multilinear technique with 8 neighbors presented in this section, whose results are presented in the right column. "Avg." refers to the multiple-shift technique. The results presented in the upper row correspond to the interpolation from the 4x4x4 grid to the 8x8x8 grid, while the lower row corresponds to the interpolation from the 8x8x8 grid to the 16x16x16 grid.

Method	Peak I		Peak II		Peak III	
	Pos. (eV)	Max.	Pos. (eV)	Max.	Pos. (eV)	Max.
4x4x4	3.19	126.03	4.19	74.53	5.13	17.26
4x4x4 + M1(8NB)	3.46	41.69	4.23	63.32	5.34	13.47
4x4x4 + M2(8NB)	3.35	41.44	4.10	64.31	5.22	14.28
4x4x4 + M3(8NB)	3.35	43.17	4.11	64.50	5.22	14.06
4x4x4 + M1(1NB)	3.44	44.02	4.21	60.66	5.33	14.68
4x4x4 + M2(1NB)	3.36	41.90	4.12	62.59	5.25	13.93
4x4x4 + M3(1NB)	3.36	43.50	4.13	62.93	5.25	13.81
4x4x4 + Avg.	3.23	38.71	3.99	50.97	5.15	16.38
8x8x8	3.37	41.25	4.14	60.74	5.24	13.60
8x8x8 + M1(8NB)	3.55	38.13	4.28	50.99	5.25	14.71
8x8x8 + M2(8NB)	3.51	36.81	4.24	51.58	5.19	15.02
8x8x8 + M3(8NB)	3.51	37.71	4.23	51.56	5.19	14.83
8x8x8 + M1(1NB)	3.55	38.72	4.27	51.00	5.21	14.29
8x8x8 + M2(1NB)	3.51	36.62	4.24	51.05	5.19	14.80
8x8x8 + M3(1NB)	3.51	37.59	4.23	50.98	5.18	14.66
8x8x8 + Avg.	3.58	36.49	4.21	48.34	5.17	14.43
16x16x16	3.50	38.37	4.23	50.80	5.19	14.57

Table 1: Peak position (Pos.) and maximum amplitude (Max.) of the three main peaks of the absorption spectra of silicon represented in Fig. 7. See the caption of the figure for a complete description of the notations.

Method	Peak I		Peak II		Peak III	
	Pos. (eV)	Max.	Pos. (eV)	Max.	Pos. (eV)	Max.
4x4x4	1.70	31.67	2.62	104.08	4.34	72.43
4x4x4 + M1(8NB)	1.93	4.75	2.86	37.60	4.52	35.65
4x4x4 + M2(8NB)	1.82	4.62	2.73	36.39	4.37	33.79
4x4x4 + M3(8NB)	1.82	4.67	2.73	37.17	4.36	33.52
4x4x4 + M1(1NB)	1.93	4.85	2.83	37.79	4.48	31.67
4x4x4 + M2(1NB)	1.82	4.62	2.74	36.08	4.39	33.57
4x4x4 + M3(1NB)	1.82	4.67	2.74	36.85	4.39	33.27
4x4x4 + Avg.	1.70	4.53	2.60	33.93	4.28	30.57
8x8x8	1.82	4.57	2.74	36.16	4.40	34.45
8x8x8 + M1(8NB)	2.04	2.95	3.00	25.08	4.47	38.08
8x8x8 + M2(8NB)	2.00	2.83	2.95	24.66	4.42	38.14
8x8x8 + M3(8NB)	2.00	2.87	2.94	25.00	4.41	38.12
8x8x8 + M1(1NB)	2.03	3.12	2.99	25.92	4.45	37.36
8x8x8 + M2(1NB)	1.98	2.88	2.95	25.06	4.42	38.02
8x8x8 + M3(1NB)	1.98	2.91	2.94	25.40	4.41	37.77
8x8x8 + Avg.	1.91	2.69	2.91	23.32	4.38	35.58
16x16x16	1.98	2.95	2.93	25.84	4.41	37.74

Table 2: Peak position (Pos.) and maximum amplitude (Max.) of the three main peaks of the absorption spectra of gallium arsenide represented in Fig. 8. See the caption of the figure for a complete description of the notations.

Method	Peak I		Peak II		Peak III	
	Pos. (eV)	Max.	Pos. (eV)	Max.	Pos. (eV)	Max.
4x4x4	11.77	15.52	12.96	7.15	14.22	2.02
4x4x4 + M1(8NB)	12.67	15.02	14.06	2.23	14.61	1.49
4x4x4 + M2(8NB)	12.24	13.77	13.37	2.11	13.83	3.37
4x4x4 + M3(8NB)	12.08	14.92	13.35	1.80	13.82	2.61
4x4x4 + M1(1NB)	12.12	15.88	13.27	1.47	13.72	1.81
4x4x4 + M2(1NB)	12.10	16.82	13.37	1.95	13.79	3.07
4x4x4 + M3(1NB)	11.91	17.91	13.35	1.57	13.78	2.34
4x4x4 + Avg.	11.97	11.71	12.96	1.32	13.43	2.21
8x8x8	12.0	18.4	13.35	1.85	13.77	2.62
8x8x8 + M1(8NB)	12.20	18.00	13.88	3.04	14.21	1.75
8x8x8 + M2(8NB)	12.12	16.52	13.56	3.46	14.00	1.72
8x8x8 + M3(8NB)	11.95	17.80	13.54	3.05	14.00	1.51
8x8x8 + M1(1NB)	12.02	18.06	13.52	2.68	13.72	1.81
8x8x8 + M2(1NB)	12.07	17.16	13.54	3.53	13.99	1.65
8x8x8 + M3(1NB)	11.90	18.31	13.51	3.34	13.86	1.47
8x8x8 + Avg.	11.98	18.39	13.47	2.23	13.77	1.62
16x16x16	11.99	18.49	13.52	3.22	13.99	1.51

Table 3: Peak position (Pos.) and maximum amplitude (Max.) of the three main peaks of the absorption spectra of lithium fluoride represented in Fig. 9. See the caption of the figure for a complete description of the notations.

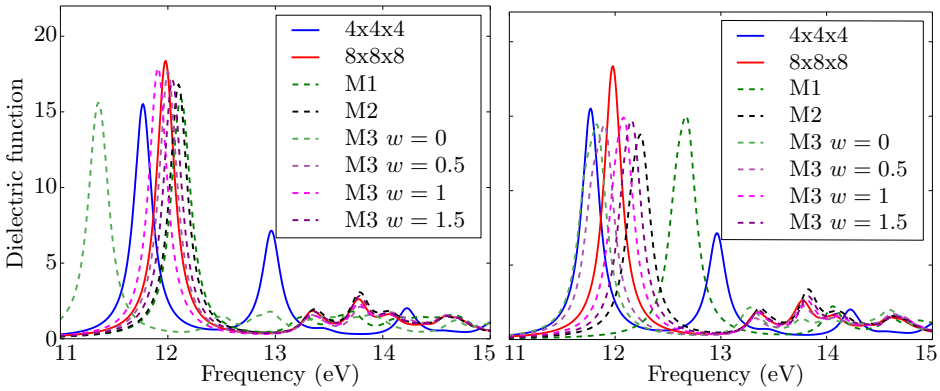

(a) $4 \times 4 \times 4$ with 1 neighbor (b) $4 \times 4 \times 4$ with 8 neighbors

Figure 10: Optical absorption spectrum of LiF obtained with different values of the width w used for the treatment of the divergence in "Method 3".

convergence study is needed for M3 in order to find values of w giving a good compromise between accuracy and efficiency.

If we compare the method using one neighbor (1NB) and the eight neighbors (8NB), we observe that the original Rohlfing and Louie interpolation (1NB) gives results for GaAs and Si whose quality is comparable to the multilinear interpolation and even better results for the special case of LiF. This is somehow puzzling and our current understanding is as follows. As already mentioned in the previous paragraph, the description of the divergent behavior along the diagonal of the Hamiltonian for LiF is extremely important to get a correct binding energy. In practice, the number of bands used in Eq. (49) must be truncated and therefore the expansion is not exact. Furthermore, in the expansion, we neglect possible contributions to valence (conduction) states coming from the conduction (valence) manifold in Eq. (53). This approximation is also used in Ref. [34]. Some terms are therefore neglected and they lead to some loss of information when building the interpolated matrix element from multiple neighbors.

Our results indicate that, although the multilinear interpolation was expected to give more accurate results, the practical implementation and the numerical approximations tend to favor a "simple" 1-neighbor interpolation. This interpolation gives sufficient accuracy at a lower computational cost as summations over 1 neighbor are cheaper than summations over 8 neighbors.

For the sake of completeness, we have also compared our methods with the multiple-shift technique introduced in Ref. [35, 81], described in

more detail in Sec. 3.4 and also used recently in Ref. [37]. Different coarse grids are obtained by shifting an initial homogeneous mesh so that the full set of points forms a much denser sampling. An approximate dielectric function is then obtained by averaging the results obtained on the coarse grids. As can be seen in Fig. 7, 8 and 9, this technique tends to smooth the spectrum and the amplitude of the peaks is underestimated. As stated in Ref. [37], due to the localized character of the exciton in LiF, a small number of points in the coarse grids is enough to converge the peak position but the correct description of the fine details of the spectrum requires more accurate methods. The methods developed in the present section are more accurate than this technique and are significantly cheaper as they do not require multiple expensive calculations of BSE Hamiltonians.

As far as the computational efficiency is concerned, one should notice that the time required to produce an interpolated spectrum for LiF in sequential with the above-mentioned parameters is respectively 22200 sec for M1 (8NB), 120000 sec for M2 (8NB), 3000 sec for M1 (1NB) and 80000 sec for M2 (1NB). As a reference, the time needed to compute the matrix elements of the BSE Hamiltonian on the coarse mesh is around 15000 sec and around 1×10^6 sec for the dense mesh. To sum up, M1 leads to a gain of two orders of magnitude in terms of CPU time while the high-accuracy M2 gives a speedup of one order of magnitude. The memory required by M1 is of the same order as the one needed for a calculation on the coarse mesh whereas M2 is much more memory demanding since the whole dense matrix must be stored.

The technique based on multiple shifts, on the other hand, requires 8 calculations of a coarse Hamiltonian. These calculations are independent and can be executed in parallel but the final results cannot reach the same frequency resolution as the ones obtained with a fast interpolation on a dense k-mesh.

2.4.3.2 *Numerical scaling of the interpolation technique*

In order to assess the numerical scaling of our implementation, we have performed several benchmarks for silicon with unconverged parameters. A cut-off energy of 4 Ha has been used for the wavefunctions and 2 Ha for the dielectric function. Only one valence and one conduction band are included in the Bethe-Salpeter kernel. This allowed us to increase the number of wavevectors of the dense grid to more than 100000 wavevectors in the BZ.

	`Matmul`	`Hinterp`
M1	$\mathcal{O}(\tilde{N}_k^2 + \tilde{N}_k N_{div})$	-
M2	$\mathcal{O}(\tilde{N}_k^2 N_{div}^2)$	$\mathcal{O}(\tilde{N}_k^2 N_{div}^2)$
M3	$\mathcal{O}(\tilde{N}_k N_{div}^2 + \tilde{N}_k^2)$[*]	$\mathcal{O}(\tilde{N}_k N_{div}^2)$

Table 4: Theoretical scalings of the routines used in the three methods described in the text. [*] Scaling of an optimal implementation that takes advantage of sparse matrices. The scaling becomes $\mathcal{O}(\tilde{N}_k^2 N_{div}^2)$ if the method is solved with dense matrices.

For the three different methods, we have analyzed the time spent in the most important routines. Different benchmarks have been performed by changing the initial coarse grid as well as the final dense mesh of $\tilde{N}_k \times N_{div}$ wavevectors. The most CPU-critical sections are `Hinterp` for the calculation of the interpolated matrix elements and `Matmul` for the matrix-vector multiplications needed for the Lanczos method. The theoretical scaling is given in Tab. 4 while the results of the tests are reported in Fig. 11. Several interesting observations on the major trends can be derived from the benchmarks. If we look at the interpolated matrix-vector product (`Matmul`), we observe that M1 is very efficient as it scales with the square of the size of the coarse mesh. On the other hand, both M2 and M3 are less performant. Finally, the time spent by M3 in the routine `Hinterp` (interpolation of matrix elements) is much smaller than the one spent by M2 at dense meshes.

2.4.3.3 *Comparison with the Kammerlander double-grid technique*

In this section, we compare our method with the technique proposed by Kammerlander in Ref. [84]. In this approach, the polarizability $L(\omega)$ is expressed in the transition space according to

$$L_{vc\mathbf{k},v'c'\mathbf{k}'}(\omega) = \sum_{v''c''\mathbf{k}''} (1 - L^0(\omega)K)^{-1}_{vc\mathbf{k},v''c''\mathbf{k}''} L^0_{v''c''\mathbf{k}'',v'c'\mathbf{k}'}(\omega), \tag{69}$$

where the RPA polarizability $L^0(\omega)$ is given by

$$L^0_{vc\mathbf{k},v'c'\mathbf{k}'}(\omega) = \frac{f_{c\mathbf{k}} - f_{v\mathbf{k}}}{\varepsilon_{c\mathbf{k}} - \varepsilon_{v\mathbf{k}} - \omega - i\eta} \delta_{cc'} \delta_{vv'} \delta_{\mathbf{k},\mathbf{k}'}. \tag{70}$$

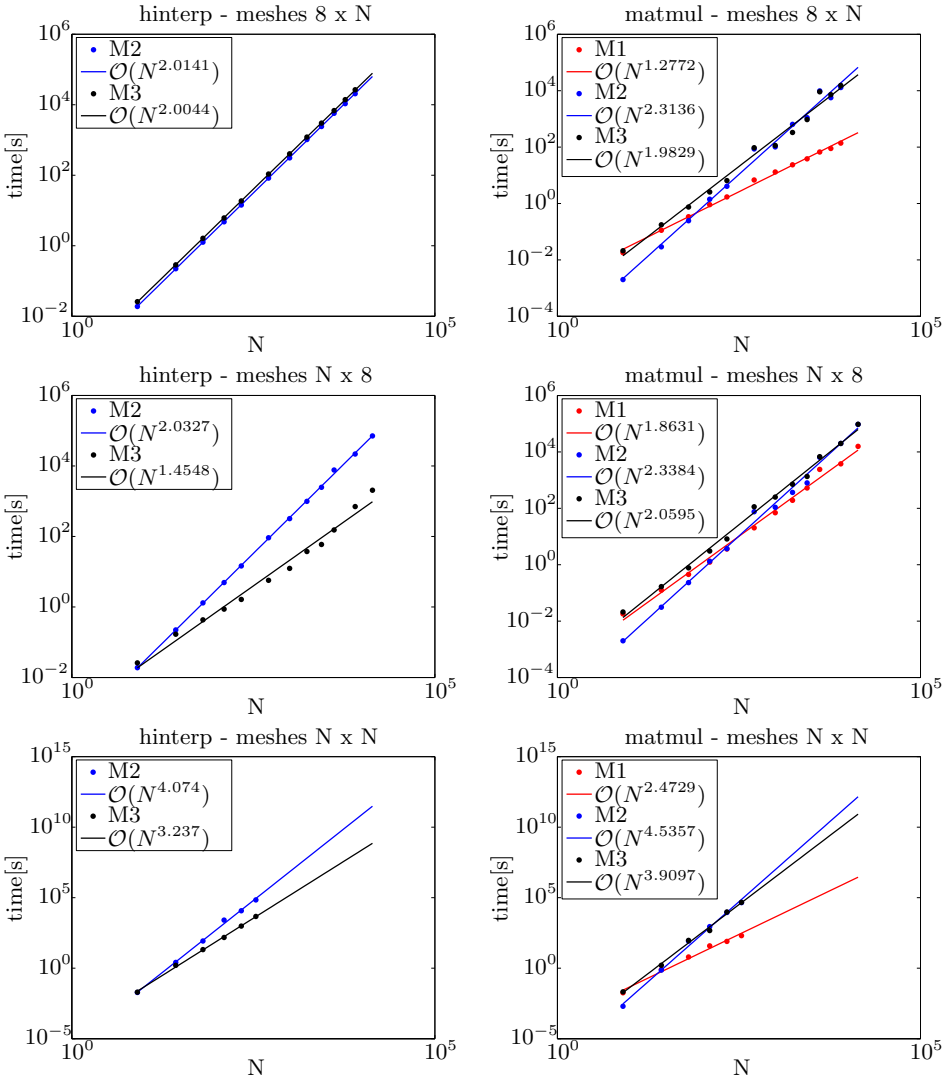

Figure 11: Measured scaling for the three interpolation methods as a function of the number of points N.

In order to avoid the direct inversion of the large matrix, an iterative scheme is used for the computation of

$$L_{vck,v'c'k'}(\omega) = \sum_{m} \sum_{v''c''k''} \left[L^0(\omega)K\right]^m_{vck,v''c''k''} L^0_{v''c''k'',v'c'k'}(\omega). \tag{71}$$

The BSE is solved for every frequency iteratively and a double grid technique is used to reduce the number of k-points for which the kernel must be computed explicitly. The RPA polarizability is averaged on a dense mesh yielding

$$L^0_{vck,v'c'k'}(\omega) = \frac{1}{N_{nb}} \sum_{\bar{k}\in N(k)} \frac{f_{c\bar{k}} - f_{v\bar{k}}}{\varepsilon_{c\bar{k}} - \varepsilon_{v\bar{k}} - \omega - i\eta} \delta_{cc'}\delta_{vv'}\delta_{k,k'}, \tag{72}$$

where the $\bar{k}$ are taken from the set $N(k)$ of N_{nb} dense points located around k.

Finally, the averaged values are used in the iterative BSE solver [see Eq. (71)]. This approach has the advantage that the wavefunctions on the dense mesh are not needed but the divergence is not accurately reproduced. The scaling of the Kammerlander technique is linear with the number of frequencies and quadratic with the number of points in the coarse mesh. On the contrary, our technique is able to describe the frequency dependence with a computational cost that does not depend on the number of frequency points, since, as discussed in Sec. 2.3, $\varepsilon_M(\omega)$ is evaluated with Eq. (42) whose cost is negligible.

2.4.3.4 *Wavefunction interpolation*

In this section, we assume that the entire set of wavefunctions on the dense set of points is available. For the systems investigated in this study, the calculation of wavefunctions starting from an already converged density is not the most computationally demanding part. Moreover, only wavefunctions in the transition basis set are required, that is a small fraction of the set of bands required for the screening, for example.

However, for some more complex systems, one might take advantage of interpolation techniques to obtain the wavefunctions on denser meshes. In the work of Kammerlander [84] presented in the previous section, Wannier functions were used to obtain eigenenergies on these dense meshes. Recently, Gilmore *et al.* [92] have used optimized basis functions described in the work of Shirley [93] to compute wavefunctions on a dense mesh. These different techniques could be easily inter-

faced with our technique to compute the overlap matrix elements, that can afterwards be used in the interpolation of the BSE Hamiltonian.

2.4.4 *Summary of the interpolation techniques*

We have presented a fast and memory-efficient technique that combines the interpolation of the Bethe-Salpeter matrix elements with the Lanczos algorithm. The treatment of the matrix elements is similar in spirit to the Rohlfing and Louie approach but we avoid the storage and the diagonalization of large matrices. Three possible approaches for the treatment of the Coulomb singularity have been presented and discussed in detail.

The effectiveness of the method has been analyzed through calculations of optical spectral in Si, GaAs and LiF. According to our tests, the multilinear interpolation of the wavefunctions does not perform better than simple constant interpolation, already proposed by Rohlfing and Louie (although used by them only for the set up of the Hamiltonian on the dense mesh).

In conclusion of this section, we suggest using Method 1 for a quick qualitative analysis of optical spectra e.g. for a high-throughput screening to rapidly identify possible candidates. Method 3 with the on-the-fly interpolation is the recommended approach for BSE calculations requiring dense k-meshes since it is significantly faster than M2 and the Coulomb divergence is taken into account. The downside is that one has to check the convergence with the width w, but we believe this is a small price to pay, especially when compared with the significant speedup that can be achieved.

The algorithmic improvements presented in this thesis will facilitate BSE calculations in complex systems and will also significantly ease the ab initio study of piezoreflectance, thermoreflectance and RI in systems with excitonic effects.

2.5 CONCLUSIONS

In this chapter, we have briefly reminded the main ingredients needed for ab initio calculations of optical materials in solids. We first started from the ground state ingredients (wavefunctions and eigenenergies). Then we moved to the independent-particle pictures and we discussed in detail the BSE formalism. As these calculations are usually cumbersome, we also discussed one way to improve the convergence rate using an interpolation technique in reciprocal space. In the forthcoming chap-

ter, we will discuss how to compute Raman intensities, a more advanced property, related to derivatives of the dielectric function.

3

RAMAN SPECTRUM CALCULATIONS FROM FIRST PRINCIPLES

Raman scattering has been known for a long time, since the discovery by C.V. Raman and K.S. Krishnan in 1922, that received the Nobel Prize in 1930.

As we will see in the forthcoming sections, the Raman intensity is linked to a modification of the dielectric function induced by atomic displacements. Therefore, a way to compute these intensities goes through the evaluation of the dielectric properties. Models have been used extensively for such an evaluation. The bond-polarizability model determines the total polarizability of the system as a sum over polarizabilities associated to each bonds [2, 94]. The parameters of the different models are then obtained from fits with respect to experimental measurements. Empirical pseudopotentials [95] and tight-binding [96] approaches have also been used to evaluate the susceptibility and its derivative. However, these approaches still require external parameters and this raises concerns about their transferability and their predictive power.

Ab initio calculations, on the other hand, are not affected by these serious limitations. Phonon band structures have been evaluated for a long time using ab initio techniques. Raman intensities have been computed by a mix of ab initio techniques for the phonon eigenvalue problem with polarizability models for the intensities, as e.g. in the work of Windl [97].

Concerning ab initio Raman intensities, the pioneer work of Baroni and Resta [12] shows how to compute Raman tensors from a FP approach, i.e. numerically evaluating the derivative by freezing the phonon displacements.

As the Raman susceptibility can be extracted from third-order derivative of the total energy, DFPT expressions, introduced by Veithen [14], allow for a direct evaluation.

Unfortunately, these works have been mostly done in the DFT-LDA framework and in the static limit, therefore valid only for laser frequency very small compared to electronic transitions.

Evaluation of frequency-dependent Raman intensities has been proposed already in [98, 99] for Ge and Si, based on fitting procedures, deformation potentials and derivatives of the dielectric function with

respect to frequencies, evaluated experimentally. Alternatively, models for critical points are also available for such resonant behaviors, as presented in more detail in [1].

However, the combination of ab initio methods with resonant conditions has remained a challenge. Actually, in these conditions, DFT might not be enough for an accurate description of optical properties, as already discussed in the previous chapter, and therefore a priori not for Raman intensities. In 2000, Weber and Merlin [2], said "However, it is unlikely that a practical ab initio theory of Raman intensities will be developed in the near future for measurements in this regime. An accurate description of the electronic structure (including the conduction bands) becomes critically important, and this requires computer-intensive methods beyond the LDA." We believe that we provide a general methodology for calculations in resonant regimes, that should allow ab initio calculations of frequency-dependent RI of a broad range of materials in the future.

In this section, we present this general methodology. We first remind the definition of phonons in Sec. 3.1 and of Raman intensities in Sec. 3.2. We then explain the methodology based on FP approach in Sec. 3.3. Finally, we apply this methodology to the case of silicon for first-order scattering and second-order scattering in Sec. 3.4 and 3.5. The content of Sec. 3.4 has already been published in Ref. [81].

3.1 DYNAMICAL PROPERTIES

In this thesis, we consider Raman scattering by phonons. Before being able to define Raman intensities, we therefore briefly remind the main equations of interest for the phonon eigenvalue problem.

The phonon frequencies ω_m are obtained by solving the eigenvalue problem associated with the matrix of inter-atomic force constants $\tilde{C}$

$$\sum_{\kappa',\beta} \tilde{C}_{\kappa\alpha,\kappa'\beta} U^m_{\kappa'\beta} = M_\kappa \omega_m^2 U^m_{\kappa\alpha}. \tag{73}$$

From the mass-scaled quantities

$$\xi_{\kappa\alpha} = \sqrt{M_\kappa} U^m_{\kappa\alpha} \tag{74}$$

$$D_{\kappa\alpha,\kappa'\gamma} = \frac{1}{\sqrt{M_\kappa}} C_{\kappa\alpha,\kappa'\gamma} \frac{1}{\sqrt{M_{\kappa'}}}, \tag{75}$$

the dynamical equation is readily obtained as

$$\sum_{\kappa\alpha} D_{\kappa\alpha,\kappa'\gamma}\xi^{m}_{\kappa\alpha} = \omega^{2}_{m}\xi^{m}_{\kappa'\gamma}. \tag{76}$$

We apply the following orthonormalization on the eigenvectors

$$\sum_{\kappa\alpha} (\xi^{m}_{\kappa\alpha})^{*}\,\xi^{n}_{\kappa\alpha} = \delta_{mn} \tag{77}$$

$$\sum_{\kappa\alpha} M_{\kappa}\,(U^{m}_{\kappa\alpha})^{*}\,U^{n}_{\kappa\alpha} = \delta_{mn}. \tag{78}$$

We define $Q^{m}(\mathbf{q})$ as the normal coordinate of the mode m at point $\mathbf{q}$. The displacement of atom κ, in direction α in l^{th} cell for this mode m is then given by

$$U^{l,m}_{\kappa\alpha}(\mathbf{q}) = Q^{m}(\mathbf{q})U^{m}_{\kappa\alpha}(\mathbf{q})e^{i\mathbf{q}.\mathbf{R}^{l}}. \tag{79}$$

The wavevector $\mathbf{q}$ gives a measure of the wavelength of the vibration mode. In polar materials, when the wavevector $\mathbf{q} \to 0$, a macroscopic electric field is generated for optical modes. This field leads to a splitting between the longitudinal and the transverse optical modes, the so-called LO-TO splitting. In the limit $\mathbf{q} \to 0$, one needs therefore to introduce correctly the macroscopic electric field. The matrix $\tilde{C}$ can be expressed as a non-analytic and analytic part

$$\tilde{C}_{\kappa\alpha,\kappa'\beta}(\mathbf{q}\to 0) = \tilde{C}^{AN}_{\kappa\alpha,\kappa'\beta}(\mathbf{q}=0) + \tilde{C}^{NA}_{\kappa\alpha,\kappa'\beta}(\mathbf{q}\to 0), \tag{80}$$

where the non-analytic part is given by

$$\tilde{C}^{NA}_{\kappa\alpha,\kappa'\beta}(\mathbf{q}\to 0) = \frac{4\pi}{\Omega_0}\frac{\left(\sum_{\gamma} q_{\gamma} Z^{*}_{\kappa,\gamma\alpha}\right)\left(\sum_{\gamma'} q_{\gamma'} Z^{*}_{\kappa',\gamma'\beta}\right)}{\sum_{\alpha\beta} q_{\alpha}\epsilon^{\infty}_{\alpha\beta} q_{\beta}}, \tag{81}$$

with $Z^{*}_{\kappa,\gamma\alpha}$ the Born effective charge

$$Z^{*}_{\kappa,\gamma\alpha} = \Omega_0 \frac{\partial P_{\gamma}}{\partial R_{\kappa\alpha}} = \frac{\partial F_{\kappa\alpha}}{\partial E_{\gamma}} \tag{82}$$

where Ω_0 is the unit cell volume, P_{γ} is the polarization by unit cell along direction γ, $R_{\kappa\alpha}$ is a collective periodic displacement of atoms κ in direction α, $F_{\kappa\alpha}$ is the force acting on atom κ in direction α, E_{γ} is an electric field along direction γ. As one can observe from Eq. (81), the non-analytic term is dependent on the direction of $\mathbf{q}$.

Mathematically, the problem of finding the LO eigenvalues and eigendisplacements can be rewritten as an eigenvalue problem in the basis of the TO eigendisplacements

$$\sum_n A_{m',n} W_{m,n} = \omega_m^2(\mathbf{q} \to 0) W_{m,m'}, \tag{83}$$

where $W_{m,n}$ are the basis expansion coefficients of the m^{th} LO eigendisplacement $U^m_{\kappa\alpha} = \sum_n W_{m,n} \tilde{U}^n_{\kappa\alpha}$ with respect to the zero-wavevector displacements $\tilde{U}$, and $A_{m',n}$ is the coupling matrix

$$A_{m',n} = \tilde{\omega}^2_{m'} \delta_{m',n} + \frac{4\pi}{\Omega_0} \frac{\left(\sum_\gamma q_\gamma \sum_{\kappa\alpha} Z^*_{\kappa,\gamma\alpha} (\tilde{U}^{m'}_{\kappa\alpha})^*\right)\left(\sum_{\gamma'} q_{\gamma'} \sum_{\kappa'\beta} Z^*_{\kappa',\gamma'\beta} \tilde{U}^n_{\kappa'\beta}\right)}{\sum_{\alpha\beta} q_\alpha \varepsilon^\infty_{\alpha\beta} q_\beta}, \tag{84}$$

with $\tilde{\omega}_m$ the frequency of the m^{th} TO mode.

If the eigendisplacements of LO are the same as the TO modes, as is the case for zinc-blende materials such as SiC or GaAs (see Chap. 4), and if we define mode-oscillator strength $S^m_{\alpha,\beta}$ as

$$S^m_{\alpha\beta} = \left(\sum_{\kappa\alpha'} Z^*_{\kappa,\alpha\alpha'} (U^m_{\kappa\alpha'}(\mathbf{q}=0))^*\right)\left(\sum_{\kappa'\beta'} Z^*_{\kappa',\beta\beta'} U^m_{\kappa'\beta'}(\mathbf{q}=0)\right), \tag{85}$$

then we obtain the link between LO and TO modes

$$\omega^2_m(\mathbf{q} \to 0) = \omega^2_m(\mathbf{q}=0) + \frac{4\pi}{\Omega_0} \frac{\sum_{\alpha\beta} q_\alpha S^m_{\alpha\beta} q_\beta}{\sum_{\alpha\beta} q_\alpha \epsilon^\infty_{\alpha\beta} q_\beta}. \tag{86}$$

However, in general LO and TO eigendisplacements are not the same and a complete diagonalization of the dynamical matrix or of Eq. (84) is required along the different directions of the long-wavelength limit. This is the case, for example, for $BiFeO_3$, as discussed in Chap. 6.

A last quantity of interest is the mode-effective charge $Z^*_{m,\alpha}$, which is a vector, defined as

$$Z^*_{m,\alpha} = \frac{\sum_{\kappa\alpha'} Z^*_{\kappa,\alpha\alpha'} U^m_{\kappa\alpha'}}{\sum_{\kappa\alpha'} \left(U^m_{\kappa\alpha'}\right)^* U^m_{\kappa\alpha'}}. \tag{87}$$

Now that we know how to solve the phonon eigenvalue problem and obtain phonon frequencies and displacements, we move in the next section to Raman intensities.

3.2 RAMAN INTENSITIES FROM DERIVATIVES OF THE DIELECTRIC FUNCTION

3.2.1 *Generalities*

The complete field-theoretic expression for the Raman susceptibility and intensities is presented in Ref. [1]. In this thesis, we have chosen to work in the adiabatic approximations of such expressions, i.e. letting the electrons respond immediately to the vibrations. In that case, it is possible to show that the full theoretical expression is equivalent to the derivative of the dielectric function with respect to phonon displacements.

Mathematically, this is translated as

$$\omega_m \ll |\omega_L - \omega_{gap} + i\eta|, \tag{88}$$

where ω_L is the laser frequency, ω_{gap} the frequency corresponding to the direct band gap, ω_m is the phonon frequency, and η the lifetime broadening of the gap. A complete derivation of the equivalence between the Feynman diagrammatic approach [1] and the derivative of the susceptibility is presented in App. A in the case of independent particles for first-order Raman intensities.

In this section, we show how to compute Raman intensities from derivatives of the dielectric function in the adiabatic approximation.

The Raman scattering efficiency S induced by a transition from the initial state $|i\rangle$ to a final state $|f\rangle$ is [20, 21]

$$S_{\alpha\beta}^{i\to f} = \Omega_0 \frac{(\omega_L - \omega)^4}{c^4(4\pi)^2} \left(\left[\delta\varepsilon_{\alpha\beta}^{i\to f}\right]\right)^2, \tag{89}$$

where $\left[\delta\varepsilon_{\alpha\beta}^{i\to f}\right]$ is the fluctuation of the dielectric function induced by a transition from i to f, ω_L is the laser frequency, c the speed of light, ω is the Raman shift, and α, β are Cartesian coordinates indices.

For finite displacements of the atoms, the dielectric function can be Taylor-expanded around the equilibrium position

$$\begin{aligned}\varepsilon_{\omega_L}(Q^1, \ldots) = \varepsilon^0_{\omega_L} &+ \sum_{m,\mathbf{q}} \frac{\partial \varepsilon_{\omega_L}}{\partial Q^m(\mathbf{q})} Q^m(\mathbf{q}) \\ &+ \frac{1}{2} \sum_{m_1\mathbf{q}_1, m_2\mathbf{q}_2} \frac{\partial^2 \varepsilon_{\omega_L}}{\partial Q^{m_1}(\mathbf{q}_1)\partial Q^{m_2}(\mathbf{q}_2)} Q^{m_1}(\mathbf{q}_1) Q^{m_2}(\mathbf{q}_2) \\ &+ \cdots\end{aligned} \tag{90}$$

where $\varepsilon^0_{\omega_L}$ is the equilibrium dielectric function.

At this stage, one needs to remember that because of momentum conservation, the sum of the wavevectors of all phonon modes implied in the process is negligible with respect to the size of the BZ. Therefore, at each order, $\sum_i \mathbf{q}_i = \mathbf{0}$. For first-order derivatives, only Γ-point phonons will therefore contribute, while at second-order, all phonons pairs with $\mathbf{q}_1 = -\mathbf{q}_2$ will contribute.

The Raman spectrum can be built by combining the efficiency with the possible selection rules for frequencies. The scattering efficiency reads then [20]

$$S^{\alpha\beta}(\omega) = \Omega_0 \frac{(\omega_L - \omega)^4}{c^4(4\pi)^2} \sum_n \sum_{m, m^{(2)}, \ldots, m^{(n)}} \frac{\sum_\mu e^{-\frac{E_\mu}{kT}} \sum_\nu \left(\left[\delta\varepsilon^{\alpha\beta}_{\mu\to\nu} \right]^{(n)} \right)^2 \delta_\gamma(\omega - \omega_{\mu\nu})}{\mathcal{Z}^{(m, \ldots m^{(n)})}}, \tag{91}$$

with n the summation index over the process orders, $m, \ldots, m^{(n)}$ are used to denote the modes indices depending on the order, $\delta_\gamma(\omega)$ a broadened Dirac-delta function[1] with a broadening parameter γ, $\mathcal{Z}^m$ the partition function

$$\mathcal{Z}^{(m, \ldots m^{(n)})} = \sum_\mu e^{-\frac{E_\mu(m, \ldots m^{(n)})}{kT}} \tag{92}$$

and where the expansion of the dielectric function Eq. (90) has been used along with the separation of the electronic part (which stays the same before and after the process) and the phononic part, going from phonon eigenstate μ to eigenstate ν

$$\left[\delta\varepsilon^{\alpha\beta}_{\mu\to\nu} \right]^{(1)}(m) = \frac{d\varepsilon^{\alpha\beta}}{dQ^m(\Gamma)} \left\langle \nu \left| \hat{Q}^m(\Gamma) \right| \mu \right\rangle \tag{93}$$

$$\left[\delta\varepsilon^{\alpha\beta}_{\mu\to\nu} \right]^{(2)}(m_1, m_2, \mathbf{q}) = \frac{1}{2} \frac{d^2\varepsilon^{\alpha\beta}}{dQ^{m_1}(\mathbf{q}) dQ^{m_2}(-\mathbf{q})} \left\langle \nu \left| \hat{Q}^{m_1}(\mathbf{q}) \hat{Q}^{m_2}(-\mathbf{q}) \right| \mu \right\rangle. \tag{94}$$

1 In this work, we use Lorentian functions

In these expressions, the derivatives with respect to Q^m are defined from the collective atomic displacements ($R_{\kappa\alpha}(\mathbf{q})$) derivatives as follows:

$$\frac{d\varepsilon^{\alpha\beta}}{dQ^m(\Gamma)} \triangleq \sum_{\kappa\alpha} \frac{d\varepsilon^{\alpha\beta}}{dR_{\kappa\alpha}(\Gamma)} U^m_{\kappa\alpha}(\Gamma) \tag{95}$$

$$\frac{d^2\varepsilon^{\alpha\beta}}{dQ^{m_1}(\mathbf{q})dQ^{m_2}(\mathbf{q})} \triangleq \sum_{\kappa\alpha\kappa'\beta} \frac{d^2\varepsilon^{\alpha\beta}}{dR_{\kappa\alpha}(\mathbf{q})dR_{\kappa'\beta}(-\mathbf{q})} U^{m_1}_{\kappa\alpha}(\mathbf{q}) U^{m_2}_{\kappa'\beta}(-\mathbf{q}). \tag{96}$$

3.2.2 *Phonon matrix elements in the harmonic approximation*

The Raman efficiency presented in Eq. (91) requires the evaluation of the derivatives of the dielectric function combined with matrix elements in the phonon space. In this section, we show how to simplify the phononic matrix elements when assuming the potential to be quadratic, neglecting all higher-order terms. [2]

3.2.2.1 *First-order Raman efficiency*

In the case of first-order Raman scattering, the complete expression Eq. (91) simplifies to [20]

$$\begin{aligned} S^{\alpha\beta}(\omega) =& \Omega_0 \frac{(\omega_L - \omega)^4}{c^4(4\pi)^2} \sum_m \frac{1}{\mathcal{Z}^m} \sum_\mu e^{-\frac{E^m_\mu}{kT}} \\ & \sum_\nu \left(\frac{d\varepsilon^{\alpha\beta}}{dQ^m(\Gamma)} \left\langle \nu \left| \hat{Q}^m(\Gamma) \right| \mu \right\rangle \right)^2 \delta_\gamma(\omega - \omega^m_{\mu\nu}). \end{aligned} \tag{97}$$

In the harmonic approximation, it is possible to show [100] that

$$E^m_\mu = (\mu + \frac{1}{2})\omega_m \tag{98}$$

$$\left(\left\langle \nu \left| \hat{Q} \right| \mu \right\rangle \right)^2 = \frac{1}{2\omega_m}(\mu+1)\delta_{\nu,\mu+1} + \frac{1}{2\omega_m}(\mu)\delta_{\nu,\mu-1} \tag{99}$$

$$\omega_{\mu\nu} = \omega_m \delta_{\nu,\mu+1} - \omega_m \delta_{\nu,\mu-1}, \tag{100}$$

2 We refer the reader to Ref. [20, 21] for the treatment of anharmonicities.

so that the general equation becomes, since we only consider Stokes scattering ($\nu = \mu + 1$)

$$S^{\alpha\beta}(\omega) = \Omega_0 \frac{(\omega_L - \omega)^4}{c^4(4\pi)^2} \sum_m \frac{1}{2\omega_m} \left(\frac{d\varepsilon^{\alpha\beta}}{dQ^m}\right)^2 \delta_\gamma(\omega - \omega_m) \frac{\sum_\mu e^{-(\mu+\frac{1}{2})\frac{\omega_m}{kT}}(\mu+1)}{\sum_\mu e^{-(\mu+\frac{1}{2})\frac{\omega_m}{kT}}} \tag{101}$$

and because higher-order terms are neglected.

The right part can be rewritten, using $\alpha_m = \frac{\omega_m}{kT}$ as

$$\frac{\sum_\mu e^{-(\mu+\frac{1}{2})\alpha_m}(\mu+1)}{\sum_\mu e^{-(\mu+\frac{1}{2})\alpha_m}} = \frac{\frac{e^{-\alpha_m}}{(1-e^{-\alpha_m})^2} + \frac{1}{1-e^{-\alpha_m}}}{\frac{1}{1-e^{-\alpha_m}}} = n_m(T) + 1 \tag{102}$$

with the phonon occupation factor defined as

$$n_m(T) = \frac{1}{e^{\frac{\omega_m}{kT}} - 1}. \tag{103}$$

Therefore, the final expression for first-order Stokes scattering is

$$S^{\alpha\beta}(\omega) = \Omega_0 \frac{(\omega_L - \omega)^4}{c^4(4\pi)^2} \sum_m \frac{1}{2\omega_m} \left(\frac{d\varepsilon^{\alpha\beta}}{dQ^m}\right)^2 \delta_\gamma(\omega - \omega_m)(n_m(T) + 1), \tag{104}$$

where the $n_m(T) + 1$ factor plays a weighting role. From the knowledge of the phonon frequencies and displacements, only derivatives of the dielectric functions are left unknown.

At this stage, we can attribute to each mode a Raman susceptibility tensor $\boldsymbol{\alpha}^m(\omega_L)$ for the phonon m

$$\alpha_{ij}^m(\omega_L) = \sqrt{\Omega_0} \frac{1}{4\pi} \sum_{\tau\beta} \frac{\partial \varepsilon_{ij}(\omega_L)}{\partial R_{\tau\beta}} U_{\tau\beta}^m. \tag{105}$$

The scattering efficiency of the phonon of frequency ω_m for a photon of frequency ω_L is therefore defined as [14]

$$S^m = \frac{(\omega_L - \omega_m)^4}{c^4} |\mathbf{e}_o . \boldsymbol{\alpha}^m(\omega_L) . \mathbf{e}_i|^2 \frac{n_m + 1}{2\omega_m}, \tag{106}$$

where $\mathbf{e}_o$ and $\mathbf{e}_i$ are the outgoing and in-going polarization of the light.

For more details about the derivation of Eq. (106), we refer the reader to Refs. [14] and [99].

3.2.2.2 *Second-order Raman efficiency*

Similarly as for first-order phonon terms, second-order phonon terms can also be analytically evaluated.

Indeed, 2D harmonic phononic systems are fully separable and the total wavefunction can be written as a product of two wavefunctions

$$\chi_{\mu}^{m_1,m_2}(Q^{m_1},Q^{m_2}) = \chi_{\mu_1}^{m_1}(Q^{m_1}) \times \chi_{\mu_2}^{m_2}(Q^{m_2}), \tag{107}$$

both obtained as solutions of 1D problem. The energy of this state is written

$$E_{\mu}^{m_1,m_2} = E_{\mu_1}^{m_1} + E_{\mu_2}^{m_2} = (\mu_1 + \frac{1}{2})\omega_{m_1} + (\mu_2 + \frac{1}{2})\omega_{m_2}, \tag{108}$$

so the index μ is in fact a "2D-index" (μ_1,μ_2).

The matrix elements with two different phonons can then be computed according to

$$\left\langle (\nu_1,\nu_2) \left| \hat{Q}^1 \hat{Q}^2 \right| (\mu_1,\mu_2) \right\rangle = \left\langle \nu_1 \left| \hat{Q}^1 \right| \mu_1 \right\rangle \left\langle \nu_2 \left| \hat{Q}^2 \right| \mu_2 \right\rangle. \tag{109}$$

The scattering efficiency at second-order is written as

$$\begin{aligned} S^{\alpha\beta}(\omega) =& \Omega_0 \frac{(\omega_L - \omega)^4}{(4\pi)^2 c^4} \frac{1}{N_q} \sum_{\mathbf{q}} \sum_{m_1,m_2} \frac{1}{\mathcal{Z}^{(m_1,m_2)}} \\ & \sum_{\mu} e^{-\frac{E_{\mu}^{(m_1,m_2)}}{kT}} \sum_{\nu} \delta_{\gamma}(\omega - \omega_{\mu\nu}) \\ & \left(\frac{1}{2} \frac{d^2\varepsilon^{\alpha\beta}}{dQ^{m_1}(\mathbf{q}) dQ^{m_2}(-\mathbf{q})} \left\langle \nu \left| \hat{Q}^{m_1}(\mathbf{q}) \hat{Q}^{m_2}(-\mathbf{q}) \right| \mu \right\rangle \right)^2, \end{aligned} \tag{110}$$

where the integral over the wavevectors has been replaced by a summation over N_q points of the BZ.

Using the harmonicity of the phononic potential, $\mu = (\mu_1,\mu_2)$ and $\nu = (\nu_1,\nu_2)$, $\mathcal{Z}^{(m_1,m_2)} = \mathcal{Z}^{m_1}\mathcal{Z}^{m_2}$, we get, for two-Stokes processes [3]

$$\begin{aligned} S^{\alpha\beta}(\omega) =& \Omega_0 \frac{(\omega_L - \omega)^4}{(4\pi)^2 c^4} \frac{1}{N_q} \sum_{\mathbf{q}} \sum_{m_1,m_2} \\ & \left(\frac{1}{2} \frac{d^2\varepsilon^{\alpha\beta}}{dQ^{m_1}(\mathbf{q}) dQ^{m_2}(-\mathbf{q})} \right)^2 \frac{1}{4\omega_{m_1}(\mathbf{q})\omega_{m_2}(-\mathbf{q})} \\ & \left\{ (n_{m_1\mathbf{q}}(T)+1)(n_{m_2\mathbf{q}}(T)+1)\delta_{\gamma}(\omega - (\omega_{m_1}(\mathbf{q}) + \omega_{m_2}(\mathbf{q}))) \right\}. \end{aligned} \tag{111}$$

Again in this expression, only Bose-Einstein occupation factors and phonon frequencies appear, leaving the only unknown quantities to be the derivatives of the dielectric functions.

3.3 FROZEN-PHONON APPROACH

Up to now, we have shown the general expressions to compute first and second-order Raman spectra, and their simplification in the harmonic case.

In this framework, the electronic part, related to the derivatives of the dielectric function, remains the last unknown quantity.

These derivatives can be computed numerically in the so-called FP method, using the results obtained with distorted geometries in which the atoms are displaced by a small amount along the phonon eigenvector.

In this section, we detail how to compute first and second-order Raman scattering using this method.

3.3.1 *First-order Raman scattering*

The first step is a computation of the solution of the phonon eigenvalue problem, usually done using DFPT techniques. From the phonon frequencies, the phonon matrix elements can be evaluated as shown in Sec. 3.2.2.

Then, the dielectric function is computed for several finite displacements along the phonon eigenmodes, and these results are combined to extract the derivatives, via a fitting procedure or via finite difference formulae. This can also be done along Cartesian atomic displacements since

$$\frac{\partial \varepsilon^{\alpha\beta}(\omega_L)}{\partial Q^m} = \sum_{\kappa\alpha} \frac{\partial \varepsilon^{\alpha\beta}(\omega_L)}{\partial R_{\kappa\gamma}} U^m_{\kappa\gamma}. \tag{112}$$

Finally, we apply directly Eq. (104) that has been derived for the first-order case.

A last remark about first-order scattering must be raised. The derivative in (105) is a total derivative of the dielectric function. For TO modes, there is no electric field and so it is directly the partial derivative:

$$\frac{d\chi^{(1)}_{ij}(\omega_L)}{dR_{\kappa\alpha}}(TO) = \left.\frac{\partial \chi^{(1)}_{ij}(\omega_L)}{\partial R_{\kappa\alpha}}\right|_{E=0}, \tag{113}$$

where the susceptibility has been used instead of the dielectric function

$$\varepsilon_{ij} = 1 + 4\pi\chi_{ij}. \tag{114}$$

In polar materials, the phonon can induce a macroscopic field (LO phonon), which first changes the phonon frequency and displacements (see section 3.1) but also modifies the intensity

$$\frac{d\chi^{(1)}_{ij}(\omega_L)}{dR_{\kappa\alpha}}(LO) = \left.\frac{\partial\chi^{(1)}_{ij}(\omega_L)}{\partial R_{\kappa\alpha}}\right|_{E=0} + \sum_\beta \frac{\partial\chi^{(1)}_{ij}(\omega_L)}{\partial E_\beta}\frac{\partial E_\beta}{\partial R_{\kappa\alpha}}. \tag{115}$$

From the definition of Born effective charge and the electric field induced by a phonon of wavevector $\mathbf{q}$, one gets [101]

$$\frac{\partial E_\beta}{\partial R_{\kappa\alpha}} = -\frac{4\pi}{\Omega_0} q_\beta \frac{\sum_\gamma Z^*_{\kappa,\gamma\alpha} q_\gamma}{\sum_{\gamma\gamma'} q_\gamma \epsilon^\infty_{\gamma\gamma'} q_{\gamma'}}. \tag{116}$$

Since $\dfrac{\partial\chi^{(1)}_{ij}(\omega)}{\partial E_k} = 2\chi^{(2)}_{ijk}(-\omega,\omega,0)$,

$$\begin{aligned}\frac{d\chi^{(1)}_{ij}(\omega_L)}{dR_{\kappa\alpha}}(LO) =& \frac{d\chi^{(1)}_{ij}(\omega_L)}{dR_{\kappa\alpha}}(TO) \\ &- \frac{8\pi}{\Omega_0}\frac{\left(\sum_\beta q_\beta \chi^{(2)}_{ij\beta}(-\omega_L,\omega_L,0)\right)\left(\sum_\gamma Z^*_{\kappa,\gamma\alpha} q_\gamma\right)}{\sum_{\gamma\gamma'} q_\gamma \epsilon^\infty_{\gamma\gamma'} q_{\gamma'}}.\end{aligned} \tag{117}$$

We therefore obtain in Eq. (113) and (117) a complete expression that allows the calculation of TO and LO with the frequency-dependence included.

The second-order susceptibility $\chi^{(2)}_{ijk}(-\omega,\omega,0)$ can be computed in the IPA with a sum-over-states approach from the knowledge of position operator matrix elements. We reproduce the expressions in App. B where we also show the link between the electro-optic tensor and the Linear Electro-Optic (LEO) susceptibility.

3.3.2 *Second-order Raman scattering*

Similarly to first-order Raman, the only missing part in second-order RI is the second-order derivative of the dielectric function for each pair of mode

$$\frac{d^2\varepsilon^{\alpha\beta}}{dQ^{m_1}(\mathbf{q})dQ^{m_2}(-\mathbf{q})}. \tag{118}$$

In order to obtain this derivative for each q-point, a finite difference-FP approach can be used. We therefore compute ε on several distorted geometries as follows. For the selected $\mathbf{q}$ wavevectors, a supercell, compatible with $\mathbf{q}$ is generated: the axes of this supercell $\left\{\mathbf{R}'_j\right\}$ fulfills the constraint $e^{i\mathbf{q}\mathbf{R}'_j} = 1$, which means that $\mathbf{q}$ is a reciprocal vector of the supercell. The atoms of the supercell are then displaced with real displacements defined from the phonon eigendisplacements and phase factors

$$u_{\kappa\alpha l} \triangleq \frac{1}{2}\left[U_{\kappa\alpha}(\mathbf{q})e^{i\mathbf{q}\mathbf{R}_l} + U_{\kappa\alpha}(-\mathbf{q})e^{-i\mathbf{q}\mathbf{R}_l}\right] \tag{119}$$

$$v_{\kappa\alpha l} \triangleq \frac{-i}{2}\left[U_{\kappa\alpha}(\mathbf{q})e^{i\mathbf{q}\mathbf{R}_l} - U_{\kappa\alpha}(-\mathbf{q})e^{-i\mathbf{q}\mathbf{R}_l}\right]. \tag{120}$$

The supercell is chosen in such a way that $\mathbf{q}$ is a reciprocal lattice vector of the supercell, $\mathbf{k}+\mathbf{q}$ points are folded back to $\mathbf{k}$ points of the supercell.

3.3.3 *Approximations to second-order Raman scattering*

We now detail why, even for a small system like silicon, the calculations of second-order Raman intensities, if done using simply brute force, are extremely demanding. First, for any wavevector, the summations over the N_{modes} phonon modes in Eq. (111) require $N_{modes} \times N_{modes}$ evaluations of the derivative. If the dielectric tensor is evaluated on a grid of 5×5 pairs of displacements, in order to get the second-order derivatives, this amounts to $25 \times 6^2 = 900$ evaluations of the dielectric tensor for silicon. This shows the large number of evaluations of the dielectric function required for adequate extraction of the numerical derivatives. These numerous calculations must be repeated for each wavevector in the BZ. In contrast, for first-order calculations, the number of evaluations for the only zone-center wavevector amounts to 5 evaluations for each mode, thus $5 \times 6 = 30$ [3] evaluations of the dielectric function to reach the final Raman spectrum of silicon.

It should also be noted that, unlike first-order spectra, second-order resonant Raman scattering requires the use of supercells commensurate with the wavevectors, and the computational cost increases quickly with the size of the supercell. Indeed, the number of bands included in the calculations scales linearly with the number of atoms. In the case of IPA, the number of electronic transitions scales linearly with the product of

3 This number can be even reduced to only 5 by using symmetry arguments: acoustic modes do not contribute and the three other modes are degenerate.

the number of valence and conduction bands and linearly with the number of k-points. Taking into account the folding of bands in the case of supercell, and the computational cost required for the dipole matrix elements, the overall scaling is roughly cubic with the size of the supercell. In BSE, however, the kernel introduces coupling between transitions, and the number of matrix elements in the transition basis set scales with the square of the product of the number of valence and conduction bands, and with the square of the number of k-points. Because of the reduction of the number of k-points with larger supercells, the number of matrix elements therefore increases with the square of the size of the supercell. Since the evaluation of the screened Coulomb matrix elements requires a double sum over planewaves, we conclude that the ratio between a BSE run for a supercell and the one for a unit cell increases as the fourth power of the number of replicas in the supercell. Finally, as we observe in Sec. 3.4, the derivatives of the dielectric function are highly sensitive to the sampling of the BZ, leading to very demanding calculations in the case of BSE.

Even if the FP methodology requires a large amount of evaluations of dielectric functions, we have succeeded to apply the technique to three-dimensional materials by using approximations and numerical techniques that are presented in the following paragraphs. Results on first-order and second-order Raman scattering of silicon are then presented in Sec. 3.4 and 3.5 respectively.

3.3.3.1 *Overtones approximation in second-order Raman scattering*

Overtones in the second-order Raman spectrum are obtained by combining twice the same phonon modes, so explicitly, terms with $m_1 = m_2 = m$

$$\sum_{\mathbf{q}} \frac{d^2\varepsilon^{\alpha\beta}}{dQ^m(\mathbf{q})dQ^m(-\mathbf{q})}. \tag{121}$$

To compute overtones derivatives, one therefore only needs one-dimensional derivatives, along the same phonon displacement. To compute general second-order derivatives with respect to two different modes one needs two-dimensional derivatives. This is also true in the presence of degeneracies, where two-dimensional derivatives are also required, even for overtones, as shown in Sec. 3.3.3.3. In this thesis, the second-order derivatives are extracted by using a set of 5 points along each phonon displacement. This means that 5 points are used for overtones derivatives and 25 evaluations of the dielectric function are required for each derivatives for different modes.

In Eq. (111) this approximation corresponds to neglecting all terms where $\omega_{m_1} \neq \omega_{m_2}$ and leads to the following expression

$$S^{\alpha\beta}(\omega, \omega_L, T) = \Omega_0 \frac{(\omega_L - \omega)^4}{(4\pi)^2 c^4} \frac{1}{N_q} \sum_{\mathbf{q}} \sum_{m}$$
$$\left\{ \left[\frac{1}{2} \frac{\partial^2 \varepsilon^{\alpha\beta}(\omega_L)}{\partial Q^m(\mathbf{q}) \partial Q^m(-\mathbf{q})} \right]^2 \frac{1}{4\omega_m(\mathbf{q})\omega_m(-\mathbf{q})} [n_{m\mathbf{q}}(T) + 1]^2 \right.$$
$$\left. \delta_\gamma(\omega - 2\omega_m(\mathbf{q})) \right\}. \quad (122)$$

In this framework, the corresponding overtone density of states becomes

$$\frac{1}{N_q} \sum_{\mathbf{q}} \sum_{m} \delta_\gamma(\omega - 2\omega_m(\mathbf{q})), \quad (123)$$

that is the one-phonon density of states scaled by a factor two in the frequency range. From a group-theoretical point of view, derivatives with respect to twice the same phonon mode will always be active and contribute to the fully symmetric component of the spectrum [3].

3.3.3.2 *Smallest supercell generation*

Frozen-phonon calculations of the dielectric function with finite $\mathbf{q}$-point phonon requires the generation of supercells. In order to decrease the computational cost as much as possible, an automatic generation of the smallest supercell has been developed in the Abipy framework[4].

The $\mathcal{R}$ and the $\mathcal{G}$ matrix contain the real space $\mathbf{R}$ and reciprocal space vectors $\mathbf{G}$ column-wise and are defined such as

$$\mathcal{R}^T \mathcal{G} = 2\pi. \quad (124)$$

The phase factor associated with the phonon displacement is $e^{i\mathbf{q}\cdot\mathbf{R}^l}$. We need to find three new axis $\mathbf{R}_1^{sc}$, $\mathbf{R}_2^{sc}$ and $\mathbf{R}_3^{sc}$ such as $e^{i\mathbf{q}\cdot\mathbf{R}_j^{sc}} = 1$. The components of the $\mathbf{R}_j^{sc}$ axis should be integer number in real space coordinates

$$\mathbf{R}_j^{sc} = \mathcal{R}\, \mathbf{l}_j = \mathcal{R} \begin{pmatrix} l_j^1 \\ l_j^2 \\ l_j^3 \end{pmatrix}. \quad (125)$$

4 The Abipy framework contains a set of tools for generating ABINIT input files, automatic management of the calculations and post-processing tools. It is available on http://github.com/gmatteo/abipy

We define a matrix M, called scaling matrix such as

$$M = \begin{pmatrix} l_1^1 & l_2^1 & l_3^1 \\ l_1^2 & l_2^2 & l_3^2 \\ l_1^3 & l_2^3 & l_3^3 \end{pmatrix}. \tag{126}$$

This matrix will be used to generate the supercell and the displaced atoms.

The components of the $\mathbf{q}$ point are given in terms of the reciprocal space coordinates

$$\mathbf{q} = \mathcal{G}\,\mathbf{q}_c = \mathcal{G}\begin{pmatrix} q^1 \\ q^2 \\ q^3 \end{pmatrix}, \tag{127}$$

so that the phase factor is given by

$$e^{i\mathbf{q}\cdot\mathbf{R}_j^{sc}} = e^{i\mathbf{q}_c^T\mathcal{G}^T\mathcal{R}\,l_j} = e^{2\pi i\mathbf{q}_c^T\mathbf{l}_j} = 1 \Rightarrow \mathbf{q}_c^T\mathbf{l}_j = integer. \tag{128}$$

In order to get the smallest supercell, i.e. looking for three integer $\mathbf{l}_j$ vectors so the supercell is the smallest possible, we use the technique available in the Exciting code [102].

First, the smallest non-zero $\mathbf{R}_1^{sc}$ is determined, such as $\mathbf{q}_c^T\mathbf{l}_1 = integer$. Then, we find the smallest non-zero $\mathbf{R}_2^{sc}$, non-parallel to $\mathbf{R}_1^{sc}$ and such as $\mathbf{q}_c^T\mathbf{l}_2 = integer$. And finally, we compute the smallest $\mathbf{R}_3^{sc}$ which is non-coplanar with both $\mathbf{R}_1^{sc}$ and $\mathbf{R}_2^{sc}$ and such as $\mathbf{q}_c^T\mathbf{l}_3 = integer$.

3.3.3.3 *Phonon mode degeneracies*

Since some modes are degenerate, we need to find some way to present results that are invariant upon the choice of particular eigenvectors of the dynamical matrix.

A quantity such as

$$I^D_{\kappa\alpha,\kappa'\beta} = \sum_{m\in D} (U^m_{\kappa\alpha})^*\, U^m_{\kappa'\beta} \tag{129}$$

where D is the degenerate subspace, is invariant upon the gauge choice.

For first-order Raman, the Raman efficiency is proportional to

$$S \propto \left[\sum_{\kappa\alpha} \frac{\partial \varepsilon^{\alpha\beta}}{\partial R_{\kappa\alpha}(\mathbf{q})} U^{m_1}_{\kappa\alpha}(\mathbf{q})\right]^2, \tag{130}$$

that gives an invariant quantity when summed over the degenerate phonons

$$\sum_{m\in D}\left[\sum_{\kappa\alpha}\frac{\partial\varepsilon^{\alpha\beta}}{\partial R_{\kappa\alpha}(\mathbf{q})}U^{m}_{\kappa\alpha}(\mathbf{q})\right]^2. \tag{131}$$

For second-order Raman, the intensity is linked to

$$S\propto\left[\sum_{\kappa\alpha,\kappa'\beta'}\frac{\partial^2\varepsilon^{\alpha\beta}}{\partial R_{\kappa\alpha}(\mathbf{q})\partial R_{\kappa'\beta}(-\mathbf{q})}U^{m_1}_{\kappa\alpha}(\mathbf{q})U^{m_2}_{\kappa'\beta}(-\mathbf{q})\right]^2 \tag{132}$$

which leads an invariant term by summing over the degeneracies of both modes [103]

$$\sum_{m\in D,m'\in D'}\left[\sum_{\kappa\alpha,\kappa'\beta'}\frac{\partial^2\varepsilon^{\alpha\beta}}{\partial R_{\kappa\alpha}(\mathbf{q})\partial R_{\kappa'\beta}(-\mathbf{q})}U^{m}_{\kappa\alpha}(\mathbf{q})U^{m'}_{\kappa'\beta}(-\mathbf{q})\right]^2. \tag{133}$$

However, in the overtone approximations, summing with $m'=m$ does not provide an invariant quantity since

$$\sum_{m\in D}\left[\sum_{\kappa\alpha,\kappa'\beta'}\frac{\partial^2\varepsilon^{\alpha\beta}}{\partial R_{\kappa\alpha}(\mathbf{q})\partial R_{\kappa'\beta}(-\mathbf{q})}U^{m}_{\kappa\alpha}(\mathbf{q})U^{m}_{\kappa'\beta}(-\mathbf{q})\right]^2 \tag{134}$$

is not invariant (we miss the contributions from two different modes that are degenerate). Therefore, for highly-symmetric k-points, we need still to compute two-dimensional derivatives between different degenerate states.

3.3.3.4 *Integration over the Brillouin Zone*

The integral over q-points is discretized as a sum over the q-points. A convergence study is therefore required, increasing the number of q-points. However, since increasing the density of q-points increases the size of supercells used for the FP, we want to keep the number of q-points as low as possible.

For the FP approach, commensurate q-points with the lattice must be used, that means that we should be able to get Eq. (128) fulfilled for some integer l values. This forbids the use of random q points.

In order to reduce the amount of q-points, symmetries for q-points are used: it is possible to relate the second-order derivatives from one

q-point to another symmetric q-point using symmetry operations. Therefore, we can compute only the irreducible set of q-points and then use symmetries to rebuild entire information on the Raman tensors. More technical detail is available in App. C.

3.3.3.5 *"Double-Grid" technique*

The expression for second-order Raman intensities have been derived in a previous paragraph, leading to

$$\begin{aligned} S^{\alpha\beta}(\omega) =& \Omega_0 \frac{(\omega_L - \omega)^4}{(4\pi)^2 c^4} \frac{1}{N_q} \sum_{\mathbf{q}} \sum_{m_1,m_2} \\ & \left(\frac{1}{2} \frac{d^2\varepsilon^{\alpha\beta}}{dQ^{m_1}(\mathbf{q}) dQ^{m_2}(-\mathbf{q})} \right)^2 \frac{1}{4\omega_{m_1}(\mathbf{q})\omega_{m_2}(-\mathbf{q})} \\ & (n_{m_1\mathbf{q}}(T)+1)(n_{m_2\mathbf{q}}(T)+1)\delta_\gamma(\omega - (\omega_{m_1}(\mathbf{q}) + \omega_{m_2}(\mathbf{q}))). \end{aligned} \tag{135}$$

We can rewrite the summation of the $\mathbf{q}$-points as a summation over a coarse grid of $N_{q,c}$ $\mathbf{q}_c$ wavevectors, and then for each $\mathbf{q}_c$, a summation of the $N_{q,d}$ dense wavevectors around $\mathbf{q}_c$, denoted $\mathbf{q}_d$. If the derivatives change smoothly in the $\mathbf{q}$-space, they can be factorized out of the summation on the dense grid

$$\begin{aligned} S^{\alpha\beta}(\omega) =& \Omega_0 \frac{(\omega_L - \omega)^4}{(4\pi)^2 c^4} \frac{1}{N_{q,c}} \sum_{\mathbf{q}_c} \sum_{m_1,m_2} \left(\frac{1}{2} \frac{d^2\varepsilon^{\alpha\beta}}{dQ^{m_1}(\mathbf{q}_c) dQ^{m_2}(-\mathbf{q}_c)} \right)^2 \\ & \frac{1}{N_{q,d}} \sum_{\mathbf{q}_d} \frac{1}{4\omega_{m_1}(\mathbf{q}_d)\omega_{m_2}(-\mathbf{q}_d)} \\ & (n_{m_1\mathbf{q}_d}(T)+1)(n_{m_2\mathbf{q}_d}(T)+1) \\ & \delta_\gamma(\omega - (\omega_{m_1}(\mathbf{q}_d) + \omega_{m_2}(\mathbf{q}_d))), \end{aligned} \tag{136}$$

where the sum over dense wavevectors $\mathbf{q}_d$ is done only in the neighborhood of $\mathbf{q}_c$.

Since the computation of phonon frequencies on a dense mesh can be obtained from interpolation techniques based on Inter-atomic Force Constants [8], the sum over q-points in the dense mesh is not a big problem.

So the proposed approach is the following. For a given $\mathbf{q}_c$, compute

$$P_{m_1 m_2}(\mathbf{q}_c, \omega) = \frac{1}{N_{q,d}} \sum_{\mathbf{q}_d} \frac{1}{4\omega_{m_1}(\mathbf{q}_d)\omega_{m_2}(-\mathbf{q}_d)} (n_{m_1\mathbf{q}_d}(T)+1)(n_{m_2\mathbf{q}_d}(T)+1)\delta_\gamma(\omega - (\omega_{m_1}(\mathbf{q}_d)+\omega_{m_2}(\mathbf{q}_d)), \tag{137}$$

and then

$$S^{\alpha\beta}(\omega) = \Omega_0 \frac{(\omega_L-\omega)^4}{(4\pi)^2 c^4} \frac{1}{N_{q,c}} \sum_{\mathbf{q}_c} \sum_{m_1,m_2} \left(\frac{1}{2}\frac{d^2\varepsilon^{\alpha\beta}}{dQ^{m_1}(\mathbf{q}_c)dQ^{m_2}(-\mathbf{q}_c)}\right)^2 P_{m_1 m_2}(\mathbf{q}_c, \omega). \tag{138}$$

One should note that Eq. (137) presents the same singularities and therefore behaves similarly as the two-phonon density of states if the frequencies and the occupation factors are taken for $\mathbf{q}_c$ instead of $\mathbf{q}_d$.

3.4 FIRST-ORDER RAMAN OF SILICON

3.4.1 *Introduction*

The theoretical basis needed for the computation of the frequency-dependent RI has already been described previously in this chapter. We chose to study silicon, for which the experimental frequency-dependent enhancement factor is particularly strong. The available data cover the frequency range between 1.8 eV and 3.8 eV [104], and the experimental value of the direct gap is at 3.4 eV. Due to the high symmetry of silicon, there is only one Raman-active phonon mode, whose eigenvector is determined by symmetry.

The numerical procedure applied for the calculations of RI of silicon is presented in Sec. 3.4.2. In Sec. 3.4.3, the problem associated with the slow convergence of the results with respect to the sampling of the BZ is analyzed. Sec. 3.4.4 presents the theoretical results, including excitonic effects. Finally, in Sec. 3.4.5, theoretical and experimental results for the silicon Raman intensity are compared.

3.4.2 *Numerical procedure*

Calculations are performed using ABINIT [86, 87]. The pseudopotential used to simulate the silicon atom is of the Troullier-Martins type and has been generated with the LDA parametrization proposed by Teter [105].

The DFT-LDA calculations are performed with a 4 times shifted 4x4x4 Monkhorst-Pack grid to sample the BZ [106], and a plane-wave basis set kinetic energy cut-off of 16 Ha. The theoretical lattice cell for silicon is 10.20 Bohr, which gives an error of 0.6 % with respect to the experimental results (10.26 Bohr) [107]. Using this theoretical lattice constant, the DFT-LDA indirect gap is 0.45 eV, while the direct gap is 2.52 eV.

Quasi-particle corrections are computed within the so-called *one-shot* GW or G_0W_0 approximation [29]. We use a cut-off energy of 8 Ha for the screening and 16 Ha for the self-energy matrix elements. An extrapolar energy of 3 Ha is used to reduce the number of bands needed to converge to 100 bands [108]. The computed GW corrections give a direct gap of 3.20 eV. These results are comparable to other GW results [109, 110] and in good agreement with the experimental band gap of 3.4 eV [111]. During the computation of the BSE optical spectrum, the opening of the gap is simulated by a rigid scissor [112] with a value of 0.65 eV to reproduce the theoretical GW gap unless stated otherwise.

Convergence of the Bethe-Salpeter computations with respect to the BZ sampling is particularly difficult, and is discussed in the next section. The cut-off energies are 16 Ha for the wavefunctions and 3 Ha for the screening. The transition space used to solve the BSE includes from the second to the ninth band. A broadening factor of 0.1 eV is used for the dielectric function.

The adiabatic approximation (see Sec. 3.2) that is used extensively in this work is justified in the case of silicon since the lifetime broadening (≈ 0.1 eV) is larger than the phonon frequency ≈ 0.065 eV [99].

In this adiabatic approximation, two-band as well as three-band contributions to the resonant Raman are included, the latter coming from the matrix element changes due to changes in the wavefunctions produced by phonon-induced admixture of the two bands under consideration with a third band [98].

In order to compute derivatives with the displacements, we add $h \times \sqrt{2}/2$ to the x-position of the first atom and $-h \times \sqrt{2}/2$ to the x-position of the other atom, for different values of h. The derivative is obtained by computing $\chi_{yz}(\omega)$ for $h = 0.01$ and $h = 0$ in the convergence studies

and is obtained by computing $\chi_{yz}(\omega)$ for $h = 0.01$ and $h = -0.01$ for the final result.

We have analyzed the behavior of the G_0W_0 scissor shift, as a function of the frozen phonon amplitude. Because the Raman amplitude corresponds to a first-order derivative with respect to atomic displacement, see Eq. (105), we only have to consider the linear response. For non-degenerate eigenstates, due to the high symmetry of the crystals, such derivative of the scissor shift with respect to atomic positions vanishes. For degenerate eigenenergies, linear variations of eigenenergies are present, but the mean variation vanishes over the set of degenerate states. Hence, the modification of the G_0W_0 corrections with respect to atomic displacement does not have any effect on the Raman intensity of silicon, within the present formalism. Of course, this is a very specific situation. For the analysis of most other materials, the variation of the eigenenergies at linear order will have to be taken into account.

As told in Eq. (19), the values of the dielectric functions may differ along different directions q. We want to extract the tensor components from the long-wavelength limits calculations. Because of the symmetry of the tensor, the values of $\hat{\varepsilon}$ for each pair of Cartesian coordinates may be obtained by computing the macroscopic dielectric function for 6 different directions q. The directions used in the calculations are (0,1,1), (1,0,1), (1,1,0), (1,0,0), (0,1,0) and (0,0,1).

The macroscopic dielectric function (Eq. (34)) is computed using the iterative Haydock technique [77]. The algorithm is terminated when a relative error of 1%, for the real and the imaginary part of ε, is achieved for each frequency in the frequency range under investigation.

3.4.3 *Sampling of the Brillouin zone*

As already mentioned in Sec. 2.4, achieving converged results with respect to the sampling of the BZ is a very difficult issue. In particular, we will show in this section that grids that are appropriate for obtaining a converged macroscopic dielectric function in the whole frequency range are not sufficiently dense for derivatives, such as the RI, at least in the resonance region.

In order to accelerate the convergence of BSE spectra, shifted homogeneous meshes are traditionally used. A symmetry-breaking shift allows one to sample more non-equivalent points and therefore leads to a more representative sampling of the band dispersion: with respect to

non-shifted meshes, its presence lowers the computational load for an equivalent convergence criterion.

To ease the discussion, we introduce specific notations. The meshes are characterized by the number of divisions along each axis of the primitive cell in reciprocal space, namely n_1, n_2 and n_3. For a crystalline cubic structure these three numbers are taken as equal ($n_1 = n_2 = n_3 = n_k$). The total number of points inside this mesh is therefore $N_k = n_1 n_2 n_3 = n_k^3$. All the points of the mesh are shifted by a certain vector characterized by three real numbers s_i between -0.5 and 0.5, $\mathbf{s} = (s_1, s_2, s_3)$. This shift is such that the point $(s_1/n_1, s_2/n_2, s_3/n_3)$ belongs to the shifted mesh. We use the notation $(n_1 \times n_2 \times n_3|\mathbf{s})$ to refer to such a mesh.

Fig. 12 presents the macroscopic dielectric function (from BSE) for different grids with increasing number of wavevectors, while Fig. 13 presents the corresponding RI, both with excitonic contributions (BSE), and without excitonic contributions (IPA). These grids, of size N_k, are shifted by the vector $\mathbf{s} = (0.11, 0.21, 0.31)$ in reciprocal space along a non-symmetric direction.

As seen in Fig. 12, for the computation of the macroscopic dielectric function, the oscillations present in the $(10 \times 10 \times 10|\mathbf{s})$ case are progressively damped when the density of the mesh is increased and a $(16 \times 16 \times 16|\mathbf{s})$ grid gives converged results.

However, from Fig. 13, we observe that the convergence is much more difficult for the square of the Raman susceptibility, in the region beyond 3.2 eV (which corresponds to the optical gap). Important features still change going from $(16 \times 16 \times 16|\mathbf{s})$ to $(18 \times 18 \times 18|\mathbf{s})$. Interestingly, such a difficult convergence is present both with and without excitonic contributions, as exemplified by the upper and lower parts of Fig. 13.

With the method of shifted grids, convergence is not achievable beyond 3.2 eV, given our computational resources. Indeed, the scaling of the method with respect to the sampling of the BZ is $\mathcal{O}(N_k^2)$, with N_k the total number of k-points in the full BZ. With N_k=18^3, the convergence is not yet reached.

By contrast, convergence is much better below the gap value. In the next paragraphs, we first perform an analysis of the convergence for such frequencies, then turn to the higher-frequency part of the spectrum, for which we use a multiple-shift technique.

3.4.3.1 *The convergence below the band gap*

In order to have a quantitative understanding of the convergence in the low-energy part, we use a Taylor expansion and give coefficients similar

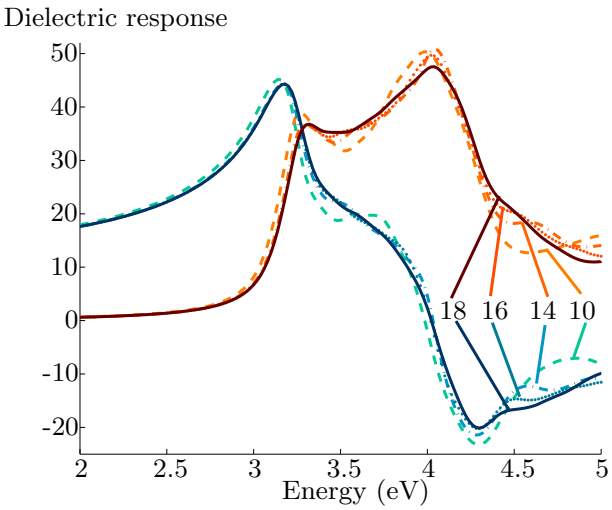

Figure 12: Convergence of $\varepsilon(\omega)$ (BSE) with respect to a traditional homogeneous sampling of the BZ. A shift s in a non-symmetric direction is used (see text). The number indicated is n_k and the grid is therefore $(n_k \times n_k \times n_k|s)$. The imaginary part is given in blue color while the real part is in orange-red. The full line corresponds to the finest grid that we have used, with n_k=18. Oscillations appear for energies larger than 3.2 eV, but are damped with increasing n_k.

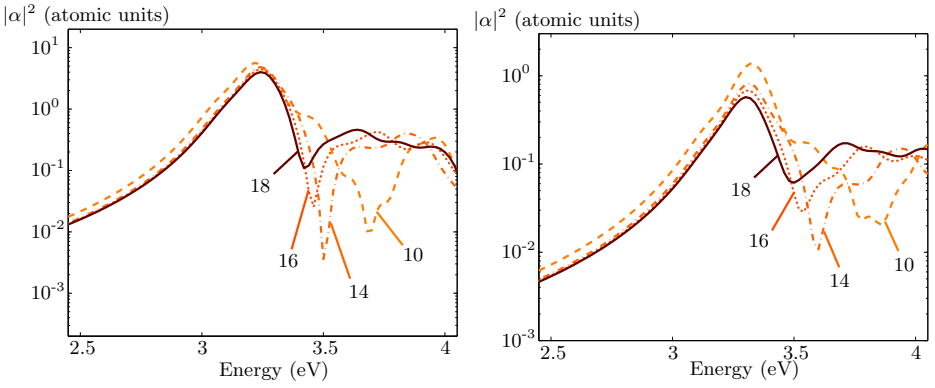

(a) BSE (b) IPA

Figure 13: Convergence of $|\alpha|^2$ with respect to a traditional homogeneous sampling of the BZ for (a) BSE and (b) IPA. A shift along a non-symmetric direction is used (see text). The number indicated is n_k and the grid is therefore $(n_k \times n_k \times n_k|s)$. The convergence is difficult to achieve for energies larger than 3.2 eV.

n_k	**12**	**14**	**16**	**18**
ε_0	$1.3276\ 10^{+1}$	$1.3259\ 10^{+1}$	$1.3256\ 10^{+1}$	$1.3256\ 10^{+1}$
C_2^ε	$7.7792\ 10^{-1}$	$7.7571\ 10^{-1}$	$7.7527\ 10^{-1}$	$7.7543\ 10^{-1}$
C_4^ε	$5.2340\ 10^{-2}$	$5.2084\ 10^{-2}$	$5.2020\ 10^{-2}$	$5.2030\ 10^{-2}$
C_6^ε	$5.8317\ 10^{-3}$	$5.7806\ 10^{-3}$	$5.7638\ 10^{-3}$	$5.7605\ 10^{-3}$
α_0	$2.5167\ 10^{-2}$	$2.4464\ 10^{-2}$	$2.4159\ 10^{-2}$	$2.4027\ 10^{-2}$
C_2^α	$4.8710\ 10^{-3}$	$4.7337\ 10^{-3}$	$4.6719\ 10^{-3}$	$4.6460\ 10^{-3}$
C_4^α	$5.7303\ 10^{-4}$	$5.5503\ 10^{-4}$	$5.4689\ 10^{-4}$	$5.4347\ 10^{-4}$
C_6^α	$1.2462\ 10^{-4}$	$1.1894\ 10^{-4}$	$1.1618\ 10^{-4}$	$1.1491\ 10^{-4}$

Table 5: Cauchy coefficients for ε and for α within the BSE framework (see Eqs. (139) and (140)). The grids used are $(n_k \times n_k \times n_k|s)$.

to the so-called Cauchy coefficients for the macroscopic dielectric function [113]. Since the function is even with respect to the frequency, we can expand the absolute value of the Raman tensor and the real part of the dielectric function with even powers of the frequency

$$\alpha(\omega) = \alpha_0 + C_2^\alpha \omega^2 + C_4^\alpha \omega^4 + C_6^\alpha \omega^6 \tag{139}$$

$$\Re\varepsilon(\omega) = \varepsilon_0 + C_2^\varepsilon \omega^2 + C_4^\varepsilon \omega^4 + C_6^\varepsilon \omega^6. \tag{140}$$

The coefficients can be obtained by a least-square fitting of the finite difference results until 1.5 eV (see Tab. 5).

The results of the fit obtained with this technique are presented in Fig. 14. The range of validity of this fit goes beyond 2 eV. A fitting above 2 eV leads to an oscillatory behaviour in the very low energy range: the four-term expansion in Eq. (139) and (140) is not accurate enough to describe the higher-energy part.

Cauchy coefficients are already well-converged for the 14^3 grid (within a few percent for the first and second ones). However, such a fit does not correctly describe the resonance close to the gap energy.

3.4.3.2 *The convergence above the band gap*

As mentioned earlier, we analyze the convergence of the RI in both the BSE case (Fig. 13 (a)) and in the IPA approximation (Fig. 13 (b)). Both IPA and BSE present similar difficulties to converge the final results. Hence, we can conclude that the convergence issue is *not* primarily due to the building up of the excitons that arises from the off-diagonal couplings,

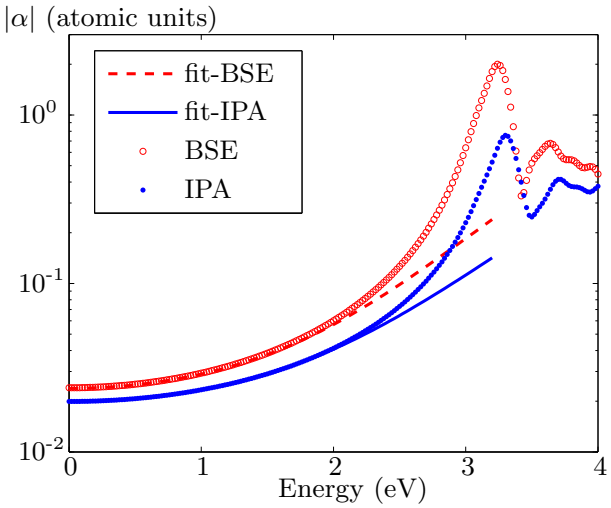

Figure 14: Comparison between the absolute value of the Raman tensor obtained from the BSE and IPA, and their Cauchy polynomial fits in the low-frequency part of the spectrum. Coefficients have been obtained by fitting the data up to 1.5 eV for a uniformly shifted 18x18x18 k-point grid.

but is already present at the independent-particle level. Why the convergence rate in the case of Raman susceptibility is smaller than in the macroscopic dielectric function can be understood as follows. The imaginary part of the dielectric function, for a given wavevector grid, is made of numerous broadened Dirac delta contributions, each of which corresponds to one transition from a valence band to a conduction band

$$\Im\left(\chi(\omega)\right) = \sum_i f_i \delta_\eta(\omega - \Delta E_i). \tag{141}$$

In order for such spectrum to look smooth, the broadening should be comparable to the typical spacing between delta functions. By contrast, the frequency-dependent RI is obtained by differentiating the dielectric function. Hence, the RI evolution corresponds to the superposition of numerous *derivatives* of broadened delta functions, whose oscillatory character are much stronger than the broadened Dirac functions

$$\Im\left(\frac{\partial\chi(\omega)}{\partial\tau}\right) \overset{\left(\text{if } \frac{\partial f_i}{\partial\tau} \text{ is small}\right)}{\Rightarrow} \sum_i f_i \frac{\partial\Delta E_i}{\partial\tau} \delta'_\eta(\omega - \Delta E_i). \tag{142}$$

This is reflected at the level of the RI. A graphical representation of this effect is presented in Fig. 15 where a model system with three possible transitions is used to represent the dielectric function and its derivative.

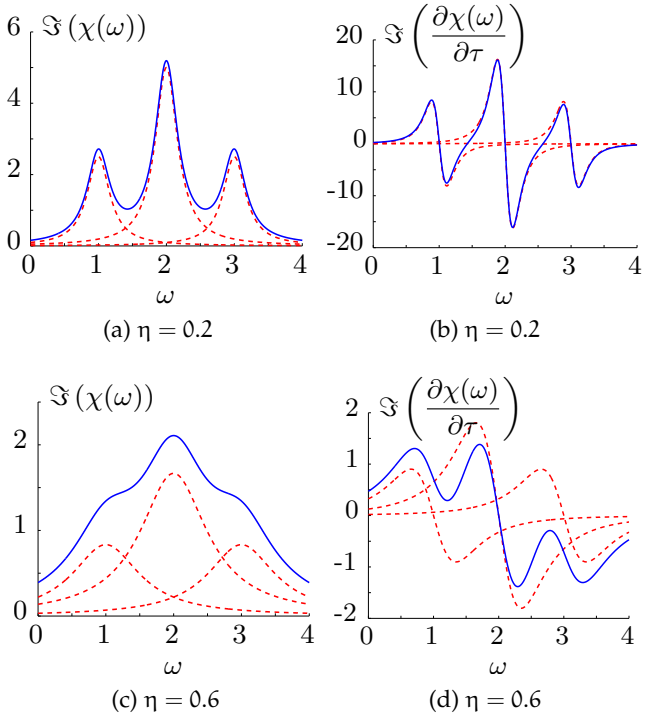

Figure 15: Model representation of a fictitious imaginary part of the susceptibility $\Im(\chi(\omega))$ and its derivative with respect to an external parameter τ. (a) and (c) Imaginary part of the susceptibility with a numerical broadening of $\eta = 0.2$ and $\eta = 0.6$ respectively. (b) and (d) Imaginary part of the derivative of the susceptibility with a numerical broadening of $\eta = 0.2$ and $\eta = 0.6$ respectively.

Having identified the problem, we use another strategy for sampling the BZ, that largely reduces the computational burden and memory requirements. This technique has already been briefly introduced in Sec. 2.4, and used for comparison with other interpolation techniques. Here we give a more formal description of the technique using the above-mentioned notations.

We perform a set of BSE calculations, indexed by the label i, each with the same number of points in the BZ forming a "coarse" grid, differing by their shift $\mathbf{s}_i$

$$\{\mathbf{k}\}_i = (n_k \times n_k \times n_k | \mathbf{s}_i). \tag{143}$$

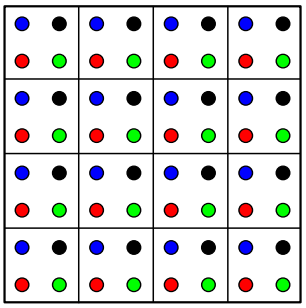

Figure 16: Schematic representation of the sampling of the BZ by a multiple-shifts technique in 2D, with $n_k = 4$ and $n_{div} = 2$ (see text for notations). One BSE computation is done on each grid (represented by four different colors in this picture). The final result is obtained by averaging the $n_{div}^2 = 4$ different computations.

The shifts $\mathbf{s}_i$ are chosen in order to obtain an homogeneous sampling of the subspace between the coarse points

$$\{\mathbf{s}_i\} = (n_{div} \times n_{div} \times n_{div}|\mathbf{h}), \tag{144}$$

where n_{div} is the number of subdivisions in each direction and $\mathbf{h} = (1/2, 1/2, 1/2)$. A 2D schematic representation is illustrated in Fig. 16.

With this technique, the macroscopic dielectric function is obtained by averaging the different results computed on the "coarse" grids

$$\varepsilon^{av}(\omega) = \frac{1}{n_{div}^3} \sum_i \varepsilon(\omega|\{\mathbf{k}\}_i), \tag{145}$$

where $\varepsilon(\omega|\{\mathbf{k}\}_i)$ is the macroscopic dielectric function obtained for the "coarse" computation with the grid $\{\mathbf{k}\}_i$, Eq. (143).

Fig. 17 presents the results obtained with different coarse mesh samplings (different n_k), averaging over 64 calculations ($n_{div} = 4$ is kept constant). Of course, when n_k becomes very large, the Raman spectrum must tend to the same spectrum as without this multiple-shift technique. But the computational effort is largely reduced. Indeed, the residual fluctuation when going from $n_k = 14$ to $n_k = 16$ can be seen to be rather small already. In the IPA case, $n_k = 16$ with $n_{div} = 4$ corresponds exactly to a $(64 \times 64 \times 64|(1/2, 1/2, 1/2))$ uniform grid, that would be intractable in the BSE case. It is worth stressing that in the current method, we can take advantage of symmetries to reduce the number of "coarse" grid calculations, since some meshes are equivalent. For example, the number of required computations with $n_{div} = 4$ falls down to 20 for the case where an atom is displaced and to 10 for the equilibrium position.

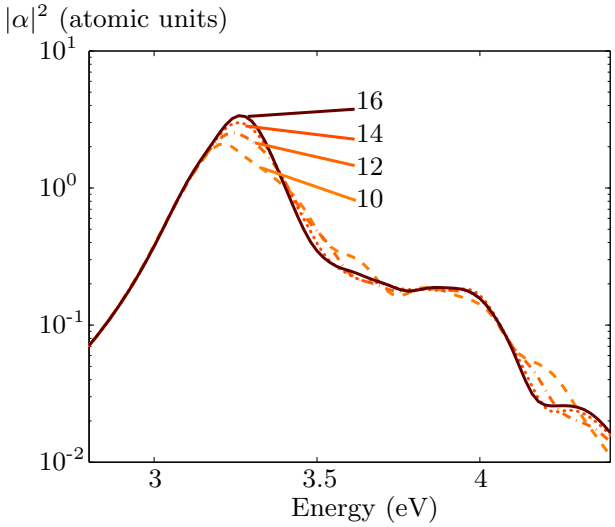

Figure 17: Convergence of $|\alpha|^2$ with respect to the sampling of the Brillouin zone obtained with the multiple-shift technique. The number indicates n_k for the "coarse" sampling of the Brillouin zone in each direction. 64 points are sampled in the subspace between the coarse points.

3.4.4 *Analysis of the theoretical results*

In this section, we analyze in more details the importance of excitonic effects on the Raman spectrum. A comparison between BSE and IPA results is reported in Fig. 18. Note how the excitonic effects amplify the RI by more than an order of magnitude in the band gap region. Much smaller amplifications are observed for low frequencies.

Since the integral of the imaginary part of the dielectric susceptibility is related to the plasmon frequency ω_p (the so-called f-sum rule) [114]

$$\int_0^\infty \omega \, \Im\{\varepsilon_{ij}(\omega)\} d\omega = \frac{1}{2}\pi\omega_p^2\delta_{ij}, \tag{146}$$

and since ω_p does not depend on atomic positions, the integral of the imaginary part of the Raman susceptibility vanishes

$$\int_0^\infty \omega \, \Im\{\alpha_{ij}(\omega)\} d\omega = 0. \tag{147}$$

Fig. 19 confirms that this relation is satisfied. On the basis of Eq. (147), we can see that the difference between the BSE and IPA results for the RI is due to the lowering of the energy, and the amplification of the main peak of the imaginary part of the Raman susceptibility.

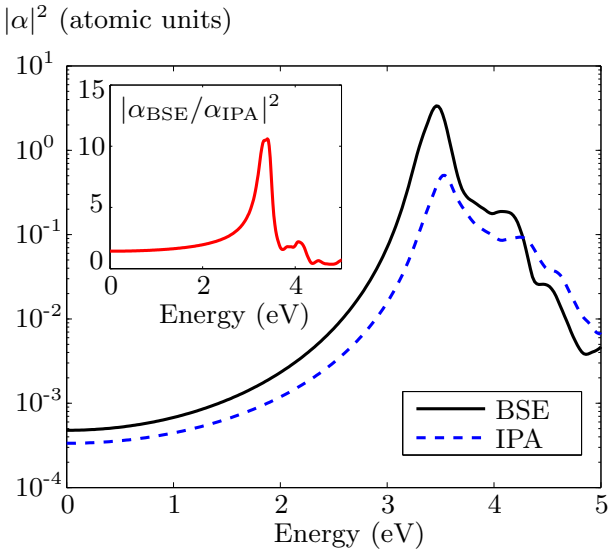

Figure 18: Comparison of the frequency evolution of $|\alpha|^2$ (in atomic units) with Bethe-Salpeter and IPA formalisms. The inset shows the ratio between the two curves. The ratio goes up to 10 at the level of the direct band gap (3.2 eV).

In the approximation for which the atomic displacement induces a global rigid shift of all the conduction bands with respect to all valence bands, with energy $\Delta\varepsilon = \varepsilon_{c\mathbf{k}} - \varepsilon_{v\mathbf{k}}$ (or, alternatively, if one transition dominates), the derivative with respect to an atomic displacement is related to the derivative with respect to frequency by

$$\left.\frac{\partial\chi}{\partial\tau}\right|_{\omega} \approx \left.\frac{\partial\chi}{\partial\Delta\varepsilon}\right|_{\omega} \frac{\partial\Delta\varepsilon}{\partial\tau} = -\left.\frac{\partial\chi}{\partial\omega}\right|_{\omega} \frac{\partial\Delta\varepsilon}{\partial\tau}. \tag{148}$$

This relation shows that the amplitude of the Raman effect will follow the variation of the band structure with the atomic displacement [2].

As represented in Fig. 19, this approximation is only valid at the onset of absorption. In this range of energies, the curves are qualitatively on top of each other. This shows that the transition corresponding to the energy gap dominates in this range of energies. For higher energies, however, this approximation is not valid since each band can contribute differently from other bands in the Raman susceptibility.

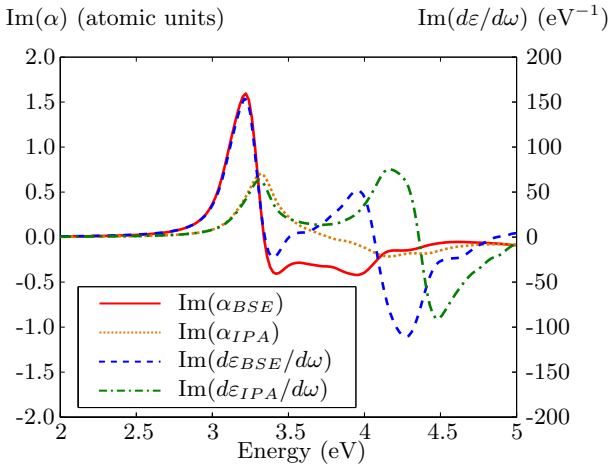

Figure 19: Comparison of the imaginary part of the Raman susceptibility and of the derivative of the susceptibility with respect to frequency for the BSE and for the IPA. These computations are achieved with the multiple-shift technique for $n_k = 16$ and $n_{div} = 4$.

3.4.5 *Comparison with experimental data*

Fig. 20 shows the ab initio results for the Raman susceptibility of silicon, and compares these results with the experimental data obtained by Compaan and Trodahl [104], who measured RI as a function of the frequency in silicon. In this figure, the theoretical results are obtained with a scissor value of 0.85 eV that reproduces the experimental gap at 0K (3.4 eV) instead of 0.65 eV, which reproduces the theoretical GW gap (3.2 eV).

In zinc-blende materials, we also define the Raman polarizability a by

$$a = \sqrt{\mu\Omega_0}\alpha \tag{149}$$

where μ is the reduced mass (in the case of silicon, $\mu = M_{Si}/2$).

In terms of absolute value, the polarizability $a_{BSE} = 19.75$ Å^2 obtained at 1.1 eV compares reasonably well with the experimental data of 23 ± 4 Å^2. The IPA value, $a_{IPA} = 15.87$ Å^2, is further away from the experimental value. This confirms the need to correctly describe excitonic effects even for energies well below the gap.

We can distinguish three different regions with different behaviour: the low-energy (pre-resonance) region, from 2 eV to 3.2 eV, the band-gap region from 3.2 eV to 3.5 eV and the higher-energy region beyond 3.5 eV.

The Bethe-Salpeter method allows reproduction of the experimental amplification of the Raman susceptibility with the frequency. Agreement

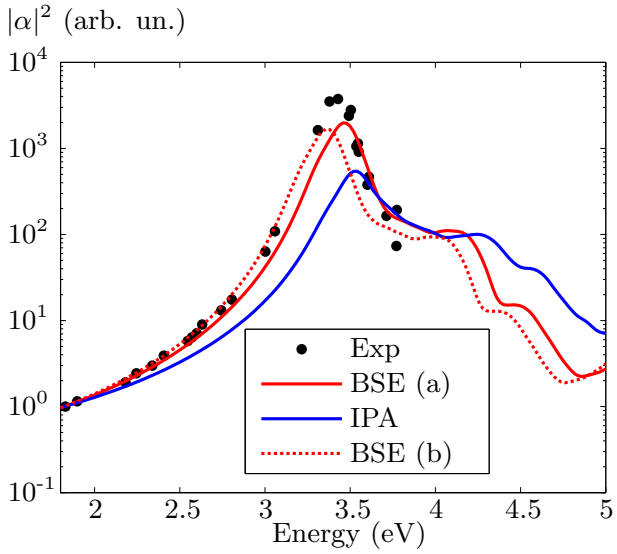

Figure 20: Comparison of the theoretical and experimental Raman susceptibility of silicon. The experimental gap is reproduced by choosing a scissor value of 0.85 eV. A rigid energy shift of -0.1 eV is applied to results called "BSE (a)" in order to obtain "BSE (b)". The vertical values are given in arbitrary units in Ref. [104]. Therefore, these data are fitted to BSE and to IPA by means of a multiplicative factor fixed to pass through the first experimental point.

using this method is significantly better than the agreement obtained by IPA. In the band-gap region, however, there is a discrepancy between the theoretical and the experimental maximal Raman susceptibility. The BSE maximum is nevertheless still closer to the experimental maximum than the IPA maximum. Moreover, it is important to note that the BSE theoretical results obtained in this work are valid only at low temperature, whereas the experimental data are measured at 300 K. The effect of the temperature on the absorption spectrum is illustrated in Fig. 21 where the first absorption peak at 10K is brought to lower energies at 297K, in agreement with the gap narrowing. On the basis of this observation, we can expect an improvement in the agreement if temperature effects are included in the ab initio calculations. As a first approximation, the effect of temperature on the gap energy can be mimicked by a rigid shift of the RI curve towards lower energies, as shown in Fig. 20 for data called "BSE (b)". With this correction, the agreement is highly improved in the low-energy part of the Raman susceptibility. The amplification factor and post-resonance are however not significantly improved. We attribute the disagreement to the different approximations we have per-

formed so far, in particular within the BSE framework and the adiabatic approximation.

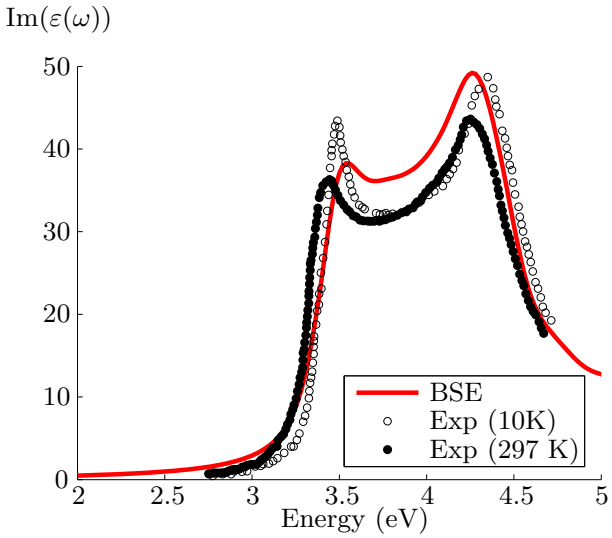

Figure 21: Theoretical (BSE) and experimental absorption spectrum of silicon for 10 K and for 297 K from Ref. [115].

Our ab initio approach is not able to describe the higher-energy region as well as the lower-energy region. Without the temperature correction, the BSE theoretical results underestimate the evolution of intensities in the pre-resonance region. The inclusion of temperature leads to a partial improvement in the overall agreement, except for the post-resonance region. The slope of decrease in the post-resonance region is in agreement with the experimental slope while the intensity value is underestimated.

The present approach relies on several approximations, whose roles still need to be analyzed. We have neglected, among others, the phonon frequency in the adiabatic approach, the quadratic response with respect to atomic displacements, the self-consistency with the *GW* approximation, the non-Hermitian coupling within BSE, the frequency dependence of the BSE hamiltonian, and indirect transitions. Calculations including all these effects would require computational resources unavailable to us at present. In addition, apart from a rigid shift of the results in energy, temperature effects induced by phonons have been mostly neglected (the experimental data have been obtained at room temperature). We will analyze these effects later in this thesis, in Chap. 5.

Despite all these effects, in all regions, the BSE results are in better agreement with experimental data than the IPA results. This clearly indi-

cates the importance of excitonic effects for an accurate ab initio description of Raman spectra.

Note also that silicon might possess specific characteristics that induce the good agreement here observed with the present method and associated approximations. Such a good agreement might not be observed for materials with different characteristics, like a lower crystalline symmetry, the presence of stronger spin-orbit coupling, the presence of some ionicity, the presence of multiple types of atoms, etc ...

3.4.6 *Summary*

A technique for the ab initio study of the resonant RI has been proposed, and applied to silicon. The technique relies on finite differences of the macroscopic dielectric function evaluated for distorted geometries, and includes excitonic effects by solving the Bethe-Salpeter equation. We found that convergence of the Raman spectrum with respect to the number of wavevectors used to sample the BZ is problematic. To tackle this problem, we described a multiple-shift averaging process that significantly improves convergence while keeping computational effort at a reasonable level.

The Bethe-Salpeter results are in better agreement with experimental results than those results obtained without excitonic effects (IPA). For laser energies in the band-gap region or lower, the agreement is excellent if one takes into account the small rigid shift that is needed to align the first peak of the theoretical dielectric absorption, as well as the experimental shift for the same temperature as the Raman spectrum. The agreement is still not perfect however in the high-energy region. This may be attributed to many effects, to be examined in future works.

Temperature effects will be analyzed later in Chap. 5, where, in particular, frequency-dependent Raman intensities of silicon are computed taking into account temperature-dependent band structure.

3.5 SECOND-ORDER RAMAN OF SILICON

First-order Raman scattering, in which only one phonon is emitted or absorbed, yields information on vibrations with very low crystalline momentum, due to the negligible momentum of light. Extracting information on phonon frequencies from the first-order spectrum is straightforward, as clear selection rules govern the appearance or extinction of usually well-isolated peaks. In contrast, second-order Raman processes

exhibit features coming from different crystalline momenta, potentially from the entire BZ, with the only constraint of negligible momentum of the phonon pairs involved in the two-phonon process. They are more complex and, hence, more difficult to interpret.

The resonance phenomenon appears independently of the number of emitted phonons, and thus, also for second-order Raman scattering. A prototypical example of resonant second-order Raman spectra is presented in Fig. 22. It shows the experimental frequency-dependent Raman spectra of silicon between 900 and 1050 cm^{-1}, as measured by Renucci and coworkers [99]. The spectra are characterized by significant variations in intensity depending on the frequency of the incoming light, even for frequencies corresponding to energies smaller than the direct gap of 3.2 eV. Such resonance effects are allowed in second-order Raman processes, due to indirect transitions between electronic states that are caused by phonons of finite wavevector. Hence, it is clear that multi-phonon processes beyond first order are crucial. Below, we will show that all the features can be well interpreted by our first-principles theoretical approach.

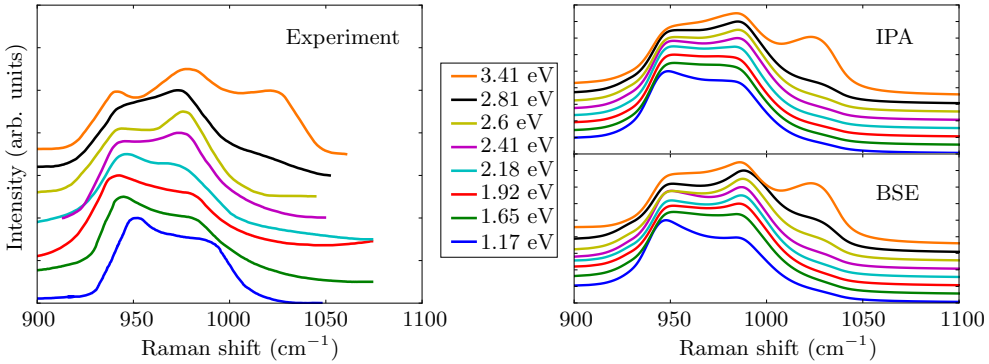

Figure 22: Experimental (left, taken from Ref. [99]) and theoretical (right) second-order Raman spectra of silicon, between 900 and 1050 cm^{-1}, for different excitation energies between 1.17 eV and 3.41 eV, normalized to their maximal values. For clarity, the curves are shifted with respect to each other (the lowest excitation energy at the bottom). Theoretical results have been obtained in the IPA and in the BSE formalism.

As described in the previous sections, we have recently included excitonic effects from first principles in first-order resonant Raman scattering. Excitonic effects were clearly observed in the absolute intensity enhancement, and proved crucial to obtain good agreement with experimental data.

In this section, we address the even more challenging computation of second-order resonant Raman scattering, including exciton-phonon coupling. Even by today standards, the computational load is quite formidable. We compute the ingredients using state-of-the-art methodology (DFPT and BSE), while also showing the adequacy of the simplifying "overtone" approximation. Applying it to the case of Si, we not only reproduce the above described experimental data, but give insight into the origin of the spectral features, and explore the role of excitonic effects on the Raman intensities.

3.5.1 *Results*

We first describe the *normalized* intensities for Raman shifts in the 900-1100 cm^{-1} range. Such results are presented in the right panel of Fig. 22. On both levels of theory, IPA and BSE, the evolution of the intensity of the Raman shift with increasing light frequency (or photon excitation energy) follows very closely the experimental data. While most of the spectral weight is localized around 950 cm^{-1} for the lowest excitation energy of 1.17 eV, the shoulder below 1000 cm^{-1} is getting more pronounced with increasing excitation energy and starts to dominate above 2.4 eV. A third peak around 1030 cm^{-1} that is hardly visible in the bottom curves, is particularly pronounced only for the highest excitation energy of 3.41 eV. In excellent agreement with experiment, its intensity is nearly the same as the peak at 950 cm^{-1}, and somewhat lower than the one at 980 cm^{-1}.

Second, we examine the *integrated* intensities. Fig. 23 shows a comparison between the IPA and the BSE absolute intensity, divided by $(\omega_L - \omega_R)^4$,[5] integrated over the range between 900 and 1100 cm^{-1}, as a function of the excitation energy. Even if in this range of frequencies the relative intensities computed in the two formalisms are very similar as shown in Fig. 22, their absolute intensities differ by a factor 5 for excitation energies around 3 eV, as exhibited in the inset of the Fig. 23. Clearly, excitonic effects are important, which will be analyzed in the Discussion section.

The Raman spectrum in a broader range of Raman shifts is also obtained. In addition to the enhancement of the absolute intensity, similar

5 The $(\omega_L - \omega_R)^4$ factor is present also in the Raman spectrum of reference wide-band gap materials, like CaF_2, to which the comparison is made in order to establish the absolute intensity. Hence, it can be discarded. Other factors are expected to be constant in wide band-gap materials.

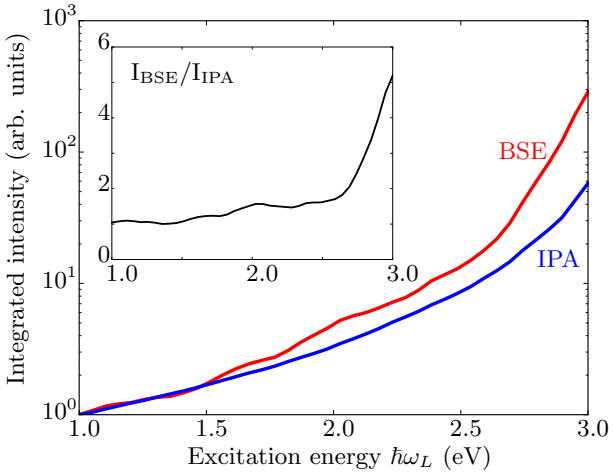

Figure 23: Integrated intensities of BSE and IPA spectra over Raman shifts ranging from 900 cm^{-1} to 1050 cm^{-1}, as a function of the excitation energy $\hbar\omega_L$. The $(\omega_L - \omega_R)^4$ prefactor, see Eq. (111) has not been included, and the spectrum has been renormalized with respect to the value at $\hbar\omega_L = 1.0$ eV. Note the logarithmic scale of the intensity. The inset shows the ratio between integrated intensities obtained by the IPA and the BSE.

to the one shown in Fig. 23, Fig. 24 shows that the use of the BSE, that is, the inclusion of exciton-phonon coupling, results in a pronounced intensity increase in the part of the Raman spectrum between 600 and 900 cm^{-1}, especially for excitation energies between 2 and 3 eV. This additional excitonic effect will also be discussed later.

In order to compute these results, we have made the approximation that the second-order contribution to Raman spectrum is dominated by the emission of two phonons that are connected by time-reversal symmetry: same frequency, and time-reversed collective eigendisplacement and momentum. From a group-theoretical point of view, derivatives with respect to such phonon pairs will always be active and contribute to the fully symmetric component of the spectrum [3]. However, group-theoretical arguments do not insure the vanishing of other contributions for arbitrary phonon wavevectors. While this approximation is justified a posteriori by the agreement show in Fig. 22, it has been nevertheless possible to theoretically examine its validity, in the specific case of vanishing excitation energy. We tested this approximation by computing the second-order derivatives of the dielectric constant obtained within DFPT, where the electric field is used as a perturbation [8]. In this approach, the excitation energy vanishes, but unlike in the IPA, the local-field effects are

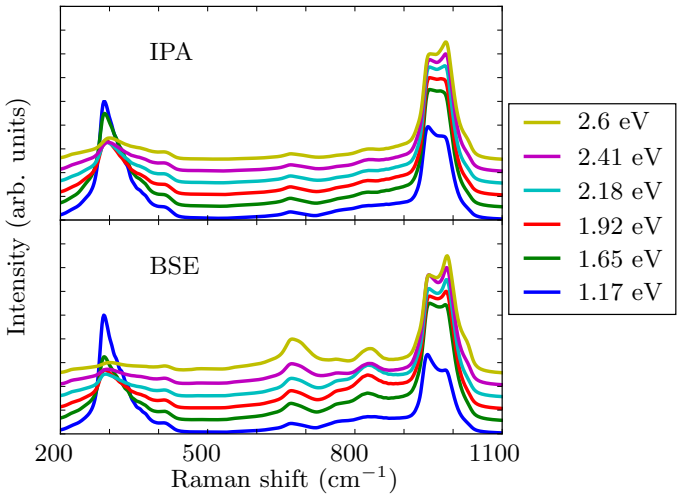

Figure 24: Second-order Raman spectra calculated within the IPA (top) and the BSE (bottom) for several excitation energies $\hbar\omega_L$. Each spectrum is normalized with respect to its highest value, as in Fig. 22.

taken into account, which makes its level of sophistication intermediate between IPA and BSE. Fig. 25 shows the dominance of the derivatives by the overtone pair of modes (by around one order of magnitude with respect to other contributions in the worst case), which fully justifies our approach. This "overtone" approximation was a crucial step in making the BSE computation tractable, and such be able to treat excitonic effects. The validity of the "overtone" approximation is thus another significant result of our work.

3.5.2 *Discussion*

Our first-principles theory can provide insight into the origin of the features seen in Fig. 22, and then can shed light on the underlying physics, especially the role of excitonic effects. As a reminder, the intensity S is given by Eq. (122). The tensorial nature of S (α and β referring to the polarization of incoming and outgoing light) will not play an important role in our discussion. Apart from prefactors, the Raman intensity is essentially obtained by summing contributions from all phonons, characterized by their momentum $\mathbf{q}$ and branch index m. Such contributions are products of the *change of the dielectric response* ε due to each phonon and its time-reversed homolog, by a function that depends *only on the phonon frequency* $\omega_m(\mathbf{q})$ and a Dirac-delta, that expresses the conserva-

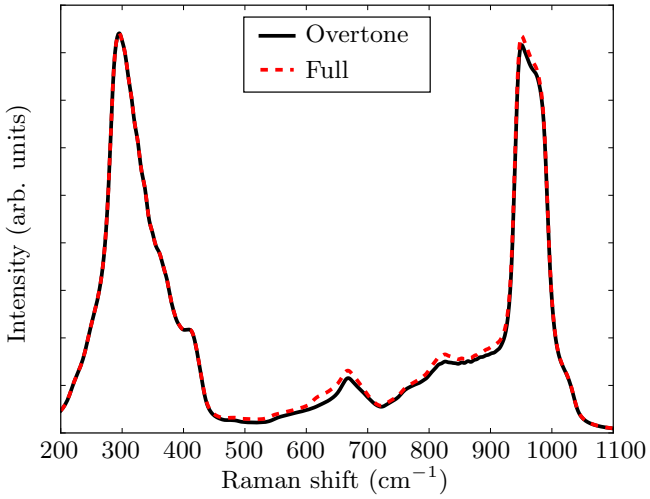

Figure 25: Raman spectrum obtained by differentiating the dielectric constant (at $\hbar\omega_L = 0$) obtained within density-functional perturbation theory. "Full" means that the emission of all possible phonon pairs are considered in the calculation, while for the "overtone" graph, only the emission of time-reversed phonon pairs are taken into account.

tion of energy. More detail on the evaluation of the intensity is provided in Sec. 3.5.3, such as the description of dielectric response calculations, with or without excitonic effects.

In Eq. (122), the Dirac-delta function, integrand of the two-phonon density of states

$$g_{2DOS}(\omega_R) = \frac{1}{N_q} \sum_{m\mathbf{q}} \delta(\omega_R - 2\omega_m(\mathbf{q})) \tag{150}$$

is actually weighted by a function of the phonon mode and excitation energy. One can expect such weighting factor to be a reasonably smooth function of the wavevector $\mathbf{q}$. By contrast, the Dirac-delta function of Eq. (150) needs to be properly integrated throughout the BZ. It induces van Hove singularities, that dominate the overall shape of the spectrum.

The second-order Raman scattering intensity can thus be decomposed into contributions coming from different points of the BZ. This is shown in Fig. 26, where the evolution of the diagonal component of the IPA Raman spectrum with respect to the excitation energy is depicted for eight characteristic wavevectors in the BZ. In this framework, 'optical' transitions between different electronic wavevectors, i.e., between $\mathbf{k}$ and $\mathbf{k}+\mathbf{q}$ with non-zero $\mathbf{q}$ are forbidden in the equilibrium structure. The phonon vibrations, however, may change some of these transitions from forbid-

den to allowed, giving rise to non-zero momentum matrix elements, thus leading to finite second-order derivatives of the dielectric function with respect to the phonon displacement. As a reference, the electronic and phononic band structures are shown in Fig. 27, along with the one-phonon density of states (related to the two-phonon density of state given in Eq. (150), by a simple scaling of the phonon frequency axis). As shown in Fig. 27 (b), at the X point, the highest phonon frequency is about 470 cm^{-1}, twice this value being 940 cm^{-1}; the electronic resonance energy is 1.24 eV. At the L point, twice the highest phonon frequency is slightly larger around 1000 cm^{-1}, with a resonance at 2.14 eV. Likewise, for the Γ point, the corresponding values are 1040 cm^{-1} and 3.2 eV. From a careful inspection of Fig. 26, we can conclude that the peak structures in Fig. 22 are related to these resonances. To highlight their behavior as a function of the excitation energy, we plot in Fig. 28 the second derivatives of the dielectric function at various points of the BZ. At the X point, it shows a clear maximum at the energy of the indirect band gap. The four curves related to the L point do not peak at their resonance frequency, but increase with excitation energy, with a reduced rate above 2 eV. The curve at Γ grows unabated even beyond 3.0 eV. From such different characteristics, one can also conclude that the two-phonon density of states alone is not sufficient to describe second-order Raman spectra in general, and even more so in resonance condition.

To assess the impact of excitonic effects, we have performed the corresponding calculations with the derivatives of the dielectric function for phonon wavevectors Γ, X, and L obtained by solving the BSE. A comparison with the IPA results is given in Fig. 29, where we emphasize the logarithmic scale of the vertical axis. The corresponding Raman spectra obtained for several excitation energies are presented in Fig. 24. As a general trend, the ratio between the BSE and IPA intensities (highlighted in the inset) increases with the excitation energy, exhibiting a maximum at the direct band gap. This effect is similar to the first-order enhancement effect reported in Ref. [81]. A very strong excitonic effect can be observed between 2 and 3 eV for the third and fourth mode of the L point, as depicted in Fig. 29 for the latter. It can be explained by the presence of bound exciton states (inside the gap) with finite momentum [116] that become visible at second order due to the presence of finite-momentum phonons. The ratio between BSE and IPA results dramatically increases in this energy range due to the changed onset of the second-order response. The other L-point modes, around 100 and 500 cm^{-1}, do not exhibit strong coupling with excitons. Overall, exciton-phonon coupling

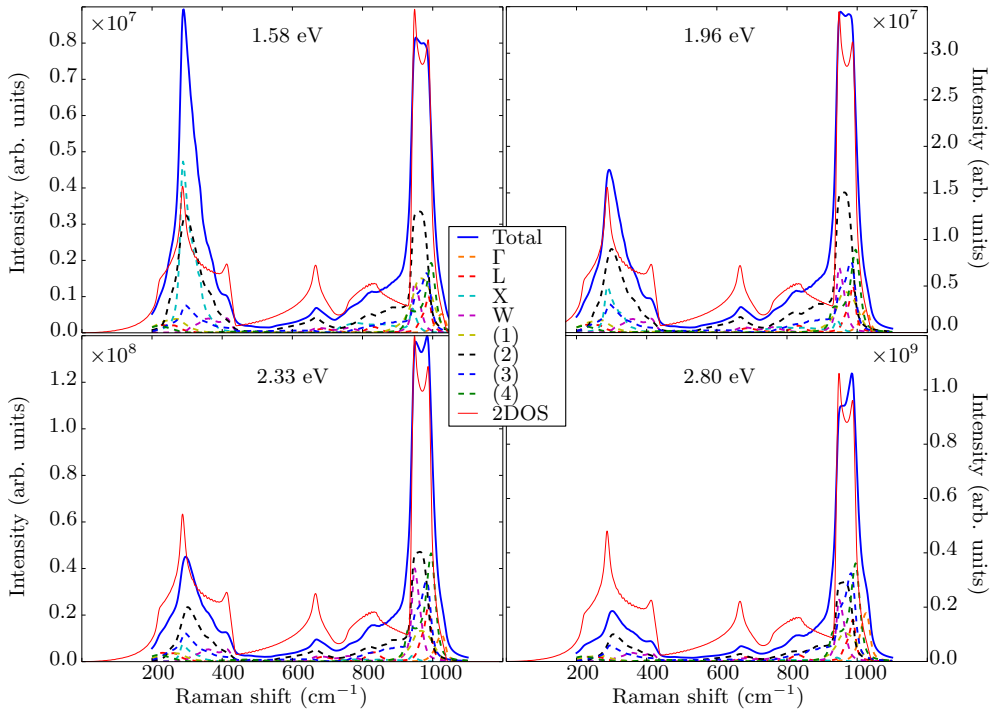

Figure 26: Diagonal component of the second-order Raman spectrum obtained in the IPA (blue lines), and its wavevector decomposition for four different excitation energies $\hbar\omega_L$: 1.58 eV, 1.96 eV, 2.33 eV and 2.80 eV. Eight $\mathbf{q}$ wavevectors are considered, in reduced coordinates: $\Gamma = (0,0,0)$, $L = (1/2,1/2,1/2)$, $X = (1/2,1/2,0)$, $W = (1/4,1/2,3/4)$, $(1) = (1/4,1/4,0)$, $(2) = (1/2,1/4,0)$, $(3) = (-1/4,1/4,0)$, $(4) = (1/4,1/4,1/4)$. The two-phonon density of states is also represented for sake of comparison (red lines).

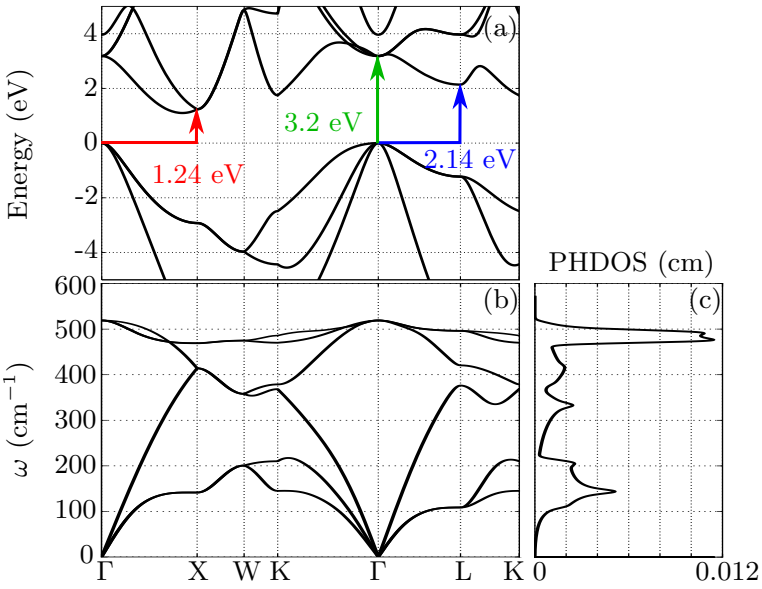

Figure 27: (a) Electronic Kohn-Sham band structure of silicon, with a scissor shift of 0.65 eV for the conduction bands. Possible direct transitions at Γ and indirect transitions from Γ to X and from Γ to L are indicated by the green, red, and blue arrows, respectively. (b) Phonon band structure and (c) phonon density of states.

results in a pronounced intensity increase in the part of the Raman spectrum which is dominated by L modes, for excitation energies between 2 and 3 eV and Raman shifts between 600 and 900 cm^{-1} (Fig. 24). This result is a central outcome of the present work.

For the other modes, indirect transitions appear less important for the resonance behavior than direct transitions. For example, in the regions around 1000 and 1200 cm^{-1}, all the intensities increase with energy with a similar rate. Since the relative intensities are well reproduced within the IPA, this explains why the IPA spectra in this range are in already quite good agreement with experiment (see Fig. 22 for a comparison between IPA and BSE in this range). On the other hand, an accurate description of absolute intensities requires the inclusion of excitonic effects as they lead to changes of one order of magnitude for excitation energies of around 3 eV, as already shown in Fig. 23.

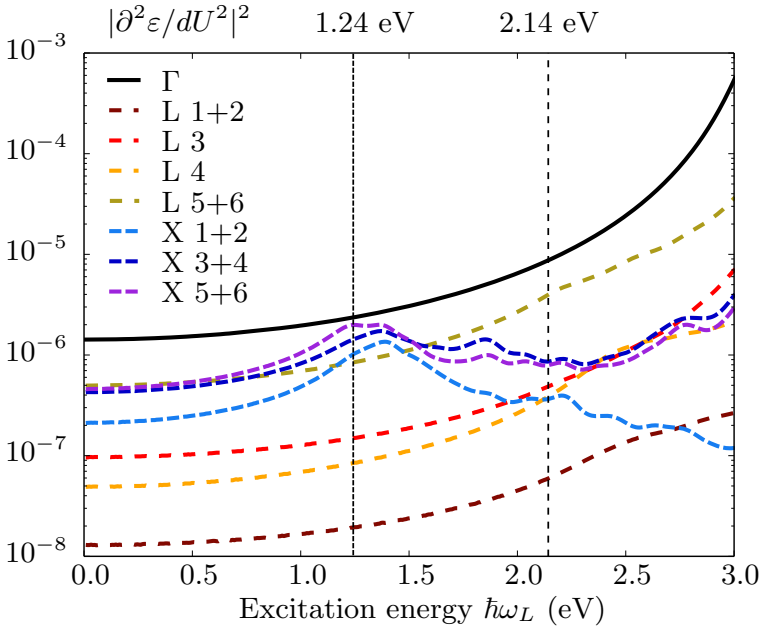

Figure 28: Second derivatives of the IPA dielectric function with respect to the excitation energy for different modes at the Γ, X, and L points. The notation "**q** m" represents the m^{th} branch of a q-point (Γ, X, or L), while "q $m+n$" represents the sum of the corresponding derivatives of the degenerate branches m and n at this point. The electronic transition thresholds for X (1.24 eV) and L (2.14 eV) are also indicated.

3.5.3 *Methods*

The methodology we use in this section for second-order Raman scattering is presented in Sec. 3.3.2. The different approximations and numerical techniques detailed in Sec. 3.3.3 are used to decrease the computational load.

The corresponding grid parameters are now described, as well as other computational details. We use the ABINIT package [86, 87], with Troullier-Martin pseudopotentials.[6] Relaxed cell parameters of 10.20 Bohr are used with cut-off values for the wavefunctions of 8 Hartree. The DFPT phonons displacements and frequencies are interpolated from a coarse Γ-centered phonon grid of $8\times8\times8$ to a non-shifted $70\times70\times70$ mesh, to obtain the phonon density of states, following Ref. [8], while a 4-times shifted $8\times8\times8$ sampling is used for the electrons.

6 Available from the ABINIT package, http://www.abinit.org

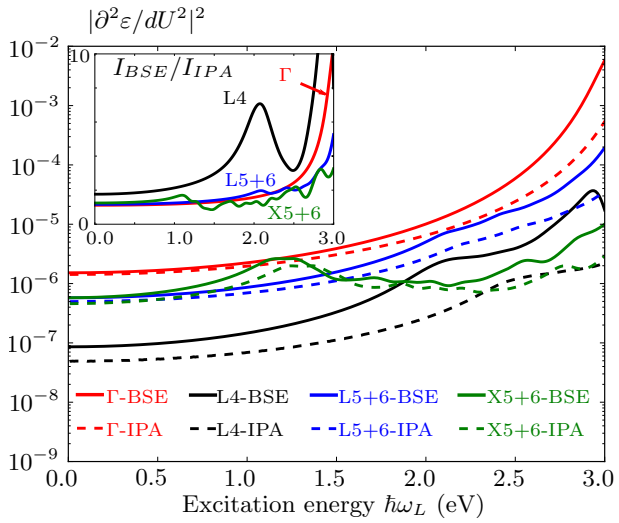

Figure 29: Second derivatives of the dielectric function with respect to the excitation energy for the highest-energy modes at Γ, X and L as well as the fourth mode at the L point. The inset shows the ratio between the BSE and the IPA results.

When simulated in the IPA (without local-fields effects) [117, 118], the dielectric function is evaluated for different supercells corresponding to a non-shifted $4 \times 4 \times 4$ phonon wavevector grid (containing 64 wavevectors), while for the electronic states, the equivalent of a centered $24 \times 24 \times 24$ grid for the primitive cell is used. In the supercell case, the BZ is folded, and the integration grid adapted accordingly. The convergence has been checked on the final Raman spectrum with respect to a 4-times shifted $2 \times 2 \times 2$ centered phonon wavevector grid (containing 32 wavevectors). A scissor operator of 0.65 eV is applied on top of the Kohn-Sham eigenvalues to mimic the opening of the gap by GW.

In order to assess the importance of excitonic effects, we have performed BSE calculations of the derivatives of the dielectric function for phonons with Γ, X and L wavevectors (corresponding to a $2 \times 2 \times 2$ Γ-centered grid). Dielectric functions obtained on $12 \times 12 \times 12$ wavevectors in the BZ have been averaged following the technique described in Ref. [81] to reach samplings equivalent to $24 \times 24 \times 24$. 3 valence bands and 6 conduction bands were used for the primitive cells, their numbers being increased proportionally with the number of atoms in the supercells. The model dielectric function described in Ref. [76] with $\varepsilon^{\infty} = 12$ has been used to calculate the screening matrix elements. A cut-off energy of 4 Ha is used to describe the screening matrix in reciprocal space.

In order to present a Raman spectrum obtained with a sufficient number of phonon frequencies, we have interpolated the ratio between BSE and IPA intensities towards a non-shifted $4 \times 4 \times 4$ k-point grid with a trilinear interpolation in reduced coordinates and used these ratios to correct the IPA intensities.

3.5.4 *Summary*

Thanks to the methodology presented in this chapter, that combines frozen-phonon supercell calculations of dielectric functions and their derivatives with phonon spectra from density-functional perturbation theory, we have been able to compute frequency-dependent second-order Raman spectra. We have applied our approach to the computation of the second-order Raman intensities of silicon for a series of excitation energies. We not only reach excellent agreement with measured spectra [99] but provide insight into the resonance behavior through analysis in terms of electronic structure and contributions from phonons at different points of the BZ. Excitonic effects turn out to be crucial to determine absolute Raman intensities as already found for the first-order scattering [81]. Moreover, we have shown that strong excitonic effects may also appear selectively for some vibrational modes of different phonon wavevectors, modifying the relative intensities of different peaks. Our approach leads to a deeper understanding of the physics involved in second-order Raman processes and facilitates the interpretation of experimental results. While in this section we have focused on silicon—a simple but prototypical material—our methodology is generally applicable to a broad range of materials.

3.6 CONCLUSIONS

In this chapter, we have presented the formalism and the methodology we propose for the evaluation of frequency-dependent Raman intensities. We have started by recalling the phonon eigenvalue problem to be solved and then we have presented the equations to evaluate Raman intensities at first and second-order. After discussions on the practical implementations relying on the frozen-phonon method and the harmonic approximations, the approach is validated for first-order and second-order Raman spectra of silicon. In both cases, excitonic effects are shown to be crucial for absolute intensities. Even if relative changes in second-order Raman spectra are globally well-described within IPA, we

have additionally shown specific exciton-phonon coupling for particular phonon modes.

In the next chapter, this methodology is applied to different materials.

4

FREQUENCY-DEPENDENT RAMAN INTENSITIES OF SELECTED SEMICONDUCTORS

In the previous chapters, we have detailed how to compute optical properties and Raman intensities from the derivatives of the dielectric function. In this chapter, we apply these methodologies to the Raman intensities of two different classes of materials. In Sec. 4.1, we consider zinc-blende structures, similar to silicon, but with two different atoms per unit cell. Sec. 4.2 presents a different case study: 2D monolayer transition-metal dichalcogenides. The content of Sec. 4.2 has been published as Ref. [48].

4.1 RAMAN SCATTERING OF ZINC-BLENDE POLAR MATERIALS

In this section, we study the Raman intensities in cubic silicon carbide (SiC) and gallium arsenide (GaAs) in the zinc-blende structure.

Both SiC and GaAs are polar materials and, as a consequence, the coupling with the electric field generated by the LO phonon modes must be taken into account.

The numerical parameters used for the computations are presented in Sec. 4.1.3. An additional note on LO intensities is presented in Sec. 4.1.4.

4.1.1 *SiC*

Silicon carbide is composed of silicon and carbon atoms with very strong covalent bonds. It is therefore very hard and strong. It is used daily as an abrasive and resists very well to high temperatures. Electroluminescence was discovered for this material by Round in 1907 [119] but it has been superseded later by gallium nitride because of its higher efficiency.

Our theoretical lattice parameter of 8.14 Bohr can be compared with other ab initio parameter ranging from 8.14 Bohr [120] to 8.21 Bohr [121, 122] and with the experimental measurement of 8.24 Bohr [123].

In terms of vibrational properties, the calculated TO frequency of SiC is 798 cm^{-1} and the LO one is 979 cm^{-1}. This is in reasonable agreement with other ab initio calculations as 779.2 cm^{-1} / 952.8 cm^{-1} [121] and in excellent agreement with experimental measurements of 794.2 cm^{-1} /

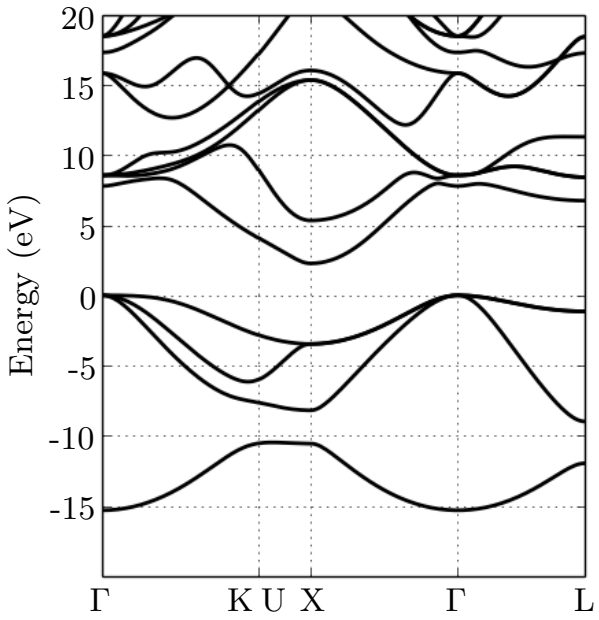

Figure 30: GW band structure of SiC obtained on a $8 \times 8 \times 8$ k-point sampling, cut-off energies of 30 Ha for the wavefunctions and 8 Ha for the screening. A set of 150 bands has been used to compute the screening part. The GW corrections have been interpolated in energy space for the band structure plot.

$972.7\ \mathrm{cm}^{-1}$ obtained in Ref. [124]. The Born effective charges are 2.73 and -2.73 for Si and C respectively. The dielectric tensor is diagonal and has a value $\varepsilon^{\infty} = 6.83$ and $\varepsilon^{0} = 10.29$ when computed with DFPT (without including any scissor shift). This can be compared with ab initio values of $\varepsilon^{\infty} = 7.02$ and $\varepsilon^{0} = 10.49$ [125] and experimental values of $\varepsilon^{\infty} = 6.52$ and $\varepsilon^{0} = 9.72$ [126].

Our GW band structure for SiC, presented in Fig. 30, is in good agreement with previous results published in Ref. [127]. The indirect gap of 2.26 eV is much smaller than the direct gap of 5.7 eV. These values compare reasonably well with the experimental values of 2.42 eV [128] and 6 eV [129].

The Bethe-Salpeter macroscopic dielectric function of SiC, presented in Fig. 31, is in good agreement with BSE spectra available in Ref. [39]. The dielectric constant, within BSE, is $\varepsilon^{\infty} = 7.2$. This value, which is too high compared to experiments, can be induced by the scissor-shift approximation or the model dielectric function (see Sec. 4.1.3 for more

detail). A full BSE calculation on top of GW corrected energies with an explicit RPA screening calculation may lead to a better description of this value.

The TO intensities are obtained via finite differences of the BSE dielectric function following the same approach used for silicon. The evolution of the square of the Raman tensor $|\alpha|^2$ as a function of the laser frequency is presented in Fig. 32, using different grids of k-points with the multiple-shift technique described in Sec. 3.4. In this material, the Raman enhancement profile shows three peaks at 5.3 eV, 7.4 eV and 8.9 eV. The first peak is a bit below the direct gap at X, the other correspond to other direct transitions like the $\Gamma - \Gamma$ transition for the second peak and the second direct gap at X for the third peak.

For a complete picture of the Raman spectrum, one needs to sum two contributions: the derivative of the dielectric function with respect to atomic displacements (TO intensities) and the LEO susceptibilities for the contribution due to the electric field of polar modes (only for LO intensities).

Second Harmonic Generation (SHG) and LEO susceptibilities are shown in Fig. 33. As expected, the SHG shows an onset from energies located at half of the direct gap, which is why it allows for frequency-doubling applications. The LEO susceptibility increases only starting from the direct gap.

Combining the results shown in Figs. 32 and 33, we obtain the evolution of the LO and the TO peaks for light propagating in the [111] direction with respect to the laser frequency displayed in Fig. 34. In this figure, we also compare with experimental measurements obtained by Ref. [130].

The behavior with respect to the laser frequency at the level of BSE agrees very well with experimental measurements. The remaining small deviation might be due to the IPA formalism used for the LEO that lacks of excitonic effects. However, at the level of IPA, because of the smaller derivatives of the dielectric function, the LO term dominates and yields bad agreement with experiments. This can be observed in Fig. 35, where the LO atomic derivatives are decomposed following Eq. (117). This clearly shows the importance of excitonic effects in the Raman intensities of SiC.

There are experimental measurements for frequencies well below the electronic transitions. After these transitions, we observe an enhancement of the I_{LO}/I_{TO} ratio, due to the LEO term.

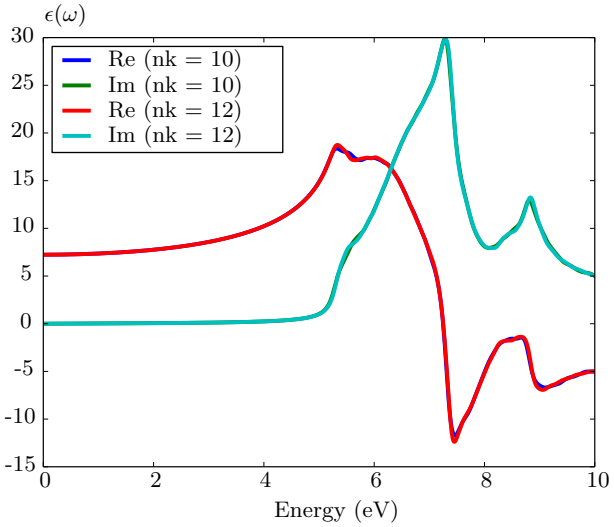

(a) Present results

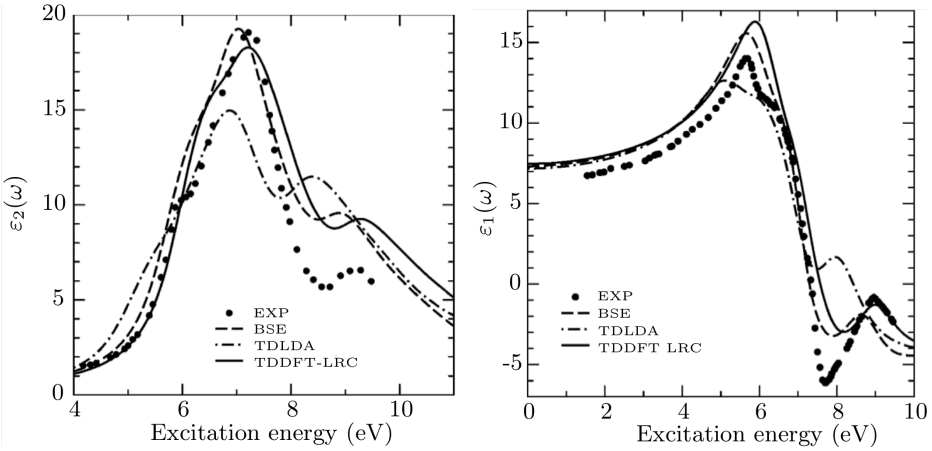

(b) [39] (c) [39]

Figure 31: (a) Macroscopic dielectric function of SiC obtained in the BSE formalism by averaging over $4 \times 4 \times 4$ shifted grids (nk represents the number of points used along each direction for the coarse grids). (b) and (c) Imaginary and real part of the dielectric function obtained by Botti *et al.* in Ref. [39].

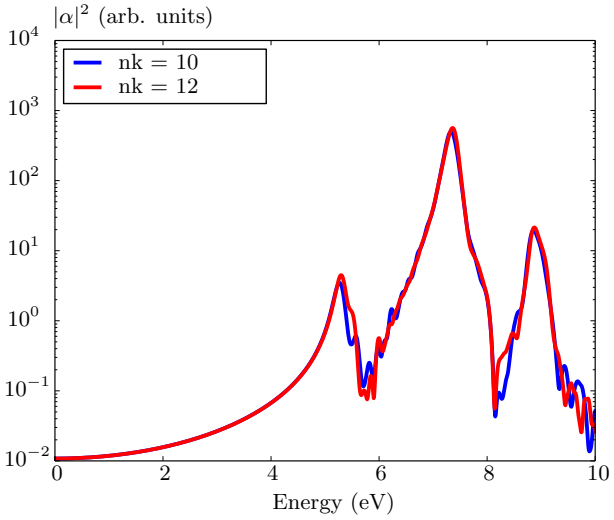

Figure 32: TO phonon derivative of the dielectric function $|\alpha|^2$ of SiC as a function of the laser frequency obtained in the BSE formalism by averaging over $4 \times 4 \times 4$ shifted grids (nk represents the number of points used along each direction for the coarse grids).

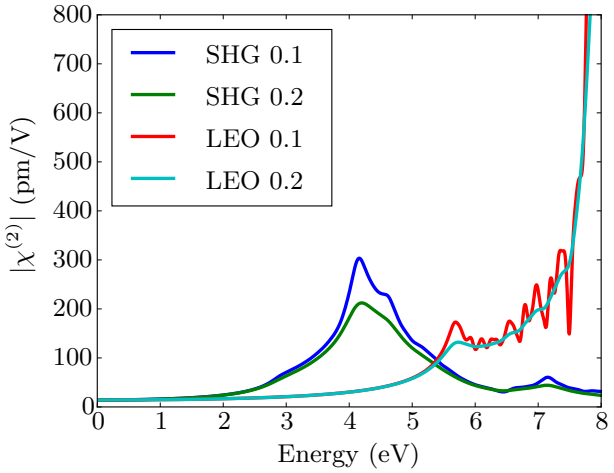

Figure 33: SHG and LEO susceptibilities of SiC. The number refers to the numerical broadening (in eV) used to shift the poles in the denominator.

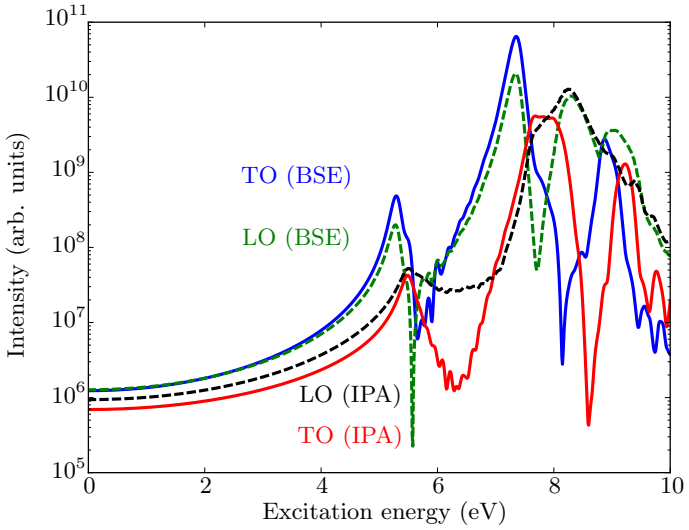

(a)

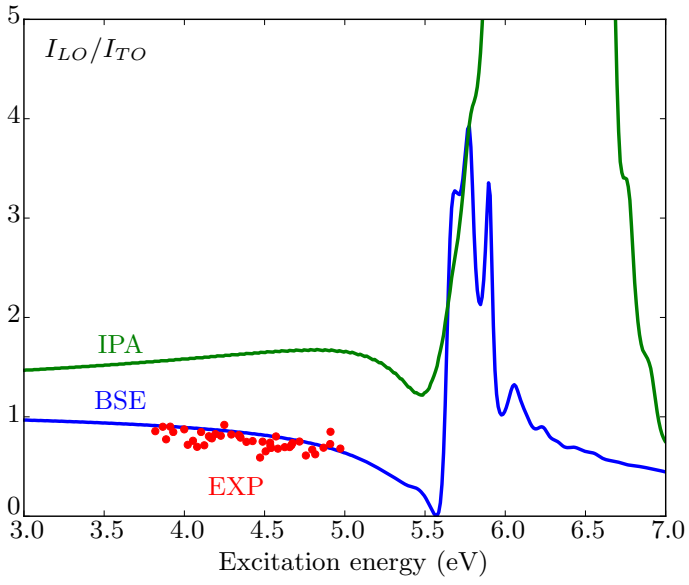

(b)

Figure 34: Intensities for TO and LO Raman peaks of SiC for parallel configuration, with light propagating in the [111] direction in the BSE and IPA framework. The intensity is obtained with formula (105). Upper panel: absolute intensities of TO (solid lines) and LO (dashed lines) modes. Lower panel: ratio of LO and TO intensities in BSE and IPA and comparison with experiments (points) obtained by Ref. [130].

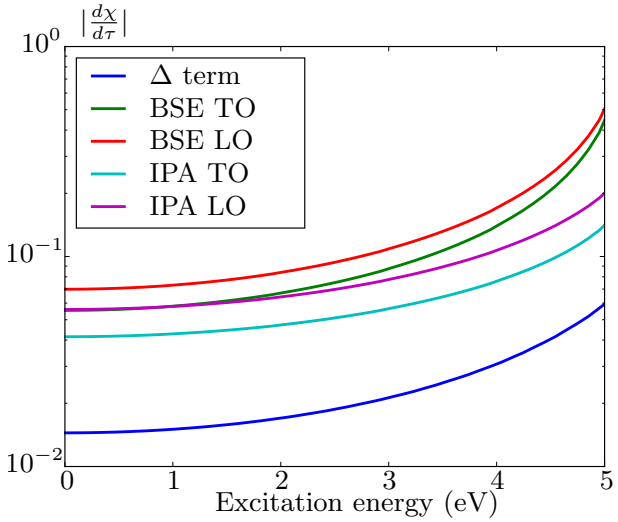

Figure 35: Atomic derivatives of the dielectric function $\left|\frac{d\chi_{yz}}{dR_{\kappa\alpha}}\right|$ for the first atom along the x-direction. The **q**-vector is aligned with the [111] direction. The decomposition corresponds to the terms of Eq. (117): BSE/IPA TO corresponds to $\left|\frac{d\chi}{dR_{\kappa\alpha}}\right|_{TO}$, BSE/IPA LO corresponds to $\left|\frac{d\chi}{dR_{\kappa\alpha}}\right|_{LO}$. The Δ term is the term proportional to $\chi^{(2)}$.

4.1.2 *GaAs*

Gallium Arsenide is a well-known material, used for its opto-electronic properties because of its direct band gap. In this section, we are going to analyze the resonance effect on the Raman spectrum of GaAs.

The relaxed lattice parameter of GaAs is 10.58 Bohr [122, 131], that gives a Kohn-Sham direct band gap of 0.49 eV. This gap has to be compared with the experimental band gap of 1.519 eV at 0K [132] (1.429 eV at room temperature [133]).

As Spin-orbit coupling (SOC) is not available in the current version of ABINIT for BSE calculations, we have chosen to work without SOC for all this study. Effect of SOC on the dynamical properties and the lattice parameters is rather small, as observed in App. D. It should be noted that the split-off energy is nevertheless neglected.

Within DFPT, the TO frequency of GaAs is 269 cm^{-1} and the LO frequency is 286 cm^{-1}, in reasonable agreement with other ab initio results (270.65 cm^{-1}/289.55 cm^{-1}) [134] and experimental measurements (267.3 cm^{-1}/285.0 cm^{-1}) [135]. The Born effective charge (BEC) of GaAs

are 2.06 and −2.06 for Ga and As respectively. The dielectric tensor is diagonal and has a value $\varepsilon^{\infty} = 13.95$ and $\varepsilon^{0} = 15.76$ predicted by DFPT, to be compared with 12.302 and 14.08 [134], also in poor agreement with experimental measurements of 10.89 and 12.9 [136].

Starting from the BSE dielectric function (see Fig. 8, Sec. 2.4), we can compute the resonant RI. The BSE dielectric constant ε^{∞} is 12.0 for a $10 \times 10 \times 10$ multiple-shifted k-point grid, showing the importance of excitonic effect to obtain good agreement of the dielectric constant ϵ^{∞} measured in experiments. The evolution of the RI with respect to the laser frequency is presented in Fig. 36. The experimental measurements of the enhancement is also reproduced in Fig. 36b. The main effect is in agreement with measurements, showing two main resonance peaks below 1.5 eV and 3.0 eV. The secondary peak at 1.8 eV, corresponding to the energy $E_0 + \Delta$, with Δ the split-off energy, is not reproduced in our calculations as SOC is not included. The difference between BSE and IPA in Fig. 36b is mainly due from the shift in the position of the peaks, as the intensities are renormalized so that the minimum is one. We believe the agreement of IPA results with experimental measurements for the first peak is quite fortuitious as SOC is not included in the calculations and the evolution of the intensities at higher laser frequencies is in any case worse than BSE. As in the case of silicon, temperature effects are not included in our calculations, while experimental measurements are corrected by shifting photon energies as referred to room temperature in Ref. [137]. Therefore, further investigation with temperature effects and SOC would be required to improve the agreement with experiments.

The LEO susceptibility is presented in Fig. 37 along with SHG calculations. They are in very good agreement with low-frequency data presented in Ref. [138]. Note that because of the double poles at transition energies in the LEO expressions (see App. B), the frequency dependence of the susceptibility oscillates a lot and is very sensitive to the BZ sampling.

In the same spirit as for SiC, we have computed the TO and LO intensities for GaAs including BSE and IPA derivatives for the TO intensity and LEO susceptibilities computed in the IPA. The results are shown in Fig. 38. Note that the convergence is very difficult for energies higher than 1.5 eV. Nevertheless, the trend is clear: as in the case of SiC, the LO intensity tends to decrease with increasing excitation energy, up to the first direct transitions where it shows a large increase. In the case of GaAs, however, excitonic effects are less marked for the relative intensi-

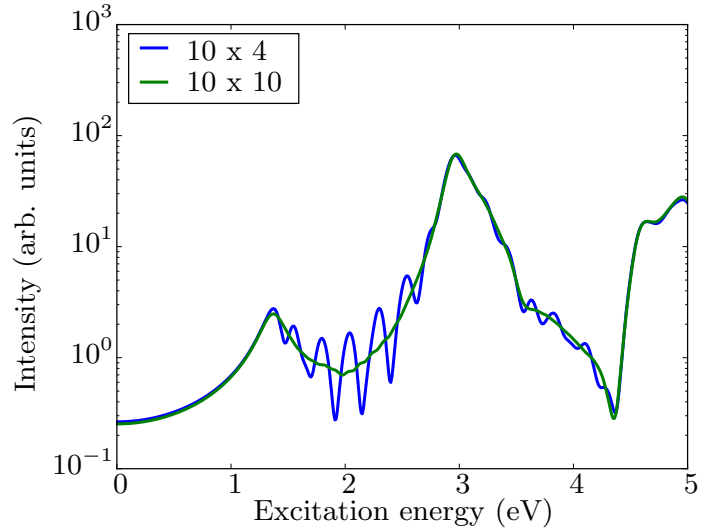

(a)

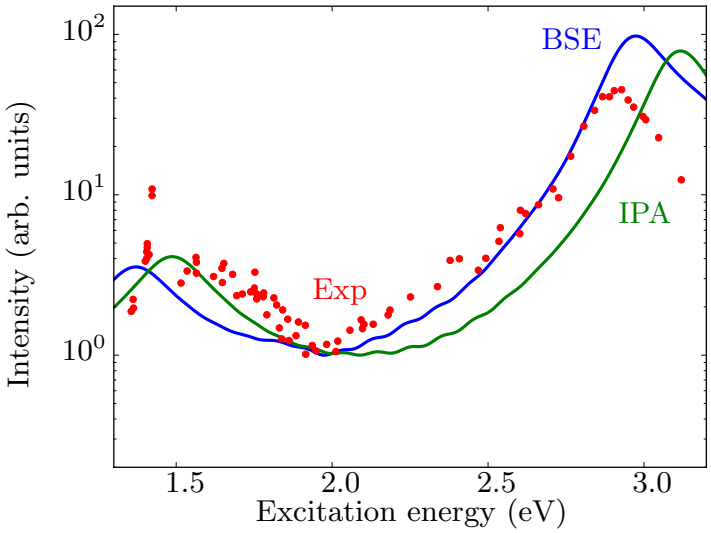

(b)

Figure 36: (a) Convergence of the RI $|\alpha|^2$ for the TO phonon of GaAs in BSE with respect to the BZ sampling for a coarse grid sampling of 10x10x10 points used with different multiple shifts sub-grids with n_{div} =4 or 10. (b) Comparison of our results (BSE and IPA) with experimental measurements (Exp) extracted from Ref. [137]. The curves are normalized such as the minimum of the intensity is set to one.

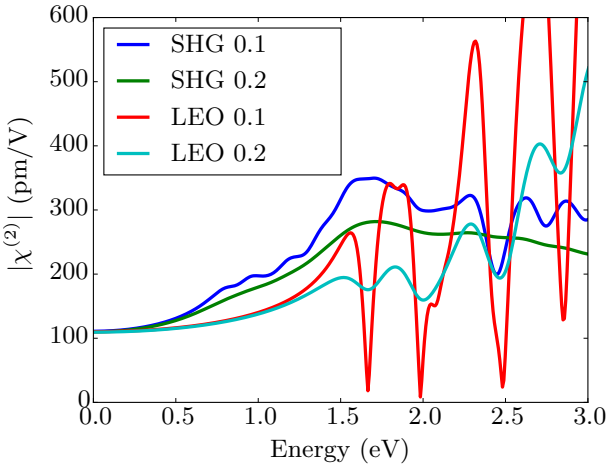

Figure 37: SHG and LEO susceptibilities of GaAs. The number refers to the numerical broadening (in eV) used to shift the poles in the denominator.

ties. Indeed, the shape of the curve is quite similar for BSE and IPA apart from a shift in the energy range.

4.1.3 *Numerical parameters*

4.1.3.1 *SiC*

The DFPT calculations on SiC have been performed with a cut-off energy of 32 Ha and a four-times shifted $6 \times 6 \times 6$ k-point grid with FHI pseudopotentials.[1]

In order to mimic the GW gap opening on top of the LDA gap of 1.36 eV in our optical properties calculations, we have used a scissor shift of 0.9 eV, toward the indirect band gap of 2.26 eV. The direct gap in our calculations is therefore 5.5 eV.

The BSE dielectric function has been obtained using the multiple-shift technique presented in Sec. 3.4, with 3 valence bands and 6 conduction bands. The model dielectric function presented in Ref. [76] has been used to model the screening with a dielectric parameter of 6.5.

The SHG and the LEO susceptibilities have been computed in the IPA for SiC. The same parameters as for DFPT have been used along with the scissor shift approximation, 24 bands, and a four-times shifted $32 \times 32 \times 32$ k-point grid.

1 Only last shell s^2 and p^2 electrons are considered as valence electrons for Si and C.

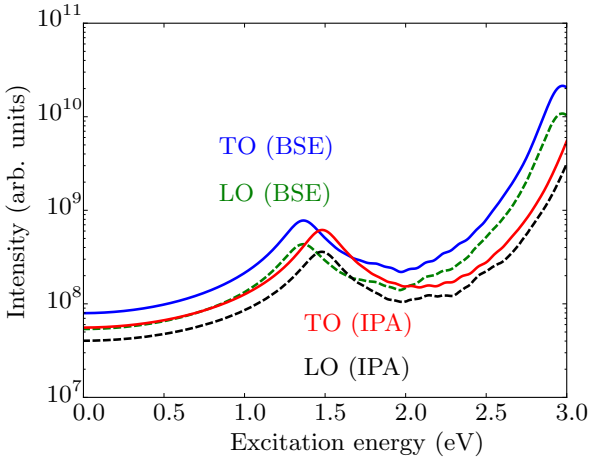

(a)

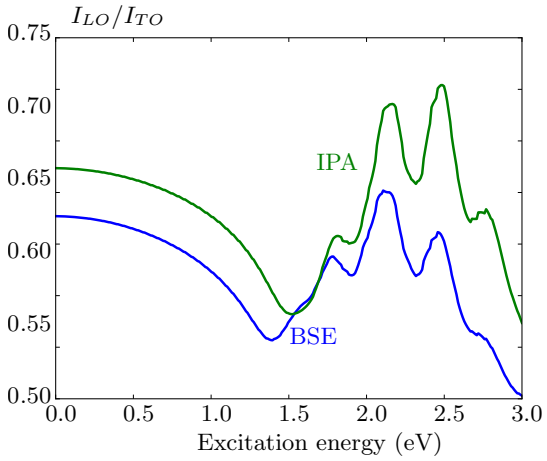

(b)

Figure 38: Intensities for TO and LO peaks of Raman spectrum of GaAs for parallel configuration, with light propagating in the [111] direction. The intensity is obtained with formula (105). Upper panel: absolute intensities of TO (solid lines) and LO (dashed lines) modes. Lower panel: ratio of LO and TO intensities in BSE and IPA.

4.1.3.2 *GaAs*

A study of the effect of pseudopotentials on the lattice parameters, dynamical properties and electronic band structure of GaAs is presented in App. D. From this study, we have chosen to work with ONCVPSP pseudopotentials with LDA functional.[2] A cut-off energy of 42 Ha and a $8 \times 8 \times 8$ k-point grid have been used to simulate the properties of this material.

BSE calculations have been performed with a scissor shift of 1.0 eV, that yields a direct band gap of 1.49 eV. 3 valence bands and 6 conduction bands are included in the BSE transition basis set. The model dielectric function with a dielectric constant of 10 has been used.

The second-order susceptibilities have been evaluated with 40 bands on a four-times shifted $24\times24\times24$ k-point grid. This grid still leads to oscillations especially for the LEO susceptibility. A numerical broadening of 0.2 eV has been used to obtain smoother data for Raman intensities.

4.1.4 *Note on LO intensities*

Before ending this section, one needs to discuss experimental measurement of LO intensities.

Starting from a Frölich Hamiltonian, as done in Ref. [139], the electron-phonon matrix elements that play a role in the quantum-mechanical formulation of the intensities of LO modes are composed of two terms [139]

$$\langle j \left| \mathcal{H}_{eph} \right| l \rangle = C_F \left[\left\langle j \left| \frac{\mathbf{q}\cdot\mathbf{p}}{|q|} \right| l \right\rangle (1 - \delta_{jl}) + \frac{\delta_{jl}}{|q|} \right] \tag{151}$$

where C_F is the Frölich constant, determined from the LO frequency and dielectric constants. The first term is giving rise to the electro-optic term already presented in Sec. 3.2. The second term actually tends to 0 in the dipole limit and should be therefore "forbidden".

In practice, however, Raman measurements are done with very small but finite value of wavevectors of phonons. The second term therefore never disappears totally. This term is strongly resonant for particular critical points of the band structure and can even lead to higher scattering rates than electro-optic or TO intensities, very close to resonance [139]. These terms are unfortunately not captured by our methodology. This prevents direct comparison of our results with LO vs TO intensities produced by Trommer [137] at the vicinity of the gaps.

2 Semi-core electrons are included for Ga and As, i.e. $3d^{10}4s^2$ and 4p electrons are considered as valence electrons

Nevertheless, as these terms are only important very close to critical points, we believe our approach is sound for the whole range of frequency except very close to resonances, where the adiabatic approach is anyway not valid anymore [139].

4.2 EXCITON-PHONON COUPLING IN 2D MATERIALS: THE CASE OF DICHALCOGENIDES

The field of two-dimensional (2D) materials has grown incredibly fast due to the fascinating and outstanding physical properties of these atom-thick layers. In particular, 2D TMD have been placed at the center of the stage along with graphene, MoS_2 being the most representative prototype [140]. Furthermore, monolayers of semiconducting TMD are very attractive for the development of novel applications in optics, optoelectronics, and magneto-optoelectronics [141–143]. However, before any of these far-reaching applications can be unambiguously targeted, proper characterization and clear understanding of their properties, particularly of the coupling between different physical phenomena (e.g., electronic and optical, optical and vibrational, or the three of them), must be achieved.

Concerning the electronic structure of these systems, monolayered WS_2 and WSe_2 exhibit a direct band gap at the corners of the BZ (k-points K and K′) [144]. This is in contrast with their bulk counterpart, where the smallest gap is indirect between k-points K and Λ (K-M) [144, 145]. Another unique aspect of the electronic structure of this material is the significant SOC that lifts the degeneracy at the K and K′ points, thus leading to a large splitting of the valence band of ca. 400 and 450 meV for WS_2 and WSe_2, respectively [144].

The weak dielectric screening of the Coulomb interaction is responsible for a strong exciton binding energy and, therefore, excitonic states dominate the absorption spectrum of these systems [146, 147]. For WS_2, the absorption spectra is characterized by three excitonic states commonly labeled as X_A, X_B, and X_C with absorption peaks at ca. 2.0, 2.4, and 2.8 eV, respectively [146–148]. The X_A and X_B peaks are associated with the first (1s) excitation of the direct band transition at K with their difference in energy ($|E(X_A) - E(X_B)|$) directly related to the SOC splitting. X_C is often attributed to practically degenerate transitions near Γ. Recent measurements of the electronic gap yield exciton binding energies of 0.7 eV for the X_A and X_B and 1.3 eV for X_C [149]. Concerning the binding energy for X_A and X_B, some controversy can be found in the

literature, and an alternative value of 0.32 eV has been reported [146]. In addition, higher orders in the excitonic Rydberg series of X_A and X_B have been identified in differential reflection experiments, with the most prominent higher order excitation of X_A ($X_A(2s)$) located at 2.18 eV [146, 148]. Qualitatively, WSe_2 monolayers are very similar with values of ca. 1.7, 2.1, and 2.4 eV for the X_A, X_B, and X_C, respectively [147, 150]. Higher order 2s excitations have been found at 1.8 and 2.3 eV for $X_A(2s)$ and $X_B(2s)$ excitons, respectively [150].

Monolayered 2H-TMD of WS_2 and WSe_2 form 2D crystals with a sandwich-like structure composed of three triangular sublattices, where the metal sits in one sublattice between the chalcogens forming two opposed tetrahedrons arranged in such a way that they all form a hexagonal network when viewed from the top (see Fig. 39). Both systems belong to the same symmetry point group, D_{3h}, and exhibit a total of nine phonon branches. Three zone-center modes ($\mathbf{q} = 0$) are Raman active and belong to the A_1', E', and E'' representations [151]. However, in the back-scattering geometry where the incident light direction is perpendicular to the basal plane only two Raman active first order bands are observed, labeled A_1' and E' bands. Along with the first-order Raman active modes, a number of features have been identified in the spectrum of WS_2 and WSe_2 which are associated with second-order processes, such as combinations or overtones of phonons with finite wavevectors ($\mathbf{q} \neq 0$) usually located at the corners and edges of the BZ. These second-order features were already observed in bulk TMD [152] but only recently a detailed explanation of their origin was proposed for monolayer WS_2 and MoS_2 [145, 153].

Raman spectroscopy was shown to play a key role in the identification of 2D materials; for example, it can be used to distinguish and identify the number of layers in graphene and TMD [44, 155–157]. Moreover, as mentioned, TMD containing Mo or W and S or Se display a direct to indirect band gap transition when going from the monolayer towards the bulk [158], thus affecting the resonant Raman conditions [44, 45, 145, 159–161]. However, the analysis of the Raman and resonant Raman response of these materials offers more information that needs to be understood, because light scattering due to phonons reveals evidence about the interplay between electronic, optical and vibrational properties. Resonant Raman spectroscopy has been proven to provide evidence concerning exciton-phonon coupling [161], SOC [162] or lifetime of the excitonic states [160], among others. The resonant Raman spectra of bulk TMD (2H-MoS_2, WS_2, WSe_2, and $MoSe_2$) have been stud-

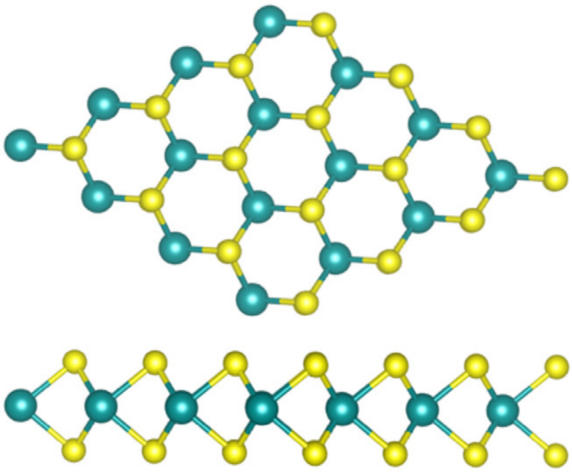

Figure 39: Top view (upper panel) and side view (lower panel) of the atomic structures of WX_2 (X = S or Se). The blue and yellow balls represent W atoms and S/Se atoms, respectively. Reproduced from Ref. [154]

ied in the past [163–165]. For bulk MoS_2 and WS_2, it was observed that the Resonant Excitation Profile (REP), that is, RI versus excitation energy, behaves differently for the out-of-plane and in-plane modes (A_{1g} and E_{12g}, respectively) because only the A_{1g} band resonates at all energies corresponding to the excitonic states. Such behavior is indicative of a symmetry dependence of the exciton-phonon coupling that governs the REP. More recently, resonant Raman studies of WSe_2 and MoS_2 systems with different number of layers have been performed and can be found in the literature [45, 160].

In this section, we compare the resonant Raman response of single layered WS_2 and WSe_2, using up to 25 excitation energies in the visible range, and we observe quite different and intriguing behavior for each material. For singlelayered WS_2, the main first and second-order Raman features (E', A_1', $2LA(M)$) are enhanced for laser energies corresponding to the first optical excitations (X_A, X_B and X_C). In contrast, the behavior of singlelayered WSe_2 is found to be more complex. On the one hand, the REP of first and second-order modes differs and on the other hand, the normal Raman modes, E', A_1', show no Raman enhancement in the energy region of the first optical excitations. Such a difference has not been previously reported, and in this work we further investigate it with the aid of state-of-the-art first-principles calculations at two different levels, starting with density functional theory (DFT) and then by solving the Bethe-Salpeter equation (BSE) for the excitonic states.

Fig. 40 shows the Raman spectrum of WS_2 and WSe_2 monolayers measured with the 488 nm excitation wavelength.

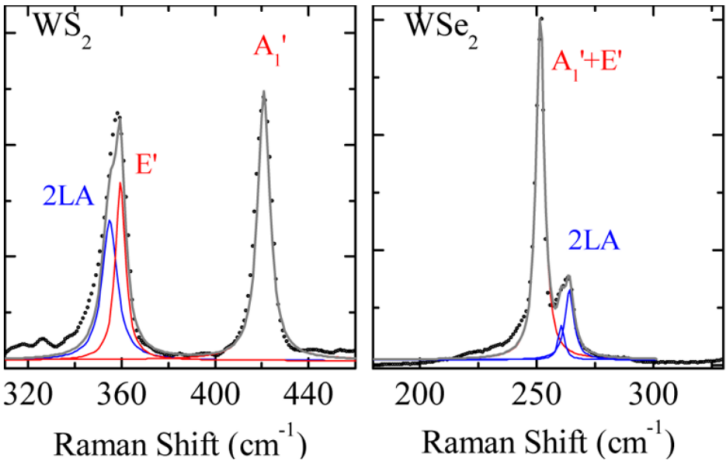

Figure 40: Raman spectra of monolayered WS_2 and WSe_2 (dots). The spectra are measured with the 488.0 nm excitation wavelength. Fitting of the spectra is shown by a solid gray line. First and second-order Raman contributions are depicted by red and blue Lorentzian fitting functions, respectively.

The two first-order modes of the Raman spectrum, E' and A_1', are present for singlelayered WS_2 around 356 and 418 cm^{-1} but for singlelayered WSe_2 they are degenerate in frequency, appearing around 250 cm^{-1} [166]. For both materials, additional second-order Raman contributions can be observed, and the most prominent one is ascribed to the $2LA(M)$ band, originated from a second-order double resonant process involving two longitudinal acoustic (LA) phonons close to the M point of the BZ [44]. However, when using different excitation lines (see Fig. 41) it is observed (especially in WSe_2) that the 2LA band is formed by more than one contribution, very close in frequency.

The origin of these 2LA Raman features was recently reported for MoS_2, and authors assigned these contributions to LA phonons at and in between the K and M points of the BZ [167]. In order to obtain the band intensities, the 2LA Raman of WS_2 and WSe_2 is arbitrarily fitted to one and two Lorentzian functions, respectively. For WS_2, this band appears at slightly lower frequency than the E' mode; for WSe_2, the 2LA contributions are observed at higher frequencies, around 260 and 263 cm^{-1}. Fig. 41 plots selected Raman spectra of monolayered WS_2 and WSe_2 recorded with excitation wavelengths within the visible range. The rela-

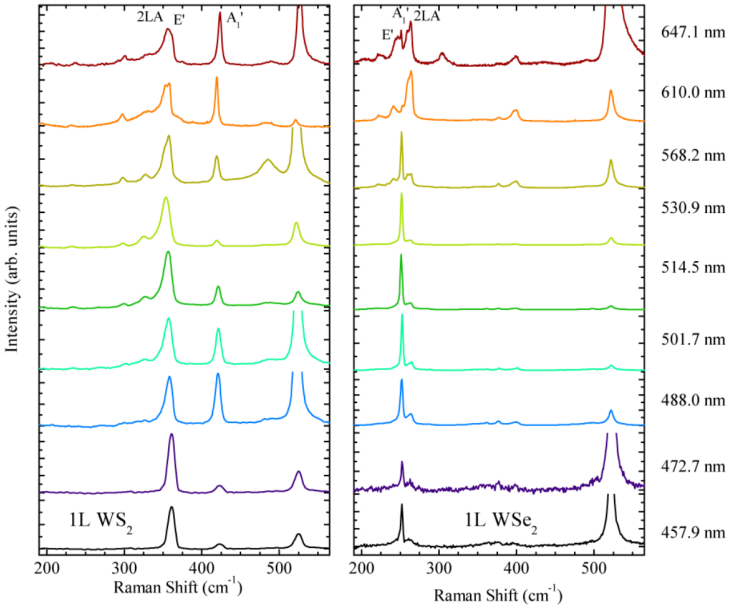

Figure 41: Selected Raman spectra of monolayered WS_2 and WSe_2 samples registered with different excitation wavelengths. The spectra intensity is arbitrarily set to improve the clarity of the results. The laser wavelength (indicated by the color of the spectra) is shown on the right.

tive intensities of the first and second-order contributions dramatically change with the excitation energy. A resonant Raman process occurs when the energy of the incident or the scattered photon matches the energy of an optical transition. As already mentioned, the TMD exhibit excitonic band gaps in the visible range. Therefore, when the incident and scattered photons are in resonance with excitonic transitions, the Raman scattering intensity increases abruptly. For the analysis of such resonant processes, the spectra in Fig. 41 are fitted with a sum of Lorentzian functions (see Supporting Information in App. E). The intensities of the Raman peaks of WS_2 and WSe_2 were normalized with the intensity of the Si Raman peak of the substrate at 521 cm^{-1}, considering its excitation energy dependence [168], already discussed in Sec. 3.4. There is a correction in the relative intensities of the TMD and Si peaks due to multiple optical interferences in the SiO_2 layer. However, as discussed by Carvalho et al. for MoS_2 samples [160], this correction is not significant and does not affect our main results and conclusions. In Fig. 42 and 43, we present the REP for WS_2 and WSe_2 monolayers, respectively.

The REP of the A_1', E', and 2LA Raman bands of monolayered WS_2 (Fig. 42) show three maxima of Raman intensity enhancement, which

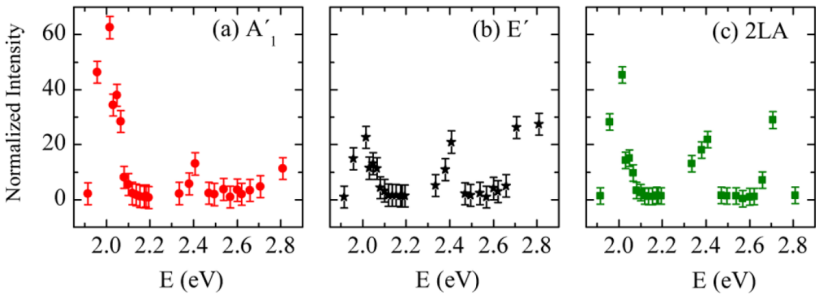

Figure 42: Resonant excitation profiles of the Raman bands A_1', E', and 2LA of monolayered WS_2. Each of the REP shows three enhancements at ca. 2.0, 2.4, and 2.7 eV, corresponding to X_A, X_B, and X_C exciton energies, respectively. The intensity of the Raman enhancement at these exciton energies differs for each Raman contribution, as previously observed for MoS_2 [160].

is in good agreement with previous optical absorption results also performed in monolayers [169]. Two enhancements appear around 2.0 and 2.4 eV, corresponding to X_A and X_B excitonic states. In addition, a third enhancement is observed at ca. 2.7 eV, and it is caused by the resonance with the X_C absorption. An interesting behavior is observed when comparing the REP of the first-order modes: while the E' band shows a REP with two peaks (at X_A and X_B energies) of similar intensity, the REP of the A_1' band displays a peak corresponding to the X_A exciton five times higher than that of the X_B. Such behavior reveals a symmetry breaking between the X_A and X_B exciton-phonon interaction, caused by a non-trivial interaction between the spin, electronic, and vibrational degrees of freedom. The analysis of the REP of WSe_2 is slightly more complex than that of WS_2. Within the excitation range studied in this work, the Raman spectrum should show enhancements at ca. 2.1 and 2.4 eV corresponding to X_B and X_C, respectively (note that the X_A exciton is out of the energy range considered in this work). Surprisingly, in Fig. 43 we observe that only the 2LA band behaves as expected, showing the mentioned enhancements.

In contrast, the first-order Raman bands only exhibit a single intensity enhancement around 2.42 eV, associated with the X_C transition. This peak in the WSe_2 REP at 2.42 eV has been previously associated with the X_B (2s) transition at 2.3 eV [45]. However, in view of the low quantum efficiency observed for this 2s transition as revealed from its low intensity in optical reflectivity spectra [150], such an alternative interpretation can be ruled out. Similar studies were performed in WSe_2 samples with

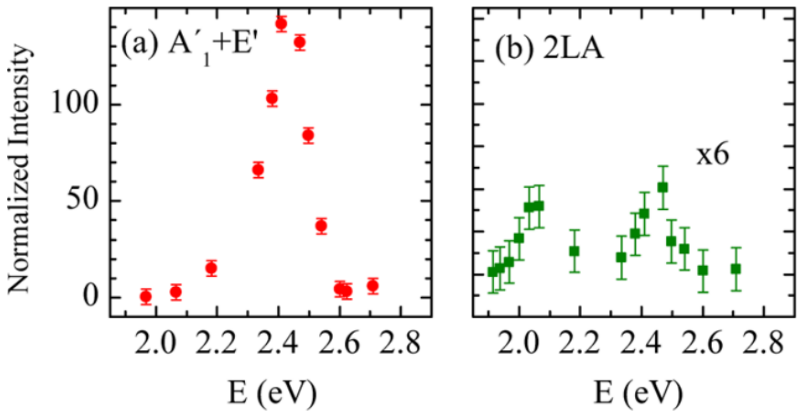

Figure 43: Resonant excitation profiles of the first-order Raman bands ($A_1' + E'$) and of the second-order 2LA band of monolayered WSe_2. For the first-order vibrational modes, the REP present a single enhancement at ca. 2.4 eV, corresponding to X_C. The 2LA band REP shows two enhancements at ca. 2.1 and 2.4 eV, which are in resonance with the X_B and X_C exciton energies. Two main contributions to the 2LA band are separated in the fitting procedure; (b) shows the REP of the 2LA contribution at 260 cm^{-1}, see Supporting Information in App. E for the REP of the 2LA contribution at 263 cm^{-1}.

more than one layer [45]. For thicker samples, the same intriguing behavior was observed: the absence of enhancement associated with X_B transition. Moreover, resonant Raman spectra were recorded in the near IR excitation range (X_A transition) but the Raman signal was negligible for all the WSe_2 samples, single to trilayered and bulk. The differences observed between the REP of WS_2 and WSe_2 are rather unexpected. There is no a priori reason for these systems to behave differently because the two crystal and electronic structures are quite similar. Moreover, the different REP showed by the first and second-order modes of WSe_2 is puzzling. In order to address such intriguing behaviors, theoretical calculations using DFT were performed, followed by solving the BSE for the excitonic states, as presented in the following section. In the simplest picture, the REP should follow the absorption spectrum, because as more light is absorbed, more phonons are excited. In this sense, the computation of the Fermi-Golden Rule (FGR) based on DFT and assuming the matrix elements to be constant would be the first approach. The advantage of this approach is that SOC is included, and that second-order Raman processes are considered [158]. More details concerning this approach are found in the App. E, and the theoretical REP of the 2LA band

of both materials is presented, see Fig. 71. However, as observed in the appendix, this computation method does not offer a good account for the difference between both materials. Thus, the discrepancy must come from the coupling between radiation, electrons, and phonons (i.e., the coupling matrices). Instead, we have considered the Raman signal as the result of the change of polarizability in the scattering crystal subject to vibrations. Thus, we have computed the REP from the derivative of the dielectric function (ε) within the BSE approximation to account for the excitonic properties of these materials. Recall that the dielectric function describes the response to an external excitation with energy (ω) considering all the excitonic states (E_λ) and their oscillator strengths (f_λ); it contains all the information regarding the optical properties. The expression of the dielectric function and its first-order derivative with respect to a phonon displacement ($\mathbf{x}$) are given respectively by

$$\varepsilon(\omega) = \sum_\lambda \frac{f_\lambda(\mathbf{x})}{\omega - E_\lambda(\mathbf{x}) - i\gamma} \tag{152}$$

$$\left|\frac{\partial \varepsilon}{\partial \mathbf{x}}(\omega)\right|^2 = \left|\sum_\lambda \left\{ \frac{f_\lambda(\mathbf{x}) E'_\lambda(\mathbf{x})}{(\omega - E_\lambda(\mathbf{x}) - i\gamma)^2} + \frac{f'_\lambda(\mathbf{x})}{\omega - E_\lambda(\mathbf{x}) - i\gamma} \right\}\right|^2 . \tag{153}$$

The advantage of computing the REP from BSE is that the interaction matrix elements are derived from first-principles with the caveat of losing the description of the SOC [169]. Because the objective is to address the difference in the Raman response of these very similar materials, we focus on the behavior of X_A and X_C as a function of the characteristic displacement of the A'_1 phonon mode, via finite differences. The calculation of second-order RI requires the evaluation of second-order derivatives of the dielectric function with respect to phonon displacements on a dense q-point grid. These calculations within the BSE framework are to-date beyond our computational resources and we therefore restrict our analysis to the first-order Raman bands in the following paragraphs.

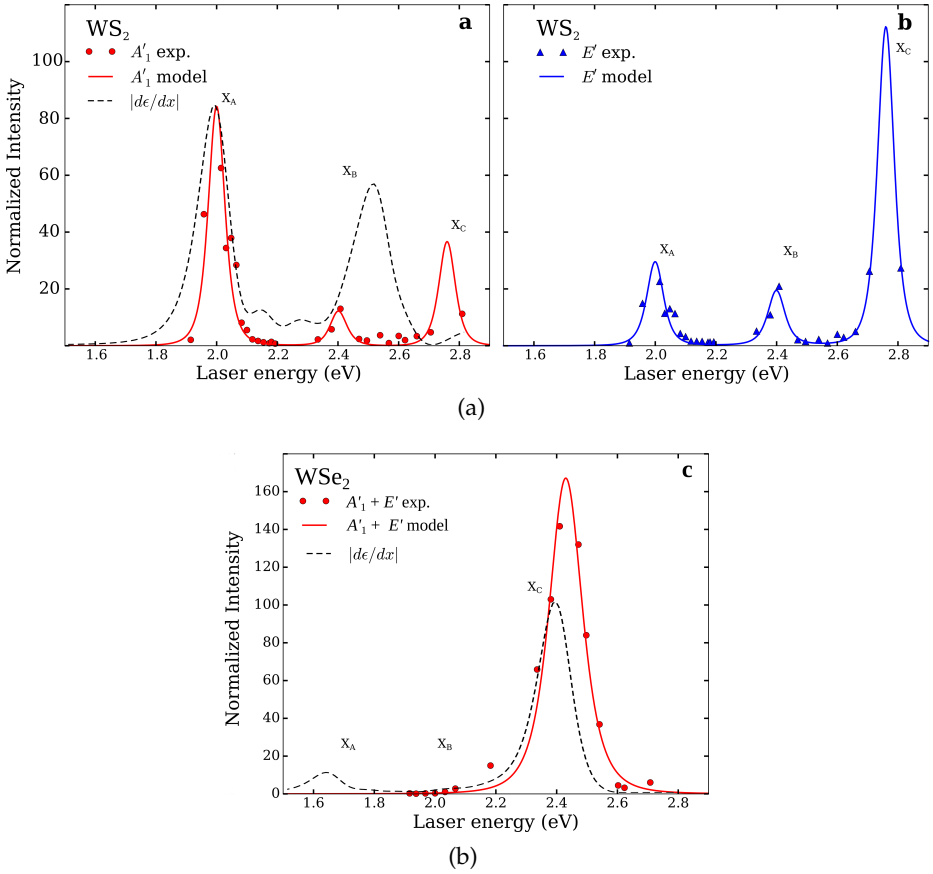

Figure 44: Experimental resonant excitation profiles for the first-order Raman bands of monolayered (a) WS_2 and (b) WSe_2. Dashed black lines represent the REP obtained by means of first-principles DFT-based BSE calculations, as the derivative with respect to displacement of the dielectric function for the A_1' mode. Solid colored lines represent the fitting of the experimental data (dots) according to Eq. (153).

Dashed lines in Fig. 44 show the response of ε to A_1' displacements for WS_2 and WSe_2. The intensity is normalized to X_C and weighted with respect to the Si REP, computed in Sec. 3.4 in order to simulate the experimental conditions. We can observe that the BSE calculations of $d\varepsilon/dx$ reveal an enhancement corresponding to the X_A exciton for WS_2 whereas almost no enhancement is present in WSe_2 at the mentioned analogous excitonic energy. According to this finding, a similar behavior is expected for exciton X_B, which would match the experimental observations. From inspection of Eq. (153), an insight on the origin of the difference between the two materials can be obtained. The values of

		A_1' mode		E' mode
		BSE	**fit**	**fit**
WS_2	X_A	173.69	0.71	0.28
	X_B	-	0.36	0.30
	X_C	-549.87	-1.00	-1.17
WSe_2	X_A	161.83		
	X_C	-1591.24	-1.00*	

Table 6: $f_\lambda E'_\lambda$ values computed either from finite differences of the dielectric function with excitonic effects (BSE) or fitted from the experimental data using the square of the first term of Eq. (153). The values are normalized with respect to the X_C peak of the A_1 mode. *This value corresponds to $f_\lambda E'_\lambda(A_1' + E')$.

E_λ and f_λ are obtained from the diagonalization of the excitonic Hamiltonian and consequently the derivatives E'_λ and f'_λ are calculated for each excitation state individually using finite differences. Therefore, the first term of Eq. (153) will hold the most important contribution to the REP due to the squared Lorentzian function, thus being $f_\lambda E'_\lambda$ the most significant factor.

The values of this product, $f_\lambda E'_\lambda$, are summarized in Tab. 6 under the BSE column. It is interesting to note that the sign of the product is due to the fact that $E'_{X_A} > 0$ and $E'_{X_C} < 0$ for the two materials. In addition, the calculated $f_\lambda E'_\lambda$ at the X_C energy is one order of magnitude larger than that at X_A in WSe_2, while it is only ca. 3 times larger in WS_2. The difference between the two materials is even more important once the intensities are considered, as they are proportional to the square of the derivatives (see Supporting Information in App. E for further details). This analysis reveals that the differences in the REP of WS_2 and WSe_2 has its origin in the different matrix elements $f_\lambda E'_\lambda$ (note that f_λ was already found to be different for WS_2 and WSe_2) [148]. The ratio of $f_\lambda E'_\lambda$ between the X_C and X_A differs for both materials explaining the unobserved enhancement of the RI for the first-order modes of WSe_2 at $X_{A/B}$ energies. Following this model, the experimental data have been fitted to a function of the square of the first term of Eq. (153). The fitted values are normalized to the X_C peak of the A_1' mode for comparison with the BSE calculations. Here, we considered the bare excitonic states (i.e., without the effect of the substrate) within an energy window of 0.05 eV around the maximum values of f_λ associated with X_A and X_C.

Note that the sign of $f_\lambda E'_\lambda$ has little impact in the fitting procedure. However, it has been kept to conserve the physical difference in the response at the diverse excitation energies. The data collected in Tab. 6 under the fit columns shows qualitative agreement in the tendency of the ratio between the X_C and X_A with respect to the BSE calculations for the A'_1 mode. The E' mode values, also normalized to X_C of the A'_1 mode, reflect the different relative coupling with the X_C exciton as described recently for MoS_2 [160]. The resulting fitted curves are displayed (solid lines) in Fig. 44 and compared with experimental results. The plotted values are normalized to the Si REP. While the WSe_2 data provide little information (due to the unobserved enhancements), the WS_2 fitted values reported in Tab. 6 provide an idea of the relative exciton-phonon-(spin) interaction for the different phonon and exciton modes, because $f_\lambda E'_\lambda$ contains the most relevant information on the matrix elements of these interactions contributing to the Raman REP.

In conclusion, in this work we studied the resonance Raman response of WS_2 and WSe_2 monolayers, both experimentally by using up to 25 laser lines in the visible range and theoretically by using state-of-the-art first-principles calculations at two different levels, DFT and BSE for the excitonic states. Concerning monolayered WS_2, the experimental Raman REP exhibits an asymmetric response for X_A and X_B. Interestingly, the Raman REP of the first-order modes of WSe_2 does not display the expected enhancement at the X_A and X_B exciton energies, which is in contrast with WS_2. Despite WS_2 and WSe_2 being nearly the same, they show a different exciton-phonon interaction, which leads to a different ratio of $f_\lambda E'_\lambda$ between X_A and X_C excitons, explaining the different REP shown by both materials. The results presented here unveil unexpected physical phenomena of WS_2 and WSe_2 monolayers, which are related to the interactions between the optical, magnetic, and vibrational properties of two-dimensional TMDs, and are relevant for potential applications. Our study should motivate further experimental and theoretical advancement for the understanding of the physics of two-dimensional materials in which the weak screening plays a very important role to couple different degrees of freedom (spin, optic, electronic).

4.3 CONCLUSIONS

In this chapter, we have applied the formalism presented in Chap. 2 and 3 to different materials: zinc-blende prototypes and transition-metal dichalcogenides. In the former case, we have more precisely studied

the Raman enhancement of the TO and the LO intensities. Excitonic effects have been shown to be important for the precise description of their Raman intensities. In the latter case, Raman intensities have been computed from first principles to improve our understanding of measured enhancement profiles in these 2D materials. The strength of the exciton-phonon coupling has been extracted and yields different Raman enhancement profiles for two a priori similar materials.

Up to now, the atoms were considered to be fixed at their equilibrium position. However, in reality, the atoms move and temperature effects may play a role on the band structure and on the Raman intensities. This effect will be examined in the next chapter.

5 TEMPERATURE-DEPENDENT OPTICAL PROPERTIES

All the calculations presented so far have been performed assuming that the atoms are located at their crystallographic positions thus neglecting temperature effects. However, a more realistic theoretical description should take into account the atomic vibrations that lead to temperature-dependent electronic properties through the electron-phonon coupling. In this chapter, we first present (Sec. 5.1) how to take the atomic motion into account for the temperature dependence of the electronic band structure, via the Allen-Heine Cardona theory. We then extend the framework to the calculation of temperature-dependent optical properties, starting with the IPA and then moving to the BSE in Sec. 5.2. Finally, we discuss how to connect the two approaches to calculate FP RI with temperature-dependent optical properties to obtain temperature-dependent Raman intensities in Sec. 5.3.

5.1 COMPUTATION OF THE TEMPERATURE DEPENDENCE OF THE BAND STRUCTURE

In this section, we summarize the main results that we have published in the two articles available as Ref. [64, 170].

In the harmonic approximation, the phonon modes are decoupled from each other. We can therefore express the temperature dependence of the eigenenergies $\epsilon_n(T)$ as the thermal average

$$\epsilon_n(T) \triangleq \langle \tilde{\epsilon}_n[z\mathbf{U}] \rangle (T) \tag{154}$$

$$= \sum_{m}^{3N} \frac{1}{\mathcal{Z}_m} \sum_{s_m} e^{\frac{-(s_m+1/2)\omega_m}{k_B T}} \int \chi^*_{m,s_m}(z) \tilde{\epsilon}_n[z\mathbf{U}_{m,\kappa}] \chi_{m,s_m}(z) dz. \tag{155}$$

In the previous expression, $z\mathbf{U}$ denotes generically a displacement from the equilibrium atomic positions with N the number of atoms, T the temperature, s_m the integer occupation of phonon mode m, $\mathcal{Z}_m = \sum_{s_m} e^{\frac{-(s_m+1/2)\omega_m}{k_B T}}$ the mode-partition function, k_B the Boltzmann's con-

stant, $\chi_{m,s_m}(z)$ the phonon eigenfunctions, z associated with a phonon mode and where bold symbols like $\mathbf{U}_{m,\kappa}$ denote Cartesian vectors.

After some algebra [64], one can show that the temperature dependence of the eigenenergy $\epsilon_n(T)$ is

$$\epsilon_n(T) = \tilde{\epsilon}_n[0] + \Delta\epsilon_n(T) \tag{156}$$

with

$$\Delta\epsilon_n(T) = \sum_m^{3N} \frac{\partial\epsilon_n}{\partial n_m}\left(n_m(T) + \frac{1}{2}\right), \tag{157}$$

where $n_m(T)$ is the Bose-Einstein occupation function, that vanishes at zero temperature.

Eqs. (156) and (157) show that the zero-temperature value $\epsilon_n(0)$ differs from the frozen-atom value $\tilde{\epsilon}_n[0]$ by the so-called zero-point motion renormalization.

Using Eq. (155), it is possible to show that the change of the eigenenergies with phonon occupation can also be rewritten as the change of phonon energy with respect to electron occupation

$$\begin{aligned}\frac{\partial\epsilon_n}{\partial n_m} =& \frac{1}{2\omega_m}\frac{d^2}{dz^2}\tilde{\epsilon}_n[z\mathbf{U}_{m,\kappa}]\Big|_{z=0} \\ =& \frac{1}{2\omega_m}\sum_{\substack{\kappa\alpha \\ \kappa'\gamma}} U^*_{m,\kappa'\gamma}\frac{\partial^2\epsilon_n}{\partial R_{\kappa\alpha}\partial R_{\kappa'\gamma}}U_{m,\kappa\alpha} = \frac{\partial\omega_m}{\partial f_n}.\end{aligned} \tag{158}$$

This important result allows expressing $\frac{\partial\epsilon_n}{\partial n_m}$ in terms of derivatives of the eigenenergies with respect to phonon eigendisplacements. In what follows, we show how to compute these terms with DFPT.

Starting from

$$\epsilon_n = \langle\Psi_n|\hat{H}|\Psi_n\rangle, \tag{159}$$

the first step is to differentiate and use the Hellmann-Feynman theorem. This yields, at equilibrium geometry,

$$\frac{\partial\epsilon_n}{\partial R_{\kappa\alpha}} = \left\langle\Psi_n^{(0)}\right|\frac{\partial\hat{H}}{R_{\kappa\alpha}}\left|\Psi_n^{(0)}\right\rangle. \tag{160}$$

Eq. (160) can be differentiated a second time, with respect to another atomic displacement. An equivalent result is obtained by exchanging the two atomic displacements. The two terms are combined together to

yield an expression that is real and explicitly symmetric with respect to the indices $\kappa\alpha$ and $\kappa'\gamma$

$$\frac{\partial^2 \epsilon_n}{\partial R_{\kappa\alpha} \partial R_{\kappa'\gamma}} = \left\langle \Psi_n^{(0)} \right| \frac{\partial^2 \hat{H}}{\partial R_{\kappa\alpha} R_{\kappa'\gamma}} \left| \Psi_n^{(0)} \right\rangle + \frac{1}{2}\left[\left(\left\langle \frac{\partial \Psi_n}{\partial R_{\kappa\alpha}} \right| \frac{\partial \hat{H}}{\partial R_{\kappa'\gamma}} \left| \Psi_n^{(0)} \right\rangle + (\kappa\alpha) \leftrightarrow (\kappa'\gamma) \right) + (\text{c.c.}) \right], \quad (161)$$

where $(\kappa\alpha) \leftrightarrow (\kappa'\gamma)$ stands for the previous term in which the indices $\kappa\alpha$ and $\kappa'\gamma$ have been exchanged, and (c.c.) stands for the complex conjugate of the previous term.

The contribution from the second-order derivative of the Hamiltonian, $\frac{\partial^2 \hat{H}}{\partial R_{\kappa\alpha} R_{\kappa'\gamma}}$, gives the Debye-Waller (DW) term. The other bracketed term originates from the first-order modifications of the wavefunction and corresponds to the Fan term when considered in MBPT.

To split this expression in a Fan and a Debye-Waller contribution, the extension of Eq. (161) to periodic systems is substituted so that

$$\begin{aligned} \frac{\partial \epsilon_{n\mathbf{k}}}{\partial n_{m\mathbf{q}}} = \frac{1}{2\omega_m(\mathbf{q})} \sum_{\substack{\kappa\alpha \\ \kappa'\gamma}} U^*_{m,\kappa'\gamma}(\mathbf{q}) U_{m,\kappa\alpha}(\mathbf{q}) \\ \left\{ \left\langle u_{n\mathbf{k}}^{(0)} \right| \frac{\partial^2 \hat{H}_{\mathbf{k},\mathbf{k}}}{\partial R_{\kappa\alpha}(-\mathbf{q}) \partial R_{\kappa'\gamma}(\mathbf{q})} \left| u_{n\mathbf{k}}^{(0)} \right\rangle \right. \\ + \frac{1}{2}\left(\left(\left\langle \frac{\partial u_{n\mathbf{k}}}{\partial R_{\kappa\alpha}(\mathbf{q})} \right| \frac{\partial \hat{H}_{\mathbf{k},\mathbf{k}}}{\partial R_{\kappa'\gamma}(\mathbf{q})} \left| u_{n\mathbf{k}}^{(0)} \right\rangle \right. \right. \\ \left. \left. \left. + (\kappa\alpha) \leftrightarrow (\kappa'\gamma) \right) + (\text{c.c.}) \right) \right\}, \end{aligned} \quad (162)$$

where $\hat{H}_{\mathbf{k},\mathbf{k}}$ is defined through the following convention

$$H_{\mathbf{k},\mathbf{k}'} = e^{-i\mathbf{k}\cdot\mathbf{r}} H e^{-i\mathbf{k}'\cdot\mathbf{r}'}. \quad (163)$$

This allows us to introduce the following notation for the DW and Fan contributions related to band n and wavevector $\mathbf{k}$ (we neglect the n and $\mathbf{k}$ indices in the left-hand side, which should not be confusing in the present context)

$$\mathcal{D}_{\substack{\kappa\alpha \\ \kappa'\gamma}}(\mathbf{q}) \triangleq \left\langle u_{n\mathbf{k}}^{(0)} \right| \frac{\partial^2 \hat{H}_{\mathbf{k},\mathbf{k}}}{\partial R_{\kappa\alpha}(-\mathbf{q}) \partial R_{\kappa'\gamma}(\mathbf{q})} \left| u_{n\mathbf{k}}^{(0)} \right\rangle \quad (164)$$

$$\mathcal{F}_{\substack{\kappa\alpha \\ \kappa'\gamma}}(\mathbf{q}) \triangleq \frac{1}{2}\left[\left(\left\langle \frac{\partial u_{n\mathbf{k}}}{\partial R_{\kappa\alpha}(\mathbf{q})} \right| \frac{\partial \hat{H}_{\mathbf{k},\mathbf{k}}}{\partial R_{\kappa'\gamma}(\mathbf{q})} \left| u_{n\mathbf{k}}^{(0)} \right\rangle + (\kappa\alpha) \leftrightarrow (\kappa'\gamma) \right) + (\text{c.c.}) \right]. \quad (165)$$

The change of eigenenergy due to a specific phonon mode, Eq. (162), thus becomes

$$\frac{\partial \epsilon_{n\mathbf{k}}}{\partial n_{m\mathbf{q}}} \triangleq \frac{\partial \epsilon^{\mathrm{FAN}}_{n\mathbf{k}}}{\partial n_{m\mathbf{q}}} + \frac{\partial \epsilon^{\mathrm{DW}}_{n\mathbf{k}}}{\partial n_{m\mathbf{q}}} \tag{166}$$

with the Fan contribution given by

$$\frac{\partial \epsilon^{\mathrm{FAN}}_{n\mathbf{k}}}{\partial n_{m\mathbf{q}}} \triangleq \frac{1}{2\omega_m(\mathbf{q})} \sum_{\substack{\kappa\alpha \\ \kappa'\gamma}} \mathcal{F}^{\kappa\alpha}_{\kappa'\gamma}(\mathbf{q}) U^*_{m,\kappa'\gamma}(\mathbf{q}) U_{m,\kappa\alpha}(\mathbf{q}), \tag{167}$$

and the Debye-Waller contribution given by

$$\frac{\partial \epsilon^{\mathrm{DW}}_{n\mathbf{k}}}{\partial n_{m\mathbf{q}}} \triangleq \frac{1}{2\omega_m(\mathbf{q})} \sum_{\substack{\kappa\alpha \\ \kappa'\gamma}} \mathcal{D}^{\kappa\alpha}_{\kappa'\gamma}(\mathbf{q}) U^*_{m,\kappa'\gamma}(\mathbf{q}) U_{m,\kappa\alpha}(\mathbf{q}). \tag{168}$$

Up to this point, the formalism is exact. However, the equations (164) or (168) require the matrix elements of the second-order Hamiltonian, that are not available in today implementations of DFPT. We therefore want to use simple approximations. The translational invariance property can be written as

$$\begin{aligned} &\sum_\beta \delta_\beta \sum_{\kappa''} \frac{\partial^2 \epsilon_{n\mathbf{k}}}{\partial R_{\kappa'\alpha}(\mathbf{\Gamma}) \partial R_{\kappa''\beta}(\mathbf{\Gamma})} [\{\mathbf{R}_{l\kappa}\}] = 0 \quad \forall \delta_\beta \in \mathbb{R} \\ &\quad \Rightarrow \sum_{\kappa''} \frac{\partial^2 \epsilon_{n\mathbf{k}}}{\partial R_{\kappa'\alpha}(\mathbf{\Gamma}) \partial R_{\kappa''\beta}(\mathbf{\Gamma})} [\{\mathbf{R}_{l\kappa}\}] = 0. \end{aligned} \tag{169}$$

If we consider rigid-ion Hamiltonian, where potentials are created independently by the nuclei, the following properties can be shown for the DW contributions

$$\mathcal{D}^{\mathrm{ri}}_{\substack{\kappa\alpha \\ \kappa'\gamma}}(\mathbf{q}) = \mathcal{D}^{\mathrm{ri}}_{\substack{\kappa\alpha \\ \kappa'\gamma}}(\mathbf{\Gamma}) \delta_{\kappa,\kappa'}. \tag{170}$$

Using these properties allows rewriting DW in terms of first-order derivatives of the Hamiltonian

$$\begin{aligned} \frac{\partial \epsilon^{\mathrm{DW_{RIA}}}_{n\mathbf{k}}}{\partial n_{m\mathbf{q}}} = \frac{-1}{4\omega_m(\mathbf{q})} \sum_{\substack{\kappa\alpha \\ \kappa'\gamma}} \mathcal{F}^{\kappa\alpha}_{\kappa'\gamma}(\mathbf{\Gamma}) \\ \Big(U^*_{m,\kappa\gamma}(\mathbf{q}) U_{m,\kappa\alpha}(\mathbf{q}) + U^*_{m,\kappa'\gamma}(\mathbf{q}) U_{m,\kappa'\alpha}(\mathbf{q}) \Big). \end{aligned} \tag{171}$$

Applying these properties to any Hamiltonian is called the rigid-ion approximation. Within this approximation, the change of electronic energies reads

$$\frac{\partial \epsilon_{n\mathbf{k}}^{\mathrm{RIA}}}{\partial n_{m\mathbf{q}}} = \frac{\partial \epsilon_{n\mathbf{k}}^{\mathrm{FAN}}}{\partial n_{m\mathbf{q}}} + \frac{\partial \epsilon_{n\mathbf{k}}^{\mathrm{DW_{RIA}}}}{\partial n_{m\mathbf{q}}}. \tag{172}$$

This simplified formula makes the calculations easier to perform, since only first-order derivatives of the DFT Hamiltonian have to be computed.

All Fan-like contributions can be derived from DFPT, as explained in the Appendix of [64]. In practice, in the AHC theory as formulated by Giustino *et al.* [56], $\mathcal{F}^{\kappa\alpha}_{\kappa'\gamma}(\mathbf{q})$ is obtained using Eq. (165) and

$$\left\langle \frac{\partial u_{n\mathbf{k}}}{\partial R_{\kappa\alpha}(\mathbf{q})} \middle| \frac{\partial \hat{H}_{\mathbf{k},\mathbf{k}}}{\partial R_{\kappa'\gamma}(\mathbf{q})} \middle| u^{(0)}_{n\mathbf{k}} \right\rangle = {\sum_{n'=1}^{\infty}}' \frac{\left\langle u^{(0)}_{n\mathbf{k}} \middle| \frac{\partial \hat{H}_{\mathbf{k},\mathbf{k}}}{\partial R_{\kappa\alpha}(-\mathbf{q})} \middle| u^{(0)}_{n'\mathbf{k}+\mathbf{q}} \right\rangle \left\langle u^{(0)}_{n'\mathbf{k}+\mathbf{q}} \middle| \frac{\partial \hat{H}_{\mathbf{k},\mathbf{k}}}{\partial R_{\kappa'\gamma}(\mathbf{q})} \middle| u^{(0)}_{n\mathbf{k}} \right\rangle}{\epsilon^{(0)}_{n\mathbf{k}} - \epsilon^{(0)}_{n'\mathbf{k}+\mathbf{q}}}, \tag{173}$$

where the infinite sum over bands is truncated in numerical calculations, while the prime after the sum symbol indicates that the terms with a vanishing denominator (such a situation always occurs at $\mathbf{q} = \Gamma$ when $n = n'$) have to be excluded.

In the resulting expression, one needs to sum over numerous empty bands since the first-order wavefunction is expressed in the sum-over-states form. As shown by Sternheimer [171], the summation over highly energetic bands can be replaced by the solution of a linear equation. This equation can then be solved iteratively with the same techniques as the ones of the DFPT approach used to calculate phonon eigenvectors and eigenenergies [7, 9, 85, 172]. The resulting expression for the first-order wavefunction is detailed in the Appendix of Ref. [64] and leads to an alternative form of Eq. (173), proposed in Ref. [58]

$$\begin{aligned}\left\langle \frac{\partial u_{n\mathbf{k}}}{\partial R_{\kappa\alpha}(\mathbf{q})} \middle| \frac{\partial \hat{H}_{\mathbf{k},\mathbf{k}}}{\partial R_{\kappa'\gamma}(\mathbf{q})} \middle| u^{(0)}_{n\mathbf{k}} \right\rangle = \\ {\sum_{n'=1}^{M}}' \frac{\left\langle u^{(0)}_{n\mathbf{k}} \middle| \frac{\partial \hat{H}_{\mathbf{k},\mathbf{k}}}{\partial R_{\kappa\alpha}(-\mathbf{q})} \middle| u^{(0)}_{n'\mathbf{k}+\mathbf{q}} \right\rangle \left\langle u^{(0)}_{n'\mathbf{k}+\mathbf{q}} \middle| \frac{\partial \hat{H}_{\mathbf{k},\mathbf{k}}}{\partial R_{\kappa'\gamma}(\mathbf{q})} \middle| u^{(0)}_{n\mathbf{k}} \right\rangle}{\epsilon^{(0)}_{n\mathbf{k}} - \epsilon^{(0)}_{n'\mathbf{k}+\mathbf{q}}} \\ + \left\langle \hat{P}_{c\mathbf{k}+\mathbf{q}} \frac{\partial u_{n\mathbf{k}}}{\partial R_{\kappa\alpha}(\mathbf{q})} \middle| \frac{\partial \hat{H}_{\mathbf{k},\mathbf{k}}}{\partial R_{\kappa'\gamma}(\mathbf{q})} \middle| u^{(0)}_{n\mathbf{k}} \right\rangle.\end{aligned} \tag{174}$$

This formulation is independent of the value of M, which is usually taken to be slightly larger than the number of bands for which the electron-phonon renormalization is sought. It removes the cumbersome sum over states, and results in a significant speed up of the calculations [58] as well as the elimination of the convergence study on the truncation of the number of empty states.

The expression for the temperature-dependent renormalization within the adiabatic and rigid-ion approximation finally reads

$$\Delta\epsilon^{(\text{adiabatic,RIA})}_{n\mathbf{k}}(T) = \Re\frac{1}{N_q}\sum_{\mathbf{q}}\sum_{m}^{3N}\left(n_{m\mathbf{q}}(T)+\frac{1}{2}\right)\frac{1}{4\omega_m(\mathbf{q})}$$
$$\sum_{\substack{\kappa\alpha\\ \kappa'\gamma}}\Bigg\{\Bigg(\Bigg(\Bigg[\sum_{n'=1}^{M}{}'\frac{\left\langle u^{(0)}_{n\mathbf{k}}\middle|\frac{\partial\hat{H}_{\mathbf{k},\mathbf{k}}}{\partial R_{\kappa\alpha}(-\mathbf{q})}\middle|u^{(0)}_{n'\mathbf{k}+\mathbf{q}}\right\rangle\left\langle u^{(0)}_{n'\mathbf{k}+\mathbf{q}}\middle|\frac{\partial\hat{H}_{\mathbf{k},\mathbf{k}}}{\partial R_{\kappa'\gamma}(\mathbf{q})}\middle|u^{(0)}_{n\mathbf{k}}\right\rangle}{\epsilon^{(0)}_{n\mathbf{k}}-\epsilon^{(0)}_{n'\mathbf{k}+\mathbf{q}}+i\delta}$$
$$+\left\langle\hat{P}_{c\mathbf{k}+\mathbf{q}}\frac{\partial u_{n\mathbf{k}}}{\partial R_{\kappa\alpha}(\mathbf{q})}\middle|\frac{\partial\hat{H}_{\mathbf{k},\mathbf{k}}}{\partial R_{\kappa'\gamma}(\mathbf{q})}\middle|u^{(0)}_{n\mathbf{k}}\right\rangle\Bigg]+(\kappa\alpha)\leftrightarrow(\kappa'\gamma)\Bigg)+(\text{c.c.})\Bigg)$$
$$U^{*}_{m,\kappa'\gamma}(\mathbf{q})U_{m,\kappa\alpha}(\mathbf{q})$$
$$-\frac{1}{2}\Bigg(\Bigg(\Bigg[\sum_{n'=1}^{M}{}'\frac{\left\langle u^{(0)}_{n\mathbf{k}}\middle|\frac{\partial\hat{H}_{\mathbf{k},\mathbf{k}}}{\partial R_{\kappa\alpha}(\Gamma)}\middle|u^{(0)}_{n'\mathbf{k}}\right\rangle\left\langle u^{(0)}_{n'\mathbf{k}}\middle|\frac{\partial\hat{H}_{\mathbf{k},\mathbf{k}}}{\partial R_{\kappa'\gamma}(\Gamma)}\middle|u^{(0)}_{n\mathbf{k}}\right\rangle}{\epsilon^{(0)}_{n\mathbf{k}}-\epsilon^{(0)}_{n'\mathbf{k}}+i\delta}$$
$$+\left\langle\hat{P}_{c\mathbf{k}}\frac{\partial u_{n\mathbf{k}}}{\partial R_{\kappa\alpha}(\Gamma)}\middle|\frac{\partial\hat{H}_{\mathbf{k},\mathbf{k}}}{\partial R_{\kappa'\gamma}(\Gamma)}\middle|u^{(0)}_{n\mathbf{k}}\right\rangle\Bigg]+(\kappa\alpha)\leftrightarrow(\kappa'\gamma)\Bigg)+(\text{c.c.})\Bigg)$$
$$\left(U^{*}_{m,\kappa\gamma}(\mathbf{q})U_{m,\kappa\alpha}(\mathbf{q})+U^{*}_{m,\kappa'\gamma}(\mathbf{q})U_{m,\kappa'\alpha}(\mathbf{q})\right)\Bigg\}, \quad (175)$$

where a small imaginary component $i\delta$ is usually introduced in the AHC equation to avoid singularities in the denominators. For example, in the case of diamond, several authors have used an δ value of 100 meV to account for the finite lifetimes of the electronic states [56, 57, 63, 173].

In 1978, Allen generalized his earlier work [53], derived within the standard Rayleigh-Schrödinger perturbation theory, using MBPT to include finite phonon frequencies [174]. These techniques describe excitations in terms of spectral functions [60, 175], where quasiparticules cannot always be unambiguously identified with the associated well defined eigenenergies. We will refer to this technique as the dynamical AHC theory, to stress the inclusion of dynamical effects beyond the Born-Oppenheimer approximation. We obtain the following equation, which

contains the electron-phonon matrix elements already calculated for the adiabatic renormalization

$$\Delta\epsilon_{n\mathbf{k}}^{(\text{dynamic,RIA})}(T,\omega) = \Re\frac{1}{N_q}\sum_{\mathbf{q}}\sum_{m}^{3N}\frac{1}{4\omega_m(\mathbf{q})}\sum_{\substack{\kappa\alpha\\ \kappa'\gamma}}$$
$$\Bigg\{\Bigg(\Bigg(\Bigg[\sum_{n'=1}^{M}\left\langle u_{n\mathbf{k}}^{(0)}\right|\frac{\partial\hat{H}_{\mathbf{k},\mathbf{k}}}{\partial R_{\kappa\alpha}(-\mathbf{q})}\left|u_{n'\mathbf{k}+\mathbf{q}}^{(0)}\right\rangle\left\langle u_{n'\mathbf{k}+\mathbf{q}}^{(0)}\right|\frac{\partial\hat{H}_{\mathbf{k},\mathbf{k}}}{\partial R_{\kappa'\gamma}(\mathbf{q})}\left|u_{n\mathbf{k}}^{(0)}\right\rangle$$
$$\frac{1}{2}\left(\frac{n_{m\mathbf{q}}(T)+f_{n'\mathbf{k}+\mathbf{q}}}{\omega-\epsilon_{n'\mathbf{k}+\mathbf{q}}^{(0)}+\omega_m(\mathbf{q})+i\eta+i\delta}+\frac{n_{m\mathbf{q}}(T)+1-f_{n'\mathbf{k}+\mathbf{q}}}{\omega-\epsilon_{n'\mathbf{k}+\mathbf{q}}^{(0)}-\omega_m(\mathbf{q})+i\eta+i\delta}\right)$$
$$+\left\langle P_{c\mathbf{k}+\mathbf{q}}\frac{\partial u_{n\mathbf{k}}}{\partial R_{\kappa\alpha}(\mathbf{q})}\right|\frac{\partial\hat{H}_{\mathbf{k},\mathbf{k}}}{\partial R_{\kappa'\gamma}(\mathbf{q})}\left|u_{n\mathbf{k}}^{(0)}\right\rangle\left(n_{m\mathbf{q}}(T)+\frac{1}{2}\right)\Bigg]$$
$$+(\kappa\alpha)\leftrightarrow(\kappa'\gamma)\Bigg)+(\text{c.c.})\Bigg)U_{m,\kappa'\gamma}^{*}(\mathbf{q})U_{m,\kappa\alpha}(\mathbf{q})$$
$$-\frac{1}{2}\Bigg(\Bigg(\Bigg[\sum_{n'=1}^{M}\frac{\left\langle u_{n\mathbf{k}}^{(0)}\right|\frac{\partial\hat{H}_{\mathbf{k},\mathbf{k}}}{\partial R_{\kappa\alpha}(\Gamma)}\left|u_{n'\mathbf{k}}^{(0)}\right\rangle\left\langle u_{n'\mathbf{k}}^{(0)}\right|\frac{\partial\hat{H}_{\mathbf{k},\mathbf{k}}}{\partial R_{\kappa'\gamma}(\Gamma)}\left|u_{n\mathbf{k}}^{(0)}\right\rangle}{\epsilon_{n\mathbf{k}}^{(0)}-\epsilon_{n'\mathbf{k}}^{(0)}+i\delta}$$
$$+\left\langle P_{c\mathbf{k}}\frac{\partial u_{n\mathbf{k}}}{\partial R_{\kappa\alpha}(\Gamma)}\right|\frac{\partial\hat{H}_{\mathbf{k},\mathbf{k}}}{\partial R_{\kappa'\gamma}(\Gamma)}\left|u_{n\mathbf{k}}^{(0)}\right\rangle\Bigg]+(\kappa\alpha)\leftrightarrow(\kappa'\gamma)\Bigg)+(\text{c.c.})\Bigg)$$
$$\left(n_{m\mathbf{q}}(T)+\frac{1}{2}\right)\left(U_{m,\kappa\gamma}^{*}(\mathbf{q})U_{m,\kappa\alpha}(\mathbf{q})+U_{m,\kappa'\gamma}^{*}(\mathbf{q})U_{m,\kappa'\alpha}(\mathbf{q})\right)\Bigg\}, \tag{176}$$

where $f_{n\mathbf{k}}$ is the electronic occupation of the wavevector $\mathbf{k}$ at band n, $i\eta$ is the mathematical (as opposed to the numerical nature of $i\delta$) infinitesimal shift of the poles $\epsilon_{n'\mathbf{k}+\mathbf{q}}^{(0)}-\omega_m(\mathbf{q})$ to the lower part of the complex plane, which is required to enforce causality in MBPT, and where (c.c.) stands for the complex conjugate of the previous term, except for $i\eta$, whose sign must not be changed in the complex conjugation.[1] It should also be noted that a convergence study on M is required in Eq. (176) for the Fan term since the Sternheimer solution neglects the phonon frequency $\omega_m(\mathbf{q})$ while the sum over the active space does not.

In this work, following Allen [174], rather than obtaining the full spectral function to describe the electronic excitation, we suppose that their

1 Please note that in Ref. [170], a mistake was present in the DW term: the denominator was $\omega-\epsilon_{n'\mathbf{k}}^{(0)}+i\delta$ instead of $\epsilon_{n\mathbf{k}}^{(0)}-\epsilon_{n'\mathbf{k}}^{(0)}+i\delta$, whereas the DW is a static and not a dynamic term.

description in terms of quasiparticles is still valid and evaluate the associated eigenenergies by correcting the DFT eigenvalues to first-order in perturbation theory, taking the self-energy evaluated at $\omega = \epsilon^{(0)}_{n\mathbf{k}}$ as the perturbation. Complex eigenenergies are obtained within this generalization, that we refer to as the non-adiabatic AHC theory [174, 176]

$$\Delta\epsilon^{(\text{non-adiabatic,RIA})}_{n\mathbf{k}}(T) = \Delta\epsilon^{(\text{dynamic,RIA})}_{n\mathbf{k}}(T, \omega = \epsilon^{(0)}_{n\mathbf{k}}). \tag{177}$$

The phonon-induced lifetime broadening $1/\tau_{n\mathbf{k}}$ is the imaginary part of Eq. (176) with $\omega = \epsilon^{(0)}_{n\mathbf{k}}$ and $i\delta = 0$ (i.e. $1/\tau_{n\mathbf{k}}$ stems from the infinitesimal shift $i\eta$ introduced by MBPT)

$$\begin{aligned}
&\frac{1}{2\tau^{(\text{non-adiabatic,RIA})}_{n\mathbf{k}}} \\
&= \frac{\pi}{N_q}\sum_{\mathbf{q}}\sum_{m}^{3N}\frac{1}{8\omega_m(\mathbf{q})}\sum_{\substack{\kappa\alpha\\ \kappa'\gamma}} U^*_{m,\kappa'\gamma}(\mathbf{q})U_{m,\kappa\alpha}(\mathbf{q})\sum_{n'=1}^{M}{}'\Bigg(\Bigg[\\
&\left[\left\langle u^{(0)}_{n\mathbf{k}}\right|\frac{\partial\hat{H}_{\mathbf{k},\mathbf{k}}}{\partial R_{\kappa\alpha}(-\mathbf{q})}\left|u^{(0)}_{n'\mathbf{k}+\mathbf{q}}\right\rangle\left\langle u^{(0)}_{n'\mathbf{k}+\mathbf{q}}\right|\frac{\partial\hat{H}_{\mathbf{k},\mathbf{k}}}{\partial R_{\kappa'\gamma}(\mathbf{q})}\left|u^{(0)}_{n\mathbf{k}}\right\rangle\right] \\
&+ (\kappa\alpha)\leftrightarrow(\kappa'\gamma)\Bigg] + (\text{c.c.})\Bigg) \\
&\Big(\big(n_{m\mathbf{q}}(T) + f_{n'\mathbf{k}+\mathbf{q}}\big)\delta(\epsilon^{(0)}_{n\mathbf{k}} - \epsilon^{(0)}_{n'\mathbf{k}+\mathbf{q}} + \omega_m(\mathbf{q})) + \\
&\qquad \big(n_{m\mathbf{q}}(T) + 1 - f_{n'\mathbf{k}+\mathbf{q}}\big)\delta(\epsilon^{(0)}_{n\mathbf{k}} - \epsilon^{(0)}_{n'\mathbf{k}+\mathbf{q}} - \omega_m(\mathbf{q}))\Big),
\end{aligned} \tag{178}$$

where δ is the Dirac delta (replaced by a Lorentzian of finite width in the practical implementation).

The phonon-induced lifetime broadening in the adiabatic limit ($\omega_m(\mathbf{q}) << \epsilon^{(0)}_{n\mathbf{k}} - \epsilon^{(0)}_{n'\mathbf{k}+\mathbf{q}}$) is

$$\begin{aligned}
&\frac{1}{2\tau^{(\text{adiabatic,RIA})}_{n\mathbf{k}}} = \frac{\pi}{N_q}\sum_{\mathbf{q}}\sum_{m}^{3N}\frac{1}{4\omega_m(\mathbf{q})}\left(n_{m\mathbf{q}}(T) + \frac{1}{2}\right) \\
&\sum_{\substack{\kappa\alpha\\ \kappa'\gamma}}\sum_{n'=1}^{M}{}'\Bigg(\Bigg[\Bigg[\left\langle u^{(0)}_{n\mathbf{k}}\right|\frac{\partial\hat{H}_{\mathbf{k},\mathbf{k}}}{\partial R_{\kappa\alpha}(-\mathbf{q})}\left|u^{(0)}_{n'\mathbf{k}+\mathbf{q}}\right\rangle \\
&\left\langle u^{(0)}_{n'\mathbf{k}+\mathbf{q}}\right|\frac{\partial\hat{H}_{\mathbf{k},\mathbf{k}}}{\partial R_{\kappa'\gamma}(\mathbf{q})}\left|u^{(0)}_{n\mathbf{k}}\right\rangle\Bigg] + (\kappa\alpha)\leftrightarrow(\kappa'\gamma)\Bigg] + (\text{c.c.})\Bigg) \\
&\qquad \delta(\epsilon^{(0)}_{n\mathbf{k}} - \epsilon^{(0)}_{n'\mathbf{k}+\mathbf{q}})U^*_{m,\kappa'\gamma}(\mathbf{q})U_{m,\kappa\alpha}(\mathbf{q}).
\end{aligned} \tag{179}$$

The adiabatic and non-adiabatic renormalizations, Eqs. (175) and (177), as well as the adiabatic lifetime Eq. (179) have been implemented in the ABINIT software (v7.11). We compute renormalizations in the non-adiabatic approximation for silicon in Sec. 5.2 and 5.3 and for $BiFeO_3$ in Sec. 6.6.

5.2 OPTICAL PROPERTIES WITH TEMPERATURE-DEPENDENT BAND STRUCTURE

In the previous section, we have shown how to compute the complex temperature-dependent energies

$$\epsilon_{n\mathbf{k}}(T) = \epsilon^0_{n\mathbf{k}} + \Delta\epsilon_{n\mathbf{k}}(T), \tag{180}$$

where $\Delta\epsilon_{n\mathbf{k}}(T)$ is a complex function of the temperature.

In this section, we start from these energies to obtain temperature-dependent optical properties at the level of independent particles in Sec. 5.2.1 and then for BSE in Sec. 5.2.3

5.2.1 *Independent-Particle Approximation*

The independent-particle approximation of the dielectric tensor writes down

$$\hat{\varepsilon}(\omega) = 1 + 4\pi \sum_{nn'\mathbf{k}} (f_{n\mathbf{k}} - f_{n'\mathbf{k}}) \frac{\langle n\mathbf{k}|\mathbf{r}|n'\mathbf{k}\rangle \langle n'\mathbf{k}|\mathbf{r}|n\mathbf{k}\rangle}{\omega - (\epsilon_{n\mathbf{k}} - \epsilon_{n'\mathbf{k}}) - i\eta} \tag{181}$$

where an artificial broadening η is generally introduced.

If we consider the temperature dependence to induce only changes at the level of eigenenergies, the temperature-dependent generalization of Eq. (181) reads

$$\hat{\varepsilon}(\omega, T) = 1 + 4\pi \sum_{nn'\mathbf{k}} \frac{(f_{n\mathbf{k}} - f_{n'\mathbf{k}}) \langle n\mathbf{k}|\mathbf{r}|n'\mathbf{k}\rangle \langle n'\mathbf{k}|\mathbf{r}|n\mathbf{k}\rangle}{\omega - (\epsilon^0_{n\mathbf{k}} - \epsilon^0_{n'\mathbf{k}}) - (\Delta\epsilon_{n\mathbf{k}}(T) - \Delta\epsilon_{n'\mathbf{k}}(T)) - i\eta}. \tag{182}$$

Actually, no artificial broadening is required anymore since the finite lifetime is already described in the temperature-dependent eigenenergies, so in the calculations we can use $\eta \to 0$. Still, the use of very dense k-point grids at low temperature may be required because of the possibly low broadening. In practice, a very small broadening is still used to avoid numerical instabilities.

5.2.2 *Interpolation*

As computing the renormalization $\Delta\epsilon_{n\mathbf{k}}$ on a dense grid of k-points is cumbersome, we present in this section a simple interpolation technique to reduce the computational load.

We start by assuming $\Delta\epsilon_{n\mathbf{k}}$ is known on a coarse mesh of points $\tilde{\mathbf{k}}$. We then perform a zeroth-order interpolation of the electron-phonon **correction** to the energies. This means that for every dense point $\mathbf{k}$ in a small volume $V(\tilde{\mathbf{k}})$ around a coarse point, the following approximated expression is used

$$\epsilon_{n\mathbf{k}}(T) = \epsilon^0_{n\mathbf{k}} + \Delta\epsilon_{n\mathbf{k}}(T) \approx \epsilon^0_{n\mathbf{k}} + \Delta\epsilon_{n\tilde{\mathbf{k}}}(T) \quad \forall \mathbf{k} \in V(\tilde{\mathbf{k}}). \tag{183}$$

The results are then symmetrized in k-point space by averaging the results over all symmetry-equivalent k-points.

In order to validate the effectiveness of the interpolation technique, we have interpolated temperature-dependent energies obtained on a $6 \times 6 \times 6$ k-point grid towards a $10 \times 10 \times 10$ k-point grid. These values are obtained using a $40 \times 40 \times 40$ q-point grid and a broadening value of $\eta = 0.1$ eV. The results of our test are summarized in Fig. 45.

We observe that the interpolated results (see Fig. 45c) allow reaching a resolution in energy space that is comparable with the one obtained with the $10 \times 10 \times 10$ k-mesh but with a considerably reduced computational cost. For the ten first bands, the interquartile space goes from 5 meV to 12 meV which is reasonable as the starting grid is coarse ($6 \times 6 \times 6$). The average and the median of the error stay close from 0 meV for this set of bands, with a maximal deviation of 5 meV.

5.2.3 *Bethe-Salpeter Equation at finite temperature*

Experiments performed at different temperatures clearly show a broadening of the optical spectra due to the finite lifetime of the excitations that usually decreases with temperature.

Standard BSE calculations, on the other hand, are usually performed at T=0K with atoms fixed at their crystallographic positions. In this context, the finite lifetime is introduced as an ad-hoc broadening η whose value is usually determined in order to improve the agreement with the experimental curves.

In 2008, A. Marini [55] solved the BSE including coupling with the lattice and therefore temperature effects. In this work, the electron-phonon

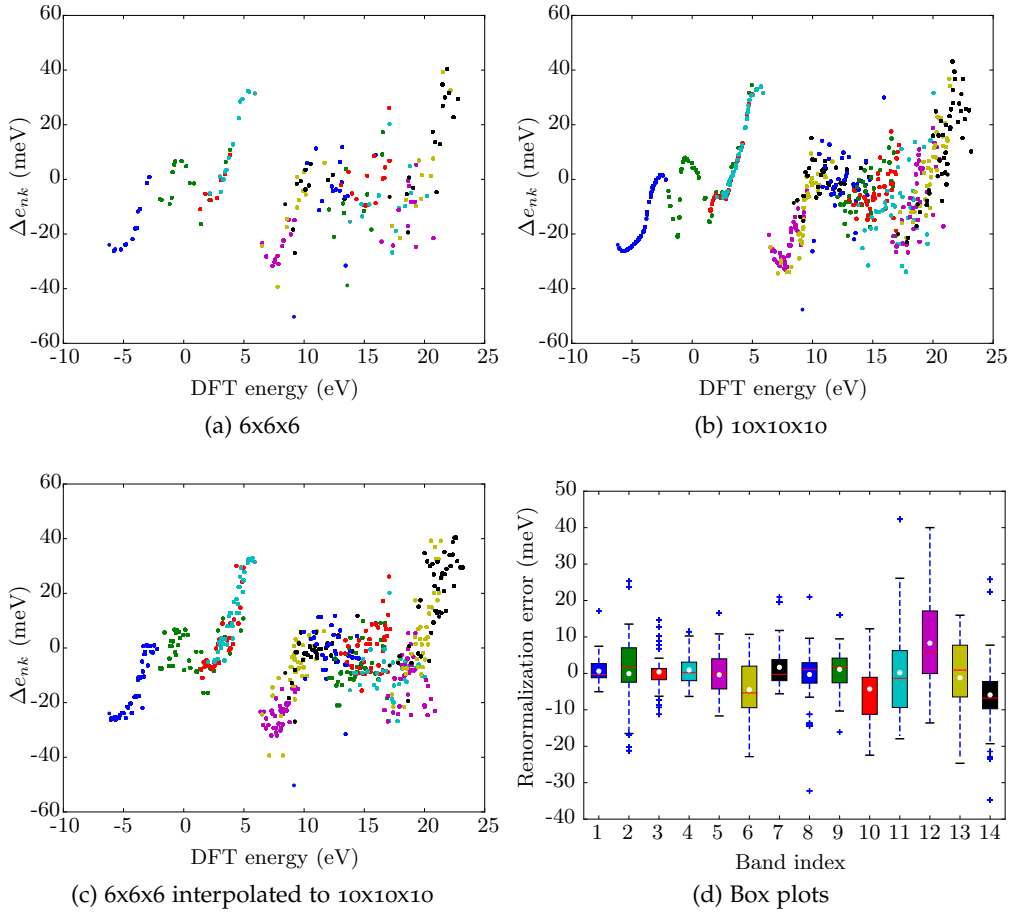

(a) 6x6x6 (b) 10x10x10

(c) 6x6x6 interpolated to 10x10x10 (d) Box plots

Figure 45: Electron-phonon renormalization with respect to frozen-atom eigenenergies on different k-point grids and interpolation technique following Eq. (183) at T=0K. The different colors correspond to the different band indices. (a) and (b): Ab initio results calculated on $6 \times 6 \times 6$ and $10 \times 10 \times 10$ k-point grids. (c) Interpolated results from the coarse $6 \times 6 \times 6$ grid to the dense $10 \times 10 \times 10$ grid. (d) Box plots representing the scattering of the error between the interpolated and the ab initio results on the $10 \times 10 \times 10$ results. The white dots represent the position of the average. The other lines follow the standard boxplot representation.

interaction renormalizes the diagonal part of the BSE Hamiltonian according to:

$$H_{vck,v'c'k'}(T) = H^{FA}_{vck,v'c'k'} + [\Delta\epsilon_{ck}(T) - \Delta\epsilon_{vk}(T)]\,\delta_{vv'}\delta_{cc'}\delta_{kk'}, \tag{184}$$

where H^{FA} is the "frozen-atom" expression for the BSE Hamiltonian introduced in Sec. 2.3.

The diagonalization of Eq. (184) gives complex excitonic eigenenergies and therefore finite (temperature-dependent) lifetimes, and therefore requires a much more careful treatment than the usual BSE. Indeed the matrix is not hermitian anymore and more advanced numerical techniques are needed to tackle the problem.

In our ABINIT implementation, we employ the iterative Bi-Lanczos algorithm to avoid the direct diagonalization of Eq. (184). More detail about the diagonalization of the temperature-dependent BSE equation and this algorithm are presented in App. F.

The next paragraph presents the application of our Bi-Lanczos method to the study of the optical spectrum of silicon including electron-phonon and temperature effects.

5.2.4 *Temperature-dependent optical spectrum of silicon*

In order to validate the implementation of temperature-dependent BSE in *ABINIT* we have performed calculations of the optical properties of silicon at different temperatures. A summary of the results are presented in Fig. 46. We observe the expected general trend: the gap is reduced with respect to bare DFT because of the zero-point motion renormalization. As temperature increases, the broadening increases and smoothens the curve while the absorption onset red-shifts. For the sake of comparison, we also reproduce in Fig. 46 the dielectric function obtained with the same k-point sampling but using a constant broadening value of 0.1 eV. We see that this "ad-hoc" broadening value allows for reproducing the shape of the optical spectrum for room temperature calculation and this explains its broad usage for BSE calculations. However, a more complete picture of temperature effects on the results requires more advanced techniques such as the one we present in this chapter. These results are in agreement with the pioneering study of Ref. [55] and experimental measurements, as illustrated in Fig. 47. The position of the peaks is well reproduced as well as the global broadening factor. However, some discrepancy can be observed at the level of the broadening in particular

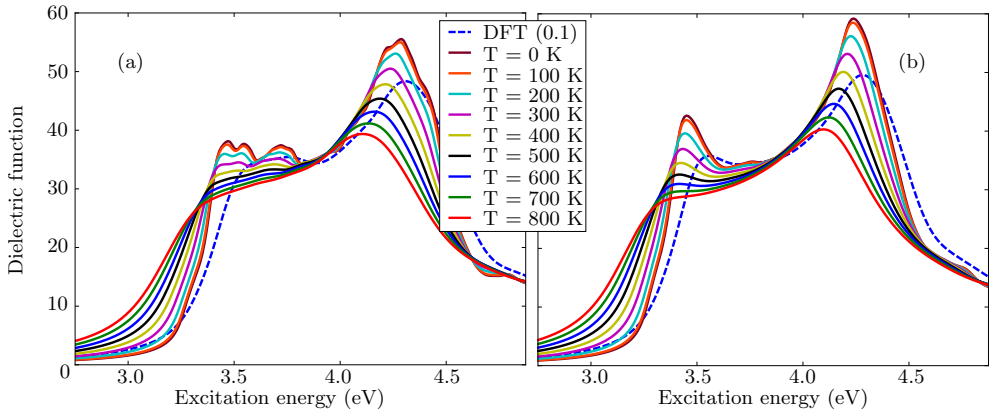

Figure 46: Imaginary part of the temperature-dependent dielectric function obtained (a) on 12x12x12 k-point grid with 2x2x2 multiple shifts and (b) 16x16x16 k-point grid with 4x4x4 multiple shifts with the technique already presented in Sec. 3.4. DFT (0.1) is the frozen-atoms results with a numerical broadening of 0.1 eV.

for the second peak of the absorption spectrum. This may be related to a different treatment used in the Yambo code for the computation of the imaginary part of the electron-phonon renormalization, that is very sensitive to the numerical details and the integration methods. Further validation of the fine details of the spectra may therefore be pursued in a future work.

To speed up the convergence of the results in Fig. 46, the dielectric function is averaged using multiple shifts as already presented in Sec. 3.4. We have tested convergence with respect to the size of the coarse mesh grid from $12 \times 12 \times 12$ to $16 \times 16 \times 16$ grids and for multiple shifts with $n_{\mathtt{div}} = 2$ and 4. The convergence of the dielectric function with the BZ sampling is mostly delicate for the low temperature range as the broadening is very small. However, for larger temperatures, the results are well converged. The other simulations parameters are the same as the ones used for first-order Raman scattering in Sec. 3.4.

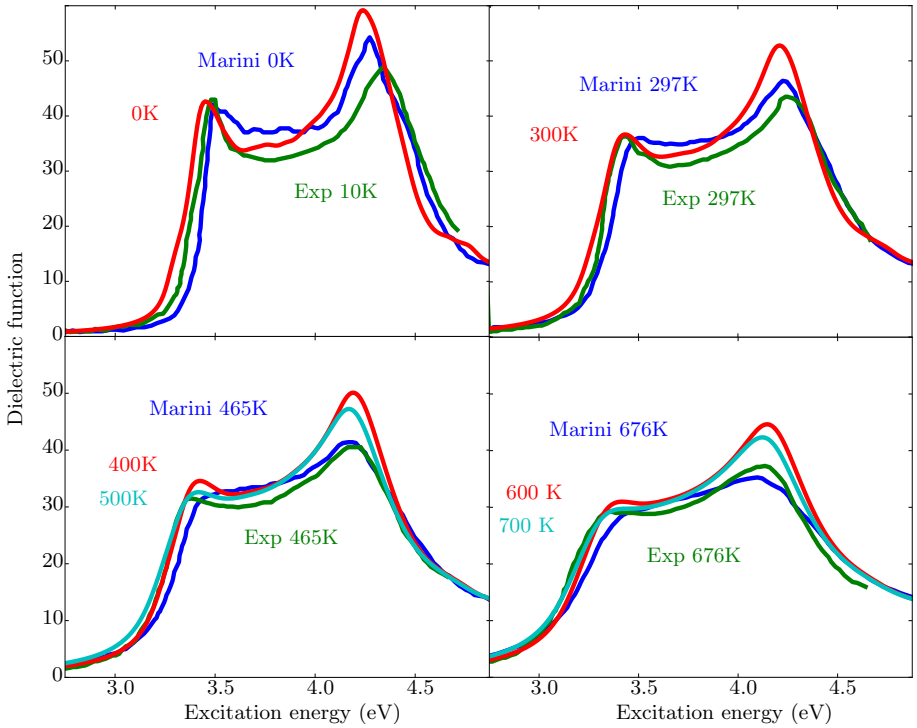

Figure 47: Comparison of the imaginary part of the dielectric function obtained in the present work (red and cyan curves) with Ref. [55] ("Marini", blue curves), and experimental measurements ("Exp", green curves) [115].

5.3 TEMPERATURE-DEPENDENT RAMAN SPECTRUM

In addition to the explicit temperature dependence of the occupation factor (see Sec. 3.2), the RI also change with temperature through the derivative of the dielectric function. Once the temperature-dependent RPA or BSE dielectric function can be obtained for any displaced geometry, the RI are available at different temperatures from the FP approach already used in Sec. 3.4.

The BSE results obtained with the $4\times4\times4$-times shifted $16\times16\times16$ grids are compared in Fig. 48 with experimental measurements at 4 different temperatures obtained by Compaan *et al.* [104].

In this figure, we observe a very nice agreement of our results with experimental measurements. Indeed, the trend is well reproduced. As expected, the gap shrinks with increasing temperature, shifting the maximum of the resonance towards lower frequencies. At the same time, the broadening induced by electron-phonon coupling increases, broadening

the entire REP. One should note that the curves are normalized with the experimental value available at 2.2 eV. This means that the position of the entire curve is highly sensitive to the measured intensity at this point. This may explain the small disagreement of the room temperature curve with experimental measurements, since all the experimental values after 2.3 eV have larger intensities than our results.

The silicon temperature-dependent renormalization of the band structure has been computed on a 10×10×10 k-point grid. They have been interpolated towards the k-point grids used for the optical properties, i.e. different shifted 16×16×16 grids. In these results, the change of the temperature renormalization with the atomic displacements is neglected, in the same way we have neglected the change of the scissor with the displacement in Sec. 3.4.

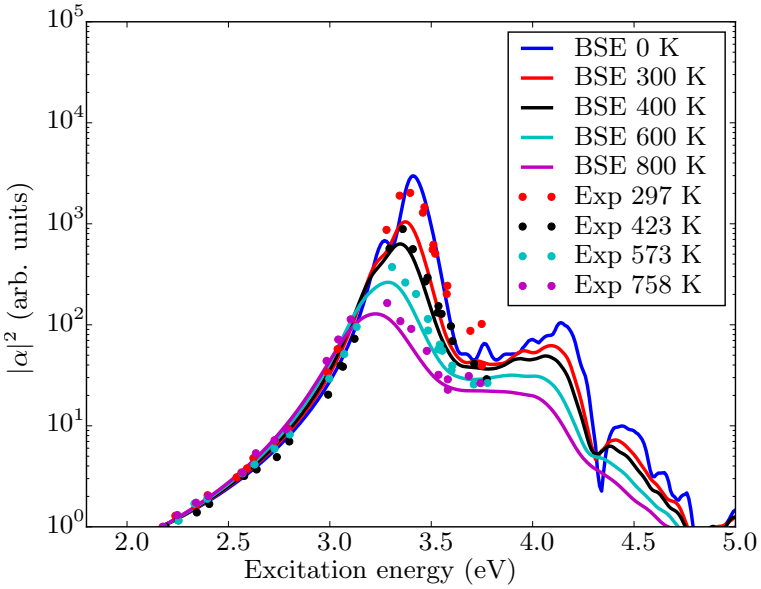

Figure 48: Temperature and wavelength-dependence of the RI of silicon at five temperatures within the BSE framework and comparison with experimental measurements (Exp) of Ref. [104]. The intensities are normalized with the experimental measurement available at 2.2 eV.

5.4 CONCLUSIONS

In this chapter, we have used the Allen-Heine Cardona theory to describe from first principles the temperature-dependent effects due to electron-phonon coupling. We have started from temperature-dependent

band structures and then moved to optical properties in the IPA and the BSE formalisms. Finally, we have established a connection between the formalism developed in Chap. 3 and in the previous sections to calculate temperature-dependent frequency-dependent Raman spectra for silicon and we obtain a good agreement with experimental measurements.

6

CHARACTERIZATION OF $BiFeO_3$ FROM RAMAN SPECTROSCOPY: LASER FREQUENCY AND TEMPERATURE EFFECTS

6.1 $BiFeO_3$, A REFERENCE MULTIFERROIC MATERIAL

Multiferroic materials (i.e. materials possessing more than one ferroic order) represent an important field of research in condensed matter physics. They allow for combined (anti)ferro-magnetism, (anti)ferro-electricity and ferro-elasticity [177–179]. One noticeable example is $BiFeO_3$ (BFO), which is anti-ferromagnetic, ferroelastic and ferroelectric at room temperature. The interaction of multiferroic materials with light has been the subject of intensive research. The coupling of the ferroelectricity with photosensitive properties is called "photoferroelectricity". Most of the recent work in this field has focused on perovskites ABO_3, and in particular on BFO for its above-bandgap photovoltages [180], tip-enhanced photovoltaic effects [181] and the important role of domain walls in the photovoltaic properties [182, 183]. BFO also shows a noticeable temperature dependence of the gap that shrinks from around 2.7 eV [184–188] at ambient temperature to 1.3 eV at 1200 K [189].

Even if the structural parameters of BFO have been known for a long time (see e.g. Ref. [190, 191]), the first-principles simulations of this material are quite recent. Wang's pioneering studies [192, 193] were followed by those of Ederer [194, 195] and Neaton *et al.* [196]. These studies reproduced experimental lattice parameters, band structures and spontaneous polarizations using the LDA+U methodology. Experimental measurements of Raman features of BFO have been performed starting from the work of Haumont [197] in bulk material and Singh [198] for thin films, which have been followed by other experimental studies of the phonon properties [199–204]. From a theoretical point of view, the work of Hermet [205] reported zone-center phonon frequencies and Raman intensities and has been followed by others to advance the lattice dynamics picture [206–211].

In this chapter, we want to pursue this large effort and further analyze lattice dynamics and Raman intensities of BFO in resonance conditions. In particular, in Sec. 6.2, we start by presenting the recent frequency-

dependent and temperature-dependent Raman measurements published in Ref. [212], that we would like to understand thanks to the techniques described in this thesis. However, the proper interpretation of the results requires to be extremely careful in view of the dependence on the sample orientation, dependence with respect to temperature and wavelength of the laser light. In this chapter, we therefore lead a complete study from first principles of the material, starting from the lattice parameters and the band structure in Sec. 6.3, and moving through the phonon characterization in Sec. 6.4. We finally compute Raman intensities in Sec. 6.5 and study temperature dependence of the band structure in Sec. 6.6 and Sec. 6.7.

6.2 EXPERIMENTAL MEASUREMENTS

In a recent experimental work lead by M. Weber in collaboration with us [212], we have employed Raman scattering spectroscopy techniques to characterize the light-material interaction in BFO. The inelastic scattering of the photons impinging on the material, indeed, provides useful information about the coupling between light, electrons and vibrations. In particular, resonance Raman scattering reveals strong changes in the spectrum when the energy of the photon matches one of the excitation energies of the material. In the case of BFO, the measurements revealed two interesting aspects: strong Raman changes when varying the light frequency and a surprising completely different picture for first and second-order Raman scattering when varying the temperature. These experimental findings raise several questions concerning the coupling of the different Raman modes with light as well as the temperature dependence of the electronic band structure. The content of this section has been published as Ref. [212].

In a first step, we have investigated BFO single crystals oriented along the [001] pseudocubic direction (see Sec. 6.3 for more details about the structure) at room temperature with twelve different excitation wavelengths ranging from 442 nm to 785 nm.

Great care was taken in order to exclude any spurious effect related to crystal orientation, laser polarization, or oblique modes [213], i.e., the orientation of the analyzed domain with respect to the direction of propagation, and polarization of the laser was carefully checked in all cases. Fig. 49 (a) shows the normalized Raman spectra, which are well defined with sharp bands, especially at lower wave numbers, and with Raman frequencies in agreement with reported literature data (typically mea-

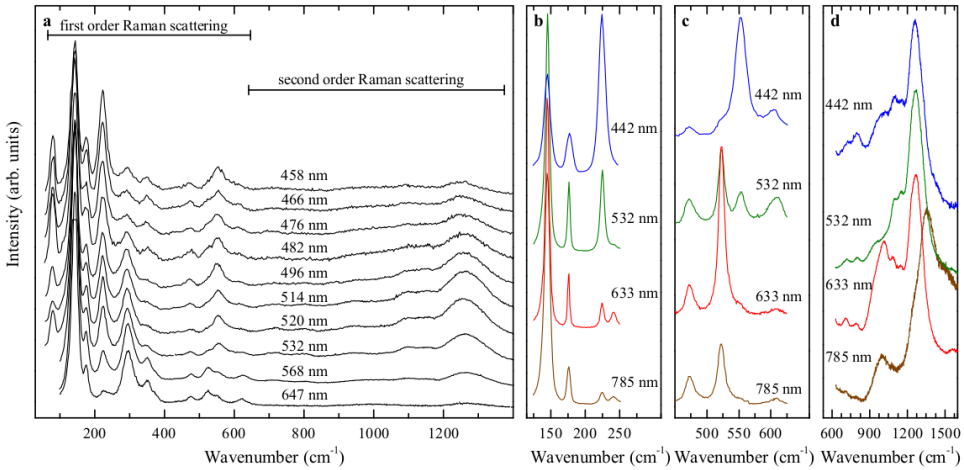

Figure 49: a) Raman spectra of BFO for different excitation wavelengths ranging from 458 nm to 647 nm. b) and c) Zoom into two low- and high-wavenumber regions. d) Second order Raman spectra for several excitation wavelengths at ambient condition.

sured with red or green exciting lasers) [199, 201, 204, 213]. The most prominent feature of the spectra is that the relative intensity of the different Raman bands greatly depends on the wavelength used. Fig. 49 (b) and (c) make this more apparent by magnification of two narrow spectral regions: for example, the band at 230 cm^{-1} is very strong at 442 nm but hardly observable at 785 nm; similar changes are observed for almost all modes when carefully considering the full series. The intensity of the second-order Raman spectrum, visible as broad bands in the 1000-1400 cm^{-1} range [see Fig. 49 (d)], also depends on the exciting wavelength in agreement with previous reports [202].

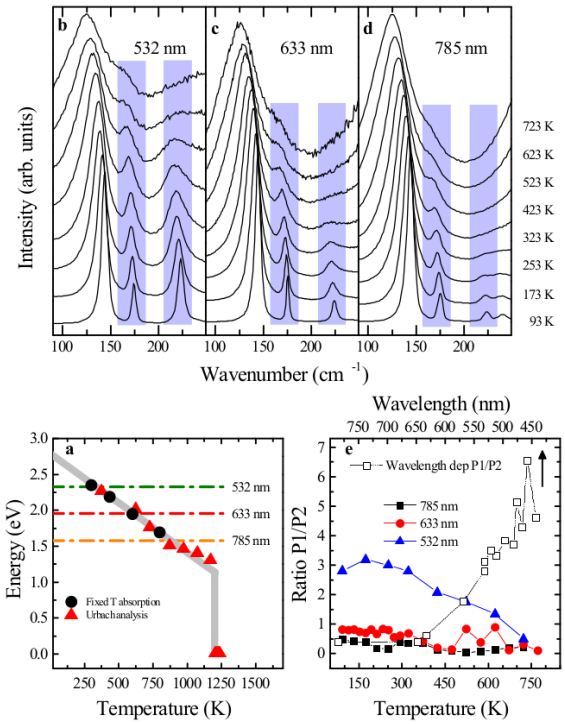

Figure 50: (a) Band gap values of BFO versus temperature taken from Ref. [189], together with the energies of the 532 nm, 633 nm and 785 nm laser lines. (b)-(d) Temperature-dependent Raman spectra in the low-frequency region for the 532 nm, 633 nm and 785 nm laser lines. The regions in blue highlight two bands that show a significant change in their intensity ratio when crossing resonance (see Fig. 49 (b)). (e) Evolution of the intensity ratio of the highlighted bands with temperature, compared to the evolution with excitation energy at ambient temperature.

Because changes of the band gaps imply changes in the Raman resonance conditions, as already mentioned in Chap. 5, resonant Raman spectroscopy can now be used to track its temperature evolution, with the objective to elucidate the intriguing shrinking of the optical gap at high temperatures. This principle is illustrated in Fig. 50 (a), where the band gap values determined by Palai et al. [189] are displayed together with the energies of three selected laser lines used in this study. Strong changes in the resonance conditions are expected when the laser energy is close to the reported band gap, which should be reflected in the intensity and the shape of the Raman signature.

Figs. 50(b)-(d) shows the low-frequency part of the first-order Raman spectra for temperatures ranging from 93 K to 773 K and for laser excitation wavelengths 532 nm, 633 nm, and 785 nm, i.e., for energies that coincide with the reported band gap at different temperatures. In all cases, the temperature evolution of the Raman spectra follows a typical behavior characterized by thermal broadening and a generalized low-frequency shift of all bands with increasing temperature. The intensity ratios between modes do not change significantly compared to the intensity ratio changes observed for different excitation wavelengths (see Fig. 49). This is quantified in Fig. 50(e) that shows the evolution of the intensity ratio for the two highlighted vibrational bands as an example. This ratio does not show any sign of the dramatic increase that characterizes the resonant regime that would be expected at high temperatures when the laser energy meets the reported optical band gap. This leads to the at first sight surprising conclusion that the resonance conditions at a given wavelength do not change with temperature. Considering that only direct electronic transitions can be involved in first-order Raman resonances, we come to the following conclusions: (i) the temperature evolution of the optical band gap cannot be related to a shrinking of a direct electronic band gap and (ii) the electronic levels underlying the resonance Raman effect under illumination with 442 nm (assigned to direct electronic transitions) and 532 nm (oxygen vacancies) are nearly temperature independent.

After the first-order part, we have scrutinized the second-order Raman spectra. Figs. 51 (a) and 51 (b) present the temperature evolution of the second-order Raman spectra for excitation of 532 nm and 633 nm. The figures show a strong qualitative change in the intensity signature, which is particularly apparent when comparing the relative intensities of the broad peaks at 1010 and 1260 cm^{-1} under excitation by the 633 nm laser line. The band at 1010 cm^{-1} is strongly reduced at higher temperatures and the shape of the spectrum gradually becomes similar to the spectrum obtained for 532 nm laser at ambient temperature, albeit with differences due to different thermal broadenings. Conversely, the 532 nm laser line spectra at low temperature revealed a small but distinct band at 1010 cm^{-1} [indicated by the arrow in Figs. 51 (a) and 51 (b)]. These qualitative changes were accompanied by a change in the overall intensity, which we quantify by the ratio between the integrated intensity (I_2) of the second-order spectrum divided by the intensity of the first-order spectrum (I_1). For both excitation wavelengths, I_2/I_1 exhibited a maximum in their temperature dependence. The observed maxima at

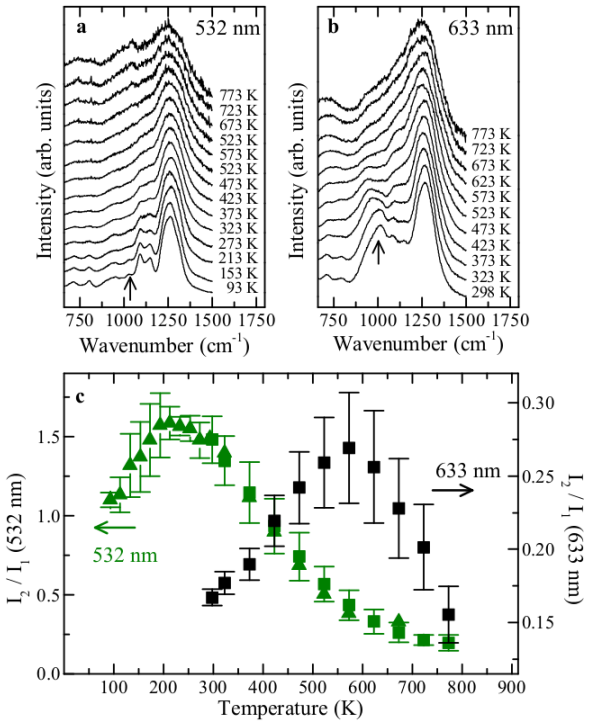

Figure 51: (a) and (b) Temperature-dependent second-order Raman spectra of BFO under excitation of 633 nm and 532 nm laser light. c) Temperature-dependent ratio of the integrated intensities of the second (I_2) to first order (I_1) Raman scattering spectra.

573 K for 633 nm and at 223 K for 532 nm follows the temperature dependence of the reported optical band gap [189]. These changes in shape and intensity of the second-order Raman signature contrasts with the temperature-independent shape of the first-order spectrum. Because any strong change in the energies of direct electronic transitions was ruled out, the observed maxima of the ratio I_2/I_1 can be related to a temperature evolution of the indirect gap.

Putting together our experimental observations therefore leads to the conclusion that the shrinking of the optical band gap is related to a temperature evolution of an electronic band gap with indirect character. This supports the view that BFO is an indirect semiconductor, at least above room temperature. On the other hand, the energies of direct electronic transitions show no temperature dependence, which implies in turn nontrivial temperature modifications of the electronic band struc-

ture. Even though only hypotheses can be formulated at this stage for the details of this temperature dependence, we note that the hypothesis of a strong electron-phonon coupling inducing an important renormalization of the electronic levels is consistent with the fact that the highest valence band originates predominantly from the oxygen p states. The low relative mass of the oxygen atom then leads naturally to comparatively large nuclear displacements in the corresponding phonon modes, and hence the largest temperature dependence of the bands with strong oxygen character. Starting from valence and conduction bands considered as nearly flat [189, 214], an increased curvature of the bands at high temperature can explain the different behavior of the direct and indirect gaps. Further work will be needed in order to confirm this picture, including both calculations at finite temperatures and experiments to follow carefully the optical absorption with temperature and probe directly electronic levels. More generally, resonant Raman scattering appears as a powerful tool to follow electronic excitations up to relatively high temperatures, in a way that should be applicable beyond BFO to a broad range of materials showing absorption in the visible range, and thereby to contribute to the understanding of electronic structures in photoferroelectrics.

In view of these experimental results, we want to use the tools we have presented in the first chapters and apply them to the case of BFO. In particular, the strong changes of RI with respect to laser frequencies may be analyzed with the FP technique presented in Chap. 3. We also want to analyze the temperature dependence of the band structure with the help of theory developed in Chap. 5. The next sections detail these theoretical studies.

6.3 GROUND STATE PROPERTIES

The R3c phase of BFO is obtained by combining two pseudo-cubic cells and tilting the oxygen octahedra.

In Fig. 52, the rhombohedral and the pseudo-cubic cells are shown as well as the polar axis [111]. In practice, the rhombohedral unit cell has been used with the polar axis along the z-Cartesian direction. The cell is defined with the angle α and the length of the rhombohedral axes a. The internal degrees of freedom are the distances between Fe and Bi, and the position of one oxygen atom. In all the simulations, BFO is enforced to stay in the G-type anti-ferromagnetic configuration.

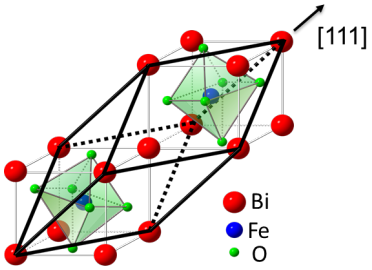

Figure 52: Crystal structure of BFO, showing the rhombohedral unit cell (thick black lines) and the pseudo-cubic cell (thin gray lines) [215]

At the ground state level, calculations have been performed using pseudopotentials generated by P. Hermet [205] (called NC pseudopotentials in this chapter) and also JTH PAW pseudopotentials [216] (called PAW pseudopotentials in this chapter) to be able to include correlation effects within the LDA+U method. Indeed, for materials with rare-earth atoms or transition metals, such as Fe, the LDA functional tends to delocalize the electrons and cannot reproduce the interactions between the localized 3d electrons correctly. Adding a on-site Hubbard-like term on those orbitals (the U term) improves the description of the on-site Coulomb repulsion for localized states [217]. As for norm-conserving pseudopotentials, LDA+U is not implemented in ABINIT, we use the PAW approach (called LDA+U/PAW), based on the method described in Ref. [218]. In this study, the influence of the U strength on the band structure and on the phonon properties is analyzed. For that purpose, values of $U_{eff} = U - J$ =0, 2, 3, 3.8 and 5 eV are chosen for the Fe atoms. In this study, $J = 0.1 \times U$.

For NC pseudopotentials, a cut-off energy of 50 Ha has been used with a $6 \times 6 \times 6$ k-point grid shifted along the $(1/2, 1/2, 1/2)$ direction. For PAW pseudopotentials, a cut-off energy of 35 Ha and of 55 Ha for the double grid have been used with the same $6 \times 6 \times 6$ k-point sampling.

The cell parameters are available in Tab. 7. The values are in good agreement with other simulations [196, 205] and experimental data, with less than 2% discrepancy at $U_{eff} = 3.8$ eV and less than 2.5% without U on the lattice parameters. For the internal degrees of freedom, the relative error is less than 0.5%. For BFO, the hybrid functionals tend to improve the lattice parameter with respect to experiments, as shown in Ref. [208].

	LDA/NC	LDA+U/PAW				
U_{eff}	-	0	2	3	3.8	5
a	5.4955	5.4596	5.5135	5.5238	5.5295	5.5360
α	60.1482	60.2620	59.8306	59.7501	59.7104	59.6708
z_{Fe}	0.2310	0.2300	0.2268	0.2260	0.2255	0.2249
x_O	0.5415	0.5409	0.5397	0.5396	0.5396	0.5397
y_O	0.9457	0.9419	0.9402	0.9401	0.9402	0.9402
z_O	0.3990	0.3973	0.3948	0.3949	0.3951	0.3955

(a)

	LDA+U [196]	Hybrids [208]	Exp. [191]
a	5.52	5.61	5.63
α	59.84	59.37	59.35
z_{Fe}	0.227	0.219	0.221
x_O	0.542	0.511	0.538
y_O	0.943	0.926	0.933
z_O	0.397	0.406	0.395

(b)

Table 7: Unit cell of BFO : lattice parameters, a rhombohedral axis length (Angstrom), α rhombohedral angle (degrees). The Wyckoff positions 2a and 6b are Bi(0,0,0), Fe(z_{Fe}, z_{Fe}, z_{Fe}), and O(x_O, y_O, z_O) in reduced coordinates with respect to rhombohedral axes. (a) Results for LDA/NC and LDA+U/PAW obtained with different values of U_{eff}. (b) Comparison with the theoretical work of Ref. [196] with $U = 4$ eV, the hybrids calculation of Ref. [208] and the experimental measurements of Ref. [191]

As far as the electronic properties are concerned, the inclusion of the U term leads to an opening of the indirect gap from 0.5 eV to 2 eV at $U = 3.8$ eV, as reported in Fig. 53 and in Tab. 8. Consequently, the electronic dielectric function ε^{∞} decreases from 20 to 8. These values are consistent with the calculations of Ref. [209], in which the authors report values of 7.54 and 6.892 for the xx and the zz components of the dielectric tensor respectively, with a value of $U = 6$ eV. The value of U also affects the position of the valence band maximum that is located between Γ and Z for U less than 2 eV and between F and Γ for U larger than 2 eV.

The comparison of the band structure obtained within LDA+U/PAW and with hybrid functionals has been published in Ref. [208]. The band structure is very similar between LDA+U and hybrids apart from the opening of the band gap from around 2 eV in LDA+U ($U_{eff} = 3.8$) to 3 eV for hybrids.

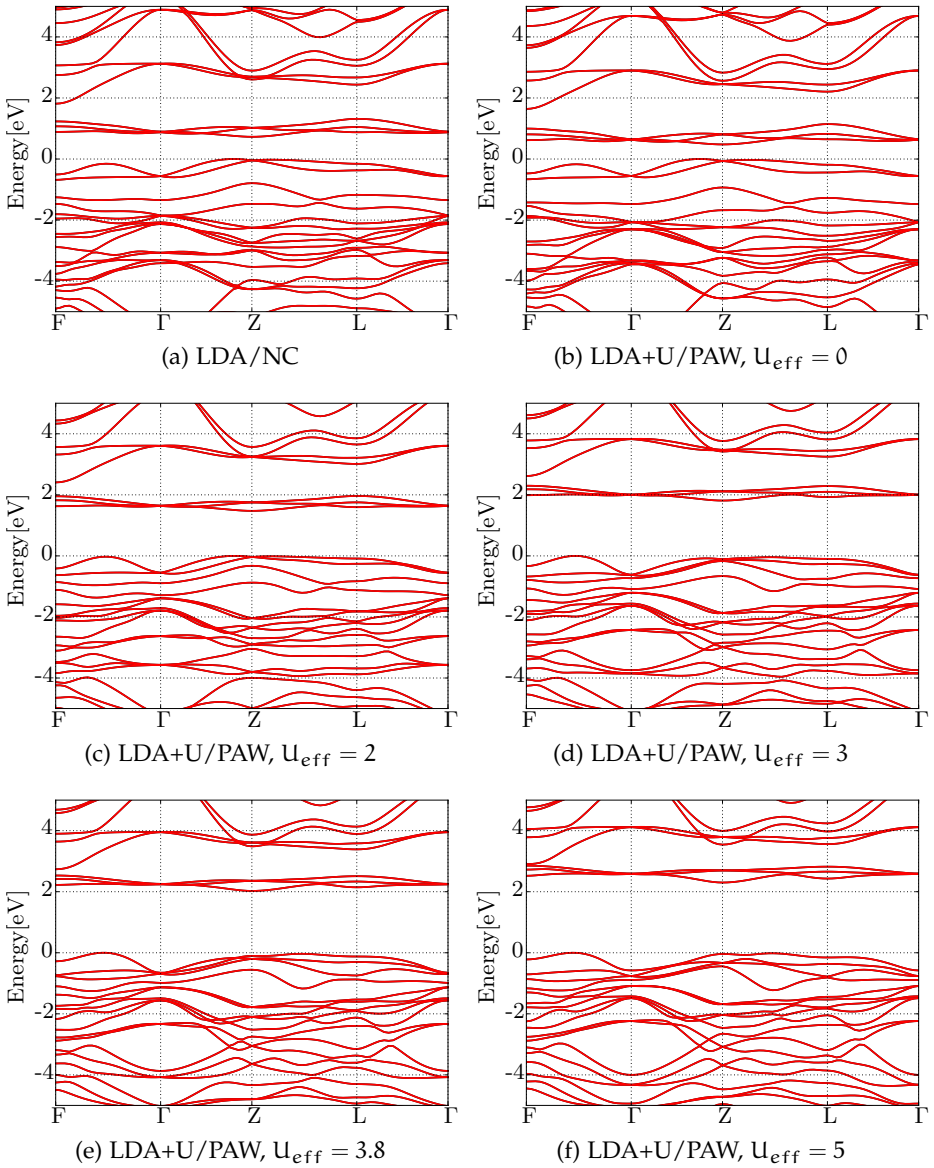

(a) LDA/NC (b) LDA+U/PAW, $U_{eff} = 0$

(c) LDA+U/PAW, $U_{eff} = 2$ (d) LDA+U/PAW, $U_{eff} = 3$

(e) LDA+U/PAW, $U_{eff} = 3.8$ (f) LDA+U/PAW, $U_{eff} = 5$

Figure 53: Electronic band structure of BFO obtained using the LDA/NC and LDA+U/PAW formalisms.

	LDA/NC	**LDA+U/PAW**				
U_{eff}	-	0	2	3	3.8	5
E_g (eV)	0.75	0.48	1.48	1.81	2.02	2.30
$\epsilon^{\infty}_{xx} = \epsilon^{\infty}_{yy}$	15.13	20.42	10.29	9.13	8.54	7.93
ϵ^{∞}_{zz}	12.60	17.23	8.79	7.97	7.56	7.15
$\epsilon^{0}_{xx} = \epsilon^{0}_{yy}$	51.61	58.26	52.04	50.84	49.98	48.89
ϵ^{0}_{zz}	30.22	34.51	28.97	28.79	28.63	28.30
$Z^*_{E(TO1)}$	-2.577	-3.084	-3.855	-4.130	-4.304	-4.505
$Z^*_{E(TO2)}$	-5.500	-5.634	-5.697	-5.645	-5.596	-5.523
$Z^*_{E(TO3)}$	0.875	1.134	2.094	2.746	2.660	2.393
$Z^*_{E(TO4)}$	2.378	2.395	4.885	-1.013	5.832	6.018
$Z^*_{E(TO5)}$	7.991	7.289	6.091	7.214	5.155	4.876
$Z^*_{E(TO6)}$	1.315	2.057	1.108	0.883	0.750	0.592
$Z^*_{E(TO7)}$	0.253	-0.291	0.539	0.520	0.494	0.452
$Z^*_{E(TO8)}$	2.117	2.260	1.761	1.621	1.523	1.403
$Z^*_{E(TO9)}$	3.208	3.248	3.220	3.177	3.147	3.106
$Z^*_{A_1(TO1)}$	-3.809	-4.003	-4.116	-4.231	-4.323	-4.446
$Z^*_{A_1(TO2)}$	3.285	2.976	3.655	3.818	3.868	3.837
$Z^*_{A_1(TO3)}$	6.340	6.248	6.075	5.914	5.804	5.690
$Z^*_{A_1(TO4)}$	2.080	1.895	2.208	2.306	2.365	2.429

Table 8: Comparison of band gaps, dielectric tensors and mode effective charges of BFO for the LDA/NC and LDA+U/PAW with different values of U_{eff}.

6.4 STUDY OF THE LATTICE DYNAMICS

In this system, the 30 phonon modes at $\mathbf{q} = \Gamma$ can be classified as

$$9E(x) \oplus 9E(y) \oplus 4A_1 \oplus 5A_2 \oplus 3 \text{ acoustic.} \tag{185}$$

The phonon eigenvalue problem requires careful inclusion of non-analytic terms, as described in Sec. 3.1. In particular, the non-analytic part of the dynamical matrix introduces some mixing between A_1 and E modes when the wavevector $\mathbf{q}$ of the photon is not along a high symmetry direction.

When the light propagates in the z direction, the A_1 mode is purely longitudinal and the E modes transverse optic. When the light propagates in the xy plane, the E degeneracy is lifted into $E(TO)$ and $E(LO)$. When the light propagates with an angle ϕ with respect to the z-axis, the situation is intermediate, with a mixing of A_1 and one of the E-mode, giving rise to the so-called oblique modes [213].

These effects can be computed easily by changing the $\mathbf{q}$ in the non-analytic term contributing to the dynamical matrix. As already discussed in Sec. 3.1, this term is directly linked with the BEC. The theoretical BEC of BFO are presented in Tab. 9. We observe a good agreement with the results reported in Ref. [196] with values of 4.37, 3.49 and -2.61 for Bi, Fe and O respectively obtained along the z direction in the LDA+U formalism with $U = 2$ eV, while our values are smaller than those obtained with GGA in Ref. [219] and in agreement with Ref. [220] (with a value of $U = 6$ eV). This may be explained if GGA tends to increase the value and U tends to decrease the values.

In all the cases, large deviations from the nominal charges (3, 3 and -2 for Bi, Fe and O respectively) are observed. Moreover, the non-diagonal components of oxygen atoms show covalent bonding between Fe and O. However, the inclusion of U does not have an important effect on the BEC charges of Bi and O, and has an impact of about 10% on the BEC of Fe, on which the U correction is applied.

From these BEC, the mode effective charges can also be computed and are presented in Tab. 8. In these tables, the charges are combined with the phonon displacements. The change in the mode effective charge observed for $U_{eff} = 3$ eV for E(TO3), E(TO4) and E(TO5) can be explained by a mixing of the eigendisplacements of these particular modes. Indeed, Fig. 54a shows the overlaps between the modes obtained within LDA+U/PAW with $U_{eff} = 3$ eV and within LDA/NC. The E(TO4) mode obtained within LDA+U/PAW is composed of a mix of 45%, 35% and 20% of E(TO3), E(TO4) and E(TO5) modes obtained in LDA/NC. A similar picture can be drawn for modes E(TO3) and E(TO5). This explains the non-monotonic trend obtained for these three mode effective charges as U is increased. Once the BEC and the mode effective charges are known, the dependence of the phonon frequencies with respect to the ϕ angle is easily obtained (the numerical results are summarized in Fig. 55).

At the level of the vibrational properties, the inclusion of U has a major effect on the high-frequency modes that increase for example from 546 cm^{-1} to 602 cm^{-1}, improving the agreement with experiments. It also tends to decrease the lowest frequency part at e.g. 100 cm^{-1}. The

	xx	yy	zz	xy	xz	yx	yz	zx	zy
	LDA/NC								
Fe	4.565	4.565	3.432	-0.385	-0.000	0.385	-0.000	-0.000	0.000
Bi	5.134	5.134	4.321	-0.044	0.000	0.044	-0.000	0.000	-0.000
O	-3.147	-3.319	-2.584	-0.260	0.425	-0.531	-0.491	0.342	-0.403
	LDA+U/PAW, $U_{eff} = 0$ **eV**								
Fe	4.434	4.434	3.262	-0.406	-0.000	0.406	-0.000	-0.000	0.000
Bi	5.124	5.124	4.285	-0.075	-0.000	0.075	-0.000	-0.000	0.000
O	-3.185	-3.187	-2.515	-0.231	0.482	-0.590	-0.440	0.370	-0.349
	LDA+U/PAW, $U_{eff} = 2$ **eV**								
Fe	4.362	4.362	3.525	-0.259	-0.000	0.259	-0.000	-0.000	0.000
Bi	5.073	5.073	4.331	0.079	-0.000	-0.079	0.000	-0.000	-0.000
O	-3.043	-3.247	-2.619	-0.261	0.468	-0.485	-0.535	0.433	-0.417
	LDA+U/PAW, $U_{eff} = 3$ **eV**								
Fe	4.241	4.241	3.550	-0.223	-0.000	0.223	-0.000	-0.000	0.000
Bi	5.042	5.042	4.344	0.137	-0.000	-0.137	0.000	-0.000	-0.000
O	-3.015	-3.174	-2.631	-0.238	0.469	-0.450	-0.535	0.449	-0.412
	LDA+U/PAW, $U_{eff} = 3.8$ **eV**								
Fe	4.142	4.142	3.545	-0.206	0.000	0.206	0.000	-0.000	0.000
Bi	5.021	5.021	4.352	0.177	0.000	-0.177	-0.000	-0.000	-0.000
O	-2.999	-3.110	-2.632	-0.218	0.472	-0.427	-0.525	0.462	-0.399
	LDA+U/PAW, $U_{eff} = 5$ **eV**								
Fe	4.002	4.002	3.513	-0.193	-0.000	0.193	-0.000	-0.000	0.000
Bi	4.994	4.994	4.363	0.228	-0.000	-0.228	0.000	-0.000	-0.000
O	-2.981	-3.017	-2.625	-0.189	0.480	-0.397	-0.503	0.480	-0.375

Table 9: Cartesian components of the BEC of BFO for LDA/NC and LDA+U/PAW calculations with different values of U_{eff} parameters.

phonon dispersion obtained with different values of U_{eff} is presented in Fig. 56. A comparison of the TO and LO frequencies is presented in Tab. 10 along with calculations performed with hybrids functionals in Ref. [208] and experimental measurements of Ref. [213]. We observe that the hybrid calculations overestimate the phonon frequencies and do not improve much the LDA+U results at the level of phonon frequencies. In

complement, the value of oblique modes for a light polarization aligned along a pseudocubic axis are presented in Tab. 11 along with a comparison with the frequencies extracted from the measurements presented in Sec. 6.2 and Ref. [212]. In these tables, we observe a general improvement of the phonon frequencies as U is included in the calculations, even for LO frequencies and oblique modes.

The inclusion of U also changes the relative order of the phonon modes, as can be seen in Fig. 54b, where we show the overlaps between the modes computed with LDA/NC and with LDA+U/PAW with $U_{eff} = 3.8$ eV. Changes in the order of the phonon frequencies occur in the region between 200 and 300 cm^{-1}, the region in which mixing of the modes is also present. All the other modes show almost 100% overlap between LDA+U/PAW and LDA/NC. As a conclusion, the introduction of U at the level of phonons mainly modifies the phonon frequencies and changes the displacements of the modes with frequencies between 200 and 300 cm^{-1}.

As an additional analysis, we compare the decomposition of the eigendisplacements with respect to the three atomic types in the unit cells. The decomposition of the TO modes obtained with LDA/NC and LDA+U/PAW is presented in Fig. 57. As already observed previously, most of the changes appear for frequencies between 200 and 300 cm^{-1}. This behavior is somehow expected because these modes mainly consist of vibrations of Fe and O.

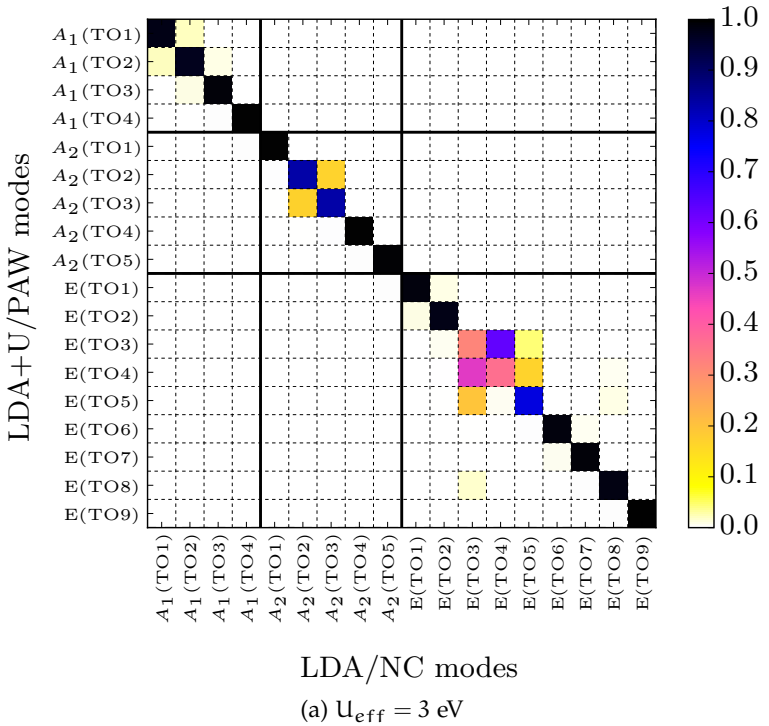

(a) $U_{eff} = 3$ eV

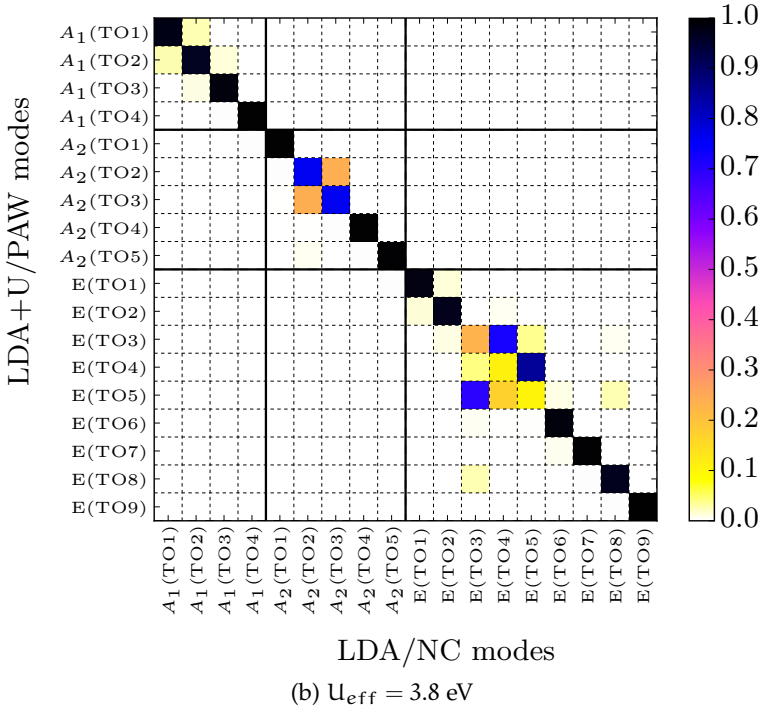

(b) $U_{eff} = 3.8$ eV

Figure 54: Overlaps between the phonon eigenvectors of BFO obtained with LDA/NC and with LDA+U/PAW. (a) $U_{eff} = 3$ eV and (b) $U_{eff} = 3.8$ eV.

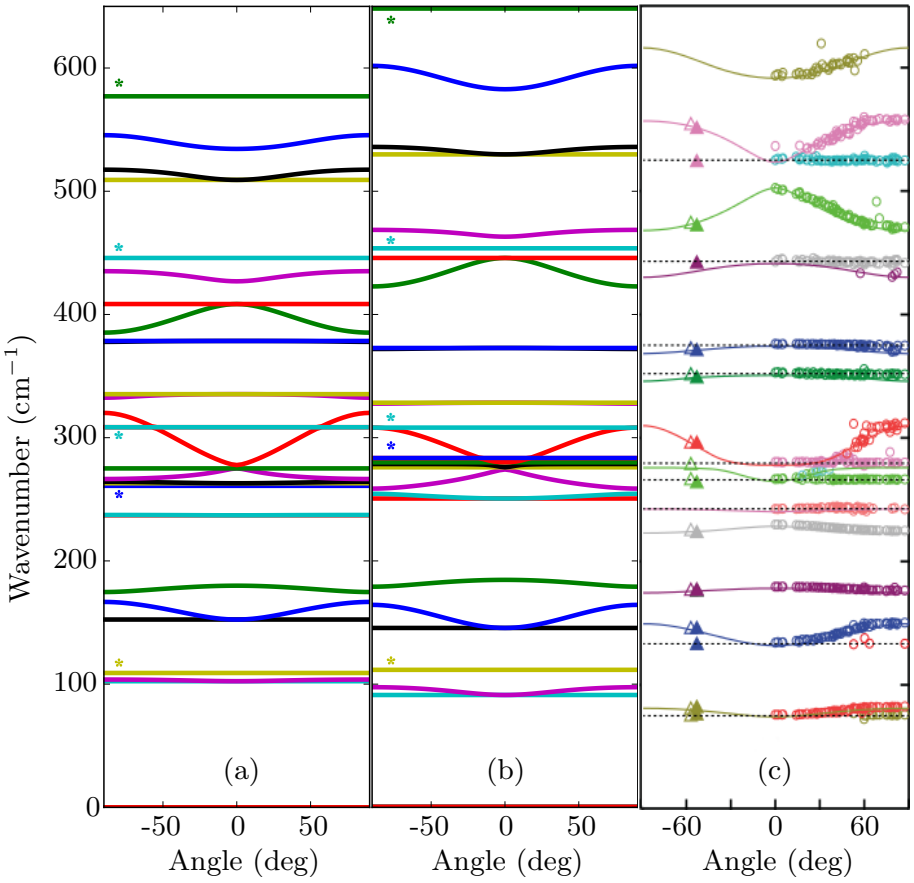

Figure 55: Comparison of the phonon frequencies of BFO at $\mathbf{q} \to 0$ with respect to the q-direction with (a) LDA/NC, (b) LDA+U/PAW with $U_{eff} = 3.8$ eV, and (c) Raman experimental measurements of Ref. [213]. The A_2 modes (denoted by *) are represented in (a) and (b) but have no experimental counterpart since they are not Raman active.

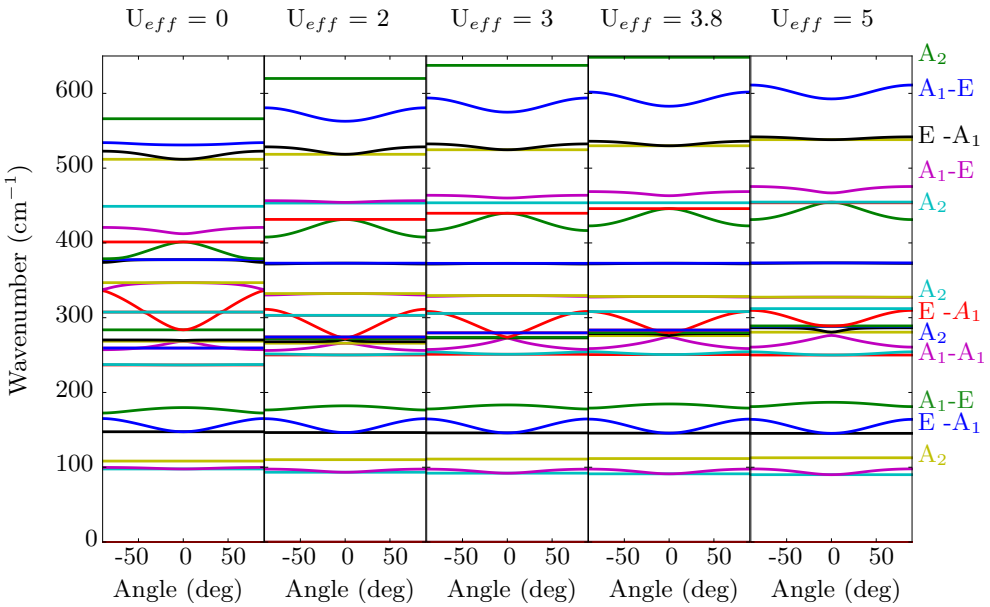

Figure 56: Comparison of the phonon frequencies of BFO at $\mathbf{q} \to 0$ with respect to the q-direction for different values of U_{eff} (in eV). The symmetry of the modes is indicated when $U_{eff} = 5$ eV: the labels on the right indicate either $X - Y$ if the symmetry is X at $\phi = 0°$ and Y at $\phi = 90°$, or A_2 modes (with no dispersion). All the other modes are E-E for oblique modes or E(TO) for TO modes (no dispersion).

Symmetry	LDA/NC	LDA+U/PAW	Hybrids [208]	Exp [213]
E(TO1)	102	91	79	74
E(TO2)	152	146	150	132
E(TO3)	237	251	256	240
E(TO4)	263	276	279	265
E(TO5)	275	280	289	278
E(TO6)	335	328	363	351
E(TO7)	379	373	394	374
E(TO8)	408	446	480	441
E(TO9)	509	530	549	523
E(LO1)	104	98	-	81
E(LO2)	175	179	-	175
E(LO3)	237	255	-	242
E(LO4)	264	279	-	276
E(LO5)	332	328	-	346
E(LO6)	378	372	-	368
E(LO7)	385	423	-	430
E(LO8)	435	469	-	468
E(LO9)	546	602	-	616
A_1(TO1)	167	164	171	149
A_1(TO2)	266	259	217	223
A_1(TO3)	320	308	343	310
A_1(TO4)	517	536	603	557
A_1(LO1)	180	185	-	178
A_1(LO2)	278	274	-	229
A_1(LO3)	427	463	-	502
A_1(LO4)	534	583	-	591
A_2(TO1)	109	111	124	-
A_2(TO2)	260	283	277	-
A_2(TO3)	308	308	309	-
A_2(TO4)	445	453	485	-
A_2(TO5)	577	648	709	-

Table 10: Comparison of pure LO and TO mode frequencies (in cm^{-1}) of BFO in LDA/NC and LDA+U/PAW, theoretical values obtained with hybrid functionals in Ref. [208] and experimental measurements in Ref. [213].

LDA/NC	**LDA+U/PAW**	Weber [212]	Dispersion path
102	91	75	E(TO1)
103	96	80	E(TO1)-E(LO1)
152	146	136	E(TO2)
162	158	145	E(TO2)-A_1(TO1)
177	182	175	A_1(LO1)-E(LO2)
267	262	225	A_1(LO2)-A_1(TO2) (†)
237	251	241	E(TO3)
237	253	241	E(TO3)-E(LO3)
263	276	265	E(TO4)
264	279	278	E(TO4)-E(LO4)
275	280	278	E(TO5)
308	300	295	E(TO5)-A_1(TO3) (†)
334	328	350	E(TO6)-E(LO5)
335	328	350	E(TO6)
378	372	373	E(TO7)-E(LO6)
379	373	373	E(TO7)
392	429	435	E(TO8)-E(LO7)
408	446	441 (*)	E(TO8)
434	468	473	A_1(LO3)-E(LO8)
509	530	523	E(TO9)
516	535	542	E(TO9)-A_1(TO4)
541	596	609	A_1(LO4)-E(LO9)

Table 11: Comparison of the Raman-active phonons frequencies of BFO for $6 \times 6 \times 6$ k-point mesh with the wavevector $\mathbf{q}$ aligned along a pseudo-cubic direction. The dispersion path indicates whether it is a pure E(TO) mode, or the symmetry of pure LO and TO frequencies the mode is linked to (see Fig. 55 and 56). The phonons are ordered with respect to experimental measurements. LDA/NC and LDA+U/PAW values are assigned based on the experimental dispersion of Ref. [213]. (*) The mode at 441 cm^{-1} in Ref. [213] has a very weak intensity in Ref. [212]. (†) In LDA/NC, the 267 cm^{-1} mode comes from E(TO5)-A_1(TO2) while the 308 cm^{-1} mode comes from A_1(LO2)-A_1(TO3).

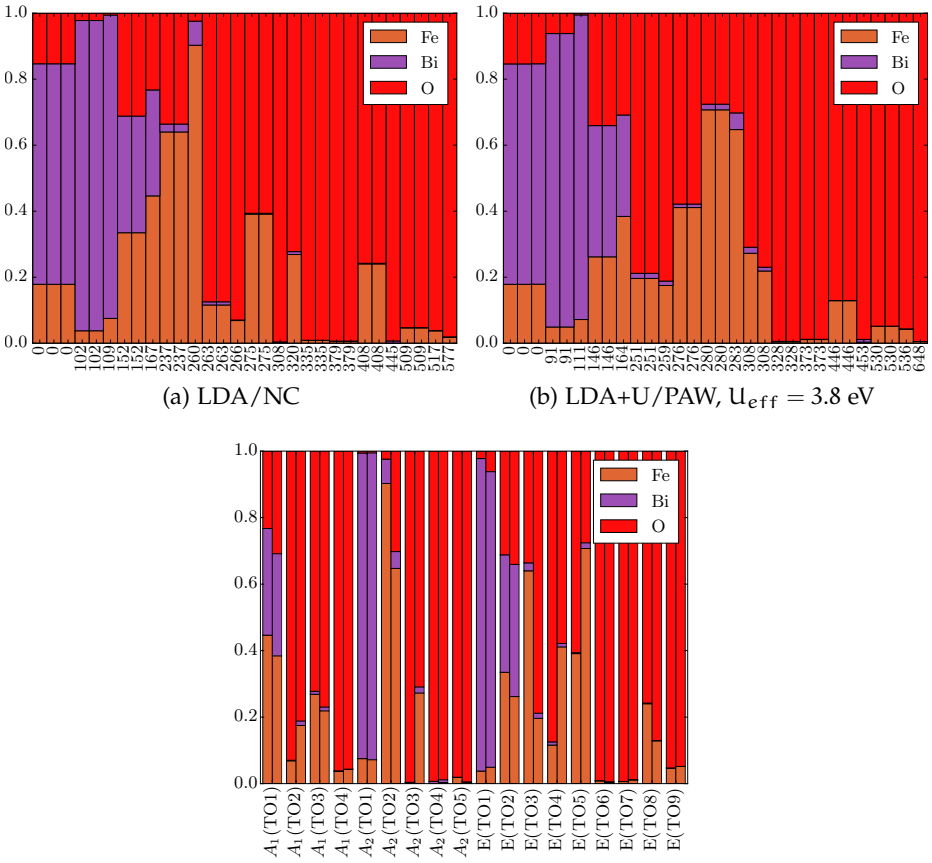

(a) LDA/NC

(b) LDA+U/PAW, $U_{eff} = 3.8$ eV

(c) Comparison between LDA/NC and LDA+U/PAW

Figure 57: Decomposition of the eigenvectors of BFO on the three atom types with LDA/NC (a) and LDA+U/PAW with $U_{eff} = 3.8$ eV (b). (c): For each mode (sorted by symmetry), comparison of the decompositions with LDA/NC (left) and with LDA+U/PAW (right).

We can also observe that the dispersion obtained for the branch associated to the $A_1(LO_3)$ mode lying around 460 cm^{-1} differs from the one observed experimentally (see Fig. 55). Starting from the LDA+U result, we now try to clarify the role played by the BEC in this dispersion. The objective is first pursued by increasing the absolute value of BEC for the O and Fe atoms on the diagonal of the matrix. Alternatively, it is possible to increase the maximum eigenvalue of O atoms and then recompute the different contributions so that the charge neutrality sum rule is fulfilled. The different dispersions are compared in Fig. 58. These tests reveal that the dispersion of the A_1 mode corresponds directly to the charge trans-

fer between oxygen and iron, that is not perfectly reproduced in LDA nor in LDA+U. This might be due to the inability of LDA+U to give accurate BEC of oxygen atoms.

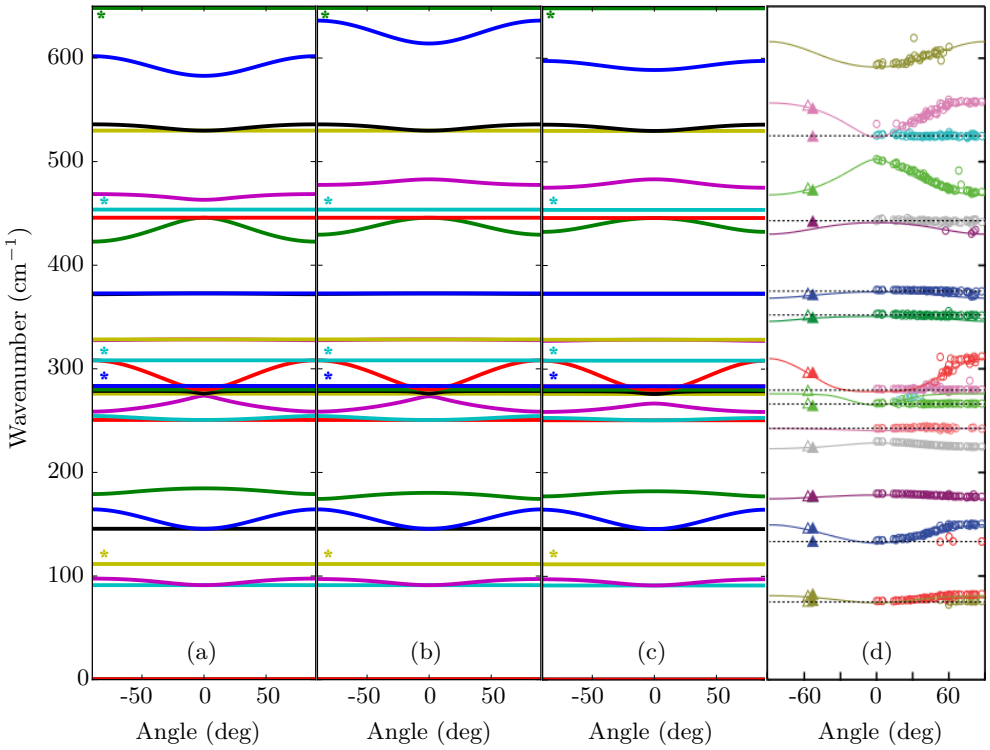

Figure 58: Phonon frequencies of BFO at $\mathbf{q} \to 0$ with respect to the q-direction obtained by modifying the BEC of O and Fe atoms by hand. (a) LDA+U/PAW without modification. (b) Transfer of 1/3 charge units from each O to Fe atoms on the diagonal. (c) Transfer of 1 charge units from the lowest eigenvalue of each O to all the atoms by charge neutrality. (d) Experimental measurements [213]. The A_2 modes (denoted by *) are represented in (a), (b), and (c) but have no experimental counterpart since they are not Raman active.

As far as the phonon band structures are concerned, as already computed from Ref. [210], the phonon frequencies agree well with experimental measurements except for the lowest optical E(TO) mode, as shown by our previous comparisons. The phonon band structures are shown in Fig. 59 with the entire range of frequencies. The inclusion of U in the calculations induces an increase of the phonon spread that has already been discussed at the Γ point and also some changes in the crossing of modes around the F modes, in the region of 200-300 cm^{-1}.

Nevertheless, the global shape of the phonon band structure remains almost the same between these two results.

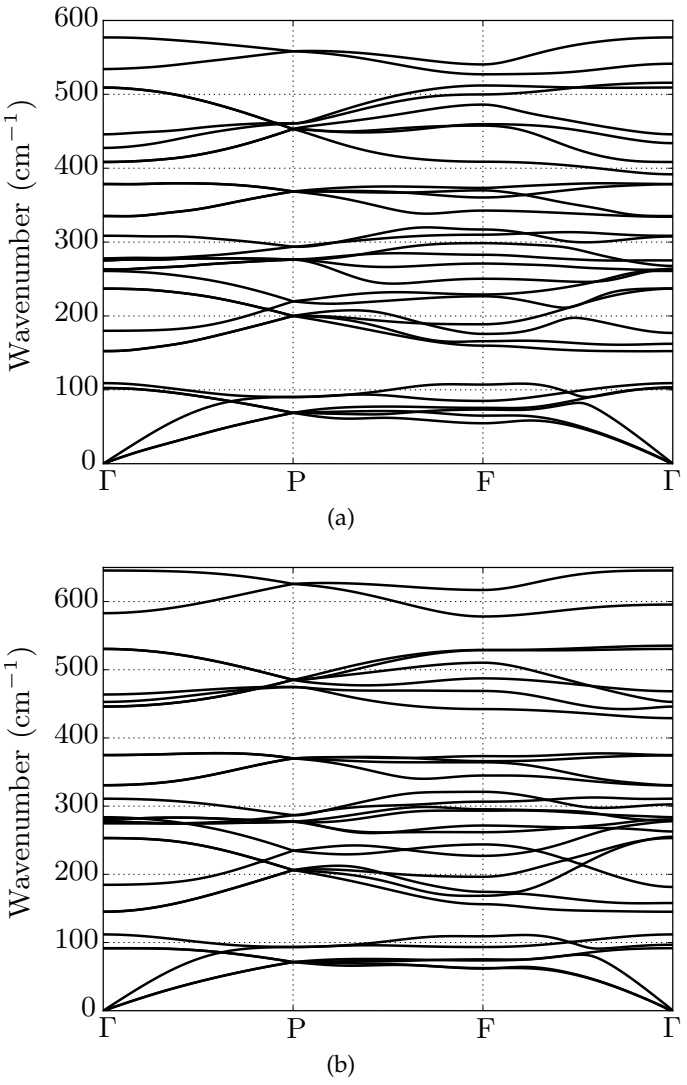

Figure 59: Phonon band structure of BFO obtained with LDA/NC and with LDA+U/PAW ($U_{eff} = 3.8$ eV) along the $\Gamma - P - F - \Gamma$ path, as in Ref. [220].

6.5 RAMAN INTENSITIES

Out of the modes, only E and A_1 are Raman active. Using the previously defined Cartesian axes, the Raman tensors of these modes can be written as

$$E(X) = \begin{pmatrix} c & . & d \\ . & -c & . \\ d & . & . \end{pmatrix}, E(Y) = \begin{pmatrix} . & -c & . \\ -c & . & d \\ . & d & . \end{pmatrix} \tag{186}$$

$$A_1(Z) = \begin{pmatrix} a & . & . \\ . & a & . \\ . & . & b \end{pmatrix}. \tag{187}$$

Along the pseudo-cubic direction in $x-z$ direction, the Raman tensors of the E(TO) and Oblique modes (Obl) become

$$E(TO) = \begin{pmatrix} . & -c & . \\ -c & . & d \\ . & d & . \end{pmatrix}, Obl = \begin{pmatrix} a & . & b \\ . & c & . \\ b & . & d \end{pmatrix}. \tag{188}$$

In order to take into account the direction of propagation of the light, as well as polarization rules, the following general procedure is followed:

1. Diagonalize the dynamical matrix along a particular **q** direction, getting phonon frequencies and eigendisplacements.
2. Compute the derivatives of the dielectric function along Cartesian directions or along axes of the unit cell.
3. Combine the partial derivatives with the LO contribution.
4. Combine the total derivatives with the eigendisplacements to get the Raman tensors.
5. Use polarization vectors to select the correct Raman components.

6.5.1 *Static limit for Raman intensities*

For negligible laser frequencies, the Raman tensor obtained along the Cartesian axis has already been studied by Hermet *et al.* [205]. Only

specific directions were reproduced in this work, that is Z(XY)$\bar{Z}$ and X(ZZ)Y,[1] exhibiting E(TO) and A_1(TO) modes respectively.

In the parallel polarization configuration, i.e. Z(XX)Z, however, A_1 modes are active as well and this gives rise to additional peaks in the spectrum, as shown in Figs. 60 (a) and (c).

From FP calculations of the derivatives on top of LDA+U/PAW DFPT evaluations of the dielectric function, we are also able to produce Raman spectrum in the static regime. The results are shown in Figs. 60 (b) and (d). In the perpendicular configuration, the Raman spectra are very similar to the LDA/NC case apart from the relative intensities of the three last peaks. In the parallel configurations, more changes are observed between LDA/NC and LDA+U/PAW at the level of relative intensities, even if an assignment of the peaks is still possible.

Figs. 60 (e) and (f) compare the Raman spectrum obtained in the parallel polarization for a crystal oriented along the pseudocubic direction. Here, the picture is completely different between LDA/NC and LDA+U/PAW results, in particular low-energy modes are much more Raman intense. Globally, this leads to a much better agreement with off-resonance Raman measurements done at 647 nm reproduced in Fig. 49.

As shown previously, the phonon displacements in the LDA/NC and the LDA+U/PAW formalism are close to each other and therefore the difference between Raman intensities in the two formalisms must come from the derivatives of the dielectric functions where the U parameter plays an important role.

Nevertheless, only the static limit of the Raman intensities are available in this framework. In the next section, we study resonance effects on Raman intensities.

1 In this thesis, the so-called Porto notation is used to describe the experimental setup of Raman scattering: a(bc)d means that the incoming light propagates along a and is polarized along b while the outgoing light propagates along d and is polarized along c.

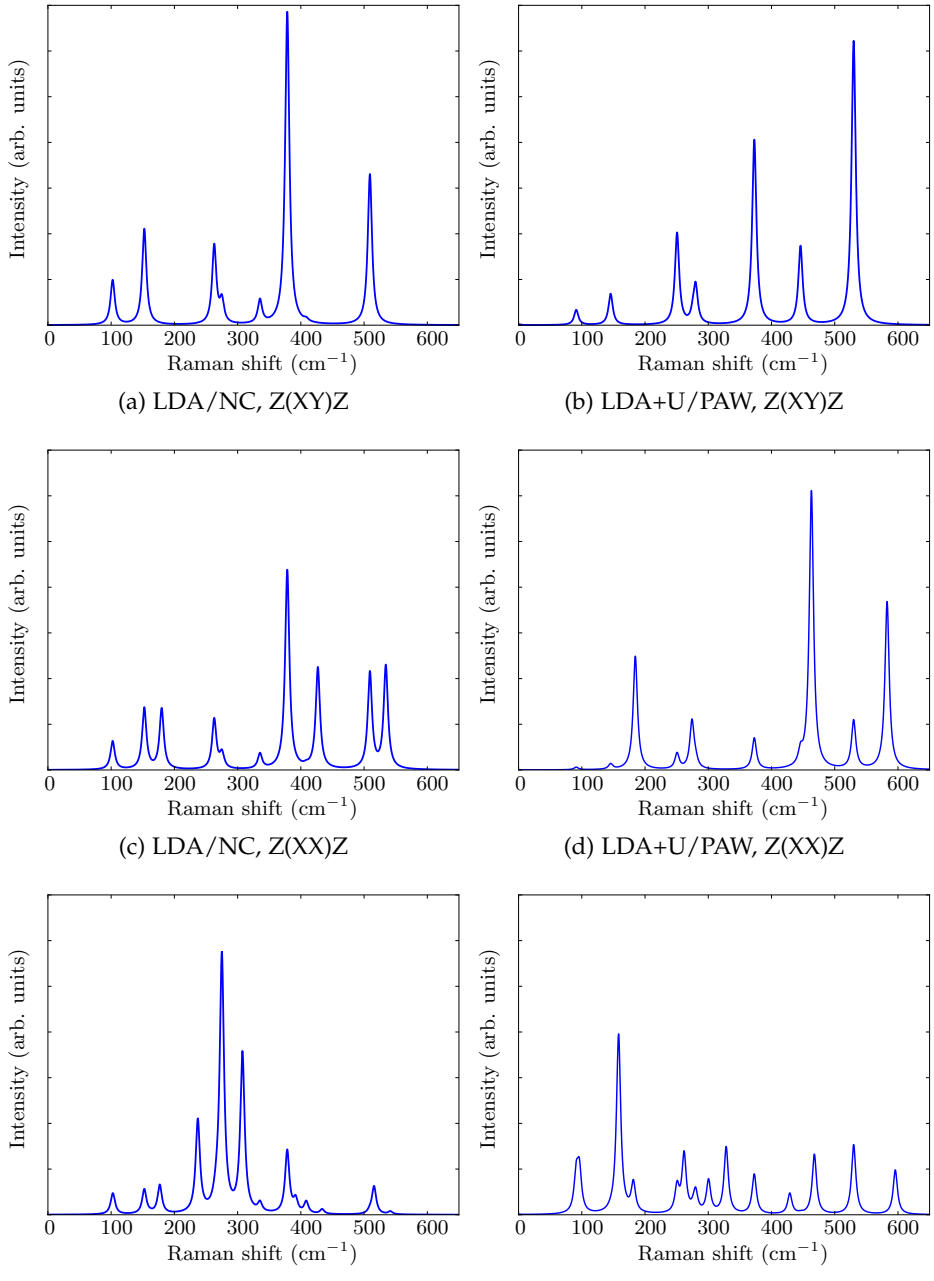

(a) LDA/NC, Z(XY)Z

(b) LDA+U/PAW, Z(XY)Z

(c) LDA/NC, Z(XX)Z

(d) LDA+U/PAW, Z(XX)Z

(e) LDA/NC, pseudocubic

(f) LDA+U/PAW, pseudocubic

Figure 60: Low frequency Raman spectrum of BFO with LDA/NC and LDA+U/PAW (U_{eff} = 3.8eV). (a) and (b): Z(XY)Z polarization. (c) and (d): Z(XX)Z polarization. (e) and (f): Parallel polarization with a crystal oriented along one pseudocubic axis.

6.5.2 *Frequency-dependent Raman intensities*

As already introduced in Sec. 3.2 and in Chap. 4, we use the FP approach to compute TO Raman intensities and then add the LO contributions.

In Fig. 61 and Fig. 62, we show the dependence of the Raman intensity with respect to the laser frequency for the Z(XY)Z and the pseudo-cubic direction. In the former case, no LO modes are active and therefore only pure FP terms contribute.

We observe strong changes of the relative intensities in the spectrum, mainly located in the frequency regions around 250 cm^{-1} and around 400 cm^{-1}. This already shows that resonance effects are drastically important for the BFO material. Whenever LO terms are included, other changes of relative effects appear as well.

These changes of relative intensities occur because the phonon modes influence differently the dielectric function, leading to different resonance profiles for the modes, and therefore changes in the Raman intensities.

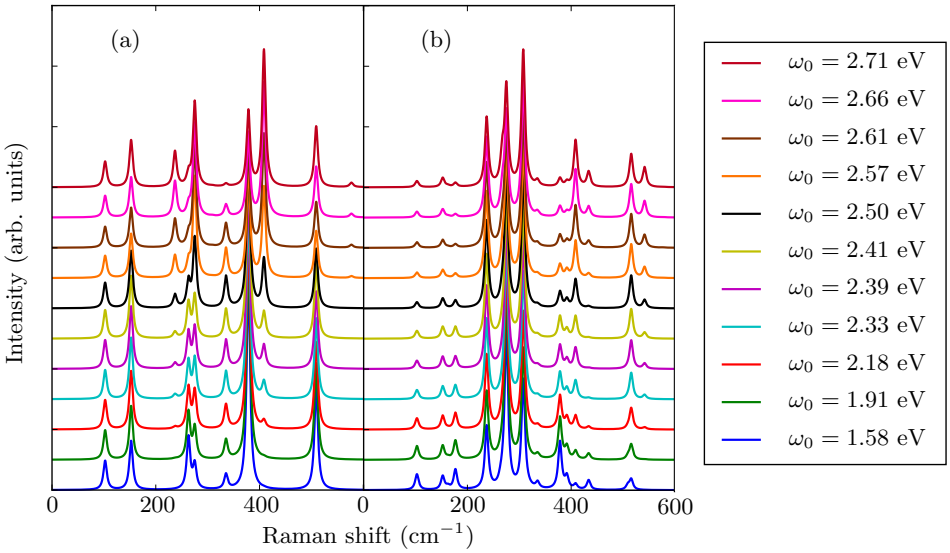

Figure 61: Frequency-dependent Raman intensities of BFO combining intensities computed in IPA and phonons in LDA/NC formalism. (a) Z(XY)Z polarized spectrum and (b) parallel configuration along the pseudocubic direction.

A further analysis of the resonance processes is shown in Fig. 63 in the LDA+U/PAW formalism, where the individual resonance enhancement factor of the modes is shown with respect to the excitation energy. As

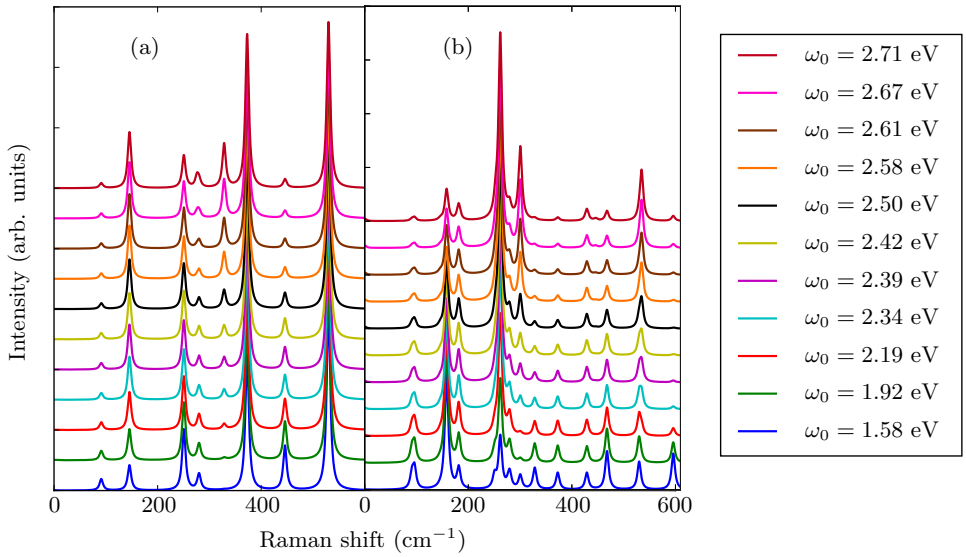

Figure 62: Frequency-dependent Raman intensities of BFO combining derivatives computed in IPA and phonons frequencies in the LDA+U/PAW formalism with $U_{eff} = 3.8$ eV. (a) Z(XY)Z polarized spectrum and (b) parallel configuration along the pseudocubic direction.

observed in Fig. 62, the mode at 146 cm^{-1} increase quicker than the 91 cm^{-1} mode. We also observe that the mode at 328 cm^{-1} increases quicker than the other modes, this is why it appears in our theoretical spectra for higher excitation energies. Some modes also decrease as, for example, the mode located at 446 cm^{-1} that decreases till 2.7 eV, well visible on Fig. 62.

This behavior can be analyzed with the help of eigenvector decompositions on the different atoms: as a very global trend, oxygen-dominated modes tend to increase with frequency, while iron-related modes tend to stay constant or even decrease in intensity till 2.7 eV. After 2.7 eV, the iron-related modes tend to increase much faster, in contrast to pre-resonance regime.

A similar behavior is observed for oblique modes. Some modes increase significantly right at resonance, like 262, 300 and 535 cm^{-1}, while, other modes tend to stay constant in intensity or even decrease, like the 158 and 182 cm^{-1} phonon modes.

Experimentally, the 262 cm^{-1} phonon mode is measured at 225 cm^{-1} and resonates as well. Around 530 cm^{-1}, the theoretical mode does not change much, but the mode at 535 cm^{-1} resonates strongly, that repro-

duces the experimental change of relative intensities in the regime between 523 and 542 cm^{-1}.

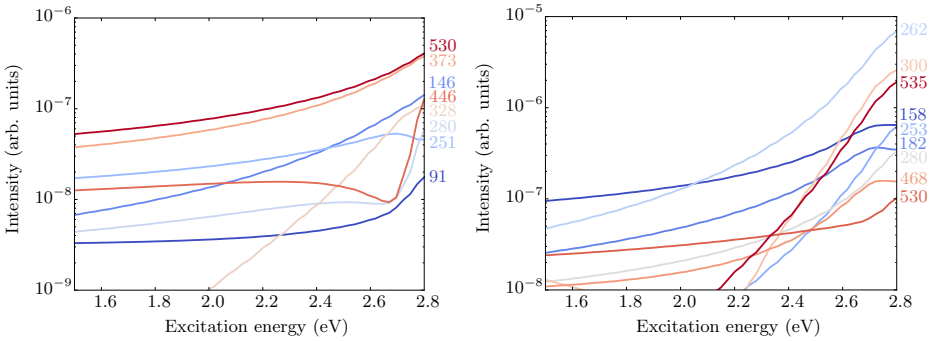

(a) Z(XY)Z (b) pseudocubic direction

Figure 63: Evolution of the intensity (without the $(\omega_L - \omega_0)^4$ prefactor) of the dominating modes in the Z(XY)Z and along the pseudocubic configuration with respect to the excitation energy in LDA+U/PAW with $U_{eff} = 3.8$ eV.

A grid of $8 \times 8 \times 8$ has been used with a $2 \times 2 \times 2$ sub-sampling grid of shifts (see Sec. 3.4 for more details on the methodology) for the TO intensities while the "static" DFPT value obtained with LDA/NC for $\chi^{(2)}$ has been used for LO intensities. Indeed, in ABINIT, the non-linear properties cannot be computed with LDA+U/PAW at present.

In these studies, it is important to note that a scissor shift (0.6 eV for LDA+U/PAW and 2.1 eV for LDA/NC pseudopotentials) has been used to mimic the GW opening of the direct band gap towards the experimental band gap of 2.8 eV. We also assume that this scissor shift as well as the value of the U parameter do not change by displacing the atoms along the phonon displacements. The validation of these assumptions would require computing the GW renormalization with frozen displacements and ab initio values for U, which is beyond the scope of this study.

This completes our discussion of the resonant Raman intensities in BFO. In the next section, we study the renormalization of the electronic band structure due to temperature and electron-phonon coupling.

6.6 TEMPERATURE DEPENDENCE OF THE BAND STRUCTURE

Using the implementation of the formalism presented in Sec. 5.1, we now study the temperature dependence of the band structure of BFO.

The electronic bands are shown in Fig. 64, the width of each band is proportional to the linewidth (inverse of lifetime) introduced by the electron-phonon coupling.

These results are obtained using the non-adiabatic AHC formalism presented in Chap. 5. The ab initio results obtained with $6 \times 6 \times 6$ q-point grids on a set of k-point along symmetrically-equivalent paths have been combined and interpolated using splines to produce the band structures in Fig. 64. Due to a technical limitation of the present implementation, we work with LDA/NC in this section.

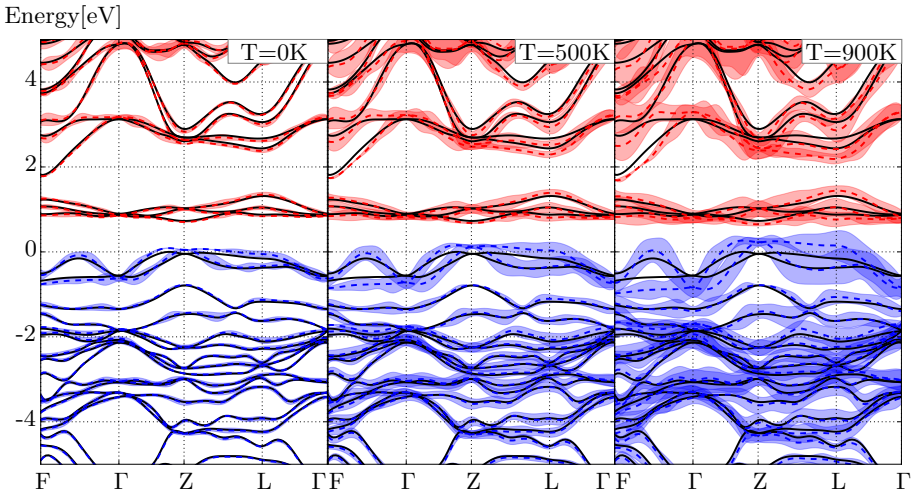

Figure 64: Band structure of BFO with electron-phonon renormalization included at T = 0 K, T = 500 K and T = 900 K. The black lines represent DFT eigenvalues, the dashed lines represent the renormalized eigenenergies and the dashed regions show the linewidth of the electron-phonon renormalization.

A careful analysis of Fig. 64 reveals that the highest occupied bands (mainly formed by oxygen orbitals) are strongly affected by the temperature while Fe-dominated bands show a less pronounced dependence. This effect might be related to the mass of the atoms, the lighter the mass the easier the motion of the atoms and the larger coupling between electronic and nuclei properties.

One should also note that the temperature dependence is highly dispersive, as the $Z - Z$ direct gap tends to reduce with temperature while the $\Gamma - \Gamma$ value tends to increase. This is clearly shown in Fig. 65, while Tab. 12 reports band gap, renormalization and high-temperature coefficients of several gaps. On that figure, one also observes that F^*, the minimum the second group of conduction bands at around 1.8 eV, is

also affected by temperature dependence leading to a big change in the indirect band gap $Z - F^*$ and a very small temperature dependence of the direct gap $F - F^*$.

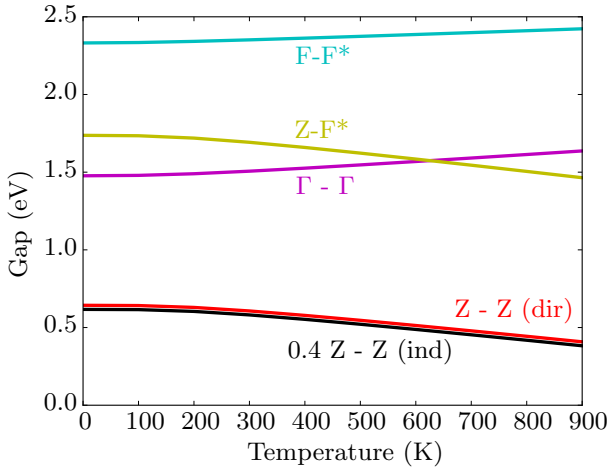

Figure 65: Temperature dependence of different gaps of the BFO band structure: $Z - Z$ (direct gap), $0.4Z - Z$ (indirect gap), $\Gamma - \Gamma$, $F - F^*$ and $Z - F^*$ where F^* refers to the band minimum at F of the second group of conduction bands at around 1.8 eV in Fig. 64.

Gap	DFT (eV)	ZPR (eV)	$dGap/dT_{T\to\infty}$ (meV/K)
$Z - Z$ (dir)	0.760	-0.12	-0.39
$0.4Z - Z$ (ind)	0.728	-0.11	-0.38
$\Gamma - \Gamma$	1.437	0.04	0.22
$Z - F^*$	1.858	-0.12	-0.44
$F - F^*$	2.32	0.01	0.11

Table 12: Value of the BFO DFT band gap, the zero-point motion renormalization and slope of the renormalization with the temperature for the direct band gap at Γ, the fundamental indirect band gap and the direct band gap at $Z - Z$. Note that values for the renormalization are converged with an error of less than 10%.

Although the electron-phonon renormalization of the electronic states will consequently significantly change the ab initio Raman spectra, the theoretical prediction of temperature effects is still in disagreement with experiment at that stage.

Indeed, changes in the direct gap of BFO should lead to changes in the resonant conditions for first-order intensities which are not visible in the

experimental data. There are different possible explanations for the disagreement between theory and experiment. First, the band structure and the electron-phonon matrix elements used here are obtained in the LDA framework and important features of BFO are not captured by this approximation. It is reasonable to expect that these inaccuracies are somehow amplified when we compute the electron-phonon renormalization that is very sensitive to the quality of the input data. Increasing the U parameters indeed reveals a decrease of the distance between the first and the second group of conduction bands. The $Z - F^*$ gap may then become the fundamental indirect band gap of the material as temperature increases, showing different temperature-dependent effects. Second, a complete comprehension of the temperature-dependence of RI of BFO would require the combination of temperature-dependent eigenenergies with optical activities, as proposed in Chap. 5. Several effects are not taken into account in our calculations. A first effect which is not considered in this study is the strong spin-phonon coupling that may induce lattice variations due to magnetic ordering in the sample [221, 222]. As another example, anharmonic effects are neglected is this framework: the dependence of the lattice parameter and the internal degrees of freedom of the $BiFeO_3$ unit cell with temperature may play an important role on the band gap of the material. Indeed, strong changes in the band structure are observed between the R3c structure considered in this thesis and the high temperature cubic phase, stable after 1200 K [189, 223, 224]. The inclusion of such effects could reduce the disagreement between theory and experiment, as discussed in the next section.

6.7 DEPENDENCE OF THE BAND STRUCTURE ON INTERNAL PARAMETERS

In the previous section, we have observed strong electron-phonon renormalization of the band structure. However, this renormalization alone is not able to explain the measured temperature dependence of the gap neither the temperature dependence of the Raman intensities. As a reminder, in Sec. 6.2, we deduced from Raman intensities measurements that the direct transitions are not affected much by temperature. However, the indirect transitions undergo a strong temperature dependence.

In order to assess the importance of changes in the band structure induced by thermal expansion and the motion of the ions in the unit cell, we show, in Fig. 66, the band gaps obtained at the experimental lat-

tice parameters and internal degrees of freedom measured by Fischer *et al.* [225] for different temperatures.

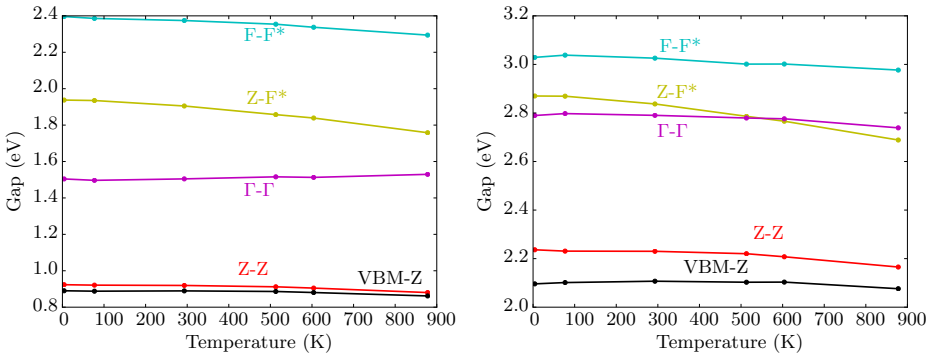

(a) LDA/NC (b) LDA+U/PAW, $U_{eff} = 3.8$ eV

Figure 66: Dependence of the different band gaps of BFO on temperature with experimental lattice parameters and internal coordinates of ions as measured by Ref. [225]. The VBM is 0.4 Z for LDA/NC and 0.5 F for LDA+U/PAW. F* refers to the band minimum at F of the second group of conduction band.

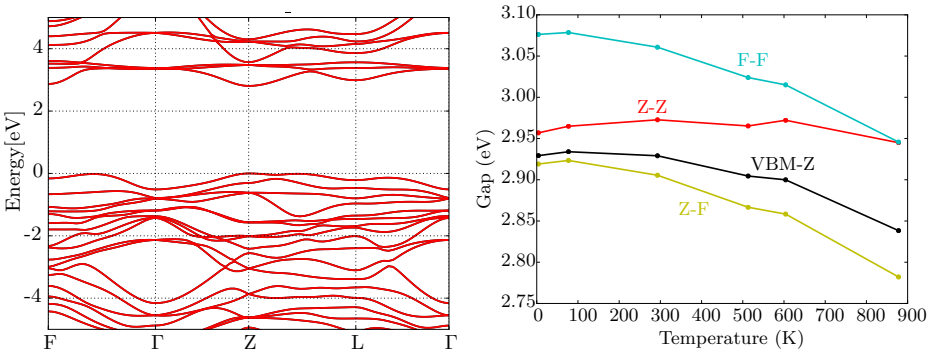

(a) (b)

Figure 67: (a) Band structure at relaxed lattice parameters and (b) temperature dependence of gaps of BFO obtained with LDA+U/PAW and $U_{eff} = 8$ eV. Temperature-dependent lattice parameters and internal coordinates of the ions are extracted from Ref. [225]. The VBM is 0.5 F.

From these results, we observe that, additionally to the electron-phonon coupling, anharmonicities in the potentials lead to changes in the band

structure. The direct band gap show little variations while the $Z - F^*$ gap shows a shrinking of about -0.2 meV/K.

Nevertheless, with LDA/NC or LDA+U/PAW with a $U_{eff} = 3.8$ eV, the experimental measurements are still not matched.

In Fig. 67, we further investigate these effects with additional results for a value of $U_{eff} = 8$ eV, evaluated following the same procedure with experimental parameters at different temperatures. For such a high value of U, the two groups of conduction bands cross each other, as shown in Fig. 67a. The so-called F^* conduction band becomes the conduction band minimum F. As temperature increases, the anharmonicities induce a large modification in the F conduction band (the $Z - F$ gap has a temperature coefficient of about -0.2 meV/K). This modification must be added to the AHC renormalization of about -0.44 meV/K evaluated within LDA/NC for the $Z - F^*$ gap. This correction must be compared to the experimental temperature dependence that is more than -1 meV/K (see Fig. 50(a)). However, the direct band gap $Z - Z$ stays around 2.95 eV for the entire range of temperature considered in these calculations.

This goes in the direction of important changes in the band structure induced by temperature. The direct and indirect band gap show different profiles in BFO and this may explain the changes in second-order Raman intensities observed in Sec. 6.2, while first-order Raman intensities show few resonance effects with temperature.

However, the electron-phonon renormalization cannot be calculated with the current versions of ABINIT with LDA+U/PAW and even further studies with more advanced frameworks such as DMFT or hybrids functionals may be required to pursue an accurate analysis of this phenomenon.

6.8 CONCLUSIONS

In this chapter, we have applied the methodology of computing resonance Raman intensities to the complex material $BiFeO_3$. We observe that already at the ground state level, or for lattice dynamics, LDA is not sufficient to get a nice agreement with experiments. LDA+U is able to capture some additional correlation physics missing in LDA, as shown for lattice dynamics where a much better agreement with experiments is observed. We have therefore computed the frequency-dependent Raman spectrum in the LDA as well as for LDA+U and the inclusion of U also improves the agreement of results with experiments. However, the agree-

ment is still not completely satisfactory and we believe that this is due to the approximations we have relied on, particularly the description of the band structure and the optical properties at the independent-particle levels. Finally, temperature-dependent band structures calculations have been performed and have shown strong electron-phonon renormalization with heavy dependence of the band and on the wavevector. We also show that anharmonicities and in particular temperature-dependent unit cell parameters and internal degrees of freedoms are important to get a complete picture of temperature-dependent band structures. As a summary, the approach developed in this thesis allows us to explain some effects observed experimentally, such as the strong relative intensities change in the spectrum. Further investigations with more accurate formalisms might be required to obtain a better agreement for this material.

7 CONCLUSIONS AND PERSPECTIVES

Simulations of Raman and optical spectra require accurate and reliable techniques not only for reproducing experimental measurements but also for predicting properties of new materials. Standard techniques for Raman simulations based on DFPT or frozen-phonon are usually performed neglecting the laser frequency. They also lack a description of excitonic and temperature effects. Based on a methodology for computing frequency-dependent (resonant) Raman intensities, we have achieved two main objectives in this thesis: assessing the importance of excitonic effects in Raman intensities and including temperature effects at different levels from the band structure to the Raman intensities going through the optical properties.

To reach these two main goals, Chap. 2 summarized the underlying theories for optical properties calculations, namely the calculations of band structures from DFT, followed by the two main approximations used in this work: the independent-particle approximation (cheap but inaccurate) and the BSE, giving good results but at a much higher computational cost. An important part of this chapter discussed the very slow convergence of the optical properties with respect to the sampling of the Brillouin zone. Numerical techniques designed to circumvent this issue have also been presented.

In Chap. 3, we described a complete methodology for the calculation of first and second-order Raman intensities. This methodology is based on FP evaluations of the dielectric function and is completely general. It does not depend on a specific implementation or approximations used for the dielectric function. We then applied and validated this methodology to the prototypical case of silicon, for which the results with the BSE showed the importance of the inclusion of excitonic effects for computing absolute intensities. We also observed strong exciton-phonon coupling for particular phonons.

Chap. 4 showed the application of the methodology to two different classes of materials, the zinc-blende SiC and GaAs and 2D TMD: WS_2 and WSe_2. In the former case, the two polar materials required additional treatment of the electric field-light coupling for longitudinal optical (LO) modes. Excitonic effects were also found to be important to

reproduce the Raman intensities of these materials, improving the results with respect to the independent-particle approximation. In the latter case, WS_2 and WSe_2, while being similar materials, show different frequency-dependent Raman behavior. Employing the above-mentioned methodology on these TMD allowed us to explain part of the difference as a result of the strength of the exciton-phonon coupling.

Temperature dependence effects have been introduced in Chap. 5, where the Allen-Heine-Cardona formalism was briefly summarized. This formalism was subsequently used to compute the temperature-dependent dielectric function of silicon and finally temperature-dependent Raman intensities of silicon with success with respect to experimental measurements.

Finally, the last Chap. 6 was devoted to the study of Bismuth Ferrite (BFO). This material shows strong frequency dependence of the Raman intensities but an atypical temperature dependence. We observed that DFT has difficulties to reproduce accurately the lattice dynamics so we studied the influence of correlation with the help of the LDA+U. The inclusion of U in the calculations improved the Raman intensities compared with experiments. The theoretical frequency dependence of BFO presents strong changes in the relative intensities, giving a consistent picture with experiments. Finally, this chapter also showed that temperature-dependent band structure obtained at the level of the AHC theory has difficulties to reproduce experiments. We observed that temperature-induced changes in the lattice parameters and internal degrees of freedom improves the agreement with experiments. Further analysis of such effects are required in a future work.

We believe this thesis improves our current knowledge of Raman intensities in general, but it definitely does not close the study of Raman intensities from first principles. Further studies may be of two kinds: application of these methodologies to a much broader set of materials and developments of new tools or new theories to ease the calculations.

On the one hand, we show results on a limited set of materials. It would be very important to enlarge the set of materials and show whether the conclusions we draw for silicon or simple materials are transferable to other materials as well. In particular, we have observed the importance of excitonic effects at the level of quantitative simulation of absolute Raman intensities for silicon. We have also shown the role of excitonic effects for TO and LO absolute and relative intensities in the case of SiC. Globally, in most of the cases, the independent-particle framework allowed us to get a cheap, first insight about the resonance phe-

nomenon, while excitonic effects improved the quantitative description with respect to experiments. In this work, we focused on very simple cases with one symmetry-allowed Raman peak (and its LO counterpart). We think that further work should be done to evaluate the importance of excitonic effects when different modes are present in the first-order Raman spectra, in particular for the study of their relative intensities.

The methodology developed here for Raman intensities is very general and can be applied to any material, as soon as the dielectric function is available. Scripts have been written on top of the Abipy-Pymatgen framework and should be transferred in the main Abipy infrastructure to allow for direct application to other materials. As soon as the methodology is validated, a much broader application of the techniques may be considered. Databases of materials properties start to emerge these last years, such as the Materials Project and the NoMaD repository for instance. A database containing hundreds of theoretical spectra already exists within the WURM project at the level of DFPT. A long-term goal would be to allow for automatic calculations of resonant Raman intensities to improve these databases, with more accurate and more complete data. Other properties that are linked to derivatives of the dielectric function may also be considered, such as the piezoreflectance, for instance. In general, high-throughput calculation of optical properties or more advanced properties such as Raman spectra will certainly be of importance in the nextcoming years.

Nevertheless, as we have seen throughout this thesis, different levels of approximations are available. The choice among them will be driven by the level of accuracy and the computer resources we are able to afford, but may also depend on the material classes. As an example, for $BiFeO_3$, we observe that accurate Raman intensity would require additional levels of approximations that go beyond standard functionals (LDA,GGA) or DFT, such as hybrid functionals or DMFT. This should improve the accuracy for systems where standard DFT shows severe limitations. Another part that can be improved in terms of accuracy is the description of coupling of light with polar vibrational modes, that has remained at the level of independent particles in this thesis and that could be developed to include excitonic effects. Of course, improving accuracy of the calculations has to be considered with respect to available computer power. Trade-offs are usually required between accuracy and computer resources limitations. However, numerical techniques may help at this level. As an example, we have shown difficult convergence studies with respect to the sampling of the Brillouin Zone. In that respect, we have

developed interpolation techniques in the reciprocal space to improve the speed of these convergences. After all, if computer resources continue their increase, most limiting cases for current research will become tractable in the future. This also involves improvement of the implementations of our current ab initio codes at the level of efficiency and parallelism on large computing centers.

On the other hand, the frozen-phonon calculations require a huge amount of evaluations of the dielectric functions, already for small systems (see for example the second-order Raman calculations for silicon in Sec. 3.5). Even if the calculations are possible for small systems nowadays thanks to automation frameworks and large clusters, the direct application of such calculations to larger systems will require additional development work. A possible approach is the combination of DFPT calculations with optical properties (i.e. BSE for excitonic effects, or TDDFT). This should reduce a lot the computational load as the derivatives would be evaluated directly and would not require additional numerical post-processing. We believe this is one way to go for new developments in this field.

As a final word, this work has not been done alone. It started from the huge effort done by scientists in the past and still working for future developments. During this work, we have had the chance to collaborate with many people in UCLouvain, in Luxembourg, in Berlin, or even further in the world. These collaborations are usually based on theoretical and experimental sides. We strongly believe that these kinds of collaborations help a lot to the development of sciences and that it is the way to improve our current knowledge of the world, via collaborations with the world.

APPENDICES

A

LINK BETWEEN FEYNMAN DIAGRAMMATIC APPROACH AND DERIVATIVES OF THE DIELECTRIC FUNCTION

In Sec. 3.2, we present Raman intensities obtained from derivatives of the dielectric function. In this appendix, we show that it is indeed a good approximation of the perturbation expansion of quantum mechanics [1, 139] when the phonon frequencies are negligible.

We restrict ourselves to first-order Raman intensities in the independent-particles pictures.

In that framework, the dielectric function

$$\chi(\omega) = \sum_{\sigma=\pm 1} \sum_{c,v} \frac{\left\langle v\mathbf{k}\middle|\mathbf{r}\middle|c\mathbf{k}\right\rangle\left\langle c\mathbf{k}\middle|\mathbf{r}\middle|v\mathbf{k}\right\rangle}{(\epsilon_{c\mathbf{k}} - \epsilon_{v\mathbf{k}}) - \sigma(\omega + i\delta^+)}, \tag{189}$$

can easily be differenciated to yield

$$\begin{aligned}
\alpha(\omega) = \frac{\partial\chi}{\partial\tau} = &\sum_{\sigma=\pm 1} \sum_{c,v} \frac{\left\langle \frac{\partial v\mathbf{k}}{\partial\tau}\middle|\mathbf{r}\middle|c\mathbf{k}\right\rangle\left\langle c\mathbf{k}\middle|\mathbf{r}\middle|v\mathbf{k}\right\rangle}{(\epsilon_{c\mathbf{k}} - \epsilon_{v\mathbf{k}}) - \sigma(\omega + i\delta^+)} \\
&+ \sum_{\sigma=\pm 1} \sum_{c,v} \frac{\left\langle v\mathbf{k}\middle|\mathbf{r}\middle|\frac{\partial c\mathbf{k}}{\partial\tau}\right\rangle\left\langle c\mathbf{k}\middle|\mathbf{r}\middle|v\mathbf{k}\right\rangle}{(\epsilon_{c\mathbf{k}} - \epsilon_{v\mathbf{k}}) - \sigma(\omega + i\delta^+)} \\
&+ \sum_{\sigma=\pm 1} \sum_{c,v} \frac{\left\langle v\mathbf{k}\middle|\mathbf{r}\middle|c\mathbf{k}\right\rangle\left\langle \frac{\partial c\mathbf{k}}{\partial\tau}\middle|\mathbf{r}\middle|v\mathbf{k}\right\rangle}{(\epsilon_{c\mathbf{k}} - \epsilon_{v\mathbf{k}}) - \sigma(\omega + i\delta^+)} \\
&+ \sum_{\sigma=\pm 1} \sum_{cv} \frac{\left\langle v\mathbf{k}\middle|\mathbf{r}\middle|c\mathbf{k}\right\rangle\left\langle c\mathbf{k}\middle|\mathbf{r}\middle|\frac{\partial v\mathbf{k}}{\partial\tau}\right\rangle}{(\epsilon_{c\mathbf{k}} - \epsilon_{v\mathbf{k}}) - \sigma(\omega + i\delta^+)} \\
&- \sum_{\sigma=\pm 1} \sum_{cv} \frac{\left\langle v\mathbf{k}\middle|\mathbf{r}\middle|c\mathbf{k}\right\rangle\left\langle c\mathbf{k}\middle|\mathbf{r}\middle|v\mathbf{k}\right\rangle}{((\epsilon_{c\mathbf{k}} - \epsilon_{v\mathbf{k}}) - \sigma(\omega + i\delta^+))^2} \frac{\partial(\epsilon_{c\mathbf{k}} - \epsilon_{v\mathbf{k}})}{\partial\tau}.
\end{aligned} \tag{190}$$

The derivative of the eigenvalue $\frac{\partial \epsilon_{b\mathbf{k}}}{\partial \tau}$, entering the previous equation can be obtained by using the definition

$$\epsilon_{b\mathbf{k}} = \left\langle b\mathbf{k} \middle| \mathcal{H} \middle| b\mathbf{k} \right\rangle, \tag{191}$$

where $\mathcal{H}$ is the Hamiltonian and the Hellman-Feynman theorem

$$\begin{aligned}
\frac{\partial \epsilon_{b\mathbf{k}}}{\partial \tau} &= \left\langle b\mathbf{k} \middle| \frac{\partial \mathcal{H}}{\partial \tau} \middle| b\mathbf{k} \right\rangle + \left\langle \frac{\partial b\mathbf{k}}{\partial \tau} \middle| \mathcal{H} \middle| b\mathbf{k} \right\rangle + \left\langle b\mathbf{k} \middle| \mathcal{H} \middle| \frac{\partial b\mathbf{k}}{\partial \tau} \right\rangle && (192)\\
&= \left\langle b\mathbf{k} \middle| \frac{\partial \mathcal{H}}{\partial \tau} \middle| b\mathbf{k} \right\rangle + \epsilon_{b\mathbf{k}} \left(\langle \frac{\partial b\mathbf{k}}{\partial \tau} | b\mathbf{k} \rangle + \langle b\mathbf{k} | \frac{\partial b\mathbf{k}}{\partial \tau} \rangle \right) && (193)\\
&= \left\langle b\mathbf{k} \middle| \frac{\partial \mathcal{H}}{\partial \tau} \middle| b\mathbf{k} \right\rangle. && (194)
\end{aligned}$$

and $\frac{\partial \mathcal{H}}{\partial \tau} = H'_{e-ion}$.

We can compute the derivative of the wavefunction $\frac{\partial b\mathbf{k}}{\partial \tau}$. Starting from Schrödinger equation:

$$\mathcal{H} \, |b\mathbf{k}\rangle = \epsilon_{b\mathbf{k}} \, |b\mathbf{k}\rangle \tag{195}$$

and plug-in the Taylor expansions

$$\begin{aligned}
\mathcal{H} &= \mathcal{H}_0 + \tau \frac{\partial \mathcal{H}}{\partial \tau} && (196)\\
\epsilon_{b\mathbf{k}} &= \epsilon^0_{b\mathbf{k}} + \tau \frac{\partial \epsilon_{b\mathbf{k}}}{\partial \tau} + \cdots && (197)\\
|b\mathbf{k}\rangle &= |b\mathbf{k}^0\rangle + \tau \, |\frac{\partial b\mathbf{k}}{\partial \tau}\rangle + \cdots, && (198)
\end{aligned}$$

we get

$$\begin{aligned}
&\mathcal{H}_0 \, |b\mathbf{k}^0\rangle + \tau \left(\mathcal{H}_0 \, |\frac{\partial b\mathbf{k}}{\partial \tau}\rangle + \frac{\partial \mathcal{H}}{\partial \tau} \, |b\mathbf{k}^0\rangle \right) + \cdots && (199)\\
&\qquad = \epsilon^0_{b\mathbf{k}} \, |b\mathbf{k}^0\rangle + \tau \left(\frac{\partial \epsilon_{b\mathbf{k}}}{\partial \tau} \, |b\mathbf{k}^0\rangle + \epsilon^0_{b\mathbf{k}} \, |\frac{\partial b\mathbf{k}}{\partial \tau}\rangle \right) + \cdots && (200)
\end{aligned}$$

The Sternheimer equation at first-order reads

$$\left(\mathcal{H}_0 - \epsilon^0_{b\mathbf{k}}\right) |\frac{\partial b\mathbf{k}}{\partial \tau}\rangle = -\left(\frac{\partial \mathcal{H}}{\partial \tau} - \frac{\partial \epsilon_{b\mathbf{k}}}{\partial \tau} \right) |b\mathbf{k}^0\rangle \, . \tag{201}$$

Taking the product with a state b' non-degenerate with b, and skipping the ^{0} index yields

$$\left(\epsilon_{b'\mathbf{k}} - \epsilon_{b\mathbf{k}}\right) \langle b'\mathbf{k} | \frac{\partial b\mathbf{k}}{\partial \tau} \rangle = -\left\langle b'\mathbf{k} \middle| \frac{\partial \mathcal{H}}{\partial \tau} \middle| b\mathbf{k} \right\rangle. \tag{202}$$

Finally, using the closure relation, we obtain (choice of gauge)

$$|\frac{\partial b\mathbf{k}}{\partial \tau}\rangle = -\sum_{b'\neq b}{}' |b'\mathbf{k}\rangle \frac{\left\langle b'\mathbf{k}\middle|\frac{\partial \mathcal{H}}{\partial \tau}\middle|b\mathbf{k}\right\rangle}{\epsilon_{b'\mathbf{k}}-\epsilon_{b\mathbf{k}}}. \tag{203}$$

where the summation is done only for $\epsilon_{b'\mathbf{k}} \neq \epsilon_{b\mathbf{k}}$.

Inserting Eq. (203) into Eq. (190) yields

$$\begin{aligned}
\alpha(\omega) = \frac{\partial \chi}{\partial \tau} = &-\sum_{\sigma=\pm 1}\sum_{vc,n'\neq v} \frac{\left\langle v\mathbf{k}\middle|\frac{\partial \mathcal{H}}{\partial \tau}\middle|n'\mathbf{k}\right\rangle\left\langle n'\mathbf{k}\middle|\mathbf{r}\middle|c\mathbf{k}\right\rangle\left\langle c\mathbf{k}\middle|\mathbf{r}\middle|v\mathbf{k}\right\rangle}{((\epsilon_{c\mathbf{k}}-\epsilon_{v\mathbf{k}})-\sigma(\omega+i\delta^{+}))\,(\epsilon_{n'\mathbf{k}}-\epsilon_{v\mathbf{k}})} \\
&-\sum_{\sigma=\pm 1}\sum_{vc,n'\neq c} \frac{\left\langle v\mathbf{k}\middle|\mathbf{r}\middle|n'\mathbf{k}\right\rangle\left\langle n'\mathbf{k}\middle|\frac{\partial \mathcal{H}}{\partial \tau}\middle|c\mathbf{k}\right\rangle\left\langle c\mathbf{k}\middle|\mathbf{r}\middle|v\mathbf{k}\right\rangle}{((\epsilon_{c\mathbf{k}}-\epsilon_{v\mathbf{k}})-\sigma(\omega+i\delta^{+}))\,(\epsilon_{n'\mathbf{k}}-\epsilon_{c\mathbf{k}})} \\
&-\sum_{\sigma=\pm 1}\sum_{vc,n'\neq c} \frac{\left\langle v\mathbf{k}\middle|\mathbf{r}\middle|c\mathbf{k}\right\rangle\left\langle c\mathbf{k}\middle|\frac{\partial \mathcal{H}}{\partial \tau}\middle|n'\mathbf{k}\right\rangle\left\langle n'\mathbf{k}\middle|\mathbf{r}\middle|v\mathbf{k}\right\rangle}{((\epsilon_{c\mathbf{k}}-\epsilon_{v\mathbf{k}})-\sigma(\omega+i\delta^{+}))\,(\epsilon_{n'\mathbf{k}}-\epsilon_{c\mathbf{k}})} \\
&-\sum_{\sigma=\pm 1}\sum_{vc,n'\neq v} \frac{\left\langle v\mathbf{k}\middle|\mathbf{r}\middle|c\mathbf{k}\right\rangle\left\langle c\mathbf{k}\middle|\mathbf{r}\middle|n'\mathbf{k}\right\rangle\left\langle n'\mathbf{k}\middle|\frac{\partial \mathcal{H}}{\partial \tau}\middle|v\mathbf{k}\right\rangle}{((\epsilon_{c\mathbf{k}}-\epsilon_{v\mathbf{k}})-\sigma(\omega+i\delta^{+}))\,(\epsilon_{n'\mathbf{k}}-\epsilon_{v\mathbf{k}})} \\
&-\sum_{\sigma=\pm 1}\sum_{vc} \frac{\left\langle v\mathbf{k}\middle|\mathbf{r}\middle|c\mathbf{k}\right\rangle\left\langle c\mathbf{k}\middle|\mathbf{r}\middle|v\mathbf{k}\right\rangle}{((\epsilon_{c\mathbf{k}}-\epsilon_{v\mathbf{k}})-\sigma(\omega+i\delta^{+}))^{2}}\left(\left\langle v\mathbf{k}\middle|\frac{\partial \mathcal{H}}{\partial \tau}\middle|v\mathbf{k}\right\rangle\right).
\end{aligned} \tag{204}$$

Separating the indices n' in terms of valence and conduction bands gives

$$\alpha(\omega) = \frac{\partial \chi}{\partial \tau} = -\sum_{\sigma=\pm 1} \sum_{vc,v'\neq v} \frac{\left\langle vk\middle|\frac{\partial \mathcal{H}}{\partial \tau}\middle|v'k\right\rangle\left\langle v'k\middle|r\middle|ck\right\rangle\left\langle ck\middle|r\middle|vk\right\rangle}{((\epsilon_{ck}-\epsilon_{vk})-\sigma(\omega+i\delta^{+}))\,(\epsilon_{v'k}-\epsilon_{vk})} \tag{205}$$

$$-\sum_{\sigma=\pm 1} \sum_{vc,c'} \frac{\left\langle vk\middle|\frac{\partial \mathcal{H}}{\partial \tau}\middle|c'k\right\rangle\left\langle c'k\middle|r\middle|ck\right\rangle\left\langle ck\middle|r\middle|vk\right\rangle}{((\epsilon_{ck}-\epsilon_{vk})-\sigma(\omega+i\delta^{+}))\,(\epsilon_{c'k}-\epsilon_{vk})}$$

$$-\sum_{\sigma=\pm 1} \sum_{vc,v'} \frac{\left\langle vk\middle|r\middle|v'k\right\rangle\left\langle v'k\middle|\frac{\partial \mathcal{H}}{\partial \tau}\middle|ck\right\rangle\left\langle ck\middle|r\middle|vk\right\rangle}{((\epsilon_{ck}-\epsilon_{vk})-\sigma(\omega+i\delta^{+}))\,(\epsilon_{v'k}-\epsilon_{ck})}$$

$$-\sum_{\sigma=\pm 1} \sum_{vc,c'\neq c} \frac{\left\langle vk\middle|r\middle|c'k\right\rangle\left\langle c'k\middle|\frac{\partial \mathcal{H}}{\partial \tau}\middle|ck\right\rangle\left\langle ck\middle|r\middle|vk\right\rangle}{((\epsilon_{ck}-\epsilon_{vk})-\sigma(\omega+i\delta^{+}))\,(\epsilon_{c'k}-\epsilon_{ck})} \tag{206}$$

$$-\sum_{\sigma=\pm 1} \sum_{vc,v'} \frac{\left\langle vk\middle|r\middle|ck\right\rangle\left\langle ck\middle|\frac{\partial \mathcal{H}}{\partial \tau}\middle|v'k\right\rangle\left\langle v'k\middle|r\middle|vk\right\rangle}{((\epsilon_{ck}-\epsilon_{vk})-\sigma(\omega+i\delta^{+}))\,(\epsilon_{v'k}-\epsilon_{ck})}$$

$$-\sum_{\sigma=\pm 1} \sum_{vc,c'\neq c} \frac{\left\langle vk\middle|r\middle|ck\right\rangle\left\langle ck\middle|\frac{\partial \mathcal{H}}{\partial \tau}\middle|c'k\right\rangle\left\langle c'k\middle|r\middle|vk\right\rangle}{((\epsilon_{ck}-\epsilon_{vk})-\sigma(\omega+i\delta^{+}))\,(\epsilon_{c'k}-\epsilon_{ck})} \tag{207}$$

$$-\sum_{\sigma=\pm 1} \sum_{vc,v'\neq v} \frac{\left\langle vk\middle|r\middle|ck\right\rangle\left\langle ck\middle|r\middle|v'k\right\rangle\left\langle v'k\middle|\frac{\partial \mathcal{H}}{\partial \tau}\middle|vk\right\rangle}{((\epsilon_{ck}-\epsilon_{vk})-\sigma(\omega+i\delta^{+}))\,(\epsilon_{v'k}-\epsilon_{vk})} \tag{208}$$

$$-\sum_{\sigma=\pm 1} \sum_{vc,c'} \frac{\left\langle vk\middle|r\middle|ck\right\rangle\left\langle ck\middle|r\middle|c'k\right\rangle\left\langle c'k\middle|\frac{\partial \mathcal{H}}{\partial \tau}\middle|vk\right\rangle}{((\epsilon_{ck}-\epsilon_{vk})-\sigma(\omega+i\delta^{+}))\,(\epsilon_{c'k}-\epsilon_{vk})}$$

$$-\sum_{\sigma=\pm 1} \sum_{vc} \frac{\left\langle vk\middle|r\middle|ck\right\rangle\left\langle ck\middle|r\middle|vk\right\rangle}{((\epsilon_{ck}-\epsilon_{vk})-\sigma(\omega+i\delta^{+}))^{2}} \left(\left\langle ck\middle|\frac{\partial \mathcal{H}}{\partial \tau}\middle|ck\right\rangle\right) \tag{209}$$

$$+\sum_{\sigma=\pm 1} \sum_{vc} \frac{\left\langle vk\middle|r\middle|ck\right\rangle\left\langle ck\middle|r\middle|vk\right\rangle}{((\epsilon_{ck}-\epsilon_{vk})-\sigma(\omega+i\delta^{+}))^{2}} \left(\left\langle vk\middle|\frac{\partial \mathcal{H}}{\partial \tau}\middle|vk\right\rangle\right). \tag{210}$$

These formulae can be simplified with a bit of algebra

$$\left[\frac{1}{(\epsilon_{c'\mathbf{k}}-\epsilon_{\nu\mathbf{k}})-\sigma(\omega+i\delta^{+})}-\frac{1}{(\epsilon_{c\mathbf{k}}-\epsilon_{\nu\mathbf{k}})-\sigma(\omega+i\delta^{+})}\right]\left(\frac{1}{\epsilon_{c\mathbf{k}}-\epsilon_{c'\mathbf{k}}}\right) \tag{211}$$

$$=\frac{1}{(\epsilon_{c'\mathbf{k}}-\epsilon_{\nu\mathbf{k}})-\sigma(\omega+i\delta^{+})}\times\frac{1}{(\epsilon_{c\mathbf{k}}-\epsilon_{\nu\mathbf{k}})-\sigma(\omega+i\delta^{+})} \tag{212}$$

Combining different terms of the previous equations gives

$$(206)+(207)+(209)=$$

$$-\sum_{\sigma=\pm1}\sum_{\nu c'c}\frac{\left\langle \nu\mathbf{k}\middle|\mathbf{r}\middle|c\mathbf{k}\right\rangle\left\langle c\mathbf{k}\middle|\frac{\partial\mathcal{H}}{\partial\tau}\middle|c'\mathbf{k}\right\rangle\left\langle c'\mathbf{k}\middle|\mathbf{r}\middle|\nu\mathbf{k}\right\rangle}{((\epsilon_{c'\mathbf{k}}-\epsilon_{\nu\mathbf{k}})-\sigma(\omega+i\delta^{+}))\,((\epsilon_{c\mathbf{k}}-\epsilon_{\nu\mathbf{k}})-\sigma(\omega+i\delta^{+}))} \tag{213}$$

$$(205)+(208)+(210)=$$

$$\sum_{\sigma=\pm1}\sum_{\nu c\nu'}\frac{\left\langle \nu\mathbf{k}\middle|\frac{\partial\mathcal{H}}{\partial\tau}\middle|\nu'\mathbf{k}\right\rangle\left\langle \nu'\mathbf{k}\middle|\mathbf{r}\middle|c\mathbf{k}\right\rangle\left\langle c\mathbf{k}\middle|\mathbf{r}\middle|\nu\mathbf{k}\right\rangle}{((\epsilon_{c\mathbf{k}}-\epsilon_{\nu\mathbf{k}})-\sigma(\omega+i\delta^{+}))\,((\epsilon_{c\mathbf{k}}-\epsilon_{\nu'\mathbf{k}})-\sigma(\omega+i\delta^{+}))}. \tag{214}$$

The final result for the derivative reads then

$$
\begin{aligned}
\alpha(\omega) = \frac{\partial \chi}{\partial \tau}
&= \sum_{\sigma=\pm 1} \sum_{\nu c \nu'} \frac{\left\langle \nu \mathbf{k} \middle| \frac{\partial \mathcal{H}}{\partial \tau} \middle| \nu' \mathbf{k} \right\rangle \left\langle \nu' \mathbf{k} \middle| \mathbf{r} \middle| c \mathbf{k} \right\rangle \left\langle c \mathbf{k} \middle| \mathbf{r} \middle| \nu \mathbf{k} \right\rangle}{((\epsilon_{c\mathbf{k}} - \epsilon_{\nu\mathbf{k}}) - \sigma(\omega + i\delta^+))\,((\epsilon_{c\mathbf{k}} - \epsilon_{\nu'\mathbf{k}}) - \sigma(\omega + i\delta^+))} \\
&- \sum_{\sigma=\pm 1} \sum_{\nu c' c} \frac{\left\langle \nu \mathbf{k} \middle| \mathbf{r} \middle| c \mathbf{k} \right\rangle \left\langle c \mathbf{k} \middle| \frac{\partial \mathcal{H}}{\partial \tau} \middle| c' \mathbf{k} \right\rangle \left\langle c' \mathbf{k} \middle| \mathbf{r} \middle| \nu \mathbf{k} \right\rangle}{((\epsilon_{c'\mathbf{k}} - \epsilon_{\nu\mathbf{k}}) - \sigma(\omega + i\delta^+))\,((\epsilon_{c\mathbf{k}} - \epsilon_{\nu\mathbf{k}}) - \sigma(\omega + i\delta^+))} \\
&- \sum_{\sigma=\pm 1} \sum_{\nu c, c'} \frac{\left\langle \nu \mathbf{k} \middle| \frac{\partial \mathcal{H}}{\partial \tau} \middle| c' \mathbf{k} \right\rangle \left\langle c' \mathbf{k} \middle| \mathbf{r} \middle| c \mathbf{k} \right\rangle \left\langle c \mathbf{k} \middle| \mathbf{r} \middle| \nu \mathbf{k} \right\rangle}{((\epsilon_{c\mathbf{k}} - \epsilon_{\nu\mathbf{k}}) - \sigma(\omega + i\delta^+))\,(\epsilon_{c'\mathbf{k}} - \epsilon_{\nu\mathbf{k}})} \\
&- \sum_{\sigma=\pm 1} \sum_{\nu c, \nu'} \frac{\left\langle \nu \mathbf{k} \middle| \mathbf{r} \middle| \nu' \mathbf{k} \right\rangle \left\langle \nu' \mathbf{k} \middle| \frac{\partial \mathcal{H}}{\partial \tau} \middle| c \mathbf{k} \right\rangle \left\langle c \mathbf{k} \middle| \mathbf{r} \middle| \nu \mathbf{k} \right\rangle}{((\epsilon_{c\mathbf{k}} - \epsilon_{\nu\mathbf{k}}) - \sigma(\omega + i\delta^+))\,(\epsilon_{\nu'\mathbf{k}} - \epsilon_{c\mathbf{k}})} \\
&- \sum_{\sigma=\pm 1} \sum_{\nu c, \nu'} \frac{\left\langle \nu \mathbf{k} \middle| \mathbf{r} \middle| c \mathbf{k} \right\rangle \left\langle c \mathbf{k} \middle| \frac{\partial \mathcal{H}}{\partial \tau} \middle| \nu' \mathbf{k} \right\rangle \left\langle \nu' \mathbf{k} \middle| \mathbf{r} \middle| \nu \mathbf{k} \right\rangle}{((\epsilon_{c\mathbf{k}} - \epsilon_{\nu\mathbf{k}}) - \sigma(\omega + i\delta^+))\,(\epsilon_{\nu'\mathbf{k}} - \epsilon_{c\mathbf{k}})} \\
&- \sum_{\sigma=\pm 1} \sum_{\nu c, c'} \frac{\left\langle \nu \mathbf{k} \middle| \mathbf{r} \middle| c \mathbf{k} \right\rangle \left\langle c \mathbf{k} \middle| \mathbf{r} \middle| c' \mathbf{k} \right\rangle \left\langle c' \mathbf{k} \middle| \frac{\partial \mathcal{H}}{\partial \tau} \middle| \nu \mathbf{k} \right\rangle}{((\epsilon_{c\mathbf{k}} - \epsilon_{\nu\mathbf{k}}) - \sigma(\omega + i\delta^+))\,(\epsilon_{c'\mathbf{k}} - \epsilon_{\nu\mathbf{k}})}. \qquad (215)
\end{aligned}
$$

In comparison, the many-body formulation of Raman gives the following expression [1, 139]

$$
\begin{aligned}
\alpha(\omega) = \frac{\partial \chi}{\partial \tau} &= \delta(\omega_i - \omega_s - \omega_0) \\
&\sum_{n,n'} \frac{\langle i|\mathcal{H}_{e-ion}|n\rangle\langle n|\mathcal{H}_{eR}(\omega_s)|n'\rangle\langle n'|\mathcal{H}_{eR}(\omega_i)|i\rangle}{(-\omega_0 - (\epsilon_n - \epsilon_i))\,(-\omega_0 - \omega_s - (\epsilon_{n'} - \epsilon_i))} \\
&\quad + \frac{\langle i|\mathcal{H}_{e-ion}|n\rangle\langle n|\mathcal{H}_{eR}(\omega_i)|n'\rangle\langle n'|\mathcal{H}_{eR}(\omega_s)|i\rangle}{(-\omega_0 - (\epsilon_n - \epsilon_i))\,(-\omega_0 + \omega_i - (\epsilon_{n'} - \epsilon_i))} \\
&\quad + \frac{\langle i|\mathcal{H}_{eR}(\omega_i)|n\rangle\langle n|\mathcal{H}_{eR}(\omega_s)|n'\rangle\langle n'|\mathcal{H}_{e-ion}|i\rangle}{(\omega_i - (\epsilon_n - \epsilon_i))\,(\omega_i - \omega_s - (\epsilon_{n'} - \epsilon_i))} \\
&\quad + \frac{\langle i|\mathcal{H}_{eR}(\omega_s)|n\rangle\langle n|\mathcal{H}_{eR}(\omega_i)|n'\rangle\langle n'|\mathcal{H}_{e-ion}|i\rangle}{(-\omega_s - (\epsilon_n - \epsilon_i))\,(-\omega_s + \omega_i - (\epsilon_{n'} - \epsilon_i))} \\
&\quad + \frac{\langle i|\mathcal{H}_{eR}(\omega_i)|n\rangle\langle n|\mathcal{H}_{e-ion}|n'\rangle\langle n'|\mathcal{H}_{eR}(\omega_s)|i\rangle}{(\omega_i - (\epsilon_n - \epsilon_i))\,(\omega_i - \omega_0 - (\epsilon_{n'} - \epsilon_i))} \\
&\quad + \frac{\langle i|\mathcal{H}_{eR}(\omega_s)|n\rangle\langle n|\mathcal{H}_{e-ion}|n'\rangle\langle n'|\mathcal{H}_{eR}(\omega_i)|i\rangle}{(-\omega_s - (\epsilon_n - \epsilon_i))\,(-\omega_s - \omega_0 - (\epsilon_{n'} - \epsilon_i))},
\end{aligned}
\tag{216}
$$

which gives, using second-quantized operators forms, in the independent particle framework

$$
\begin{aligned}
\alpha(\omega) = \frac{\partial \chi}{\partial \tau} = \delta(\omega_i - \omega_s - \omega_0) \\
&\sum_{vcc'\mathbf{k}} \frac{\langle v|\mathcal{H}_{e-ion}|c\rangle\langle c|\mathcal{H}_{eR}(\omega_s)|c'\rangle\langle c'|\mathcal{H}_{eR}(\omega_i)|v\rangle}{(\omega_0 + (\epsilon_c - \epsilon_v))\,(\omega_0 + \omega_s + (\epsilon_{c'} - \epsilon_v))} \\
&+ \sum_{vcv'\mathbf{k}} \frac{\langle v|\mathcal{H}_{e-ion}|c\rangle\langle v|\mathcal{H}_{eR}(\omega_s)|v'\rangle\langle c|\mathcal{H}_{eR}(\omega_i)|v'\rangle}{(\omega_0 + (\epsilon_c - \epsilon'_v))\,(\omega_0 + \omega_s + (\epsilon_c - \epsilon_v))} \\
&+ \sum_{vcc'\mathbf{k}} \frac{\langle v|\mathcal{H}_{e-ion}|c\rangle\langle c|\mathcal{H}_{eR}(\omega_i)|c'\rangle\langle c'|\mathcal{H}_{eR}(\omega_s)|v\rangle}{(-\omega_0 - (\epsilon_c - \epsilon_v))\,(-\omega_0 + \omega_i - (\epsilon_{c'} - \epsilon_v))} \\
&+ \sum_{vcv'\mathbf{k}} \frac{\langle v|\mathcal{H}_{e-ion}|c\rangle\langle v|\mathcal{H}_{eR}(\omega_i)|v'\rangle\langle c|\mathcal{H}_{eR}(\omega_s)|v'\rangle}{(-\omega_0 - (\epsilon_c - \epsilon'_v))\,(-\omega_0 + \omega_i - (\epsilon_c - \epsilon_v))} \\
&+ \sum_{vcc'\mathbf{k}} \frac{\langle v|\mathcal{H}_{eR}(\omega_i)|c\rangle\langle c|\mathcal{H}_{eR}(\omega_s)|c'\rangle\langle c'|\mathcal{H}_{e-ion}|v\rangle}{(\omega_i - (\epsilon_c - \epsilon_v))\,(\omega_i - \omega_s - (\epsilon_{c'} - \epsilon_v))} \\
&+ \sum_{vcv'\mathbf{k}} \frac{\langle v|\mathcal{H}_{eR}(\omega_i)|c\rangle\langle v|\mathcal{H}_{eR}(\omega_s)|v'\rangle\langle c|\mathcal{H}_{e-ion}|v'\rangle}{(\omega_i - (\epsilon_c - \epsilon'_v))\,(\omega_i - \omega_s - (\epsilon_c - \epsilon_v))} \\
&+ \sum_{vcc'\mathbf{k}} \frac{\langle v|\mathcal{H}_{eR}(\omega_s)|c\rangle\langle c|\mathcal{H}_{eR}(\omega_i)|c'\rangle\langle c'|\mathcal{H}_{e-ion}|v\rangle}{(-\omega_s - (\epsilon_c - \epsilon_v))\,(-\omega_s + \omega_i - (\epsilon_{c'} - \epsilon_v))} \\
&+ \sum_{vcv'\mathbf{k}} \frac{\langle v|\mathcal{H}_{eR}(\omega_s)|c\rangle\langle v|\mathcal{H}_{eR}(\omega_i)|v'\rangle\langle c|\mathcal{H}_{e-ion}|v'\rangle}{(-\omega_s - (\epsilon_c - \epsilon'_v))\,(-\omega_s + \omega_i - (\epsilon_c - \epsilon_v))} \\
&+ \sum_{vcc'\mathbf{k}} \frac{\langle v|\mathcal{H}_{eR}(\omega_i)|c\rangle\langle c|\mathcal{H}_{e-ion}|c'\rangle\langle c'|\mathcal{H}_{eR}(\omega_s)|v\rangle}{(\omega_i - (\epsilon_c - \epsilon_v))\,(\omega_i - \omega_0 - (\epsilon_{c'} - \epsilon_v))} \\
&+ \sum_{vcv'\mathbf{k}} \frac{\langle v|\mathcal{H}_{eR}(\omega_i)|c\rangle\langle v|\mathcal{H}_{e-ion}|v'\rangle\langle c|\mathcal{H}_{eR}(\omega_s)|v'\rangle}{(\omega_i - (\epsilon_c - \epsilon'_v))\,(\omega_i - \omega_0 - (\epsilon_c - \epsilon_v))} \\
&+ \sum_{vcc'\mathbf{k}} \frac{\langle v|\mathcal{H}_{eR}(\omega_s)|c\rangle\langle c|\mathcal{H}_{e-ion}|c'\rangle\langle c'|\mathcal{H}_{eR}(\omega_i)|v\rangle}{(-\omega_s - (\epsilon_c - \epsilon_v))\,(-\omega_s - \omega_0 - (\epsilon_{c'} - \epsilon_v))} \\
&+ \sum_{vcv'\mathbf{k}} \frac{\langle v|\mathcal{H}_{eR}(\omega_s)|c\rangle\langle v|\mathcal{H}_{e-ion}|v'\rangle\langle c|\mathcal{H}_{eR}(\omega_i)|v'\rangle}{(-\omega_s - (\epsilon_c - \epsilon'_v))\,(-\omega_s - \omega_0 - (\epsilon_c - \epsilon_v))}. \qquad (217)
\end{aligned}
$$

We can observe that the derivative Eq. (215) and the many-body approach Eq. (217) are equivalent if $\omega_0 \approx 0$ and consequently $\omega_i = \omega_s = \omega$.

As a final word about this derivation, the expressions available in Eq. (215) could be evaluated numerically directly with respect to the

frequency. Indeed, all the ingredients are available from DFT (eigenenergies) and DFPT (optical transition matrix elements and electron-phonon matrix elements). A preliminary analysis of these expressions would be required before practical implementation, in particular concerning terms with optical transition matrix elements between equivalent bands.

B

SECOND-ORDER SUSCEPTIBILITY IN THE INDEPENDENT-PARTICLE APPROXIMATION

As we have seen in Sec. 3.2, Raman intensities calculations for polar phonons require the knowledge of second-order susceptibilities. In this section, we show how to compute these terms in the independent-particle picture.

Starting from the knowledge of the matrix elements of the momentum operator, Sipe, Ghahramani and Hughes developed expressions for the second-order susceptibility tensor [138, 226]. These expressions have been developed and rewritten by other authors [117, 227]. More recently, Tancogne-Dejean derived again the expressions and presented non-linear properties for simple materials and then to surfaces [228], stressing the importance of anti-resonant terms in the susceptibilities.

As already mentioned, the ingredients required are the band energies $\omega_m(\mathbf{k})$, frequency differences $\omega_{mn} = \omega_m - \omega_n$, occupation numbers $f_m(\mathbf{k})$, occupation differences $f_{mn} = f_m - f_n$, and the matrix elements of the position operator, obtained from the momentum matrix element when $\omega_{nm} \neq 0$

$$r^a_{nm}(\mathbf{k}) \coloneqq \frac{v^a_{nm}(\mathbf{k})}{i\omega_{nm}}, \tag{218}$$

where a, b, c are labels for Cartesian coordinates, $v^a_{nm}(\mathbf{k}) = m_e^{-1} p^a_{nm}(\mathbf{k})$, p_{nm} is the momentum matrix element, and m_e is the electron mass. Diagonal matrix elements of the position operator are set to 0.

The momentum matrix elements can be obtained from the commutator $\frac{1}{i\hbar}[\mathbf{r}, H]$ or via the derivative with respect to the wavevector. Only the latter option is available in the current "optic" plugin of ABINIT.

From these basic quantities, we define

$$\Delta^c_{mn} = v^c_{mm} - v^c_{nn} \tag{219}$$

$$r^b_{mn;c} = -\frac{r^b_{mn}\Delta^c_{mn} + r^c_{mn}\Delta^b_{mn}}{\omega_{mn}} - i\sum_p \frac{\omega_{mp} r^b_{mp} r^c_{pn} - \omega_{pn} r^c_{mp} r^b_{pn}}{\omega_{mn}} \tag{220}$$

$$\left[\frac{r^b_{mn}}{\omega_{mn}}\right]_{;c} = \frac{r^b_{mn;c}}{\omega_{mn}} - r^b_{mn}\frac{\Delta^c_{mn}}{\omega^2_{mn}}. \tag{221}$$

The second-order susceptibility can then be written in the form

$$\begin{aligned}\chi^{abc}(-\omega_\beta-\omega_\gamma,\omega_\beta,\omega_\gamma) = {}& \chi_{II}^{abc}(-\omega_\beta-\omega_\gamma,\omega_\beta,\omega_\gamma)\\ &+\eta_{II}^{abc}(-\omega_\beta-\omega_\gamma,\omega_\beta,\omega_\gamma)\\ &+\frac{i}{\omega_\beta+\omega_\gamma}\sigma_{II}^{abc}(-\omega_\beta-\omega_\gamma,\omega_\beta,\omega_\gamma)\end{aligned} \tag{222}$$

where the first term is a purely interband contribution, the second term arises from the change of linear response from intraband motions and the third term comes from the modification of intraband motion by the polarization associated with interband motion [138, 226].

Expressions are available for second-harmonic generation (SHG), i.e. $\chi^{(2)}(-2\omega,\omega,\omega)$, [1]

$$\begin{aligned}\chi_{II}^{abc}(-2\omega,\omega,\omega) = {}& \sum_{nml}\int\frac{d\mathbf{k}}{4\pi^3}\frac{r^a_{nm}\{r^b_{ml}r^c_{ln}\}}{(\omega_{ln}-\omega_{ml})}\\ &\left\{\frac{2f_{nm}}{(\omega_{mn}-2\omega)}+\frac{f_{ml}}{(\omega_{ml}-\omega)}+\frac{f_{ln}}{(\omega_{ln}-\omega)}\right\}\end{aligned} \tag{223}$$

$$\begin{aligned}\eta_{II}^{abc}(-2\omega,\omega,\omega) = {}& \int\frac{d\mathbf{k}}{4\pi^3}\sum_{nml}\omega_{mn}r^a_{nm}\{r^b_{ml}r^c_{ln}\}\\ &\left\{\frac{f_{nl}}{\omega_{ln}^2(\omega_{ln}-\omega)}-\frac{f_{lm}}{\omega_{ml}^2(\omega_{ml}-\omega)}\right\}\\ &-8i\sum_{nm}\frac{f_{nm}r^a_{nm}}{\omega_{mn}^2(\omega_{mn}-2\omega)}\{\Delta^b_{mn}r^c_{mn}\}\\ &+2\sum_{nml}\frac{f_{nm}r^a_{nm}\{r^b_{ml}r^c_{ln}\}(\omega_{ml}-\omega_{ln})}{\omega_{mn}^2(\omega_{mn}-2\omega)}\end{aligned} \tag{224}$$

$$\begin{aligned}\frac{i}{2\omega}\sigma_{II}^{abc}(-2\omega,\omega,\omega) = {}& \frac{i}{2}\int\frac{d\mathbf{k}}{4\pi^3}\\ &\sum_{nml}\frac{f_{nm}}{\omega_{mn}^2(\omega_{mn}-\omega)}\\ &[\omega_{nl}r^a_{lm}\{r^b_{mn}r^c_{nl}\}-\omega_{lm}r^a_{nl}\{r^b_{lm}r^c_{mn}\}]\\ &+\sum_{nm}\frac{f_{nm}r^a_{nm}\{\Delta^b_{mn}r^c_{nm}\}}{\omega_{mn}^2(\omega_{mn}-\omega)},\end{aligned} \tag{225}$$

1 Please note that Ref. [138] wrongly includes a term $\Delta^a_{nm}\{r^b_{mn}r^c_{nm}\}$ in σ which is zero by time-reversal symmetry as shown in Ref. [226].

and for linear electro-optic (LEO) coefficient, i.e. $\chi^{(2)}(-\omega,\omega,0)$

$$\begin{aligned}\chi^{abc}_{II}(-\omega,\omega,0) =& \frac{1}{2}\sum_{nml}\int\frac{d\mathbf{k}}{4\pi^3}\\ & \frac{f_{nm}}{(\omega_{mn}-\omega)}\left[\frac{r^a_{nm}r^c_{ml}r^b_{ln}}{\omega_{lm}}+\frac{r^a_{nm}r^b_{ml}r^c_{ln}}{\omega_{ln}}\right]\\ & +\left[\frac{f_{nl}r^a_{nm}r^c_{ml}r^b_{ln}}{(\omega_{ln}-\omega)\omega_{ml}}+\frac{f_{ml}r^a_{nm}r^b_{ml}r^c_{ln}}{(\omega_{ml}-\omega)\omega_{ln}}\right]\end{aligned} \tag{226}$$

$$\begin{aligned}\eta^{abc}_{II}(-\omega,\omega,0) =& \frac{i}{2}\sum_{nm}\int\frac{d\mathbf{k}}{4\pi^3}\\ & \frac{f_{nm}r^a_{nm}}{(\omega_{mn}-\omega)}\left[\frac{r^c_{mn}}{\omega_{mn}}\right]_{;c}\\ & +\left(\frac{f_{nm}}{2(\omega_{mn}-\omega)^2}(r^a_{nm}r^b_{nm;c}-r^a_{nm;c}r^b_{mn})\right)\end{aligned} \tag{227}$$

$$\begin{aligned}\frac{i}{\omega}\sigma^{abc}_{II}(-\omega,\omega,0) =& \frac{i}{2}\int\frac{d\mathbf{k}}{4\pi^3}\\ & \frac{1}{2}\sum_{nm}\frac{f_{nm}\Delta^a_{nm}}{\omega^2_{mn}(\omega_{mn}-\omega)}(r^b_{nm}r^c_{mn}-r^c_{nm}r^b_{mn})\\ & -\sum_{nm}\frac{f_{nm}}{\omega_{mn}(\omega_{mn}-\omega)}r^c_{nm;a}r^b_{mn}.\end{aligned} \tag{228}$$

These expressions have been implemented in the ABINIT software and they are available in the "optic" plugin of version 8.

As commonly done in the literature, we rewrite the SHG in terms of the $\mathbf{d}$ tensor according to

$$\chi^{(2)}_{\alpha\beta\gamma}(-2\omega,\omega,\omega) = 2d_{\alpha\beta\gamma}(\omega). \tag{229}$$

In LEO effect, we define the electro-optic tensor $\mathbf{r}$ defined between the change of inverse dielectric tensor and the electric field

$$\Delta(\epsilon^{-1}_{\alpha\beta}) = r_{\alpha\beta\gamma}E_\gamma. \tag{230}$$

The electro-optic tensor is composed of three terms in the Born-Oppenheimer approximation: the electronic (r^{el}), ionic (r^{ion}) and piezoelectric part (r^{piezo}). Here, we briefly summarize these contributions. For more details and derivations, we refer the reader to Ref. [14].

The electronic part of the LEO coefficient (clamped coefficient) can be linked to $\chi^{(2)}$, following the expression

$$r^{el}_{\alpha\beta\gamma} = -8\pi\sum_{\alpha'\beta'}(\epsilon^{-1}_{\alpha\alpha'})\chi^{(2)}_{\alpha'\beta'\gamma}(\epsilon^{-1}_{\beta'\beta}), \tag{231}$$

which can be rewritten along the principal axis as

$$r^{el}_{ij\gamma} = -\frac{8\pi}{n_i^2 n_j^2}\chi^{(2)}_{ij\gamma}. \tag{232}$$

From now on, we only use principal axis conventions for ij indices in this section.

The electric field induces displacements of ions that, in turn, change the dielectric function. The ionic part of the electro-optic coefficients comes from this effect and is therefore related to the Raman susceptibilities α and the Born effective charge

$$r^{ion}_{ij\gamma} = -\frac{4\pi}{\sqrt{\Omega_0} n_i^2 n_j^2}\sum_m \frac{\alpha^m_{ij} p_{m,\gamma}}{\omega^2_m}, \tag{233}$$

where $p_{m,\gamma}$ is the mode polarity

$$p_{m,\gamma} = \sum_{\kappa\alpha} Z^*_{\kappa,\gamma\alpha} U^m_{\kappa\alpha}. \tag{234}$$

The ion and electronic part of the electro-optic tensor form the clamped electro-optic tensor

$$r^{\eta}_{ij\gamma} = r^{el}_{ij\gamma} + r^{ion}_{ij\gamma}. \tag{235}$$

The last contribution to the electro-optic tensor is related to the converse piezoelectric effect. The electric field can induce a strain inside the crystal, through the piezo-electric strain coefficients ($d_{\gamma\nu\mu}$)

$$\eta_{\nu\mu} = \sum_\gamma d_{\gamma\nu\mu} E_\gamma, \tag{236}$$

and the change of the inverse dielectric tensor with the strain is given by the elasto-optic coefficients $p_{\alpha\beta\nu\mu}$, so that

$$r^{piezo}_{\alpha\beta\gamma} = \sum_{\mu\nu} p_{\alpha\beta\mu\nu} d_{\gamma\mu\nu}. \tag{237}$$

The total unclamped electro-optic coefficient is therefore

$$r_{ij\gamma} = r^{\eta}_{ij\gamma} + \sum_{\nu\mu} p_{ij\nu\mu} d_{\gamma\nu\mu}. \tag{238}$$

The three contribution arise in different frequency ranges, depending whether the crystal is allowed to relax or not (MHz regime), and

whether optical phonons vibrations are allowed (THz regime). This allows for selective experimental measurements, below the MHz regime for unclamped coefficient, in the MHz-GHz regime for clamped coefficients and in the near-infrared for electronic contributions. In our calculations, we focus on the electronic part of the electro-optic coefficient, that we call LEO coefficient for $\chi^{(2)}(-\omega, \omega, 0)$. The LEO coefficients are of importance for the longitudinal-optical phonons intensities in Raman spectroscopy, as discussed in Sec 3.2. They are used in Chap. 4 to compute ab initio Raman intensities of SiC and GaAs.

C

USE OF SYMMETRIES IN FROZEN-PHONON RAMAN CALCULATIONS

In this appendix, we detail how to use symmetry operations to reduce the number of calculations required for first-order but mainly for second-order Raman intensities.

In order to do so, we introduce new notations. The phonon mode $\mathfrak{m}$ can be written as a pair of two indices $\sigma\lambda(\sigma)$ where σ stands for the different mode frequencies and λ is an index looping on all the degenerate modes of the σ mode. For the sake of simplicity, we skip the σ dependence of λ in the equations. We also introduce the notations

$$\varepsilon^{\alpha\beta}(\mathbf{q},\sigma\lambda) = \frac{\partial \varepsilon^{\alpha\beta}}{\partial Q^{\sigma\lambda}(\mathbf{q})} \tag{239}$$

$$\varepsilon^{\alpha\beta}(\mathbf{q},\sigma\lambda,\sigma'\lambda') = \frac{\partial^2 \varepsilon^{\alpha\beta}}{\partial Q^{\sigma\lambda}(\mathbf{q})\partial Q^{\sigma'\lambda'}(-\mathbf{q})}. \tag{240}$$

From a direct generalization of Ref. [229], we can express the derivative at one $\mathbf{q}$-point with respect to another one, if they are related by symmetry operation $\mathbf{S}$

$$\varepsilon^{\alpha\beta}(\mathbf{S}\mathbf{q},\sigma\lambda) = \sum_{\gamma,\xi} S_{\gamma\alpha} S_{\xi\beta} \sum_{\lambda_1} \tau^{\sigma}_{\lambda_1\lambda}(\mathbf{q};\mathbf{S})\varepsilon^{\gamma\xi}(\mathbf{q},\sigma\lambda_1) \tag{241}$$

$$\varepsilon^{\alpha\beta}(\mathbf{S}\mathbf{q},\sigma\lambda,\sigma'\lambda') = \sum_{\gamma,\xi} S_{\gamma\alpha} S_{\xi\beta} \sum_{\lambda_1\lambda_2} \tau^{\sigma}_{\lambda_1\lambda}(\mathbf{q};\mathbf{S})\tau^{\sigma'}_{\lambda_2\lambda'}(\mathbf{q};\mathbf{S})\varepsilon^{\gamma\xi}(\mathbf{q},\sigma\lambda_1,\sigma'\lambda_2), \tag{242}$$

where $\tau^{\sigma}_{\lambda\lambda'}(\mathbf{q};\mathbf{S})$ are unitary matrices linking degenerate eigendisplacements of the same branch σ when the symmetry operation $\mathbf{S}$ is applied on the system.

Since these matrices are unitary, the following relation can be applied

$$\sum_{\lambda''} \tau^{(\sigma)}_{\lambda\lambda''}\tau^{*(\sigma)}_{\lambda'\lambda''} = \delta_{\lambda\lambda'}. \tag{243}$$

Now we can show how the invariants behave when applying a symmetry operation.

For first order, the invariant at $\mathbf{Sq}$ is

$$I_1^{(\sigma),\alpha\beta}(\mathbf{Sq}) = \sum_{\lambda} \left|\varepsilon^{\alpha\beta}(\mathbf{Sq},\sigma\lambda)\right|^2, \tag{244}$$

by substituting Eq. (241) into (244), we get

$$I_1^{(\sigma),\alpha\beta}(\mathbf{Sq}) = \sum_{\lambda_1} \left| \sum_{\gamma,\xi} S_{\gamma\alpha} S_{\xi\beta}\, \varepsilon^{\gamma\xi}(\mathbf{q},\sigma\lambda_1) \right|^2. \tag{245}$$

For second-order Raman, the invariant is

$$I_2^{(\sigma,\sigma'),\alpha\beta}(\mathbf{Sq}) = \sum_{\lambda\lambda'} \left|\varepsilon^{\alpha\beta}(\mathbf{Sq},\sigma\lambda,\sigma'\lambda')\right|^2. \tag{246}$$

Using the same approach, substituting (242) in (246)

$$I_2^{(\sigma,\sigma'),\alpha\beta}(\mathbf{Sq}) = \sum_{\lambda_1\lambda_2} \left| \sum_{\gamma,\xi} S_{\gamma\alpha} S_{\xi\beta}\, \varepsilon^{\gamma\xi}(\mathbf{q},\sigma\lambda_1,\sigma'\lambda_2) \right|^2. \tag{247}$$

For first-order Raman the invariant I_1 has to be evaluated at Γ only, so we can apply the equation (245) to symmetrize the tensor

$$\tilde{I_1}^{\alpha\beta}(\omega) = \sum_{\sigma} C(\sigma,\omega) \frac{1}{N_{sym}} \sum_{\mathbf{S}} \sum_{\lambda_1} \left| \sum_{\gamma,\xi} S_{\gamma\alpha} S_{\xi\beta}\, \varepsilon^{\gamma\xi}(\Gamma,\sigma\lambda_1) \right|^2 \delta(\omega-\omega^{\sigma}), \tag{248}$$

where $C(\sigma,\omega)$ contains the phonons frequencies, Bose-Einstein occupation factors, laser frequencies and physical constants.

For second-order Raman, we have to integrate over the whole BZ, but we can reduce the computational cost by restricting the q-points to the irreducible BZ part of the Full BZ

$$\tilde{I_2}^{\alpha\beta}(\omega) = \sum_{\sigma,\sigma'} C(\sigma,\sigma',\omega) \sum_{\mathbf{q}}^{BZ} I_2^{(\sigma,\sigma'),\alpha\beta}(\mathbf{q}) \delta(\omega-(\omega^{\sigma}+\omega^{\sigma'})) \tag{249}$$

$$= \sum_{\sigma,\sigma'} C(\sigma,\sigma',\omega) \sum_{\tilde{\mathbf{q}}}^{IBZ} w(\mathbf{q}) \frac{1}{N_{sym}} \sum_{\mathbf{S}} \sum_{\lambda_1\lambda_2} \left| \sum_{\gamma,\xi} S_{\gamma\alpha} S_{\xi\beta}\, \varepsilon^{\gamma\xi}(\mathbf{q},\sigma\lambda_1,\sigma'\lambda_2) \right|^2 \delta(\omega-(\omega^{\sigma}+\omega^{\sigma'})), \tag{250}$$

where $S(\mathbf{q})$ is the star of $\mathbf{q}$ and $w(\mathbf{q})$ is the weight of $\mathbf{q}$.

D

GAAS STUDY WITH DIFFERENT PSEUDOPOTENTIALS

Gallium Arsenide has been studied in Chap. 4 for the frequency-dependent LO and TO RI.

In Tab. 13, we report lattice parameters, dielectric properties, lattice dynamics and band structure obtained with different pseudopotentials.

The Trouiller-Martins pseudopotentials[1] contain only valence states with $4s^2\ 4p^1$ configuration and $4s^2\ 4p^3$ electronic configurations for Ga and As respectively. Cut-off energy of 15 Ha and 4-times shifted $6 \times 6 \times 6$ are sufficient to converge dielectric properties.

The so-called ONCVPSP pseudopotentials have been generated using the ONCVPSP package [230] and validated within the PseudoDojo framework [231]. The electronic configuration of Ga and As contain the semi-core electrons and are therefore $3d^{10}\ 4s^2\ 4p^1$ and $3d^{10}\ 4s^2\ 4p^3$ respectively. For all the flavours of ONCVPSP pseudopotentials used in this work (LDA or PBE, scalar-relativistic or fully-relativistic pseudopotentials), a cut-off energy of 42 Ha has been used with a 4-times shifted $8 \times 8 \times 8$ k-point grid, necessary to converge dielectric properties.

For FHI pseudopotentials, the same cut-off energy of 42 Ha as well as a 4-times shifted $8 \times 8 \times 8$ kpoint-grid has been used. The Ga pseudopotentials contains semi-core electrons ($3d^{10}\ 4s^2\ 4p^1$) while As has only 5 electrons in the valence states ($4s^2\ 4p^3$).

From these results, we observe that TM pseudopotentials are badly describing the system. Indeed, the relaxed band structure has an indirect band gap and the experimental lattice parameters gives very bad lattice dynamics.

The other LDA pseudopotentials (either FHI or ONCVPSP-LDA) are in much better agreement with experiments, leading to less than 1% of relative error on lattice parameters and very good phonon frequencies. This is in agreement with the all-electron calculation of 10.61 Bohr with LDA functional [232].

The PBE-GGA functional for ONCVPSP pseudopotentials is leading to an overestimation of less than 2% of error, consistently with all-electron

1 Available from the abinit package.

calculations of 10.88 Bohr with PBE functional [232]. This results in a less accurate description of phonon properties.

In all the cases, the band gap of the material is small in DFT, ranging from 0.15 to 0.5 eV (without considering TM). The split-off energy induced by SOC is consistently described as 0.34 eV for all the ONCVPSP pseudopotentials.

	a (Bohr)	ε^{∞}	ε^{0}	ω_{TO} (cm^{-1})	ω_{LO} (cm^{-1})	Z^*	E_g (eV)	Δ (eV)
TM (rel)	10.30	12.30	14.04	284.11	303.34	2.04	1.55	-
TM (exp)	10.68	14.07	16.36	250.18	269.81	2.18	0.61	-
FHI (rel)	10.64	14.46	16.27	266.22	282.42	2.05	0.37	-
FHI (exp)	10.68	14.77	16.65	262.98	279.2	2.07	0.297	-
ONCVPSP-PBE (rel)	10.86	15.10	17.30	252.27	270.06	2.21	0.15	-
ONCVPSP-PBE-SOC (rel)	10.86	15.24	17.45	252.06	267.72	2.21	0.04	0.33
ONCVPSP-PBE (exp)	10.68	13.59	15.45	268.26	286.09	2.11	0.52	-
ONCVPSP-PBE-SOC (exp)	10.68	13.59	15.45	268.26	286.09	2.11	0.42	0.34
ONCVPSP-LDA (rel)	10.58	13.95	15.76	268.97	285.94	2.06	0.49	-
ONCVPSP-LDA-SOC (rel)	10.59	13.96	15.78	268.74	285.71	2.06	0.37	0.35
ONCVPSP-LDA (exp)	10.68	14.72	16.70	260.38	277.38	2.11	0.29	-
ONCVPSP-LDA-SOC (exp)	10.68	14.72	16.70	260.38	277.38	2.11	0.18	0.35
Wang [134]	10.68	12.30	14.08	270.65	289.55	2.02	-	-
Exp [122, 131, 134]	10.68	10.89	12.5	267.3	285.0	2.07	-	-
Exp [233]	-	11.0	13.0	268.7	292.1	-	-	-
Exp [234]	-	10.86	12.85	268.41	292.01	-	-	-
Exp [133]	10.68	10.92	12.8	267.77	285.5	-	1.429	0.34

Table 13: Comparison of lattice parameters (a), dielectric properties (ε^{∞} and ε^{0}), lattice dynamics (ω_{TO}, ω_{LO} and Z^*) and band structure (direct gap E_g and split-off energy Δ if SOC is included) of GaAs.

E

ADDITIONAL INFORMATION ON TRANSITION-METAL DICHALCOGENIDES

In this appendix, we present some technical details linked with the measurements and the calculations of Raman intensities of WS_2 and WSe_2 monolayers presented in Sec. 4.2. This section has been published in Supporting Information of Ref. [48].

E.1 METHODS

E.1.1 *Sample Preparation*

Monolayered WS_2 samples synthesis is extensively described elsewhere. [235] Briefly, the sample consists of CVD grown triangular islands obtained by a two-step approach of thermal evaporation of tungsten trioxide (WO_3) onto Si/SiO_2 wafers followed by sulfurization at 800°. The islands present single crystal domains of about 30 μm^2 in area with a high degree of crystallinity. Within a single island, we can distinguish (by atomic force microscopy, AFM) the existence of two regions, the monolayer margins and the nucleation center composed by few layered WS_2. The size of the nucleation center composed of few layers of material varies from one island to others. For this study, a triangular island with a nucleation center smaller than $4\mu m^2$ was selected in order to ensure that the Raman characterization corresponded exclusively to the monolayer region. The monolayered WSe_2 sample was obtained by mechanical exfoliation of WSe_2 crystals produced using the chemical vapor transport method with iodine as transport agent. The thickness of the studied flake was analyzed by AFM, which confirmed the existence of a single layer sample (0.8 nm height) with an area larger than $40\mu m^2$.

The micro-Raman measurements were performed in both triple monochromator spectrometers, DILOR XY and Horiba T64000. Different laser sources (Ar/Kr, Ti/sapphire, and a dye laser with Rhodamine 6G and DCM) were used in order to excite the sample in a wide energy range from 457.9 to 670.0 nm. A back scattering geometry at room temperature was used and the laser power was kept below 0.6 mW to avoid sample damage. The accumulation times varied depending on the

excitation energy, ranging from 1 to 20 min. The laser spot diameter is about 2µm using the 100× objective, which ensures sampling regions more than 20 times smaller than the flake areas.

E.1.2 *Calculation details*

The FGR approximation was computed from first-principles calculations using the full-potential DFT package EXCITING [102] in which the wave functions are expanded in terms of linearized augmented plane-waves. The generalized gradient approximation for the exchange correlation was used, and the $\sigma\dot{L}$ term was added to the Hamiltonian in order to describe the spin−orbit coupling. A dense $48 \times 48 \times 1$ point grid and a scissor operator to reproduce the optical gap were used. For the calculation of the optical properties, a pseudopotential plane-wave approach (ABINIT code [86]) was preferred because of the guarantee of a complete basis set, which is particularly important and difficult to converge for optical properties. The caveat, however, is the lack of SOC implementation for the optical properties. Within this approximation, the monolayer systems were simulated in a box with a 50 Å separation between images in the perpendicular direction to the plane. A dense $32 \times 32 \times 1$ k-point grid and 300 bands were used to compute the screening, and a broadening of 0.05 and 0.07 Ha were used to reproduce the experimental measurements. For the finite difference calculations, displacements with amplitudes of 0.01 and 0.005 Å were considered and were verified to be in the linear regime. The fitting procedure presented in Tab. 14 was carried out as follows: the experimental data was first normalized and subsequently multiplied by the Si REP [81] to get the bare intensities; then, such normalized data were fitted to a function taking into account the square of the first element of Eq. (153) and finally renormalizing to the X_C peak of the A_1' band.

E.1.3 *Fitting of the Raman spectra*

The Raman spectra of TMD were fitted to a sum of Lorentzian functions as shown in Fig. 68 and 69.

WS_2 In the spectral range from 300 to 450 cm^{-1}, we include three Lorentzian functions corresponding to the A_1', E' and 2LA bands. As observed in Fig. 68, for excitation wavelengths above 488.0 nm we include an additional feature around 335 cm^{-1} which is described as the

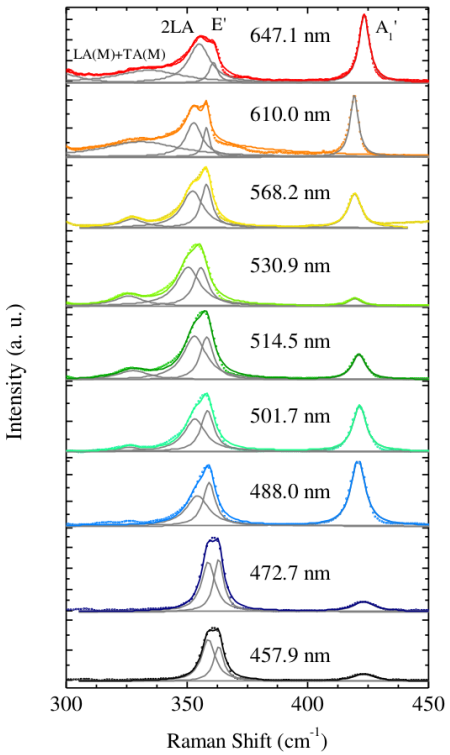

Figure 68: Selected Raman spectra of monolayered WS_2 (dots) registered with different excitation wavelengths. The Lorentzian fitting functions are shown by gray solid lines; the global fitting is shown by the colored solid line (corresponding to the excitation wavelength).

combination band between the LA and TA phonons at the M point of the Brillouin zone [157].

WSE$_2$ In the Raman spectra of WSe_2, shown in Fig. 69, the A_1' and E' bands are accidentally degenerate. Moreover, on the lower frequency side of the E' band we can observe an additional band corresponding to the E(M) phonon. Finally, the 2LA band of WSe_2 is fitted to two Lorentzian functions.

In Fig. 70 we show the REP of both 2LA contributions (260 and 263 cm^{-1}). The REPs show enhancements around 2.1 and 2.4 eV, corresponding to X_B and X_C exciton. Despite both bands are enhanced at the same excitation energies, slight differences are observed in the intensity ratio X_B /X_C, similar to what is observed for the normal bands, E' and A_1'.

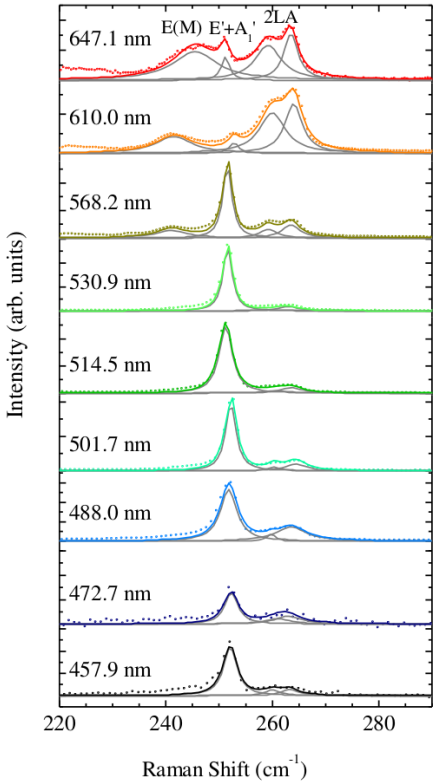

Figure 69: Selected Raman spectra of monolayered WSe_2 (dots) registered with different excitation wavelengths. The Lorentzian fitting functions are shown by gray solid lines; the global fitting is shown by the colored solid line (corresponding to the excitation wavelength).

E.2 ADDITIONAL CALCULATIONS

E.2.1 *Fermi Golden Rule Approximation*

With the FGR approximation we obtained information about the 2LA band for both materials by computing from first principles the band structure. Briefly, DFT+SOC electronic and phonon band structures are used to estimate the RI as a function of the laser energy, by taking into account the possible transitions via the FGR approximation. This approximation considers that the matrix elements related to radiation-electron, electron-phonon interactions and their combination with spin are constant.

The results are shown in Fig. 71 and they demonstrate a reasonable agreement with experimental data; the REP of the 2LA band is well re-

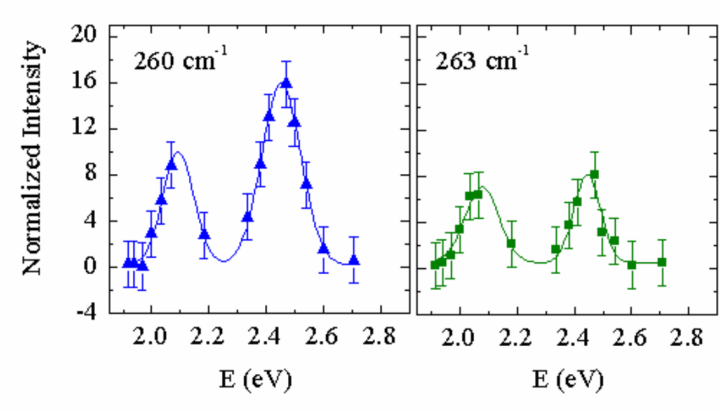

Figure 70: Experimental resonant excitation profiles of the 2LA contributions of WSe_2. The REPs of both 2LA contributions show two enhancements at ca. 2.1 and 2.4 eV, in resonance with the X_B and X_C exciton energies.

produced for both cases, WS_2 and WSe_2, showing the enhancement associated with the optical excitations. For the first-order Raman modes we observe that, in the case of WS_2, the FGR calculations reproduce the observed enhancements at the transitions X_A, X_B and X_C . However, note that the intensity of the Raman enhancement profile shown by the A_1' band is different to that of the E' band and both of them also differ from the calculated profile of Fig. 71. More interesting is the case of WSe_2 where the FGR calculations do not exhibit the lack of enhancement for the X_A and X_B transitions, observed experimentally for the first-order Raman bands. Such discrepancies cannot be captured when considering constant matrix elements. Finally, we observe that above 2.4 eV the experimental data display a peak, while the simulation keeps going up. The reason for this discrepancy is that for the LA mode we have used the M points; the FGR with constant matrix elements was obtained as the sum

$$\frac{1}{N_k N_q N_c N_v N_\alpha N_\beta} \sum_{k,q,c,v,\alpha,\beta} \frac{1}{(\omega_L - E^c_k + E^v_k - \omega^\alpha_{-q} - \omega^\beta_q - i\frac{\gamma}{2})} \times \frac{1}{(\omega_L - E^c_{k+q} + E^v_k - \omega^\alpha_{-q} - i\frac{\gamma}{2})(\omega_L - E^c_k + E^v_k - i\frac{\gamma}{2})}. \quad (251)$$

Here, we have considered q-points with energy close to half the observed energy with a tolerance of ± 5 cm^{-1}. Given the weight of the

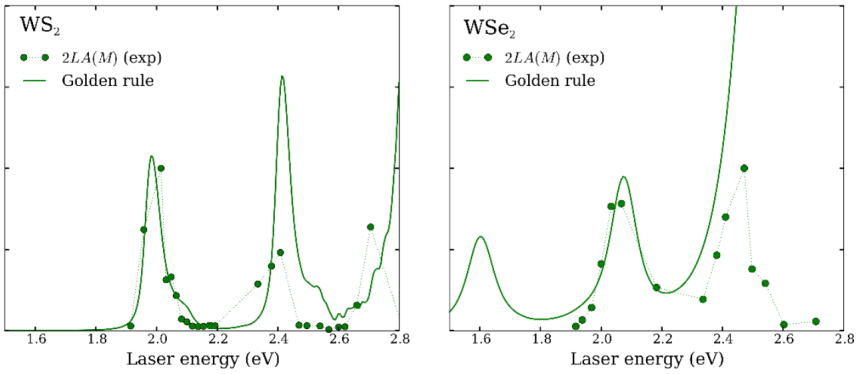

Figure 71: Comparative theoretical and experimental REP for the 2LA band. Experimental REP for the 2LA band in monolayered WS_2 and WSe_2 (dots) and the corresponding Fermi Golden rule calculations based on DFT considering SOC (solid lines). For both materials, the experimental Raman enhancement energies of the 2LA band are theoretically predicted.

q-points of high symmetry, this amounts to the same as considering the M point only. The sum goes for the two highest conduction bands and the four lowest conduction bands. Since in this model there are no many body effects, after the two peaks corresponding to the direct transitions at the K point, there will be the continuum in which all the available states sum. Thus, at higher energies the intensity keeps going up and the model breaks down.

E.2.2 *Bethe-Salpeter Equation*

The intensity of the Raman scattered signal is proportional to the change of the dielectric function (ε) with respect to vibrations (see Eq. (152) in the main manuscript). In practice, the BSE is solved in order to obtain ε which takes into account electron-hole interactions that correctly describe the excitonic states, which as mentioned above, dominate the optical properties of these systems. For technical reasons (see Methods, Sec. E.1), the approximation presented in this work is based on the single particle picture and SOC is neglected. In Tab. 14, we summarize the BSE approximation parameters.

Note that when looking at the oscillator strength only, the materials seem quite similar with $f_\lambda(X_A) < f_\lambda(X_C)$ in both cases. However, the

	WS_2		WSe_2	
	X_A	X_C	X_A	X_C
E'_λ	2.57	-0.92	2.07	-3.21
f_λ	67.66	594.63	78.32	529.24
f'_λ	-53.41	7017.50	-53.69	-5781.51
$f_\lambda E'_\lambda$	173.69	-549.87	161.83	-1591.24

Table 14: Details of the BSE-computed oscillator strength, binding energies and their corresponding derivatives for WS_2 and WSe_2.

derivative of the exciton binding energy with respect to the displacement for the two materials is different: $|E'(X_A)| > |E'(X_C)|$ for WS_2, while $|E'(X_A)| < |E'(X_C)|$ in WSe_2. One could then say that in the case of WS_2, the ratio in the change in exciton binding energy "levels up" the contribution of the two excitations to the REP, while in the case of WSe_2, the ratio increases the contribution of the two excitations to the REP. This is very clear when plotting the calculated REP intensity without renormalization with respect to the Si REP, Fig. 72.

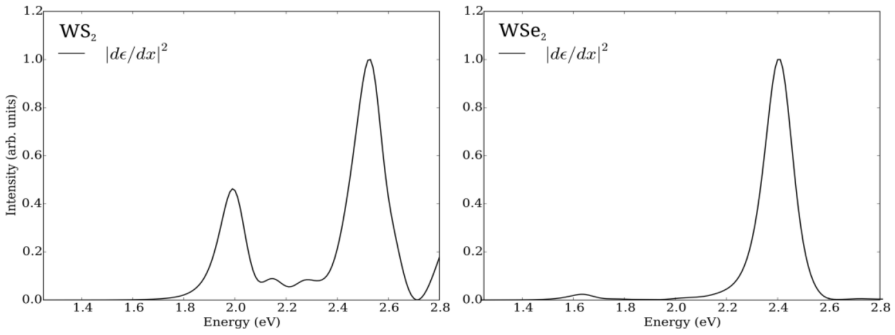

Figure 72: REP calculated from first principles as the derivative with respect to displacements of the BSE-computed dielectric function.

Therefore, we could say that the difference of the two materials comes from

$$|E'^{X_A}_\lambda / E'^{X_C}_\lambda|_{WS_2} > |E'^{X_A}_\lambda / E'^{X_C}_\lambda|_{WSe_2} \tag{252}$$

resulting in REP

$$|f_\lambda E'^{X_A}_\lambda / f_\lambda E'^{X_C}_\lambda|^2_{WS_2} >> |f_\lambda E'^{X_A}_\lambda / f_\lambda E'^{X_C}_\lambda|^2_{WSe_2}. \tag{253}$$

Since the change in exciton binding energy is not measurable, we decided to use fE' as the effective coupling term.

F

NUMERICAL TECHNIQUES FOR TEMPERATURE-DEPENDENT BETHE-SALPETER HAMILTONIAN

This section aims at describing algorithms to obtain the dielectric function $\varepsilon(\omega)$ for general complex matrix H

$$\varepsilon(\omega) = 1 - 4\pi\langle P|(H - \omega I)^{-1}|P\rangle. \tag{254}$$

F.1 DIRECT DIAGONALIZATION

For a general matrix H, two sets of eigenvectors exist: the left y and right x eigenvectors, such as

$$Hx = \lambda x \tag{255}$$
$$y^\dagger H = y^\dagger \lambda, \tag{256}$$

where λ are the eigenvalues that are the same in left and right eigenproblems[1]

We can write these relations with matrices X and Y containing the eigenvectors as columns and D containing eigenvalues on the diagonal

$$HX = XD \tag{257}$$
$$Y^\dagger H = DY^\dagger. \tag{258}$$

One can choose X and Y such as $Y^\dagger X$ is the identity matrix,[2] so

$$X = (Y^\dagger)^{-1}. \tag{259}$$

We can therefore expand the matrix H as

$$H = \sum_i \mathbf{x}_i \lambda_i \mathbf{y}_i^\dagger. \tag{260}$$

1 The notation for left eigenvectors differs from the one commonly used in which y appears without star.

2 Other normalizations are possible depending on the algorithm used to diagonalize the Hamiltonian.

The dielectric function (254) can therefore be rewritten as

$$\varepsilon(\omega) = 1 - 4\pi \sum_i \langle P|x_i\rangle (\lambda_i - \omega)^{-1} \langle y_i|P\rangle. \tag{261}$$

In the case of hermitian matrices, the left and right eigenvectors are equal ($X = Y$) and the expression (261) becomes

$$\varepsilon(\omega) = 1 - 4\pi \sum_i \langle P|x_i\rangle (\lambda_i - \omega)^{-1} \langle x_i|P\rangle. \tag{262}$$

F.2 BI-LANCZOS ALGORITHM

The goal of the Bi-Lanczos algorithm is to create two sets of vectors that are bi-orthogonal. We note these two sets of vectors $\{\psi_n\}$ and $\{\tilde{\psi}_n\}$. These sets of vectors belong to Krylov spaces made of H and $H^\dagger$ application on ψ_0 and $\tilde{\psi}_0$ respectively:

$$\psi_n \in \mathcal{K}_n := \text{span}(\psi_0, H\psi_0, ..., H^n\psi_0) \tag{263}$$
$$\tilde{\psi}_n \in \mathcal{L}_n := \text{span}(\tilde{\psi}_0, H^\dagger\tilde{\psi}_0, ..., (H^\dagger)^n\tilde{\psi}_0). \tag{264}$$

The bi-orthogonality translates to

$$\langle \tilde{\psi}_m|\psi_n\rangle = \begin{cases} 0 & \text{if} \quad m \neq n \\ \delta_n \neq 0 & \text{if} \quad m = n \end{cases}. \tag{265}$$

We immediately see that if H is hermitian, $\psi_n = \tilde{\psi}_n$ and both sets of vectors are equal and form a basis.

As $\mathcal{K}_n$ and $\mathcal{L}_n$ can be written from the set of vectors

$$\mathcal{K}_n = \text{span}(\psi_0, \psi_1, ..., \psi_n) \tag{266}$$
$$\mathcal{L}_n = \text{span}(\tilde{\psi}_0, \tilde{\psi}_1, ..., \tilde{\psi}_n) \tag{267}$$

one directly notices that

$$\psi_n \perp \mathcal{L}_{n-1} \tag{268}$$
$$\tilde{\psi}_n \perp \mathcal{K}_{n-1}. \tag{269}$$

Building the n^{th} vector of the chain can be done as

$$\psi_n \tau_{n,n-1} = H\psi_{n-1} - \tau_{n-1,n-1}\psi_{n-1} - ... - \tau_{0,n-1}\psi_0 \tag{270}$$
$$\tilde{\psi}_n \tau^c_{n,n-1} = H^\dagger\tilde{\psi}_{n-1} - \tau_{n-1,n-1}\tilde{\psi}_{n-1} - ... - \tau_{0,n-1}\tilde{\psi}_0 \tag{271}$$

by choosing the values of $\tau_{k,n-1}$ to get the orthogonality fulfilled. The value of $\tau_{n,n-1} = \gamma_{n-1}$ is arbitrary and changes the normalization of the vectors.

The matrices X, Y, T, T^c and the diagonal matrix D are now introduced to ease the writing

$$X_{nm} = [\psi_m]_n \tag{272}$$
$$Y_{nm} = [\tilde{\psi}_m]_n \tag{273}$$
$$T_{nm} = \tau_{n,m} \tag{274}$$
$$T^c_{nm} = \tau^c_{n,m} \tag{275}$$
$$D_{nm} = \delta_n \delta_{n,m}. \tag{276}$$

One can immediately see that T and T^c are upper Hessenberg matrices, by definition.

In matrix notation, the bi-orthogonality property (265) becomes

$$Y^\dagger X = D \tag{277}$$

whereas the iteration procedure Eqs. (270) and (271) become

$$HX = XT + \psi_n \tau_{n,n-1} e_n^T \tag{278}$$
$$H^\dagger Y = YT^c + \tilde{\psi}_n \tau^c_{n,n-1} e_n^T, \tag{279}$$

where e_n^T is the n^{th} row of the identity matrix.

From Eqs. (268) and (269), one has

$$Y^\dagger H X = DT \tag{280}$$
$$X^\dagger H^\dagger Y = D^\dagger T^c \tag{281}$$

and therefore

$$DT = (T^c)^\dagger D. \tag{282}$$

As T is upper Hessenberg and $(T^c)^\dagger$ is lower Hessenberg, these two matrices must be tridiagonal:

$$T = \begin{bmatrix} \alpha_0 & \beta_0 & & & \\ \gamma_0 & \alpha_1 & \beta_1 & & \\ & \gamma_1 & \ddots & & \\ & & & & \beta_{n-2} \\ & & & \gamma_{n-2} & \alpha_{n-1} \end{bmatrix} \tag{283}$$

and

$$T^c = \begin{bmatrix} \alpha_0^c & \beta_0^c & & & \\ \gamma_0^c & \alpha_1^c & \beta_1^c & & \\ & \gamma_1^c & \ddots & & \\ & & & & \beta_{n-2}^c \\ & & & \gamma_{n-2}^c & \alpha_{n-1}^c \end{bmatrix}. \tag{284}$$

From Eq. (282), one gets the following relations

$$\alpha_n = (\alpha_n^c)^* \tag{285}$$
$$\beta_n \delta_n = (\gamma_n^c)^* \delta_{n+1} \tag{286}$$
$$(\beta_n^c)^* \delta_n = \gamma_n \delta_{n+1}. \tag{287}$$

Different choices are possible to fulfill these relations among which

$$\beta_n = (\gamma_n^c)^* \tag{288}$$
$$\gamma_n = (\beta_n^c)^* \tag{289}$$

allows to have all $\delta_n = 1$ (if $\langle \tilde{\psi}_0 | \psi_0 \rangle = 1$) and $T^c = T^\dagger$.

The iteration procedure Eqs. (270) and (271) can now be rewritten as

$$H\psi_n = \psi_{n+1}\gamma_n + \alpha_n \psi_n + \beta_{n-1}\psi_{n-1} \tag{290}$$
$$H^\dagger \tilde{\psi}_n = \tilde{\psi}_{n+1}(\beta_n)^* + (\alpha_n)^* \tilde{\psi}_n + (\gamma_n)^* \tilde{\psi}_{n-1}, \tag{291}$$

from which the coefficients can be fixed by projecting Eq. (290) on $\tilde{\psi}_{n-1}$, $\tilde{\psi}_n$ and $\tilde{\psi}_{n-1}$ to get

$$\beta_{n-1} = \tilde{\psi}_{n-1}^\dagger H \psi_n \tag{292}$$
$$\alpha_n = \tilde{\psi}_n^\dagger H \psi_n \tag{293}$$
$$\gamma_n = \tilde{\psi}_{n+1}^\dagger H \psi_n. \tag{294}$$

The Bi-Lanczos algorithm is explicited in Code 1.

Data : ψ_0 and $\tilde{\psi_0}$ such as $\tilde{\psi_0}^\dagger \psi_0 = 1$, $\beta_{-1} = 0$
Result : ψ_i and $\tilde{\psi}_i$ the bi-orthogonal vectors sets, α_i, β_i and γ_i the tridiagonal representation of H in the basis.

for $n = 0, 1, \ldots$ **do**
  $\alpha_n = \tilde{\psi}_n^\dagger H \psi_n$
  $t = H\psi_n - \alpha_n \psi_n - \beta_{n-1}\psi_{n-1}$
  $\tilde{t} = H^\dagger \tilde{\psi}_n - (\alpha_n)^* \tilde{\psi}_n - (\gamma_{n-1})^* \tilde{\psi}_{n-1}$
  $\tilde{\delta} = \tilde{t}^\dagger t$
  if $\tilde{\delta} = 0$ **then**
    STOP ! (breakdown !)
  else
    Choose γ_n and β_n such as:
    $\gamma_n (\beta_n)^* = \tilde{\delta}$
    $\psi_{n+1} = t/\gamma_n$;
    $\tilde{\psi}_{n+1} = \tilde{t}/(\beta_n)^*$;
  end
end

Algorithm 1 : Bi-Lanczos algorithm

F.3 CONTINUED FRACTION FORMULA

The dielectric function is obtained from the inverse of $H - \omega I$. We can define the Green's function operator matrix elements G_{ij} as

$$G_{ij} = \langle \tilde{\psi}_i | (H - \omega I)^{-1} | \psi_j \rangle = (T - \omega I)^{-1}_{ij}, \tag{295}$$

and therefore the dielectric function is expressed in terms of G_{00}.

If we express $T - \omega I$ as a UDL product, with U an upper-diagonal matrix, D a diagonal matrix and L a lower-diagonal, we get

$$T - \omega I = \begin{bmatrix} \alpha_0 - \omega & \beta_0 & & & & \\ \gamma_0 & \alpha_1 - \omega & \beta_1 & & & \\ & \gamma_1 & \ddots & & & \\ & & & & \beta_{n-2} & \\ & & & \gamma_{n-2} & \alpha_{n-1} - \omega \end{bmatrix} \tag{296}$$

$$= \begin{bmatrix} 1 & u_0 & 0 & \dots & \\ 0 & 1 & u_1 & 0 & \dots \\ \dots & \ddots & & & \\ \dots & & & 0 & 1 \end{bmatrix} \begin{bmatrix} d_0 & 0 & \dots & \\ 0 & d_1 & 0 & \dots \\ \dots & \ddots & & \\ \dots & & & d_{n-1} \end{bmatrix} \begin{bmatrix} 1 & 0 & 0 & \dots \\ l_0 & 1 & 0 & \dots \\ \dots & l_1 & 1 & \ddots \\ \dots & & & 1 \end{bmatrix}. \tag{297}$$

Solving Eq. (297) gives rise to the following equations

$$u_i = \frac{\beta_i}{d_{i+1}} \tag{298}$$

$$l_i = \frac{\gamma_i}{d_{i+1}} \tag{299}$$

$$d_{n-1} = \alpha_{n-1} - \omega \tag{300}$$

$$d_i = \alpha_i - \omega - u_i l_i d_{i+1} = \alpha_i - \omega - \frac{\beta_i \gamma_i}{d_{i+1}}. \tag{301}$$

Using the UDL decomposition, one has access to the matrix elements of the Green matrix elements, as

$$(T - \omega I)_{ij} G_{j0} = \delta_{i0}, \tag{302}$$

one gets

$$G_{00} = \frac{1}{d_0} \tag{303}$$

$$G_{i+10} = -\frac{\gamma_i}{d_{i+1}} G_{i0}. \tag{304}$$

The dielectric function (254) can then be obtained from the continued fraction formula

$$\langle \psi_0 | (H - \omega I)^{-1} | \psi_0 \rangle = \cfrac{1}{\alpha_0 - \omega - \cfrac{\beta_0 \gamma_0}{\alpha_1 - \omega - \cfrac{\beta_1 \gamma_1}{\dots}}}. \tag{305}$$

In case of a hermitian matrix H, we observe that α is real and $\gamma = \beta^*$ therefore $\tilde{t} = t$ and $\tilde{\psi}_n = \psi_n^*$. The X and Y matrices are equal, $T_c = T$ and takes the hermitian tri-diagonal form

$$T = \begin{bmatrix} \alpha_0 & \beta_0 & & & \\ \beta_0^* & \alpha_1 & \beta_1 & & \\ & \beta_1^* & \ddots & & \\ & & & & \beta_{n-2} \\ & & & \beta_{n-2}^* & \alpha_{n-1}. \end{bmatrix} \tag{306}$$

The dielectric function (254) therefore becomes

$$\langle \psi_0 | (H - \omega I)^{-1} | \psi_0 \rangle = \cfrac{1}{\alpha_0 - \omega - \cfrac{\beta_0^2}{\alpha_1 - \omega - \cfrac{\beta_1^2}{\cdots}}}, \tag{307}$$

and the algorithm becomes the simple Lanczos algorithm described in Code 2.

Data : ψ_0 such as $||\psi_0||^2 = 1$, $\beta_{-1} = 0$
Result : ψ_i is an orthogonal vectors set, α_i, β_i the tridiagonal representation of H in the basis.
for $n = 0, 1, \ldots$ **do**
  $\alpha_n = \psi_n^\dagger H \psi_n$
  $t = H\psi_n - \alpha_n \psi_n - \beta_{n-1}\psi_{n-1}$
  $\delta = ||t||^2$
  if $\delta = 0$ **then**
    STOP ! (breakdown !)
  else
    $\beta_n = \sqrt{\delta}$
    $\psi_{n+1} = t/\gamma_n$;
  end
end

Algorithm 2 : Lanczos algorithm

BIBLIOGRAPHY

[1] P. Y. Yu and M. Cardona, *Fundamentals of semiconductors: physics and material properties* (Springer, 2010).

[2] W. Weber and R. Merlin, *Raman scattering in materials science*, edited by W. Weber and R. Merlin (Springer, 2000).

[3] M. Cardona and G. Guntherodt, *Light scattering in solids / edited by M. Cardona ; with contributions by M.H. Brodsky ... [et al.]* (Springer-Verlag Berlin ; New York, 1975).

[4] P. Hohenberg and W. Kohn, "Inhomogeneous electron gas," Phys. Rev. **136**, B864–B871 (1964).

[5] W. Kohn and L. J. Sham, "Self-consistent equations including exchange and correlation effects," Phys. Rev. **140**, A1133–A1138 (1965).

[6] R. M. Martin, *Electronic structure: basic theory and practical methods* (Cambridge, 2004).

[7] S. Baroni, P. Giannozzi, and A. Testa, "Green's-function approach to linear response in solids," Phys. Rev. Lett. **58**, 1861–1864 (1987).

[8] X. Gonze and C. Lee, "Dynamical matrices, born effective charges, dielectric permittivity tensors, and interatomic force constants from density-functional perturbation theory," Phys. Rev. B **55**, 10355–10368 (1997).

[9] S. Baroni, S. de Gironcoli, A. Dal Corso, and P. Giannozzi, "Phonons and related crystal properties from density-functional perturbation theory," Rev. Mod. Phys. **73**, 515–562 (2001).

[10] R. W. Godby and R. J. Needs, "Metal-insulator transition in Kohn-Sham theory and quasiparticle theory," Phys. Rev. Lett. **62**, 1169–1172 (1989).

[11] P. Ghosez, X. Gonze, and R. W. Godby, "Long-wavelength behavior of the exchange-correlation kernel in the Kohn-Sham theory of periodic systems," Phys. Rev. B **56**, 12811–12817 (1997).

[12] S. Baroni and R. Resta, "*Ab initio* calculation of the low-frequency Raman cross section in silicon," Phys. Rev. B **33**, 5969–5971 (1986).

[13] M. Veithen, X. Gonze, and P. Ghosez, "First-principles study of the electro-optic effect in ferroelectric oxides," Phys. Rev. Lett. **93**, 187401 (2004).

[14] M. Veithen, X. Gonze, and P. Ghosez, "Nonlinear optical susceptibilities, Raman efficiencies, and electro-optic tensors from first-principles density functional perturbation theory," Phys. Rev. B **71**, 125107 (2005).

[15] X. Gonze, G.-M. Rignanese, and R. Caracas, "First-principle studies of the lattice dynamics of crystals, and related properties," Z. Kristallogr. **220**, 458 (2005).

[16] P. Hermet, G. Fraysse, A. Lignie, P. Armand, and P. Papet, "Density functional theory predictions of the nonlinear optical properties in α-quartz-type germanium dioxide," J. Phys. Chem. C **116**, 8692–8698 (2012).

[17] J. Zhang, X. Li, B. Xu, and K. Yao, "First-principles study of the ferroelectric and optical properties of $BaTeMo_2O_9$," J. Alloys. Comp. **509**, 4929–4934 (2011).

[18] R. Caracas and E. Bobocioiu, *Wurm database*, `http://www.wurm.info`.

[19] R. Caracas and E. Bobocioiu, "The wurm project - a freely available web-based repository of computed physical data for minerals," Am. Mineral. **96**, 437 (2011).

[20] P Knoll and C Ambrosch-Draxl, "Raman scattering of atomic vibrations in anharmonic potentials," in Proceedings of the international workshop on anharmonic properties of high - tc cuprates, Eds. Eds. D. Mihailovic, G. Ruani, E. Kalids, and K. A. Müller (1995), p. 220.

[21] C. Ambrosch-Draxl, H. Auer, R. Kouba, E. Y. Sherman, P. Knoll, and M. Mayer, "Raman scattering in YBa2Cu3O7: a comprehensive theoretical study in comparison with experiments," Phys. Rev. B **65**, 064501 (2002).

[22] P. Puschnig, C. Ambrosch-Draxl, R. W. Henn, and A. Simon, "Electronic properties and Raman spectra of rare-earth carbide halides investigated from first principles," Phys. Rev. B **64**, 024519 (2001).

[23] P. Ravindran, A. Kjekshus, H. Fjellvag, P. Puschnig, C. Ambrosch-Draxl, L. Nordstrom, and B. Johansson, "Raman- and infrared-active phonons in superconducting and non-superconducting rare-earth transition-metal borocarbides from full-potential calculations," Phys. Rev. B **67**, 104507 (2003).

[24] J. Spitaler, E. Y. Sherman, and C. Ambrosch-Draxl, "Zone-center phonons in NaV2O5: a comprehensive ab-initio study including Raman spectra and electron-phonon interaction," Phys. Rev. B **75**, 014302 (2007).

[25] J. Spitaler, E. Y. Sherman, and C. Ambrosch-Draxl, "First-principles study of phonons, optical properties, and Raman spectra in MgV2O5," Phys. Rev. B **78**, 064304 (2008).

[26] J. Spitaler, E. Y. Sherman, C. Ambrosch-Draxl, and H. G. Evertz, "Lattice vibrations in CaV2O5 and their manifestations: a theoretical study based on density functional theory," New J. Phys. 11 **70**, 113009 (2009).

[27] A. K. Ganguly and J. L. Birman, "Theory of lattice Raman scattering in insulators," Phys. Rev. **162**, 806–816 (1967).

[28] A. Garcia-Cristobal, A. Cantarero, C. Trallero-Giner, and M. Cardona, "Excitonic model for second-order resonant Raman scattering," Phys. Rev. B **49**, 13430–13445 (1994).

[29] W. Aulbur, L. Jönsson, and J. Wilkins, "Quasiparticle calculations in solids," Solid State Phys. **54**, 1 (1999).

[30] G. Onida, L. Reining, and A. Rubio, "Electronic excitations: density-functional versus many-body Green's-function approaches," Rev. Mod. Phys. **74**, 601–659 (2002).

[31] S. Albrecht, L. Reining, R. Del Sole, and G. Onida, "*Ab Initio* calculation of excitonic effects in the optical spectra of semiconductors," Phys. Rev. Lett. **80**, 4510–4513 (1998).

[32] G. Kresse, M. Marsman, L. E. Hintzsche, and E. Flage-Larsen, "Optical and electronic properties of Si_3N_4 and α-SiO_2," Phys. Rev. B **85**, 045205 (2012).

[33] P. Rinke, A. Schleife, E. Kioupakis, A. Janotti, C. Rödl, F. Bechstedt, M. Scheffler, and C. G. Van de Walle, "First-principles optical spectra for F centers in MgO," Phys. Rev. Lett. **108**, 126404 (2012).

[34] M. Rohlfing and S. G. Louie, "Electron-hole excitations and optical spectra from first principles," Phys. Rev. B **62**, 4927–4944 (2000).

[35] J. Paier, M. Marsman, and G. Kresse, "Dielectric properties and excitons for extended systems from hybrid functionals," Phys. Rev. B **78**, 121201 (2008).

[36] M. Grüning, A. Marini, and X. Gonze, "Implementation and testing of Lanczos-based algorithms for Random-Phase approximation eigenproblems," Comp. Mater. Sci. **50**, 2148–2156 (2011).

[37] T. Sander, E. Maggio, and G. Kresse, "Beyond the Tamm–Dancoff approximation for extended systems using exact diagonalization," Phys. Rev. B **92**, 045209 (2015).

[38] E. Runge and E. K. U. Gross, "Density-functional theory for time-dependent systems," Phys. Rev. Lett. **52**, 997–1000 (1984).

[39] S. Botti, F. Sottile, N. Vast, V. Olevano, L. Reining, H.-C. Weissker, A. Rubio, G. Onida, R. Del Sole, and R. W. Godby, "Long-range contribution to the exchange-correlation kernel of time-dependent density functional theory," Phys. Rev. B **69**, 155112 (2004).

[40] E. Gross and K. Burke, edited by M. Marques, C. Ullrich, F. Nogueira, A. Rubio, K. Burke, and E. Gross, Vol. 706, Lecture Notes in Physics (Springer Berlin / Heidelberg, 2006).

[41] S. Sharma, J. K. Dewhurst, A. Sanna, and E. K. U. Gross, "Bootstrap approximation for the exchange-correlation kernel of time-dependent density-functional theory," Phys. Rev. Lett. **107**, 186401 (2011).

[42] A. C. Ferrari and D. M. Basko, "Raman spectroscopy as a versatile tool for studying the properties of graphene," Nat Nano **8**, 235–246 (2013).

[43] C. Thomsen and S. Reich, "Double resonant Raman scattering in graphite," Phys. Rev. Lett. **85**, 5214–5217 (2000).

[44] A. Berkdemir et al., "Identification of individual and few layers of WS_2 using Raman spectroscopy," Sci. Rep. **3**, 1755 (2013).

[45] E. del Corro, H. Terrones, A. Elias, C. Fantini, S. Feng, M. A. Nguyen, T. E. Mallouk, M. Terrones, and M. A. Pimenta, "Excited excitonic states in 1L, 2L, 3L, and bulk WSe_2 observed by resonant Raman spectroscopy," ACS Nano **8**, 9629–9635 (2014).

[46] A. Gaur, S. Sahoo, J. Scott, and R. Katiyar, "Electron–phonon interaction and double-resonance Raman studies in monolayer WS_2," J. Phys. Chem. C **119**, 5146–5151 (2015).

[47] G. Wang, M. M. Glazov, C. Robert, T. Amand, X. Marie, and B. Urbaszek, "Double resonant Raman scattering and valley coherence generation in monolayer WSe_2," Phys. Rev. Lett. **115**, 117401 (2015).

[48] E. del Corro et al., "Atypical exciton-phonon interactions in WS_2 and WSe_2 monolayers revealed by resonance Raman spectroscopy," Nano Lett. **16**, 2363–2368 (2016).

[49] P. Venezuela, M. Lazzeri, and F. Mauri, "Theory of double-resonant Raman spectra in graphene: intensity and line shape of defect-induced and two-phonon bands," Phys. Rev. B **84**, 035433 (2011).

[50] F. Herziger, M. Calandra, P. Gava, P. May, M. Lazzeri, F. Mauri, and J. Maultzsch, "Two-dimensional analysis of the double-resonant 2D Raman mode in bilayer graphene," Phys. Rev. Lett. **113**, 187401 (2014).

[51] A. C. Ferrari and J. e. Robertson, "Raman spectroscopy in carbons: from nanotubes to diamond," Phil. Trans. R. Soc. A **362**, 2267–2565 (2004).

[52] P. B. Allen and M. Cardona, "Temperature dependence of the direct gap of Si and Ge," Phys. Rev. B **27**, 4760–4769 (1983).

[53] P. B. Allen and V Heine, "Theory of the temperature dependence of electronic band structures," J. Phys. C: Solid State Physics **9**, 2305 (1976).

[54] P. B. Allen and M. Cardona, "Theory of the temperature dependence of the direct gap of germanium," Phys. Rev. B **23**, 1495 (1981).

[55] A. Marini, "*Ab Initio* finite-temperature excitons," Phys. Rev. Lett. **101**, 106405 (2008).

[56] F. Giustino, S. G. Louie, and M. L. Cohen, "Electron-phonon renormalization of the direct band gap of diamond," Phys. Rev. Lett. **105**, 265501 (2010).

[57] S. Poncé, G. Antonius, P. Boulanger, E. Cannuccia, A. Marini, M. Côté, and X. Gonze, "Verification of first-principles codes: comparison of total energies, phonon frequencies, electron–phonon coupling and zero-point motion correction to the gap between ABINIT and QE/Yambo," Computational Materials Science **83**, 341–348 (2014).

[58] X. Gonze and J. W. Zwanziger, "Density-operator theory of orbital magnetic susceptibility in periodic insulators," Phys. Rev. B **84**, 064445 (2011).

[59] E. Cannuccia and A. Marini, "Effect of the quantum zero-point atomic motion on the optical and electronic properties of diamond and trans-polyacetylene," Phys. Rev. Lett. **107**, 255501 (2011).

[60] E. Cannuccia and A. Marini, "Zero point motion effect on the electronic properties of diamond, trans-polyacetylene and polyethylene," The European Physical Journal B **85**, 1–7 (2012).

[61] A. Marini, S. Poncé, and X. Gonze, "Many-body perturbation theory approach to the electron-phonon interaction with density-functional theory as a starting point," Phys. Rev. B **91**, 224310 (2015).

[62] B. Monserrat, N. D. Drummond, and R. J. Needs, "Anharmonic vibrational properties in periodic systems: energy, electron-phonon coupling, and stress," Phys. Rev. B **87**, 144302 (2013).

[63] G. Antonius, S. Poncé, P. Boulanger, M. Côté, and X. Gonze, "Many-body effects on the zero-point renormalization of the band structure," Phys. Rev. Lett. **112**, 215501 (2014).

[64] S. Poncé, G. Antonius, Y. Gillet, P. Boulanger, J. Laflamme Janssen, A. Marini, M. Côté, and X. Gonze, "Temperature dependence of electronic eigenenergies in the adiabatic harmonic approximation," Phys. Rev. B **90**, 214304 (2014).

[65] J. P. Perdew and M. Levy, "Physical content of the exact Kohn-Sham orbital energies: band gaps and derivative discontinuities," Phys. Rev. Lett. **51**, 1884–1887 (1983).

[66] L. J. Sham and M. Schlüter, "Density-functional theory of the energy gap," Phys. Rev. Lett. **51**, 1888–1891 (1983).

[67] L. J. Sham and M. Schlüter, "Density-functional theory of the band gap," Phys. Rev. B **32**, 3883–3889 (1985).

[68] C. Friedrich and A. Schindlmayr, *Many-body perturbation theory: the GW approximation*, edited by J. Grotendorst, S. Blügel, and D. Marx, Vol. 31, NIC Series, pp. 335-355 (John von Neumann Institute for Computing, Jülich, 2006).

[69] F Bechstedt, *Many-body approach to electronic excitations: concepts and applications*, edited by M. Cardona, K. von Kltizing, R. Merlin, and H.-J. Queisser, Vol. 181, 0171-1873 (Springer Berlin Heidelberg, 2015).

[70] M. Giantomassi and M. Stankovski, *Many-body theory in ABINIT*, http://www.abinit.org/documentation/helpfiles/for-v8.0/tutorial/theory_mbt.html.

[71] S. Albrecht, G. Onida, and L. Reining, "Ab initio calculation of the quasiparticle spectrum and excitonic effects in Li_2O," Phys. Rev. B **55**, 10278–10281 (1997).

[72] A. L. Fetter and J. D. Walecka, *Quantum theory of many-particle systems* (McGraw-Hill, 1971).

[73] V. Olevano and L. Reining, "Excitonic effects on the silicon plasmon resonance," Phys. Rev. Lett. **86**, 5962–5965 (2001).

[74] S. L. Adler, "Quantum theory of the dielectric constant in real solids," Phys. Rev. **126**, 413–420 (1962).

[75] N. Wiser, "Dielectric constant with local field effects included," Phys. Rev. **129**, 62–69 (1963).

[76] G. Cappellini, R. Del Sole, L. Reining, and F. Bechstedt, "Model dielectric function for semiconductors," Phys. Rev. B **47**, 9892–9895 (1993).

[77] R. Haydock, "The recursive solution of the Schrödinger equation," Comput. Phys. Comm. **20**, 11–16 (1980).

[78] L. X. Benedict, E. L. Shirley, and R. B. Bohn, "Optical absorption of insulators and the electron-hole interaction: an *Ab Initio* calculation," Phys. Rev. Lett. **80**, 4514–4517 (1998).

[79] L. X. Benedict and E. L. Shirley, "Ab initio calculation of $\epsilon_2(\omega)$ including the electron-hole interaction: application to GaN and CaF_2," Phys. Rev. B **59**, 5441–5451 (1999).

[80] Y. Gillet, "Excitonic effects in frequency-dependent Raman spectra of solids: an ab initio approach," MA thesis (Université catholique de Louvain, 2012).

[81] Y. Gillet, M. Giantomassi, and X. Gonze, "First-principles study of excitonic effects in Raman intensities," Phys. Rev. B **88**, 094305 (2013).

[82] J. Deslippe, G. Samsonidze, D. A. Strubbe, M. Jain, M. L. Cohen, and S. G. Louie, "BerkeleyGW: a massively parallel computer package for the calculation of the quasiparticle and optical properties of materials and nanostructures," Comput. Phys. Comm. **183**, 1269–1289 (2012).

[83] F. Fuchs, C. Rödl, A. Schleife, and F. Bechstedt, "Efficient $\mathcal{O}(N^2)$ approach to solve the Bethe-Salpeter equation for excitonic bound states," Phys. Rev. B **78**, 085103 (2008).

[84] D. Kammerlander, S. Botti, M. A. L. Marques, A. Marini, and C. Attaccalite, "Speeding up the solution of the Bethe-Salpeter equation by a double-grid method and wannier interpolation," Phys. Rev. B **86**, 125203 (2012).

[85] X. Gonze et al., "A brief introduction to the ABINIT software package," Z. Kristallogr. **220**, 558 (2005).

[86] X. Gonze et al., "ABINIT : first-principles approach of materials and nanosystem properties," Comput. Phys. Comm. **180**, 2582 (2009).

[87] X. Gonze et al., "Recent developments in the ABINIT software package," Comput. Phys. Comm. **205**, 106 (2016).

[88] M. Rohlfing and S. G. Louie, "Electron-hole excitations in semiconductors and insulators," Phys. Rev. Lett. **81**, 2312–2315 (1998).

[89] M. A. Green, "Improved value for the silicon free exciton binding energy," AIP Advances **3**, 112104, – (2013).

[90] B. Arnaud and M. Alouani, "Local-field and excitonic effects in the calculated optical properties of semiconductors from first-principles," Phys. Rev. B **63**, 085208 (2001).

[91] A. Marini, R. Del Sole, and A. Rubio, "Bound excitons in time-dependent density-functional theory: optical and energy-loss spectra," Phys. Rev. Lett. **91**, 256402 (2003).

[92] K. Gilmore, J. Vinson, E. Shirley, D. Prendergast, C. Pemmaraju, J. Kas, F. Vila, and J. Rehr, "Efficient implementation of core-excitation Bethe–Salpeter equation calculations," Comput. Phys. Comm. **197**, 109–117 (2015).

[93] E. L. Shirley, "Optimal basis sets for detailed Brillouin-zone integrations," Phys. Rev. B **54**, 16464–16469 (1996).

[94] A. A. Maradudin and E. Burstein, "Relation between photoelasticity, electrostriction, and first-order Raman effect in crystals of the diamond structure," Phys. Rev. **164**, 1081–1099 (1967).

[95] L. Swanson and A. Maradudin, "Pseudopotential calculation of the Raman tensor for homopolar semiconductors," Solid State Commun. **8**, cited By 26, 859–865 (1970).

[96] L. Brey and C. Tejedor, "Raman tensor of covalent semiconductors," Solid State Commun. **48**, cited By 30, 403–406 (1983).

[97] W. Windl, P. Pavone, K. Karch, O. Schütt, D. Strauch, P. Giannozzi, and S. Baroni, "Second-order Raman spectra of diamond from ab initio phonon calculations," Phys. Rev. B **48**, 3164–3170 (1993).

[98] M. A. Renucci, J. B. Renucci, R. Zeyher, and M. Cardona, "Second-order Raman scattering in germanium in the vicinity of the E_1, $E_1 + \Delta_1$ edges," Phys. Rev. B **10**, 4309–4323 (1974).

[99] J. B. Renucci, R. N. Tyte, and M. Cardona, "Resonant Raman scattering in silicon," Phys. Rev. B **11**, 3885–3895 (1975).

[100] D. Griffiths, *Introduction to quantum mechanics*, Pearson international edition (Pearson Prentice Hall, 2005).

[101] W. D. Johnston, "Nonlinear optical coefficients and the Raman scattering efficiency of LO and TO phonons in acentric insulating crystals," Phys. Rev. B **1**, 3494–3503 (1970).

[102] A. Gulans, S. Kontur, C. Meisenbichler, D. Nabok, P. Pavone, S. Rigamonti, S. Sagmeister, U. Werner, and C. Draxl, "Exciting: a full-potential all-electron package implementing density-functional theory and many-body perturbation theory," J. Phys.: Condens. Matter **26**, 363202 (2014).

[103] J. L. Birman and R. Berenson, "Scattering tensors and Clebsch-Gordan coefficients in crystals," Phys. Rev. B **9**, 4512–4517 (1974).

[104] A. Compaan and H. J. Trodahl, "Resonance Raman scattering in Si at elevated temperatures," Phys. Rev. B **29**, 793–801 (1984).

[105] S. Goedecker, M. Teter, and J. Hutter, "Separable dual-space Gaussian pseudopotentials," Phys. Rev. B **54**, 1703–1710 (1996).

[106] H. J. Monkhorst and J. D. Pack, "Special points for Brillouin-zone integrations," Phys. Rev. B **13**, 5188–5192 (1976).

[107] R. W. G. Wyckoff, *Crystal structures* (Wiley, 1963).

[108] F. Bruneval and X. Gonze, "Accurate GW self-energies in a plane-wave basis using only a few empty states: towards large systems," Phys. Rev. B **78**, 085125 (2008).

[109] W. Ku and A. G. Eguiluz, "Band-gap problem in semiconductors revisited: effects of core states and many-body self-consistency," Phys. Rev. Lett. **89**, 126401 (2002).

[110] B. Arnaud and M. Alouani, "All-electron projector-augmented-wave GW approximation: application to the electronic properties of semiconductors," Phys. Rev. B **62**, 4464–4476 (2000).

[111] Landolt-Bornstein, *Zahlenwerte und funktionen aus naturwissenschaften und technik*, Vol. III, pt 23a (Springer- Verlag, 1982).

[112] Z. H. Levine and D. C. Allan, "Linear optical response in silicon and germanium including self-energy effects," Phys. Rev. Lett. **63**, 1719–1722 (1989).

[113] A. L. Cauchy, "Sur la dispersion de la lumière," B. Sci. Math. **14** (1836).

[114] D. L. Johnson, "Local field effects and the dielectric response matrix of insulators: a model," Phys. Rev. B **9**, 4475–4484 (1974).

[115] G. E. Jellison and F. A. Modine, "Optical functions of silicon between 1.7 and 4.7 eV at elevated temperatures," Phys. Rev. B **27**, 7466–7472 (1983).

[116] M. Gatti and F. Sottile, "Exciton dispersion from first principles," Phys. Rev. B **88**, 155113 (2013).

[117] S. Sharma, J. K. Dewhurst, and C. Ambrosch-Draxl, "Linear and second-order optical response of III-V monolayer superlattices," Phys. Rev. B **67**, 165332 (2003).

[118] S. Sharma and C. Ambrosch-Draxl, "Second-Harmonic optical response from first principles," Phys. Scripta **2004**, 128 (2004).

[119] H. J. Round, "A note on carborundum," Electrical World **19**, 309 (1907).

[120] M. Palummo, G. Onida, R. Del Sole, M. Corradini, and L. Reining, "Nonlocal density scheme for electronic-structure calculations," Phys. Rev. B **60**, 11329–11335 (1999).

[121] K Karch, F Bechstedt, P Pavone, and D Strauch, "Pressure-dependent dynamical and dielectric properties of cubic SiC," J. Phys.: Condens. Matter **8**, 2945 (1996).

[122] O. Madelung, *Group IV elements, IV-IV and III-V compounds.* Edited by O. Madelung, U. Rössler, and M. Schulz, Vol. 41A1 (Springer, 2001).

[123] A. Taylor and R. M. Jones, *Silicon carbide: a high temperature semiconductor. proceedings of the conference on silicon carbide. April 2-3, 1959*, edited by J. O'Connor and J. Smiltens (Oxford, Pergamon Press, 1960), pp. –.

[124] H. Nienhaus, T. Kampen, and W. Mönch, "Phonons in 3C-, 4H-, and 6H-SiC," Surf. Sci. **324**, L328 –L332 (1995).

[125] K. Karch, F. Bechstedt, P. Pavone, and D. Strauch, "Pressure-dependent properties of SiC polytypes," Phys. Rev. B **53**, 13400–13413 (1996).

[126] L. Patrick and W. J. Choyke, "Static dielectric constant of SiC," Phys. Rev. B **2**, 2255–2256 (1970).

[127] B. Wenzien, P. Käckell, F. Bechstedt, and G. Cappellini, "Quasiparticle band structure of silicon carbide polytypes," Phys. Rev. B **52**, 10897–10905 (1995).

[128] D. Bimberg, M. Altarelli, and N. O. Lipari, "A calculation of valence band masses, exciton and acceptor energies and the ground state properties of the electron-hole liquid in cubic SiC," Solid State Commun. **40**, 437–440 (1981).

[129] W. J. Choyke and L. Patrick, "Higher absorption edges in cubic SiC," Phys. Rev. **187**, 1041–1043 (1969).

[130] R. Püsche, M. Hundhausen, and L. Ley, "Raman excitation profiles of 3C-, 4H-, 6H-, 15R- and 21R-SiC," in Silicon carbide and related materials - 2002, Vol. 433, Materials Science Forum (July 2003), pp. 325–328.

[131] J. Mullin, B. Straughan, C. Driscoll, and A. Willoughby, in Inst. phys. conf. ser. Vol. 24 (1975), p. 275.

[132] D. E. Aspnes, "GaAs lower conduction-band minima: ordering and properties," Phys. Rev. B **14**, 5331–5343 (1976).

[133] A. Dargys and J. Kundrotas, *Handbook on physical properties of Ge, Si, GaAs and InP* (Science and Encyclopedia Publishers, 1994).

[134] S. Q. Wang and H. Q. Ye, "Ab initio investigation of the pressure dependences of phonon and dielectric properties for III-V semiconductors," J. Phys.: Condens. Matter **17**, 4475 (2005).

[135] D. W. Palmer, `www.semiconductors.co.uk`, 2006.02.

[136] M. Levinshtein and S. Rumyantsev, *Handbook series on semiconductor parameters*, edited by M. Levinshtein, S. Rumyantsev, and M. Shur, Vol. 1 (World Scientific, London, 1999).

[137] R. Trommer and M. Cardona, "Resonant Raman scattering in GaAs," Phys. Rev. B **17**, 1865–1876 (1978).

[138] J. L. P. Hughes and J. E. Sipe, "Calculation of second-order optical response in semiconductors," Phys. Rev. B **53**, 10751–10763 (1996).

[139] M. Cardona and G. Guntherodt, *Light scattering in solids II : basic concepts and instrumentation / edited by M. Cardona and G. Guntherodt* (Springer-Verlag Berlin [Germany], 1982).

[140] K. S. Novoselov, D. Jiang, F. Schedin, T. J. Booth, V. V. Khotkevich, S. V. Morozov, and A. K. Geim, "Two-dimensional atomic crystals," Proc. Natl. Acad. Sci. U. S. A. **102**, 10451–10453 (2005).

[141] B. Radisavljevic, A. Radenovic, J. Brivio, V. Giacometti, and A. Kis, "Single-layer MoS2 transistors," Nat Nano **6**, 147–150 (2011).

[142] H. S. Lee, S.-W. Min, Y.-G. Chang, M. K. Park, T. Nam, H. Kim, J. H. Kim, S. Ryu, and S. Im, "MoS2 Nanosheet phototransistors with thickness-modulated optical energy gap," Nano Lett. **12**, 3695–3700 (2012).

[143] H. Zeng, J. Dai, W. Yao, D. Xiao, and X. Cui, "Valley polarization in MoS2 monolayers by optical pumping," Nat Nano **7**, 490–493 (2012).

[144] R. Roldán, J. A. Silva-Guillén, M. P. López-Sancho, F. Guinea, E. Cappelluti, and P. Ordejón, "Electronic properties of single-layer and multilayer transition metal dichalcogenides MX2 (M = Mo, W and X = S, Se)," Annalen der Physik **526**, 347–357 (2014).

[145] W. Zhao, Z. Ghorannevis, K. K. Amara, J. R. Pang, M. Toh, X. Zhang, C. Kloc, P. H. Tan, and G. Eda, "Lattice dynamics in mono- and few-layer sheets of WS_2 and WSe_2," Nanoscale **5**, 9677–9683 (2013).

[146] A. Chernikov, T. C. Berkelbach, H. M. Hill, A. Rigosi, Y. Li, O. B. Aslan, D. R. Reichman, M. S. Hybertsen, and T. F. Heinz, "Exciton binding energy and nonhydrogenic rydberg series in monolayer WS_2," Phys. Rev. Lett. **113**, 076802 (2014).

[147] Y. Li, A. Chernikov, X. Zhang, A. Rigosi, H. M. Hill, A. M. van der Zande, D. A. Chenet, E.-M. Shih, J. Hone, and T. F. Heinz, "Measurement of the optical dielectric function of monolayer transition-metal dichalcogenides: MoS_2, $MoSe_2$, WS_2, and WSe_2," Phys. Rev. B **90**, 205422 (2014).

[148] H. M. Hill, A. F. Rigosi, C. Roquelet, A. Chernikov, T. C. Berkelbach, D. R. Reichman, M. S. Hybertsen, L. E. Brus, and T. F. Heinz, "Observation of excitonic Rydberg states in monolayer MoS2 and WS2 by photoluminescence excitation spectroscopy," Nano Lett. **15**, 2992–2997 (2015).

[149] Z. Ye, T. Cao, K. O'Brien, H. Zhu, X. Yin, Y. Wang, S. G. Louie, and X. Zhang, "Probing excitonic dark states in single-layer tungsten disulphide," Nature **513**, 214–218 (2014).

[150] K. He, N. Kumar, L. Zhao, Z. Wang, K. F. Mak, H. Zhao, and J. Shan, "Tightly bound excitons in monolayer WSe_2," Phys. Rev. Lett. **113**, 026803 (2014).

[151] A. Molina-Sánchez and L. Wirtz, "Phonons in single-layer and few-layer MoS_2 and WS_2," Phys. Rev. B **84**, 155413 (2011).

[152] J. M. Chen and C. S. Wang, "Second order Raman spectrum of MoS2," Solid State Commun. **14**, 857 (1974).

[153] K. Golasa, M. Grzeszczyk, P. Leszczynski, C. Faugeras, A. A. L. Nicolet, A. Wysmolek, M. Potemski, and A. Babinski, "Multiphonon resonant Raman scattering in MoS2," Appl. Phys. Lett. **104**, 092106 (2014).

[154] Q. Wang, P. Wu, G. Cao, and M. Huang, "First-principles study of the structural and electronic properties of $MoS_2 - WS_2$ and $MoS_2 - MoTe_2$ monolayer heterostructures," J. Phys. D: App. Phys. **46**, 505308 (2013).

[155] A. C. Ferrari et al., "Raman spectrum of graphene and graphene layers," Phys. Rev. Lett. **97**, 187401 (2006).

[156] B. Chakraborty, H. S. S. R. Matte, A. K. Sood, and C. N. R. Rao, "Layer-dependent resonant Raman scattering of a few layer MoS2," J. Raman Spectrosc. **44**, 92–96 (2013).

[157] M. A. Pimenta, E. del Corro, B. R. Carvalho, C. Fantini, and L. M. Malard, "Comparative study of Raman spectroscopy in graphene and MoS2-type transition metal dichalcogenides," Acc. Chem. Res. **48**, 41–47 (2015).

[158] K. F. Mak, C. Lee, J. Hone, J. Shan, and T. F. Heinz, "Atomically thin MoS_2: a new direct-gap semiconductor," Phys. Rev. Lett. **105**, 136805 (2010).

[159] N. Scheuschner, O. Ochedowski, M. Schleberger, and J. Maultzsch, "Resonant Raman profiles and μ-photoluminescence of atomically thin layers of molybdenum disulfide," physica status solidi (b) **249**, 2644–2647 (2012).

[160] B. R. Carvalho, L. M. Malard, J. M. Alves, C. Fantini, and M. A. Pimenta, "Symmetry-dependent exciton-phonon coupling in 2D and bulk MoS_2 observed by resonance Raman scattering," Phys. Rev. Lett. **114**, 136403 (2015).

[161] J.-U. Lee, J. Park, Y.-W. Son, and H. Cheong, "Anomalous excitonic resonance Raman effects in few-layered MoS2," Nanoscale **7**, 3229–3236 (2015).

[162] L. Sun et al., "Spin-orbit splitting in single-layer MoS_2 revealed by triply resonant Raman scattering," Phys. Rev. Lett. **111**, 126801 (2013).

[163] T. Sekine, T. Nakashizu, K. Toyoda, K. Uchinokura, and E. Matsuura, "Raman scattering in layered compound 2H-WS2," Solid State Commun. **35**, 371 (1980).

[164] T. Sekine, K. Uchinokura, T. Nakashizu, E. Matsuura, and R. Yoshizaki, "Dispersive Raman mode of layered compound 2H-MoS2 under the resonant condition," J. Phys. Soc. Jpn. **53**, 811 (1984).

[165] C. Sourisseau, F. Cruege, M. Fouassier, and M. Alba, "Second-order Raman effects, inelastic neutron scattering and lattice dynamics in 2H-WS2," Chem. Phys. **150**, 281 (1991).

[166] H. Terrones et al., "New first order Raman-active modes in few layered transition metal dichalcogenides," Sci. Rep. **4**, 4215–(2014).

[167] T. Livneh and J. E. Spanier, "A comprehensive multiphonon spectral analysis in mos 2," 2D Materials **2**, 035003 (2015).

[168] M. Grimsditch and M. Cardona, "Absolute cross-section for Raman scattering by phonons in silicon," Phys. Status Solidi B. **102**, 155–161 (1980).

[169] W. Zhao, Z. Ghorannevis, L. Chu, M. Toh, C. Kloc, P.-H. Tan, and G. Eda, "Evolution of electronic structure in atomically thin sheets of WS_2 and WSe_2," ACS Nano **7**, 791–797 (2013).

[170] S. Poncé, Y. Gillet, J. Laflamme Janssen, A. Marini, M. Verstraete, and X. Gonze, "Temperature dependence of the electronic structure of semiconductors and insulators," J. Chem. Phys. **143**, 102813, – (2015).

[171] R. M. Sternheimer, "Electronic polarizabilities of ions from the hartree-fock wave functions," Phys. Rev. **96**, 951–968 (1954).

[172] X. Gonze, "First-principles responses of solids to atomic displacements and homogeneous electric fields: implementation of a conjugate-gradient algorithm," Phys. Rev. B **55**, 10337–10354 (1997).

[173] S. Zollner, M. Cardona, and S. Gopalan, "Isotope and temperature shifts of direct and indirect band gaps in diamond-type semiconductors," Phys. Rev. B **45**, 3376–3385 (1992).

[174] P. B. Allen, "Solids with thermal or static disorder. I. one-electron properties," Phys. Rev. B **18**, 5217–5224 (1978).

[175] G. Antonius, S. Poncé, E. Lantagne-Hurtubise, G. Auclair, X. Gonze, and M. Côté, "Dynamical and anharmonic effects on the electron-phonon coupling and the zero-point renormalization of the electronic structure," Phys. Rev. B **92**, 085137 (2015).

[176] G. Grimvall, *The electron-phonon interaction in metals* (North-Holland Publishing Company, 1981).

[177] W. Eerenstein, N. D. Mathur, and J. F. Scott, "Multiferroic and magnetoelectric materials," Nature **442**, 759 (2006).

[178] M. Bibes, "Nanoferronics is a winning combination," Nat. Mater. **11**, 354 (2012).

[179] R. Ramesh and N. A. Spaldin, "Multiferroics: progress and prospects in thin films," Nat. Mater. **6**, 21 (2007).

[180] Y. S. Yang et al., "Above-bandgap voltages from ferroelectric photovoltaic devices," Nat Nano **5**, 143 (2010).

[181] M. Alexe and D. Hesse, "Tip-enhanced photovoltaic effects in bismuth ferrite," Nat. Commun. **2**, 256 (2011).

[182] J. Seidel, D. Fu, S.-Y. Yang, E. Alarcón-Lladó, J. Wu, R. Ramesh, and J. W. Ager, "Efficient photovoltaic current generation at ferroelectric domain walls," Phys. Rev. Lett. **107**, 126805 (2011).

[183] A. Bhatnagar, A. Roy Chaudhuri, Y. Heon Kim, D. Hesse, and M. Alexe, "Role of domain walls in the abnormal photovoltaic effect in BiFeO3," Nat. Commun. **4** (2013) 10.1038/ncomms3835.

[184] X. S. Xu et al., "Optical properties and magnetochromism in multiferroic $BiFeO_3$," Phys. Rev. B **79**, 134425 (2009).

[185] S. R. Basu, L. W. Martin, Y. H. Chu, M. Gajek, R. Ramesh, R. C. Rai, X. Xu, and J. L. Musfeldt, "Photoconductivity in bifeo3 thin films," Appl. Phys. Lett. **92**, 091905 (2008) 10.1063/1.2887908.

[186] J. F. Ihlefeld et al., "Optical band gap of $BiFeO_3$ grown by molecular-beam epitaxy," Appl. Phys. Lett. **92**, 142908 (2008) 10.1063/1.2901160.

[187] A. Kumar et al., "Linear and nonlinear optical properties of $BiFeO_3$," Appl. Phys. Lett. **92**, 121915, – (2008).

[188] A. J. Hauser, J. Zhang, L. Mier, R. A. Ricciardo, P. M. Woodward, T. L. Gustafson, L. J. Brillson, and F. Y. Yang, "Characterization of electronic structure and defect states of thin epitaxial $BiFeO_3$ films by UV-visible absorption and cathodoluminescence spectroscopies," Appl. Phys. Lett. **92**, 222901 (2008) 10.1063/1.2939101.

[189] R. Palai, R. S. Katiyar, H. Schmid, P. Tissot, S. J. Clark, J. Robertson, S. A. T. Redfern, G. Catalan, and J. F. Scott, "β phase and γ-β metal-insulator transition in multiferroic $BiFeO_3$," Phys. Rev. B **77**, 014110 (2008).

[190] C. Michel, J.-M. Moreau, G. D. Achenbach, R. Gerson, and W. James, "The atomic structure of $BiFeO_3$," Solid State Commun. **7**, 701 –704 (1969).

[191] F. Kubel and H. Schmid, "Structure of a ferroelectric and ferroelastic monodomain crystal of the perovskite $BiFeO_3$," Acta Crystallogr. B **46**, 698–702 (1990).

[192] J. Wang et al., "Epitaxial $BiFeO_3$ multiferroic thin film heterostructures," Science **299**, 1719–1722 (2003).

[193] J. Wang et al., "Response to comment on epitaxial $BiFeO_3$ multiferroic thin film heterostructures," Science **307**, 1203–1203 (2005).

[194] C. Ederer and N. A. Spaldin, "Weak ferromagnetism and magnetoelectric coupling in bismuth ferrite," Phys. Rev. B **71**, 060401 (2005).

[195] C. Ederer and N. A. Spaldin, "Influence of strain and oxygen vacancies on the magnetoelectric properties of multiferroic bismuth ferrite," Phys. Rev. B **71**, 224103 (2005).

[196] J. B. Neaton, C. Ederer, U. V. Waghmare, N. A. Spaldin, and K. M. Rabe, "First-principles study of spontaneous polarization in multiferroic $BiFeO_3$," Phys. Rev. B **71**, 014113 (2005).

[197] R. Haumont, J. Kreisel, and P. Bouvier, "Raman scattering of the model multiferroic oxide BiFeO3: effect of temperature, pressure and stress," Phase Transitions **79**, 1043–1064 (2006).

[198] M. K. Singh, H. M. Jang, S. Ryu, and M.-H. Jo, "Polarized Raman scattering of multiferroic BiFeO3 epitaxial films with rhombohedral R3c symmetry," Appl. Phys. Lett. **88**, 042907 (2006) 10.1063/1.2168038.

[199] H. Fukumura, H. Harima, K. Kisoda, M. Tamada, Y. Noguchi, and M. Miyayama, "Raman scattering study of multiferroic BiFeO3 single crystal," J. Magn. Magn. Mater. **310**, Proceedings of the 17th International Conference on MagnetismThe International Conference on Magnetism, e367 –e369 (2007).

[200] S. Kamba, D. Nuzhnyy, M. Savinov, J. **S**ebek, J. Petzelt, J. Prokle**s**ka, R. Haumont, and J. Kreisel, "Infrared and terahertz studies of polar phonons and magnetodielectric effect in multiferroic $BiFeO_3$ ceramics," Phys. Rev. B **75**, 024403 (2007).

[201] M. Cazayous, D. Malka, D. Lebeugle, and D. Colson, "Electric field effect on BiFeO3 single crystal investigated by Raman spectroscopy," Appl. Phys. Lett. **91**, 071910 (2007) 10.1063/1.2771380.

[202] M. Cazayous, A. Sacuto, D. Lebeugle, and D. Colson, "Possible interplay between a two phonon mode and high energy magnetic excitations in BiFeO3," Eur. Phys. J. B **67**, 209–212 (2009).

[203] P. Chen, X. Xu, C. Koenigsmann, A. C. Santulli, S. S. Wong, and J. L. Musfeldt, "Size-dependent infrared phonon modes and ferroelectric phase transition in bifeo3 Nanoparticles," Nano Lett. **10**, 4526–4532 (2010).

[204] R. Palai, H. Schmid, J. F. Scott, and R. S. Katiyar, "Raman spectroscopy of single-domain multiferroic $BiFeO_3$," Phys. Rev. B **81**, 064110 (2010).

[205] P. Hermet, M. Goffinet, J. Kreisel, and P. Ghosez, "Raman and infrared spectra of multiferroic bismuth ferrite from first principles," Phys. Rev. B **75**, 220102 (2007).

[206] H. M. Tütüncü and G. P. Srivastava, "Electronic structure and lattice dynamical properties of different tetragonal phases of $BiFeO_3$," Phys. Rev. B **78**, 235209 (2008).

[207] H. M. Tütüncü and G. P. Srivastava, "Electronic structure and zone-center phonon modes in multiferroic bulk BiFeO3," J. Appl. Phys. **103**, 083712 (2008) 10.1063/1.2908865.

[208] M. Goffinet, P. Hermet, D. I. Bilc, and P. Ghosez, "Hybrid functional study of prototypical multiferroic bismuth ferrite," Phys. Rev. B **79**, 014403 (2009).

[209] Y. Wang, J. E. Saal, P. Wu, J. Wang, S. Shang, Z.-K. Liu, and L.-Q. Chen, "First-principles lattice dynamics and heat capacity of BiFeO3," Acta Materialia **59**, 4229–4234 (2011).

[210] E. Borissenko, M. Goffinet, A. Bosak, P. Rovillain, M. Cazayous, D. Colson, P. Ghosez, and M. Krisch, "Lattice dynamics of multiferroic BiFeO3 studied by inelastic x-ray scattering," J. Phys.: Condens. Matter **25**, 102201 (2013).

[211] J. A. Schneeloch et al., "Neutron inelastic scattering measurements of low-energy phonons in the multiferroic $BiFeO_3$," Phys. Rev. B **91**, 064301 (2015).

[212] M. C. Weber, M. Guennou, C. Toulouse, M. Cazayous, Y. Gillet, X. Gonze, and J. Kreisel, "Temperature evolution of the band gap in $BiFeO_3$ traced by resonant Raman scattering," Phys. Rev. B **93**, 125204 (2016).

[213] J. Hlinka, J. Pokorny, S. Karimi, and I. M. Reaney, "Angular dispersion of oblique phonon modes in $BiFeO_3$ from micro-Raman scattering," Phys. Rev. B **83**, 020101 (2011).

[214] V. Shelke, D. Mazumdar, S. Faleev, O. Mryasov, S. Jesse, S. Kalinin, A. Baddorf, and A. Gupta, "Ferroelectric domain scaling and electronic properties in ultrathin BiFeO3 films on vicinal substrates," arXiv:1010.0604 (2010).

[215] H. Naganuma, *Ferroelectrics - physical effects, chapter 16*, edited by M. Lallart (InTech, 2011).

[216] F. Jollet, M. Torrent, and N. Holzwarth, "Generation of projector augmented-wave atomic data: a 71 element validated table in the XML format," Comput. Phys. Comm. **185**, 1246–1254 (2014).

[217] V. I. Anisimov, F Aryasetiawan, and A. I. Lichtenstein, "First-principles calculations of the electronic structure and spectra of strongly correlated systems: the LDA+U method," J. Phys.: Condens. Matter **9**, 767 (1997).

[218] A. I. Liechtenstein, V. I. Anisimov, and J. Zaanen, "Density-functional theory and strong interactions: orbital ordering in Mott-Hubbard insulators," Phys. Rev. B **52**, R5467–R5470 (1995).

[219] P. Ravindran, R. Vidya, A. Kjekshus, H. Fjellvåg, and O. Eriksson, "Theoretical investigation of magnetoelectric behavior in $BiFeO_3$," Phys. Rev. B **74**, 224412 (2006).

[220] Y. Wang, C. L. Zacherl, S. Shang, L. Chen, and Z. Liu, "Phonon dispersions in random alloys: a method based on special quasi-random structure force constants," J. Phys.-Condens. Mat. **23**, 485403 (2011).

[221] Y. Yang, J. Sun, K. Zhu, Y. Liu, J. Chen, and X. Xing, "Raman study of bifeo3 with different excitation wavelengths," Physica B: Condensed Matter **404**, 171–174 (2009).

[222] M. O. Ramirez et al., "Two-phonon coupling to the antiferromagnetic phase transition in multiferroic $BiFeO_3$," Appl. Phys. Lett. **92**, 022511 (2008) 10.1063/1.2829681.

[223] S. J. Clark and J. Robertson, "Energy levels of oxygen vacancies in BiFeO3 by screened exchange," Appl. Phys. Lett. **94**, 022902 (2009) 10.1063/1.3070532.

[224] O. Diéguez, O. E. González-Vázquez, J. C. Wojdeł, and J. Íñiguez, "First-principles predictions of low-energy phases of multiferroic $BiFeO_3$," Phys. Rev. B **83**, 094105 (2011).

[225] P Fischer, M Polomska, I Sosnowska, and M Szymanski, "Temperature dependence of the crystal and magnetic structures of $BiFeO_3$," J. Phys. C: Solid State Physics **13**, 1931 (1980).

[226] J. E. Sipe and E. Ghahramani, "Nonlinear optical response of semiconductors in the independent-particle approximation," Phys. Rev. B **48**, 11705–11722 (1993).

[227] R. Leitsmann, W. G. Schmidt, P. H. Hahn, and F. Bechstedt, "Second-harmonic polarizability including electron-hole attraction from band-structure theory," Phys. Rev. B **71**, 195209 (2005).

[228] N. Tancogne-Dejean, B. S. Mendoza, and V. Véniard, "Effect of material properties on the accuracy of antiresonant approximation: linear and second-order optical responses," Phys. Rev. B **90**, 035212 (2014).

[229] A. A. Maradudin and S. H. Vosko, "Symmetry properties of the normal vibrations of a crystal," Rev. Mod. Phys. **40**, 1–37 (1968).

[230] D. R. Hamann, "Optimized norm-conserving Vanderbilt pseudopotentials," Phys. Rev. B **88**, 085117 (2013).

[231] K. Lejaeghere et al., "Reproducibility in density functional theory calculations of solids," Science **351** (2016) 10.1126/science.aad3000.

[232] P. Haas, F. Tran, and P. Blaha, "Calculation of the lattice constant of solids with semilocal functionals," Phys. Rev. B **79**, 085104 (2009).

[233] E. D. Palik, "Gallium arsenide (GaAs)," in *Handbook of optical constants of solids*, edited by E. D. PALIK (Academic Press, Boston, 1985), pp. 429–443.

[234] D. Lockwood, G. Yu, and N. Rowell, "Optical phonon frequencies and damping in AlAs, GaP, GaAs, InP, inas and insb studied by oblique incidence infrared spectroscopy," Solid State Commun. **136**, 404–409 (2005).

[235] H. R. Gutiérrez, N. Perea-López, A. L. Elías, A. Berkdemir, B. Wang, R. Lv, F. López-Urías, V. H. Crespi, H. Terrones, and M. Terrones, "Extraordinary room-temperature photoluminescence in triangular WS2 monolayers," Nano Lett. **13**, 3447–3454 (2013).

LIST OF FIGURES

LIST OF TABLES